UNIVERSITY OF LJUBLJANA
FACULTY OF MATHEMATICS AND PHYSICS
PHYSICS DEPARTMENT

Elvedin TAHIROVIĆ

Aerogel Ring Imaging Cherenkov Detector with Silicon Photomultipliers

Doctoral thesis

ADVISER: Dr. Rok PESTOTNIK

Ljubljana, 2016

UNIVERZA V LJUBLJANI
FAKULTETA ZA MATEMATIKO IN FIZIKO
ODDELEK ZA FIZIKO

Elvedin Tahirović

DETEKTOR OBROČEV ČERENKOVA S SILICIJEVIMI FOTOPOMNOŽEVALKAMI

Doktorska disertacija

MENTOR: doc. dr. Rok Pestotnik

Ljubljana, 2016

Izjava o avtorstvu in objavi elektronske oblike

Izjavljam:

— da sem doktorsko disertacijo z naslovom *Detektor obročev Čerenkova s silicijevimi fotopomnoževalkami* izdelal kot rezultat lastnega raziskovalnega dela pod mentorstvom dr. Roka Pestotnika,

— da je elektronska oblika dela identična s tiskano obliko in

— da Fakulteti za matematiko in fiziko Univerze v Ljubljani dovoljujem objavo elektronske oblike svojega dela na spletnih straneh Repozitorija Univerze v Ljubljani.

Ljubljana, dne 14. februar 2016 Podpis:

To work, to finish, to publish.
FARADAY

Zahvala

Hvala mentorju dr. Roku Pestotniku za vodenje, spremljanje in potrpežljivost. Hvala prof. dr. Peteru Križanu, brez katerega ta doktorat ne bi bil možen, ter ker je verjel vame. Hvala sodelavcem z Oddelka za eksperimentalno fiziko osnovnih delcev za ustvarjalno okolje in korisne nasvete, predvsem prof. dr. Samu Korparju in dr. Roku Dolencu. Hvala Juretu Erženu za tehnično pomoč pri izdelavi detektorja.

To disertacijo posvečam svojim staršem in sestri, ki so me spremljali na moji življenski poti.

Abstract

An array of 8×8 SiPMs was characterised as a position sensitive single photon sensor for Ring Imaging Cherenkov (RICH) detector. To improve the acceptance of the array, light concentrators, in a form of truncated pyramids, were designed and machined from borosilicate glass. A very high number of photons per Cherenkov ring, about 35, were detected with a prototype module in a particle beam at DESY. Light concentrators performance was further investigated on the bench and with Monte Carlo simulations. Losses introduced by detection of timing information only were estimated.

Keywords: Ring imaging Cherenkov counter, Silicon photomultiplier, Solid state detector, Light concentrators

PACS:

— **29.40.Ka Cherenkov detectors**

— **29.40.Gx Tracking and position sensitive detectors**

— **29.40.Wk Solid state detectors**

— **42.79.Gn Optical waveguides and couplers**

Izvleček

Matrika iz 8×8 SiPM-ov je bila testirana kot krajevno občutljiv senzor posameznih fotonv v detektoru obročev Čerenkova (RICH). Za zvišanje geometrijksega izkoristka matrike so bili dizajnirani zbiralci svetlobe in nato izdelani od borosilikatnega stekla. Izredno veliko število fotonov na obroč Čerenkova, okoli 35, je bilo zaznano z prototipom fotonskega modula v testnem žarku na DESY. Delovanje zbiralcev svetlobe je nadalje raziskano na optični klopi in z simulacijo Monte Carlo. Ocenjene so izgube zaradi merenja samo časovne informacije.

Ključne besede: Detektor obročev Čerenkova, Silicijeva fotopomnoževalka, Detektorji iz trdne snovi, Zbiralniki svetlobe

PACS:

— **29.40.Ka Detektorji sevanja Čerenkova**

— **29.40.Gx Detektorji sledi in pozicijsko občutljivi detektorji**

— **29.40.Wk Detektorji iz trdne snovi**

— **42.79.Gn Optični vodniki in spojniki**

Contents

Chapter 1

Introduction

One of the unanswered cosmological questions is why matter prevails over antimatter in the visible Universe. The Standard Model of elementary particles incorporates a mechanism which can explain qualitatively the asymmetry between the matter and antimatter, namely the Kobayashi-Maskawa model of CP violation. However, the Kobayashi-Maskawa mechanism cannot explain the observed scale of the asymmetry.

In the search for an answer to this asymmetry, a dedicated experiment, such as Belle II, studies the decays of the B-meson, a particle that contains a b-quark and another quark. For the studies B-factories employ two methods: precision measurements of the Standard Model allowed decays (such as $b \to c$) and studies of the Standard Model suppressed decays (such as $b \to s\gamma$). In their final states these decays contain lighter hadrons (pions and kaons), whose separation over their whole kinematic range is crucial for studies of B meson decays. Furthermore, decays of interest have small branching ratios and the studies require a high luminosity. However, a high luminosity produces a high background that makes the particle identification difficult, and motivates experimentalists to develop new devices.

A charged particle is uniquely identified if its mass m and charge Z are known. The charge can be inferred from the sign of the curvature of particle track in a magnetic field. The mass is given by the formula that expresses the momentum p as function of the mass and velocity v:

$$p = \gamma m v,$$

where γ is the Lorentz factor. The momentum can be calculated from the curvature of the particle track in the magnetic field. Therefore, the only unknown is the particle velocity v. Among different effects which can be used to determine it, Cherenkov effect is used in Ring Imaging Cherenkov (RICH) detectors. When a charged particle traverses a medium (radiator) of refractive index n with a velocity higher than the local phase velocity of light c/n, it emits a low intensity light at an angle θ, called Cherenkov angle, given by:

$$\cos\theta = \frac{c}{v\ n}.$$

Since the refractive index of the radiator n is known, the Cherenkov angle can be exploited to determine the particle velocity v. In a typical RICH, the radiator emits a few photons (order of 10) in a cone around the particle trajectory. The cone

becomes a ring when projected on the photon detector surface. A position sensitive photon detector, able to detect single photons, is needed to reconstruct the ring and determine the angle θ. Moreover, a RICH is usually operated in a magnetic field and the photon detector insensitive to high magnetic fields is required.

The previous work of the photo-detection group at Experimental Particle Physics Department at Jožef Stefan Institute motivated me to test an alternative single photon sensor in a RICH prototype. The initial parameters of the prototype are similar to the future aerogel RICH (ARICH) sub-detector in the Belle II spectrometer. Belle II ARICH uses Hybrid Avalanche PhotoDiode (HAPD) which is being developed with the Japanese producer, Hamamatsu Photonics, as the baseline photon detector. In despite of their numerous promising characteristics, HAPDs have certain disadvantages, among which are a high voltage (8 kV) needed for its operation, sensitivity to the external magnetic field, fragility and high cost.

As an alternative to the HAPD, other position sensitive photon detectors capable of single photon detection were considered. Multi-anode photomultiplier tubes were soon discarded because their efficiency was highly reduced in the magnetic field. Another option was a Micro-Channel Plate PhotoMultiplier Tube (MCP-PMT). However, the number of registered photons was lower than in the case of HAPD and their operation degraded significantly with time.

I studied a relatively novel device, Silicon Photomultiplier (SiPM), semiconductor photon detector that is capable of single photon detection. SiPM is basically an array of reversely biased photo-diodes operating in the limited Geiger regime, hence its another name in the literature: Geiger-regime Avalanche PhotoDiode (G-APD). Since different institutes and producers use their own names that point out either the underlying structure or the use of the device, in the literature one can find it under Multi-Pixel Photon Counter (MPPC, used by Hamamatsu), Single Photon Avalanche PhotoDiode (SPAD), Multi-pixel Avalanche PhotoDiode (MAPD) and similar.

The thesis is organised as follows. In the second chapter the motivation to employ RICH detector in particle detection are explained, together with its basic principles and parameters. The needs for the photon sensor are summarised and the efficiencies of different photon sensors compared. The third chapter is devoted to the silicon photomultiplier operation basics, its characteristics and previous studies as the sensor for RICH. The fourth chapter describes the design of the prototype photon detector, methods used for the signal detection and the experimental set-up for the characterization of the SiPM and detector prototype. The fifth chapter describes the experimental set-up in the test beam and presents the results of the test. The obtained results are discussed in the sixth chapter.

Chapter 2

Ring Imaging Cherenkov Counter

A brief summary of physics motivation to construct B-factories is given at the beginning. The need for the RICH subdetector is explained. Belle II ARICH properties are listed, together with the geometry, radiator and photon detector characteristics. The alternative sensor, SiPM, and its characteristics are described. The key figure for the comparison, the number of expected photons, is calculated.

2.1 Physics Motivation

When observed from the Earth our Universe seems to be made from the matter only, and no evidence of the antimatter can be seen. Such an asymmetry of the matter over the antimatter in the Universe is extraordinary. Yet, there is no *a priori* reason to believe that in the initial state our Universe did not contain the same amount of both. How did the anti-matter disappear? This is but one of the questions to which the physicists are trying to find an answer.

The conservation laws in physics result as a symmetry of a system to certain transformations. The invariance of the equations with respect to translation in time results in the energy conservation in the system. The invariance of the equations with respect to position results in the conservation of momentum, and with respect to rotations in space in conservation of angular momentum. The dynamics of the elementary particles is described by field theory, called the Standard Model [1]. In a field theory Noether's theorem states that the invariance of the Lagrangian to a certain transformation leads to the conserved generalised charge. The group theory elegantly describes such symmetries which can be continuous or discrete. The continuous symmetries are translations and rotations in space-time. Discrete symmetries involving space and time are parity symmetry P (left-right inversion) and time inversion T (symmetry to the change of time sign). Discrete symmetry in an internal (abstract) field space is charge conjugation C.

The Standard Model of elementary particles contains three generations of leptons and quarks, given in the Table 2.1. Every fermion in the table has its own anti-particle. The interactions between these fermions are described by field theory with the electroweak gauge group $SU_L(2) \times U_Y(1)$. After a spontaneous symmetry breaking, fermions (except neutrinos) and three gauge bosons obtain masses. By now, it is generally accepted as the theory of elementary particle physics; it did not only successfully explain the observed results, but predicted in advance the existence of the new particles (charm, bottom, top quark) and phenomena, such as

Leptons	Quarks
e, μ, τ	u, c, t
ν_e, ν_μ, ν_τ	d, s, b

Table 2.1: Fermions in Standard Model. Every fermion f has its own anti-particle (not shown here), denoted with a bar $\bar{f}$.

flavour-conserving neutral currents.

It was believed that C, P and T symmetry are conserved in reactions between particles or decays of particles. To test the parity violation, Lee and Yang proposed ([2]) a series of experiments, and, following their suggestions, Wu demonstrated the parity violation in weak interaction in 1957 [3]. The combined CP invariance seemed to be preserved, until the study by Cronin *et al.* [4] in 1964. They studied the system of neutral kaons and showed that the K_L, while decaying mostly to CP-even state containing two pions, can decay also to the CP-odd state with three pions (although with small branching ratio of 10^{-3}).

Sakharov had demonstrated in 1967 that CP-violation can lead to the baryon asymmetry of the Universe [5]. Japanese physicists Kobayashi and Maskawa proposed [6] in 1972 that including a third quark doublet (t, b), a complex phase is introduced in the model, allowing the asymmetry of the matter and anti-matter through the mixing, as observed in the neutral kaon system. Kobayashi and Maskawa obtained the Nobel prize in physics in 2008.

The quark mixing is introduced in the Standard Model by a rotation, in an internal space, of the down-type quark fields with a matrix, called Cabbibo-Kobayashi-Maskawa (CKM) matrix. As a result of spontaneous symmetry breaking, the charged current $W^\pm$ interactions couple to physical up-type and down-type quarks with coupling given by [1]:

$$W = -\frac{g}{\sqrt{2}} \begin{pmatrix} u & c & t \end{pmatrix} \gamma^\mu W_\mu^+ V_{\mathrm{CKM}} \begin{pmatrix} d \\ s \\ b \end{pmatrix} + h.c. \tag{2.1}$$

where g is the coupling constant, γ_μ are the Dirac matrices and V_{CKM} is a unitary 3×3 matrix connecting the mass eigenstates (physical) d, s, b and the flavour eigenstates d', s', b' of the down-type quarks:

$$\begin{pmatrix} d' \\ s' \\ b' \end{pmatrix} = V \begin{pmatrix} d \\ s \\ b \end{pmatrix} \tag{2.2}$$

The CKM matrix has 9 complex elements:

$$V_{CKM} = \begin{pmatrix} V_{ud} & V_{us} & V_{ub} \\ V_{cd} & V_{cs} & V_{cb} \\ V_{td} & V_{ts} & V_{tb} \end{pmatrix} \tag{2.3}$$

A general complex matrix with three generations $n = 3$ has 2×3^2 real parameters and unitarity condition brings 3^2 constraints. Of these 9 parameters, 3 can be regarded as Euler angles associated with rotations in a 3-dimensional space, and the other 6 are called phases. All the phases do not have physical meaning as they can be absorbed in the redefinition of the quark fields that form the basis of representation. From these 3 up-fields and 3 down-fields, 5 can be redefined and there is 1 measurable complex phase.

There are different parametrisations of the CKM matrix in terms of the four independent parameters, namely three angles and one phase. The original parametrisation by Kobayashi and Maskawa, slightly modified[1], is given by the Particle Data Group (PDG, [1]):

$$V_{\mathrm{CKM}} = \begin{pmatrix} c_{12}\, c_{13} & s_{12}\, s_{13} & s_{13}\, e^{-i\,\delta} \\ -s_{12}\, c_{23} - c_{12}\, s_{23}\, s_{13}\, e^{i\,\delta} & c_{12}\, c_{23} - s_{12}\, s_{23}\, s_{13}\, e^{i\,\delta} & s_{23}\, c_{13} \\ s_{12}\, s_{23} - c_{12}\, c_{23}\, s_{13}\, e^{i\,\delta} & -c_{12}\, c_{23} - s_{12}\, c_{23}\, s_{13}\, e^{i\,\delta} & c_{23}\, c_{13} \end{pmatrix} \tag{2.4}$$

Here $c_{ij} \equiv \cos\theta_{ij}$, $s_{ij} \equiv \sin\theta_{ij}$, with i and j labelling quark generations. The complex phase is $i\delta$. The fact that the elements exhibit a pronounced hierarchy, that is, the diagonal elements are close to unity while the off-diagonal elements are small, is usually expressed using the Wolfenstein parametrisation. The CKM matrix in the Wolfenstein parametrisation can be obtained introducing a small parameter λ and the parameters $A, \bar{\rho}$ and $\bar{\eta}$ be of order one:

$$\sin\theta_{12} = \lambda = \frac{|V_{us}|}{\sqrt{|V_{ud}|^2 + |V_{us}|^2}} \tag{2.5}$$

$$\sin\theta_{23} = A\lambda^2 = \lambda|\frac{V_{cb}}{V_{us}}| \tag{2.6}$$

$$\sin\theta_{13}\, e^{i\delta} = V_{ub}^* = \frac{A\lambda(\bar{\rho} + i\bar{\eta})\sqrt{1 - A^2\lambda^4}}{\sqrt{1-\lambda^2}[1 - A^2\lambda^4(\bar{\rho} + i\bar{\eta})]}. \tag{2.7}$$

The coupling strengths V_{ij} in the CKM matrix are not determined by theory. They are the free parameters of the model and the only way to determine them is to measure them experimentally. It is the goal of *flavour physics* to put constraints on these parameters. The unitarity conditions $V_{CKM}\, V_{CKM}^* = 1$ mean that any linear combination of two rows or of two columns is orthogonal. For example, the first and the third column give:

$$V_{ud}\, V_{ub}^* + V_{cd}\, V_{cb}^* + V_{td}\, V_{tb}^* = 0 \tag{2.8}$$

This equation can be visualised as a triangle in the complex plane. The unitarity triangle is usually given in the Wolfenstein parametrisation, where the apex of the triangle is defined with $(\bar{\rho}, i\bar{\eta})$:

$$\bar{\rho} + i\bar{\eta} = -\frac{V_{ud}V_{ub}^*}{V_{cd}V_{cb}^*}, \tag{2.9}$$

as shown in Fig. 2.1.

[1]The modification concerns the attachment of the complex phase to different terms in the CKM matrix.

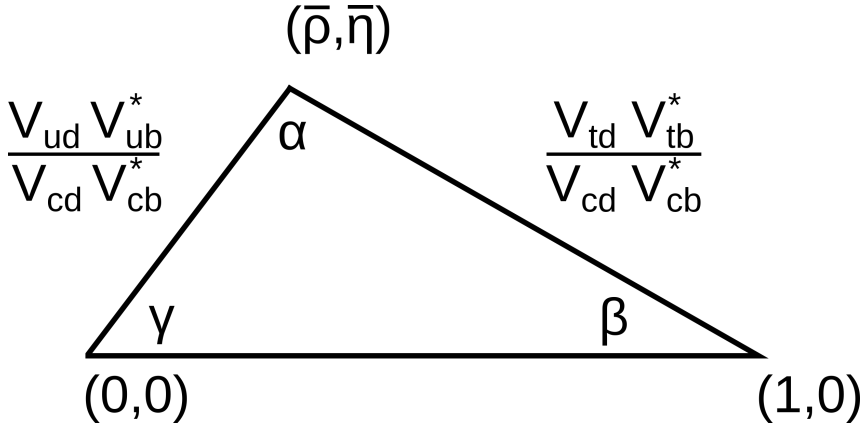

Figure 2.1: Unitarity triangle in complex plane expressed with Wolfenstein parametrisation.

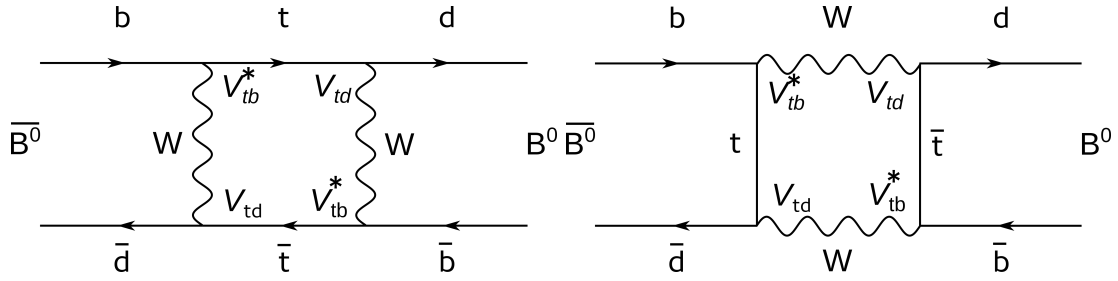

Figure 2.2: Dominant quark line diagrams for $B^0 - \bar{B}^0$ mixing.

The experiments dedicated for flavour physics studies, called B-factories, have been constructed. They are colliding experiments, in which the energy in the centre-of-mass is equal to the rest mass of $\Upsilon(4S)$ resonance. The resonance $\Upsilon(4S)$ decays almost exclusively to $B^0\bar{B}^0$ and B^+B^- pairs, each containing one b quark and a low mass quark (u,d,s). The studies of decays of B-mesons are a good tool for determination of the CKM angles and phase. The first measurement of the angle ϕ_3 was given by Belle [7], by analysis of $B \to DK$ decays, where the D subsequently decays to $K_S\pi\pi$ [8]. Belle observed the mixing-induced time-dependent CP violation in the neutral B meson system and provided the measurement of $\sin 2\phi_1$ [9]. The box diagrams responsible for B mixing are given in Fig.2.2. Eventually, the mixing in the $D - \bar{D}$ was discovered by Starič *et al.* [10].

2.2 Belle II

The upgrade of Belle, Belle II [11] is under construction at the future SuperKEKB accelerator in Tsukuba, Japan. The physics program at Belle II includes [12]:

— Precise measurement of angle γ.

— The mixing was observed in the neutral charmed meson D^0 system, but there was no evidence of CP violation. However, higher sensitivity of Belle II might give a final answer if there are physics phenomena beyond Standard Model involved.

— Rare decays $b \to s\bar{s}s$ would clarify the difference of measured $\sin 2\beta$ from $B^0 \to \phi K_S$ and $B \to J/\psi K_S$.

— Charmless 2-body B meson decays are rare processes, suppressed by a small $|V_{ub}|$ element, which would benefit from the higher luminosity.

For all these processes particle identification for the suppression of background processes is crucial.

Belle II is intended to reach the integrated luminosity of 8×10^{35} cm^{-2} s^{-1}, about 40 times higher than Belle. The cross-sectional view of the Belle II, compared to Belle is shown in Fig. 2.3. Two beams of particles are accelerated in the storage rings, 7.0 GeV electrons e^- in high energy ring (HER) and 4.0 GeV positrons e^+ in low energy ring (LER). The particles in the beams collide at the interaction point at a crossing angle of 83 mrad. Because of the asymmetry in the energy, the particles are boosted with $\beta\gamma = 0.28$ in the laboratory frame (towards right in Fig. 2.3). The main design parameters are listed in the Table 2.2. The whole spectrometer is immersed in a magnetic field, $B = 1.5$ T, produced by a solenoid, which enables the determination of particle momentum p and charge Z.

Positioned around the interaction point are the following sub-detector systems:

— Pixel Detector (PXD) and Silicon Vertex Detector (SVD) both provide the information about decay vertices with high accuracy and in full Belle II angular acceptance $17° < \theta < 150°$;

— Central Drift Chamber (CDC) provides the information about tracks of the charged particles, their momentum and the energy loss $\mathrm{d}E/\mathrm{d}x$;

— Time-of-Propagation (TOP) counter provides the particle identification information in the barrel region of the spectrometer;

— Aerogel Ring Imaging Cherenkov (ARICH) counter provides the particle identification information in the forward end-cap region.

— Electromagnetic Calorimeter (ECL) providing the detection of photons and determination of their energy;

— K_{L}^0 and μ (KLM) detector detecting muons that deposit the electromagnetic energy or range out eventually and hadronic showers produced by long living kaons.

ARICH is intended to replace Aerogel Cherenkov Counter (ACC) in the forward end-cap region in Belle spectrometer. The space dedicated for ARICH is 280 mm in the forward end-cap, between CDC and ECL. The small space has narrowed the possibilities for the choice of image focusing, as well as other parameters. This will be discussed in the Section 2.4.

Fig. 2.4 shows the kaon momentum distribution together with $\cos\theta$ distribution for two typical processes, where θ is the angle between B meson and the two-body system. In the process called tagging, B meson decays to a final state containing pions and kaons through charmed D meson: $B \to D^{(*)}\pi_s$. The D meson takes most of the momentum in the laboratory frame, therefore the π_s has low momentum. D meson decays subsequently to various channels containing kaons and pions. This

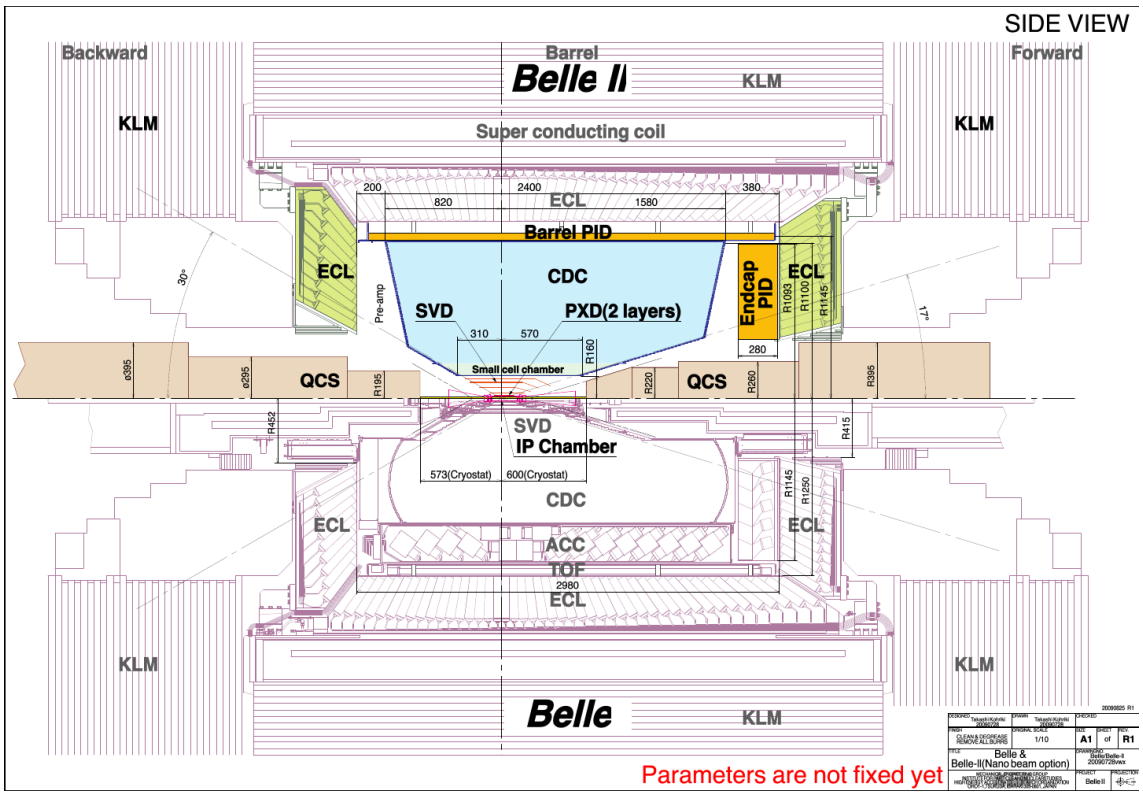

Figure 2.3: Upgraded, Belle II spectrometer (top half) as compared to the Belle detector (lower half) [12].

	e^+	e^-
Energy	4.0 GeV	7.0 GeV
Crossing angle	83 mrad	
Boost	$\beta\gamma = 0.28$	
IP tube diameter	3 mm	
Typical trigger rate	20 kHz	
Magnetic field	1.5 T	

Table 2.2: Belle II design parameters summary.

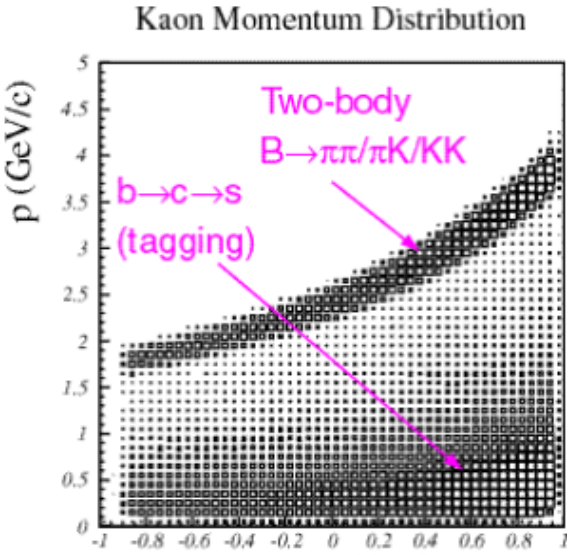

Figure 2.4: Kaon momentum distribution *vs.* $\cos\theta$ distribution for two typical processes: two-body B decays to lighter hadrons $B \to \pi\pi/\pi K/KK$ and tagging process $b \to c \to s$ (presented on the quark level). Kaon momentum lies mostly in the interval $p \in [1.5, 4.0]$ GeV/c.

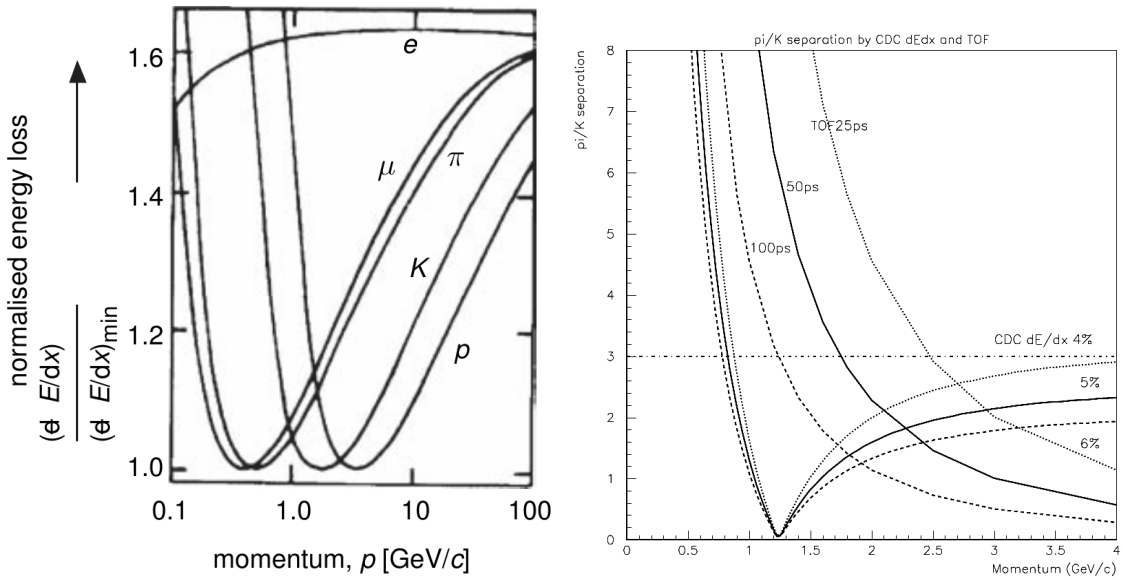

Figure 2.5: Left: Normalised energy loss as function of particle energy for electron, muon, pion, kaon and proton in the same material [14]. Right: Kaon and pion separation as obtained from energy loss and time-of-flight (TOF) measurements with Belle II sub-detectors [11].

process is represented on the quark level as a transition $b \to c \to s$. Since it provides a very clean sample of reconstructed B mesons, it is called "golden channel" and is often used for tagging of the B meson [13]. The tagging means determining the flavour (B^0 or $\bar{B}^0$) of the initial meson and is crucial step for measurement of the $B - \bar{B}$ mixing and CP violation. The second typical process is a two body B meson decay into a final state containing pions and kaons ($b \to d, s$ on the quark level).

Various phenomena can be exploited to determine the velocity of the particle, and thus for its identification. One of them is the energy deposited by particle per unit path in the detector, as measured by the CDC in Belle II. This energy loss is a function of particle velocity β and is given by Bethe-Bloch formula, which can be written for different particles in the same material as:

$$-\frac{\mathrm{d}E}{\mathrm{d}x} = Z^2 f(\beta) \tag{2.10}$$

where Z is the charge of the particle and $f(\beta)$ is only function of the particle velocity. An example of the energy loss $-{}^{\mathrm{d}E}/_{\mathrm{d}x}$ calculated with Bethe-Bloch formula is given in Fig. 2.5, left. However, in the kinematic region interesting for Belle II, $E_{\pi,K} = 1 - 4$ GeV, the stopping power for kaons and pions is almost the same or very close to each other and impractically large detectors would have to be used ($\sim$ 10 m). The same argument goes for the time-of-flight (TOF) method in this kinematic region (Fig. 2.5, right). Some other means has to be employed and in the case of B-factories it is commonly a counter employing the Cherenkov radiation.

2.3 Cherenkov effect

In 1934 Cerenkov started a series of experiments in which he studied the bluish feeble light, present around strong radioactive sources [15]. Qualitatively, the phenomenon can be explained by classical theory of dipole radiation [16]. When a charged particle traverses a medium, it polarises the atoms of that medium which become electrical dipoles. The time variation of the dipole field results in the radiation of electro-magnetic waves. If the velocity of the particle v is smaller than the phase velocity of light in that medium c/n (n is the refractive index of the medium), the dipoles follow the particle, the field is symmetric around the particle and when integrated over all dipoles, the field vanishes. If the velocity of the particle v is greater than the phase velocity of light, the dipole field is asymmetric and the dipole moment does not vanish, which leads to the emission of electro-magnetic waves. The angle of the emitted photon depends on the particle velocity $\beta = {}^{v}/_{c}$ and the refractive index n:

$$\cos\theta = \frac{1}{\beta\, n}. \tag{2.11}$$

The radiation forms a cone whose apex is at the particle position and whose axis is along the particle path. The polarization of the photon is perpendicular to the surface of the cone.

The theory of the radiation was proposed by Frank and Tamm in 1937 [17]. Their calculation gives the number of emitted photons per wavelength interval $\mathrm{d}\lambda$ per traversed path length $\mathrm{d}x$:

$$\begin{aligned} \frac{\mathrm{d}^2 N}{\mathrm{d}\lambda\, \mathrm{d}x} &= 2\pi\alpha \left(1 - \frac{1}{\beta^2\, n^2}\right) \frac{1}{\lambda^2} \\ &= 2\pi\alpha\, \sin^2\theta\, \frac{1}{\lambda^2}, \end{aligned} \tag{2.12}$$

where λ is the wavelength of the emitted photon. Integrating the radiator width d leads to:

$$\frac{\mathrm{d}N}{\mathrm{d}\lambda} = 2\pi\alpha\, d\, \sin^2\theta\, \frac{1}{\lambda^2} \tag{2.13}$$

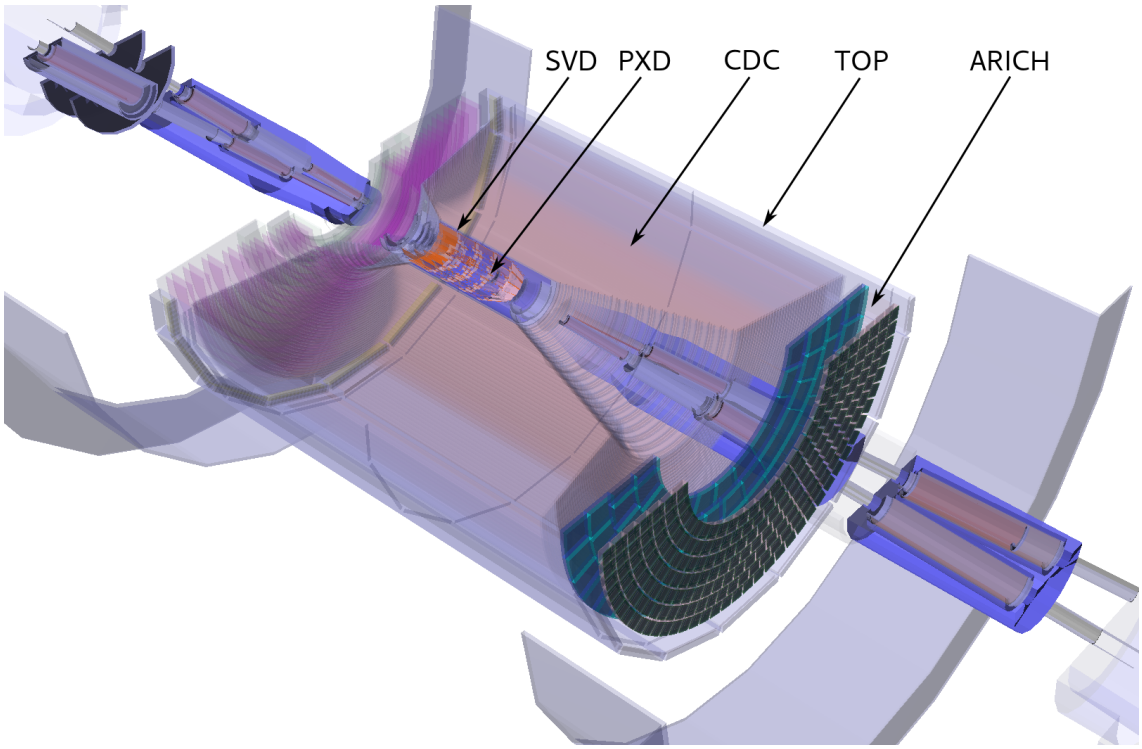

Figure 2.6: The inner sub-detectors in Belle II spectrometer. ARICH is on the right with two rings of aerogel tiles (blue) and photon detector modules positioned in 6 concentric rings (dark green).

2.4 Belle II RICH

For the identification of particles in the forward end-cap of Belle II spectrometer, aerogel RICH (ARICH) is under construction. As already said, it is positioned in the end-cap region, inside a 280 mm wide volume between the CDC and ECL (Fig. 2.6). The short description follows, while the detailed description, requirements and physics impact can be found in Belle II Technical Design Report [12]. The main elements of ARICH, sketched in Fig. 2.7, are:

1. Radiator, consisting of two layers of silica aerogel where the Cherenkov photons are emitted,
2. Expansion volume to allow the photons to form rings on the photon detector surface,
3. Array of position sensitive photon detector capable of detecting single photons,
4. Read-out electronics for the photon detector.

A specificity of the ARICH is that it uses *proximity focusing* and no optical elements to focus the ring image onto the photon detector plane. Proximity focusing was proposed by Seguinot for the DELPHI/LEP experiment [18]; it relies on the thinness of the radiator and a large lever arm to produce useful image. It is specially suited for the Belle II upgrade, where the use of mirrors or lenses for focusing would be difficult, because there is only 280 mm space in the end-cap region available for the particle identification sub-detector.

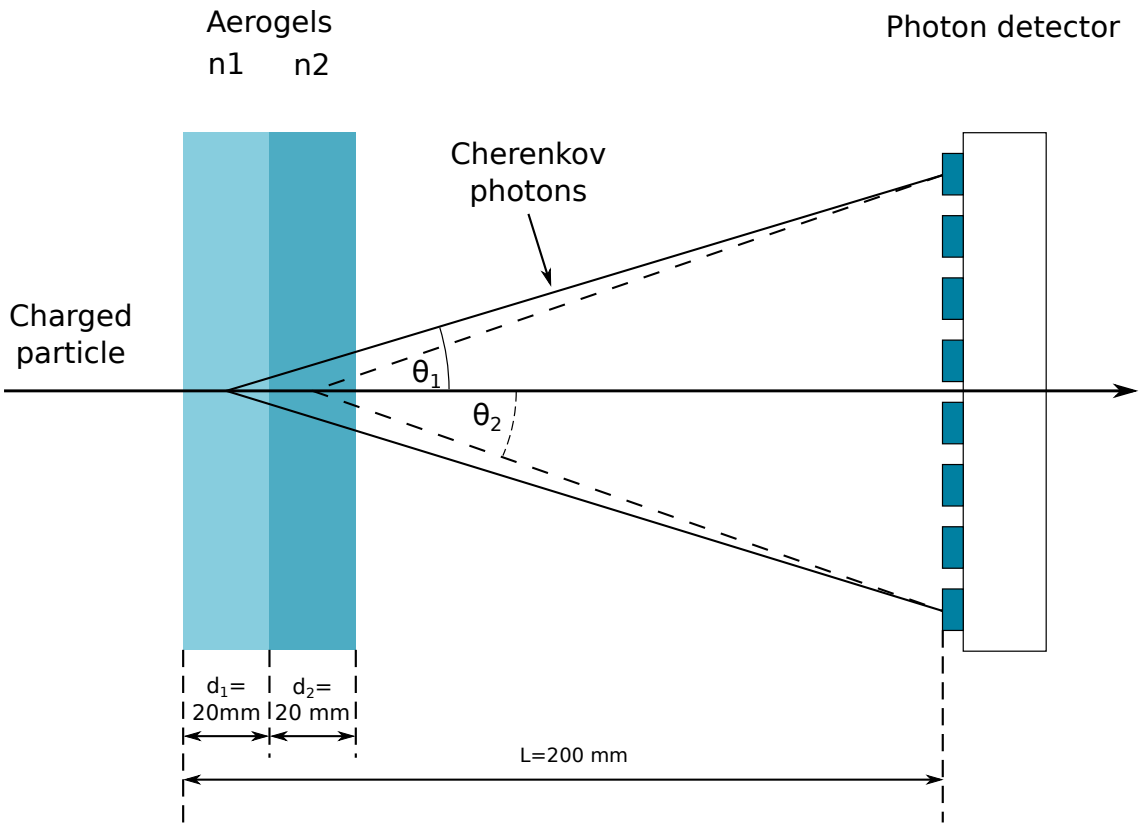

Figure 2.7: Schematic drawing of proximity focusing RICH with non-homogeneous aerogel as radiator.

The Cherenkov angle of photon produced by pions and kaons traversing radiator with $n = 1.0485$, in the kinematic range from 0.5 to 4 GeV/c, is given in Fig. 2.8. The difference between the two particle species $\delta\theta = \theta_\pi - \theta_K = 23.5$ mrad at $p = 4$ GeV/c and the requirement of the upgrade is that the particle identification should be better than 4σ. In that case, the Cherenkov angle error per particle track σ_{track} should be:

$$\sigma_\theta < \frac{23.5}{4} \text{ mrad} = 5.9 \text{ mrad}. \tag{2.14}$$

As the number of the detected photons N_{det} rises, the error of the Cherenkov angle measurement decreases. The error per particle track σ_{track} is given as the error on the mean of the single photon errors σ_θ (supposing that the number of background hits is low):

$$\sigma_{track} = \frac{\sigma_\theta}{\sqrt{N_{det}}}. \tag{2.15}$$

The requirement for separation can be achieved if:

— There are enough photons (at least 10) detected for every ring image for at least one of the particle species.

— Photon detector position resolution of a few mm, presuming the lever arm of $L = 200$ mm and the radiator length of $d = 40$ mm.

A longer radiator would produce more photons, but the resolution of the Cherenkov angle degrades due to emission point error (Fig. 2.9, left). There is an optimal

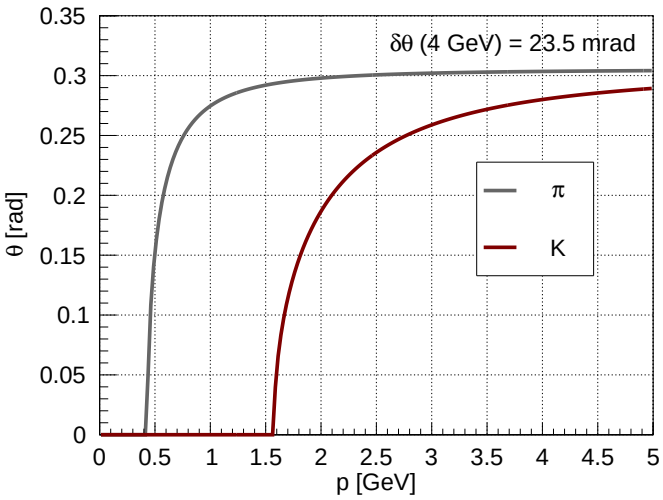

Figure 2.8: Cherenkov angle in aerogel, with refractive index $n = 1.0485$, as a function of particle type and momentum. The angle difference at $p = 4$ GeV/c (upper kinematic limit for Belle II) is $\delta\theta = 23.5$ mrad.

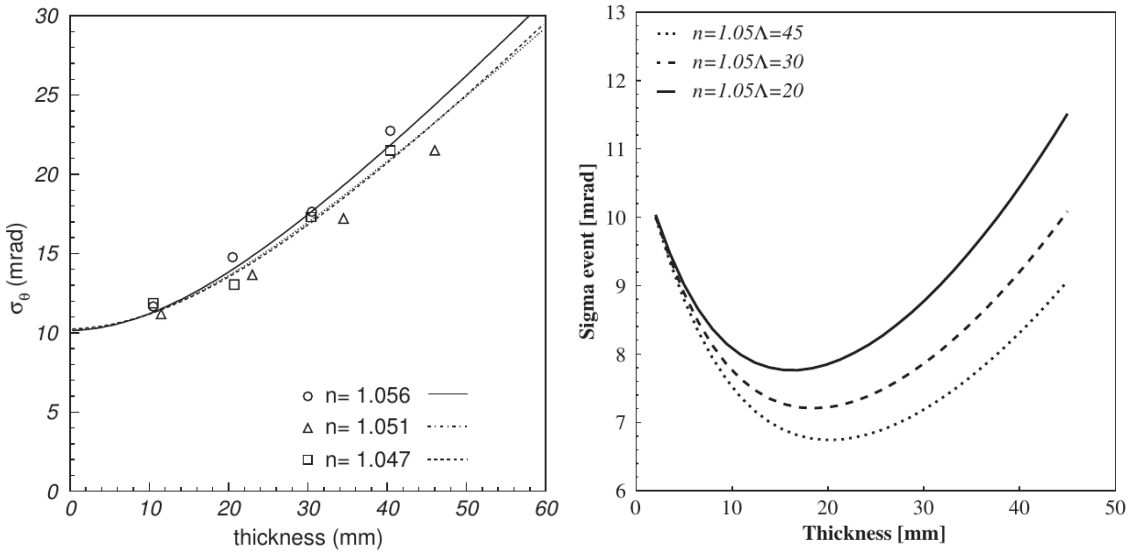

Figure 2.9: Left: Measured error for single photon as function of the radiator thickness. Right: The variation of the resolution σ_{track} with radiator thickness in the case of a single radiator proximity focusing RICH, for three different transmission lengths Λ [mm] at 400 nm. [20]

thickness and it was found to be $d = 20$ mm for several aerogel samples with different refractive indices [19, 20] (Fig. 2.9, right).

2.4.1 Radiator

Another specificity of Belle II ARICH is the use of *non-homogeneous* radiator [20, 21]. By using two layers of aerogel, the number of photons can be enlarged while keeping approximately the same angle error σ_θ. Two radiators of slightly different refractive indices n_1 and n_2 are chosen so that the emitted ring images with θ_1 and θ_2, respectively, overlap on the photon detector surface (Fig. 2.7). Such tuning

of refractive indices is possible because aerogels can be produced with the desired refractive index in the diapason $n \in 1.0026 - 1.26$ [22]. The condition for overlap is:

$$L_1 \tan\theta_2 = (L - \frac{d_1}{2}) \tan\theta_1, \tag{2.16}$$

where $L_1 = L - d_1 - {}^{d_2}/_2 = 190$ mm is the distance between the centre of the downstream radiator and the photon detector, and d_1, d_2 are the widths of upstream and downstream aerogel tiles, respectively. This condition can be used to obtain the approximate difference between the indices:

$$\delta n = n_2 - n_1 = \frac{d}{n_1 L_1}[n_1^2 - 1 - \frac{m^2 c^2}{p^2}], \tag{2.17}$$

where m and p are the particle mass and momentum. Fixing the refractive index of the upstream aerogel $n_1 = 1.04$, and taking the particle to be pion with $p = 4$ GeV/c, the optimal difference is found to be $\delta n = 0.009$. A Monte Carlo simulation shows that the error as function of difference $\sigma(\delta n)$ has a broad minimum, and the difference $\delta n \pm 0.002$ increases the error by $\sigma = 0.1$ mrad [23].

Silica aerogel is an amorphous, highly porous solid of silicon dioxide (SiO_2). Its refractive index can be related to its bulk density:

$$n = 1 + k\rho, \tag{2.18}$$

where ρ is the density and k is a constant. The density depends on the silica-to-air volume ratio (typically 1:9) which is tunable during the production process and therefore can be used to produce aerogel with the desired refractive index [24]. The aerogel has been previously employed in threshold Cherenkov counters, but first measurement to explore the feasibility of using aerogel for imaging was by Fields *et al.* [25]. The new improvements in the production of low-refraction (1.013) aerogels [26] made the way to large scale implementation. Ypsilantis and Seguinot proposed the use of aerogel in RICH for the new LHC-B experiment [27]. However, HERMES experiment was the first large scale experiment that used RICH with aerogel as radiator [28].

The size of silica particles is on the order of 10 nm and the physical processes that play important role for optical photons are absorption and Rayleigh scattering. The transmittance T of an aerogel tile of width d is the ratio of the photons that pass non-scattered through the forward side of aerogel and the photons that enter the aerogel. It can be expressed as:

$$T(\Lambda) = e^{-d/\Lambda(\lambda)}, \tag{2.19}$$

where $\Lambda(\lambda)$ is the attenuation length, which has the contribution from the absorption length Λ_A and the (Rayleigh) scattering length Λ_S:

$$\frac{1}{\Lambda(\lambda)} = \frac{1}{\Lambda_A(\lambda)} + \frac{1}{\Lambda_S(\lambda)}, \tag{2.20}$$

The absorption and scattering length can be determined from two experimental curves in Fig. 2.10, left [29]. The scattering is dominant process below 600 nm and the absorption above it. In the UV-region, the absorption length was fitted with a

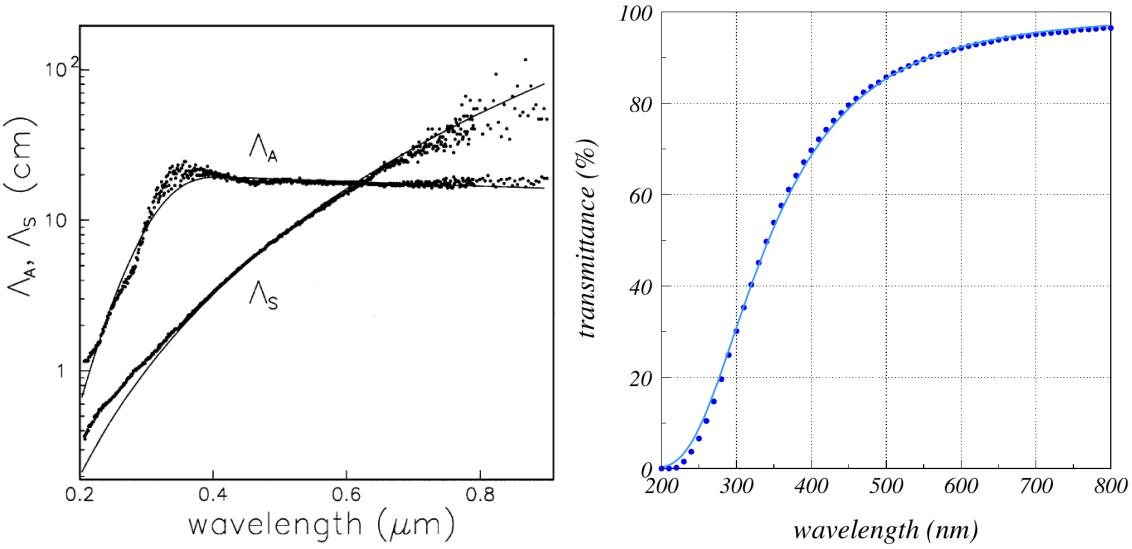

Figure 2.10: Left: The absorption and scattering lengths determined from the measurements [29]. The fit to Λ_S assumes a function of λ^4, the fit to Λ_A a complex λ-dependence function. Right: Transmittance of aerogel with $n = 1.65$ [12].

$\propto \lambda^{-8}$ dependence and becomes nearly constant in the visible region of wavelengths, while the Rayleigh scattering was fitted with $\propto \lambda^{-4}$ dependence.

The measured transmittance of an aerogel sample with refractive index $n = 1.65$ is given in Fig. 2.10, right. It is fitted with Hunt formula which assumes that the scattering cross section varies with λ^{-4} and that the absorption, characterised by A, is independent of λ:

$$T(\lambda, d) = A\, e^{-Cd/\lambda^4}. \tag{2.21}$$

The clarity coefficient C is proportional to the radiation which is scattered per unit path and is one of the main parameters of the aerogel. The fit results are $C = 0.00048\ \mu\text{m}^4/\text{mm}$ and $A = 0.9934$.

The Hunt formula (Eq. 2.21) can be parametrised with the effective transmission length Λ_0 measured at 400 nm as $\Lambda(\lambda) = \Lambda_0(\lambda/400)^4$ and constant absorption process, represented by A:

$$\begin{aligned} T(\lambda) &= A\, e^{-d/\Lambda(\lambda)} \\ &= A\, e^{-d/\Lambda_0(400/\lambda)^4} \qquad (2.22) \\ &\simeq e^{-d/\Lambda_0(400/\lambda)^4}. \qquad (2.23) \end{aligned}$$

In the last equation, it is presumed that $A \simeq 1$, since the absorption is very low and plays a significant role for long wavelengths, where a typical photon detector has a low sensitivity. This formula will be of practical significance for the calculation of the number of expected photons.

Fig. 2.11 shows a side view of two aerogel layers (dark and light cyan) in Belle II ARICH when a $p = 3.5$ GeV/c kaon traverses ARICH and Cherenkov photons are emitted in aerogels. The simulation was made using GEANT4 library [30] in Belle Analysis Framework 2 (BASF2, [12]). One can observe the scattered photons inside the aerogels which are the source of the diffuse background. If the scattered photons exit through the forward side of aerogel and get detected by the photon sensor array,

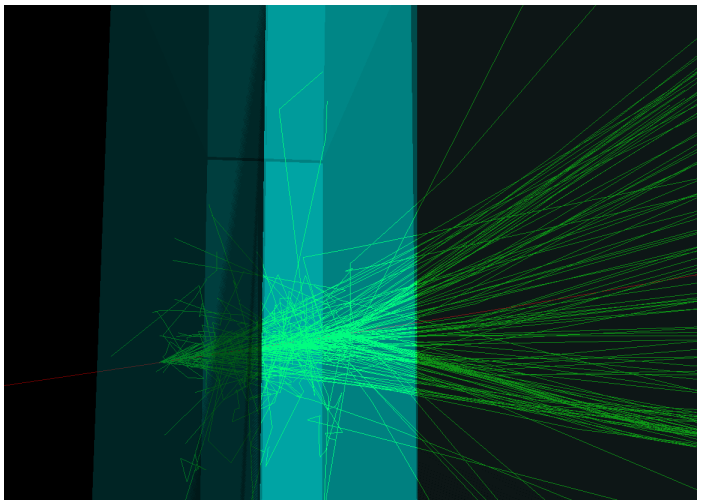

Figure 2.11: Monte Carlo simulation showing the side view of two aerogel layers in Belle II ARICH. In the event shown, the Cherenkov photons (green) are emitted as a $p = 3.5$ GeV kaon (red line) traverses two aerogel layers. One can observe the scattered photons inside both aerogel layers which are the source of the diffuse background.

they contribute to the background noise. It was shown that this noise is uniform over the detector surface [25].

2.4.2 Photon Detector

The photon detector in ARICH covers a surface of 3.5 m^2 and is an essential part of the counter. To fulfil the requirements for separation of pions and kaons, it should:

1. Be immune to the magnetic field of 1.5 T,
2. Have single photon sensitivity with high photon detection efficiency,
3. Have position resolution of about 2 mm RMS,
4. Have a high sensitivity for photons in the blue region.

Photon detector was an issue for Belle II ARICH because it has to work reliably in the high magnetic field. For this purpose a new detector, Hybrid Avalanche PhotoDiode (HAPD), was developed together with Hamamatsu Photonics as the baseline detector, while the Photonis Micro-Channel Plate PhotoMultiplier Tube (MCP-PMT) was tested as a backup option. As a third option, the SiPMs were considered.

The baseline detector for Belle II ARICH is HAPD [31, 32, 33]. The principle of operation will be shortly given here. The Cherenkov photons enter through the entrance window and produce a photoelectron in the photocathode (Fig. 2.12). Photoelectrons are accelerated in the electric field with the typical potential difference $7 - 8$ kV and are directed onto the avalanche photodiode (APD). In the APD, an additional gain of 40 is obtained when a bias voltage is provided. The photon sensor consists of 4 APD chips, each divided into 6×6 channels of 4.9×4.9 mm^2 active

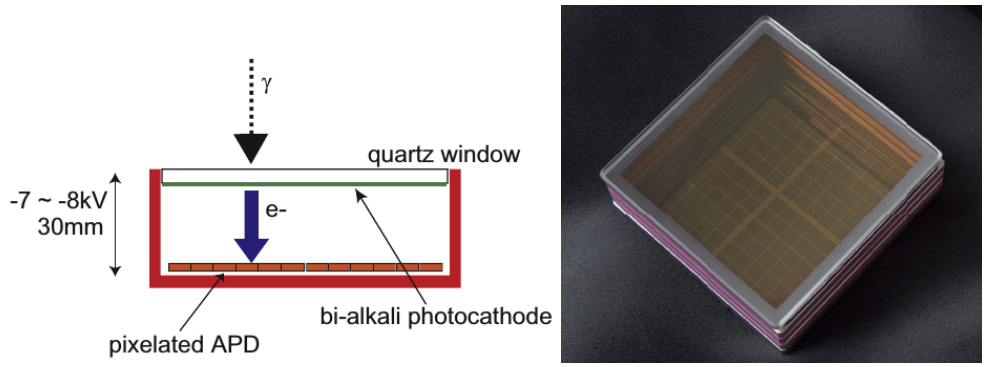

Figure 2.12: Schematic drawing (left, [34]) and a photograph (right, [33]) of hybrid avalanche photo-detector, HAPD.

Parameter	Value
Number of channels	144
Channel size	4.9×4.9 mm^2
Package size	72×72 mm^2
Geometrical acceptance	67%
Typical quantum efficiency	28%
Total gain	0.7×10^5

Table 2.3: HAPD specifications.

area. The total surface of one detector is 72×72 mm^2 and the geometrical efficiency, defined as the fraction of the source radiation which is geometrically intercepted by the detector, is 65%. The total gain obtained is about 7×10^4. The specifications are summarised in the Table 2.3.

Another option for the photon detector was a Micro-Channel Plate Photo-Multiplier Tube (MCP-PMT, Fig. 2.13). The operational principles, similar to that of the conventional PMT, can be found in textbooks on experimental methods. The main difference is that the dynode system of conventional PMT is replaced by a metal plate with channels of ≈ 10 μm in radius, which amplify the initial number of photoelectrons. Photonis 85011 MCP-PMT [35, 36], with 8×8 channels, each having an active area of 5.9×5.9 mm^2, was tested in a beam test and on the laboratory bench. The advantage of the MCP-PMT is that it can operate in the 1.5 T magnetic field and has an excellent timing resolution, which could be used to add time-of-flight information. Nevertheless, the number of registered photons per track was lower than for HAPDs. Also, in an ageing test the MCP-PMT was irradiated with light that corresponds to the total accumulated light during the Belle II life-time, after which the PDE dropped by 10% [12].

As third option for the single photon sensor Silicon PhotoMultiplier (SiPM) was considered [37, 38, 39, 40]. The detailed description of its operation, characteristics, as well as the overview of the previous studies, will be presented in the Chapter 3. A short comparison of these photon detectors will be given below.

Figure 2.13: Photograph of Photonis micro channel plate photomultiplier tube, MCP PMT.

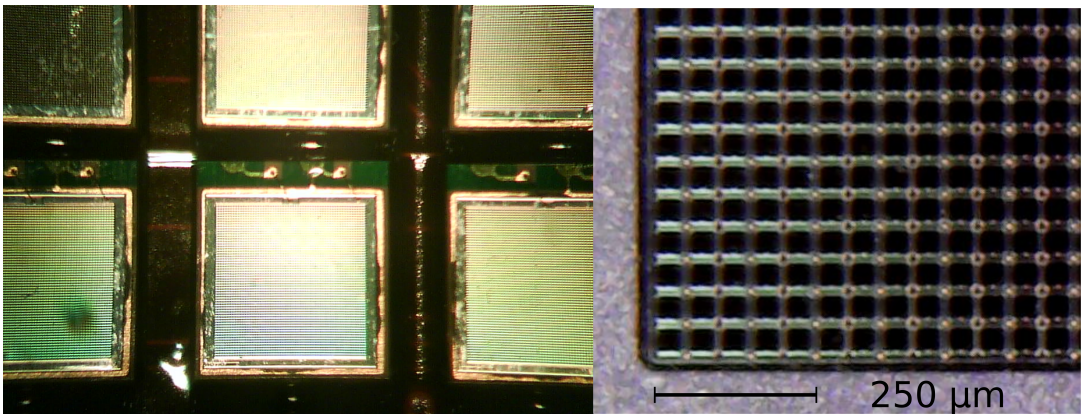

Figure 2.14: Left: Photograph with 2× magnification of one SiPM channel in the 64-channel array Hamamatsu MPPC S11834. One channel has $60 \times 60 = 3600$ cells connected electrically in parallel. Right: Photograph of Hamamatsu MPPC with single cells structure visible, magnified 100×.

As already described in Introduction, SiPM is a semiconductor based photon detector, capable of detecting single photons. It is a silicon photo-diode operating in Geiger regime. The silicon substrate is divided into mutually isolated cells (Fig.2.14) which are reversely biased and kept in a critical state above the breakdown voltage. An incoming photon converts to an electron-hole pair, which then trigger an avalanche of carriers in a cell. Many cells are connected in parallel forming one channel. Number of carriers in an avalanche started by one initial photon is called gain. The gain is function of the working voltage and cell size; it typically reaches 10^6.

The performance of SiPM is characterized by the photon detection efficiency (PDE) which includes the quantum efficiency (QE), which is the mean number of photoelectrons produced per incident photon, the probability that the photoelectron starts the avalanche and the geometrical efficiency of the cell structure. PDE depends, through the quantum efficiency and the avalanche probability, on the wavelength of the incoming light and the working voltage. The dependence of PDE on wavelength for a typical SiPM at producer recommended working voltage is given in Fig. 2.15, together with the number of Cherenkov photons produced per wavelength

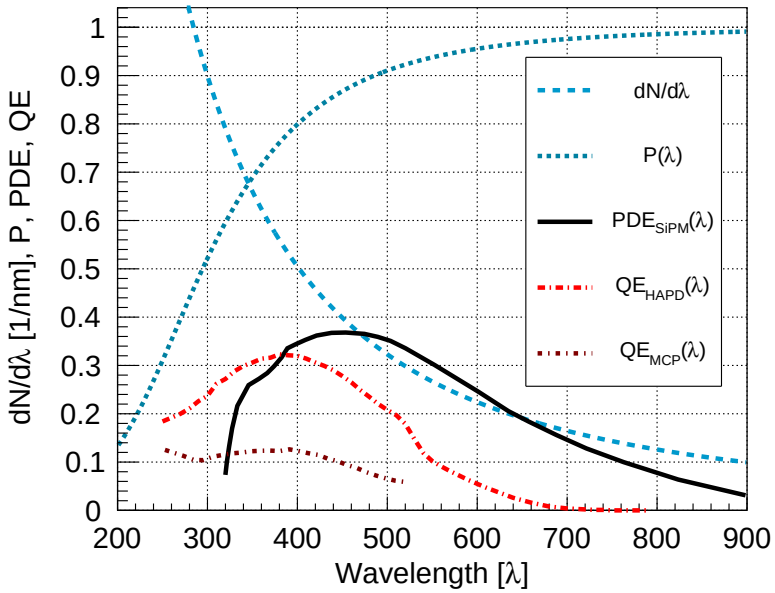

Figure 2.15: Graph shows the number of Cherenkov photons per wavelength $\mathrm{d}N/\mathrm{d}\lambda$ produced in the aerogel, the average probability P that the photon will not be scattered and PDE of SiPM at nominal operating voltage. For comparison of the photon detectors, QE of HAPD and MCP PMT is also shown.

interval (Eq. 2.13) in the aerogel ($n = 1.0485$, $d = 19.4$ mm, $\Lambda = 44.0$ mm) and the probability that the photon exits the aerogel without scattering (Eq. 2.29). For comparison, shown also are the QE of a HAPD developed for Belle II ARICH [41] and QE of Photonis MCP PMT[2]. The cut-off of the PDE of SiPM at ≈ 300 nm turns to be beneficial, as it filters out the Rayleigh scattered photons in the UV-region.

SiPMs conform to most of the Belle II ARICH requirements. Compared to HAPDs, SiPMs show the following advantages:

1. They are completely immune to operation in magnetic field (tested up to 7 T),
2. They have a higher overall PDE at lower operating voltage,
3. They have a higher peak sensitivity for photons in the blue region,
4. They are robust and small, which allows for a more compact design,
5. They have a lower price for higher quantities.

SiPMs are available with channel widths $1 - 4$ mm so that the position resolution can be matched to that of HAPD.

The main challenge of SiPMs is the noise which is detected even when no light hits the detector, called the dark counts noise. This is caused mostly by thermally generated pairs in the active region in silicon and is on the order of $100 - 1000$ kHz/mm^2. The noise is dependent on the temperature and gets lower with lower temperature. It also depends on the bias voltage and raises with the raising voltage. The noise can be considerably reduced by cooling, however this is not an option for ARICH since

[2]PDE of HAPD was not available. It is lower than the QE, mainly due to the dead space between the channels, which is observed in Fig.2.12, right.

it would cause difficulties due to the condensation on the optical elements. In order to overcome this deficiency, we employed various methods, described in Chapters 3 and 4.

2.5 Expected Number of Photons with SiPMs

The number of expected photons N_{exp} will be equal to the number of the emitted photons N, given by the equation 2.12, corrected for the optical losses in the radiator, light collecting system and photon detector. The optical losses in aerogel radiator are taken into account with transmittance $T(\lambda, z)$ (Eq. 2.22), optical collection system losses with geometrical efficiency ε_{geo} and the response of the photon detector normalized to unity $S(\lambda)$ (commonly expressed as PDE, when using SiPM). Putting these together, the number of expected photons per wavelength interval $\mathrm{d}\lambda$ per path length $\mathrm{d}z$ is:

$$\frac{\mathrm{d}^2 N_{exp}}{\mathrm{d}\lambda\,\mathrm{d}z} = N_0 \sin^2\theta\; T(\lambda, z)\,\varepsilon_{\text{geo}}\,S(\lambda)\frac{1}{\lambda^2}. \tag{2.24}$$

where the physical constants are grouped into the factor $N_0 = 2\pi\alpha$.

The geometrical efficiency of photon detector ε_{geo} consists of the acceptance of the SiPM photon array ε_{acc} and the active fraction of the detector surface in a specific tiling scheme ε_t. By employing the light concentrators, the SiPM array acceptance can be enlarged to $\varepsilon_{acc} = 0.90$ (*cf.* Chapter 4). The efficiency of the tiling scheme in Belle II ARICH is $\varepsilon_t = 0.9$. However, in the case of array of SiPMs, with specially designed front-end electronics it could be possible to obtain the active fraction of detector surface of $\varepsilon_t \simeq 1$. Then the total geometrical acceptance becomes:

$$\varepsilon_{\text{geo}} = \varepsilon_{\text{acc}}\,\varepsilon_t = 0.90. \tag{2.25}$$

The particles enter perpendicularly in the aerogel, so the path traversed by a photon $d(z)$ before leaving the aerogel is (Fig. 2.16):

$$d(z) = \frac{z}{\cos\theta}.$$

For the Cherenkov light produced uniformly along the particle path z, integrating from 0 to aerogel width d, we obtain:

$$\begin{aligned}\int_0^d T(\lambda, z)\,\mathrm{d}z &= \Lambda_0\big(\frac{\lambda}{400}\big)^4 \cos\theta\left[1 - e^{-d/\Lambda_0\cos\theta(400/\lambda)^4}\right] \\ &= \Lambda(\lambda)\cos\theta\left[1 - e^{-d/\Lambda(\lambda)\cos\theta}\right].\end{aligned} \tag{2.26}$$

Now 2.24 becomes:

$$\frac{\mathrm{d}N_{exp}}{\mathrm{d}\lambda} = N_0 \sin^2\theta\;\Lambda_0\cos\theta\big(\frac{\lambda}{400}\big)^4\left[1 - e^{-d/\Lambda_0\cos\theta\cdot(400/\lambda)^4}\right]\varepsilon_{\text{geo}}S(\lambda)\frac{1}{\lambda^2}. \tag{2.27}$$

or expressing the transmission length as function of λ:

$$\frac{\mathrm{d}N_{exp}}{\mathrm{d}\lambda} = N_0 \sin^2\theta\;\Lambda(\lambda)\cos\theta\left[1 - e^{-d/\Lambda(\lambda)\cos\theta}\right]\varepsilon_{\text{geo}}\,S(\lambda)\frac{1}{\lambda^2}. \tag{2.28}$$

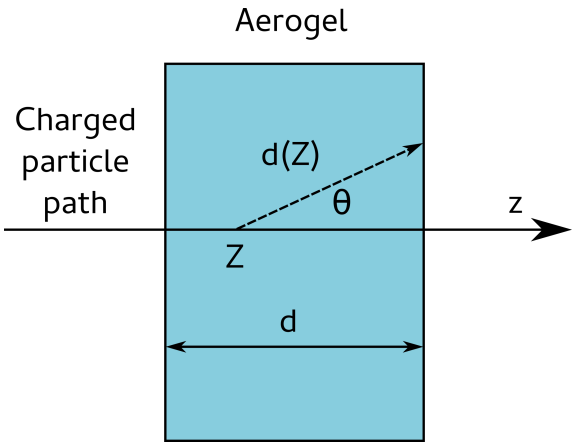

Figure 2.16: Photon path length $d(z)$ in aerogel as a function of the emission point z. The Cherenkov photon emitted at an angle θ along the charged particle path at $z = Z$ traverses path $d(Z)$. The aerogel total width is d.

The path length of the photon emitted at the entrance of the aerogel is $D = {}^{d}/_{\cos(\theta)}$. Using this to express the cosine, the right-hand side of Eq. 2.26 can be expressed with the average probability $P(\lambda)$ that the photon will not be scattered in aerogel:

$$P(\lambda) = \frac{1 - e^{-D/\Lambda(\lambda)}}{D/\Lambda(\lambda)}. \tag{2.29}$$

Now the integral Eq. 2.26 can be expressed as:

$$\begin{aligned} \int_0^d T(\lambda, z)\,\mathrm{d}z &= \Lambda(\lambda)\,\frac{d}{D}\,[1 - e^{-D/\Lambda(\lambda)}] \\ &= d\,P(\lambda). \end{aligned} \tag{2.30}$$

Expressing the rest of the terms as Cherenkov function for the emitted photons

$$C(\lambda) = N_0 \sin^2\theta\; d\;\frac{1}{\lambda^2} \tag{2.31}$$

the number of detected photons per wavelength interval (Eq.2.27) becomes:

$$\frac{\mathrm{d}N_{exp}}{\mathrm{d}\lambda} = P(\lambda)\varepsilon_{\mathrm{geo}}\,S(\lambda)C(\lambda). \tag{2.32}$$

The Eq. 2.32 is plotted in Fig. 2.17.

To obtain the total number of expected photons emitted per track, one has to integrate the equation 2.32. Numerical integration from 300 to 900 nm gives:

$$N_{exp} \approx 31 \text{ photons}. \tag{2.33}$$

In the case of two aerogels, the number of produced photons in the upstream aerogel has to be multiplied by the probability that the photon will pass non-scattered through the downstream aerogel. The expected number of photons in both aerogels

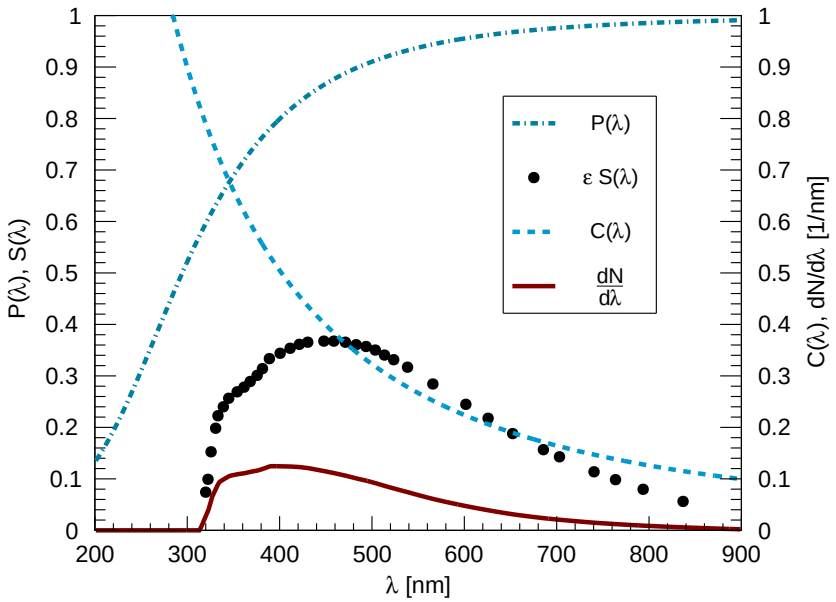

Figure 2.17: The probability of passing through the upstream aerogel tile $P(\lambda)$, response $S(\lambda)$ of the SiPM (PDE), emitted Cherenkov photons $C(\lambda)$ and detected photons per wavelength interval: $^{dN}/_{d\lambda}$ (Eq. 2.32).

is:

$$\frac{\mathrm{d}N_{exp,1}}{\mathrm{d}\lambda} = N_0 \sin^2\theta_1 \, \Lambda_1(\lambda) \, \cos\theta_1 \left[1 - e^{-d_1/\Lambda_1(\lambda)\cos(\theta_1)}\right] e^{-d_2/\Lambda_2(\lambda)\cos(\theta_1)} \varepsilon_{\mathrm{geo}} \, S(\lambda) \, \frac{1}{\lambda^2}, \tag{2.34a}$$

$$\frac{\mathrm{d}N_{exp,2}}{\mathrm{d}\lambda} = N_0 \sin^2\theta_2 \, \Lambda_2(\lambda) \, \cos\theta_2 \left[1 - e^{-d_2/\Lambda_2(\lambda)\cos(\theta_2)}\right] \varepsilon_{\mathrm{geo}} \, S(\lambda) \, \frac{1}{\lambda^2}. \tag{2.34b}$$

The probability of passing through aerogel and the detected photons per wavelength interval are plotted in Fig. 2.18. Again, numerical integration of Eqs. 2.34 gives the number of expected photons in case of two aerogels:

$$N_{exp}^{LC} = 21 + 42 = 63. \tag{2.35}$$

Without the light concentrators, the geometrical efficiency of the bare SiPM array is $\varepsilon_{geo} = 0.36$ and the number of expected photons with two aerogels is:

$$N_{exp}^{wo} = 25. \tag{2.36}$$

The expected number of photons will be compared to the number of detected photons in a beam test in the Chapter 5.

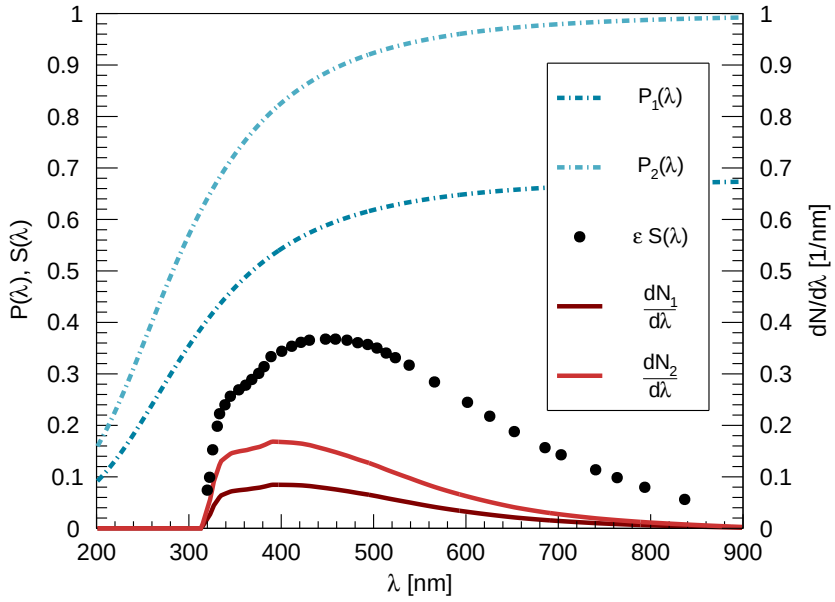

Figure 2.18: The probability of passing through both aerogel tiles $P_1(\lambda)$ and $P_2(\lambda)$, response of SiPM $S(\lambda)$ and detected photons per wavelength interval $^{\mathrm{d}N}/_{\mathrm{d}\lambda}$ (Eq. 2.34).

Chapter 3

Silicon Photomultiplier

Characteristics of semiconductors needed to understand SiPM operation are given at the beginning. The SiPM structure and operation principles are described, as well as the characteristics which result thereof. The challenges of employing the SiPM as single photon detector are listed and followed by a short summary of the previous studies of SiPM as detector for RICH.

3.1 Semiconductors

A long used electronic photon detector, capable of detecting single photons, is a PhotoMultiplier Tube (PMT). It has been in use since 1930s, but it poses a series of challenges in radiation detection, among which are the high voltage needed for the operation, the reduced efficiency in a magnetic field, the complicated structure and the hight cost. PMTs with position sensitivity, multi-anode PMTs, were developed in 1980's [42, 43]. However, they share common deficiencies with the classical PMTs, namely efficiency reduction in the magnetic field.

A novel generation of photon detectors based on semiconductors can overcome some or all of the PMTs disadvantages. Semiconductors are crystalline materials whose name comes from the fact that their conducting properties are somewhere between the properties of metals and insulators. Typical semiconductors are silicon and germanium, as well as some other elements, all classified as metalloids in the periodic table. Their properties are explained by the presence of an energy gap between the (last) valence zone and the conducting zone. This gap contains forbidden states which are not populated. The width of the energy gap in silicon is 1.12 eV. If a photon is absorbed in the material, it can give its energy to an electron in the valence band, which then jumps to the conducting band, creating an electron-hole pair.

If the electron-hole pair is collected by means of an electric field, a signal can be measured. The number of produced pairs depends on the energy of the photon and the band gap. The part of the photon energy can be absorbed by the phonons (crystal lattice vibrations). The absorption by the phonons is a statistical process in the energy region 1.12 to 3.6 eV, above which the photon has enough energy to directly produce an electron-hole pair.

The detailed principles of semiconductor formation, operation and use can be found in standard textbooks [16, 44]. Just a basic ideas needed for understanding how SiPM operate will be summarised here.

If a semiconductor is at absolute zero, the electrons have the lowest allowed energies. Every electron is bonded by a covalent bonding to its atom. Silicon has four electrons in the valence band, all of which participate in the covalent bonding of the crystal lattice. As the temperature rises, the electrons gain energy and populate higher (allowed) energy states. If the temperature rises further, the electron energies rise above the valence band and the last forbidden energy zone, of width E_g. The electron energies lie now in a conduction zone (Fig. 3.1). This means that one of the four electrons in an atom gains enough energy and becomes "free" inside the crystal, as it does not participate in the covalent bonding. When the electron leaves its position, it makes a "hole" in the valence zone.

The pure semiconductors have no atoms of another element in the lattice; they are called intrinsic. However, in a real semiconductor, there are always some atoms of another element. These other elements, called impurities, actually play a specific role. They introduce new energy levels in the forbidden zone, which act as "traps" for electrons. In pure semiconductors the number of the electrons is equal to the number of holes. Therefore, the concentrations of negative and positive charge carriers are the same, equal to the intrinsic carriers concentration n_i. If the impurities are present or added to the intrinsic semiconductor in higher concentrations (typical example 10^{13} atoms/cm^3) the semiconductor is called doped or extrinsic. Somewhat changed characteristics arise, on which most of the contemporary electronics is based.

The impurities are typically the elements of the neighbour groups in the periodic table, such as arsenic or boron. If the impurity is an element which has five electrons in the outer shell, such as arsenic, there is one electron that does not make a bond at all (donor). It is therefore loosely bound to its atom and can be easily moved around the crystal lattice. In fact, its energy is near the lower level of conductive band and with a small energy gain its energy transits to the conduction band (Fig. 3.1). Once in the conduction band it becomes the free charge carrier. Therefore, the intrinsic concentration of the negative carriers n rises to

$$n = n_i + N_D \tag{3.1}$$

where N_D is the concentration of donor atoms (*n.b.* the overall charge of the crystal stays the same). The number of positive carriers stays the same, which means that they are outnumbered by the negative carriers. Such a semiconductor is called n-type semiconductor.

If the impurity is an element which has three electrons in the outer shell, such as boron, there is one unsaturated valence bond (acceptor). An electron from the valence bond can fill this bond leaving a hole in the valence band; the concentration of the free positive carriers p_i rises to:

$$p = n_i + N_A, \tag{3.2}$$

where N_A is the concentration of acceptor atoms. Such a semiconductor is called p-type semiconductor.

The impurities introduce new energy levels into the energy gap, which can act as traps for the electrons. After some time (depending on the crystal state, order of $1 - 1000$ ns), the electron is released and can move freely again. On the other hand, it can fall to the valence band and fill a hole. This process is called recombination. The recombination is an unwanted effect, as the primarily created electron-hole pair

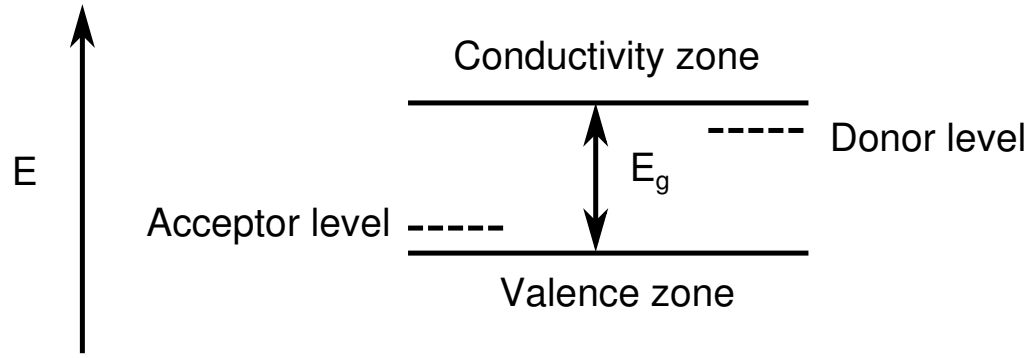

Figure 3.1: Energy zones and levels in a semiconductor with the energy gap E_g. Addition of donor impurities forms a n-type semiconductor. Addition of acceptor impurities forms a p-type semiconductor.

is destroyed and no signal is registered in this case. Apart from being impurity introduced, recombination levels can be also created by dislocations in the crystal lattice.

In an electric field, the electrons from the conduction band will move. The velocity with which they move is called the drift velocity v_e and, in the first approximation, is proportional to the electric field E:

$$v_e = \mu_e \, E, \tag{3.3}$$

The constant of proportionality μ_e is called the mobility of electrons. This equation is valid for the moderate field strength values, while at higher electric field values the drift velocity reaches a plateau (Fig 3.2) because the probability of electrons losing the energy in collisions with the crystal lattice becomes important. Holes will tend to move in the opposite way. Since the binding energy is different in the case of negative and positive carriers, the mobility of holes μ_h, and consequently the drift velocity v_h, will be different, typically 2-3 times smaller.

When the p- and n-type semiconductor crystals are joined together (at atomic distances), the free carriers will feel a force that will tend to move them across the junction towards the opposite type of the semiconductor. This is a result of local electric field produced by the different concentration of positive and negative charges. The carriers will move until the new concentration of charge of the opposite type screens the initial charge (Fig. 3.3, a). As a consequence of the field present, there is a contact potential V_0 across the junction. It can be observed as the difference of the energy levels at left and right side of the pn-junction in Fig. 3.3, b. The electric field creates a depletion zone, that is a region around the junction void of free charge carriers. The electric field (Fig. 3.3, c and d) will tend to remove any new free charge introduced in this region.

The width of the depletion zone depends on the concentration of the dopant atoms. Typically, the concentration of impurities of one type (donor or acceptor) is much higher than the concentration of intrinsic carriers, so that the concentration of the primary charge carriers is defined by the concentration of donor atoms:

$$n \simeq N_D. \tag{3.4}$$

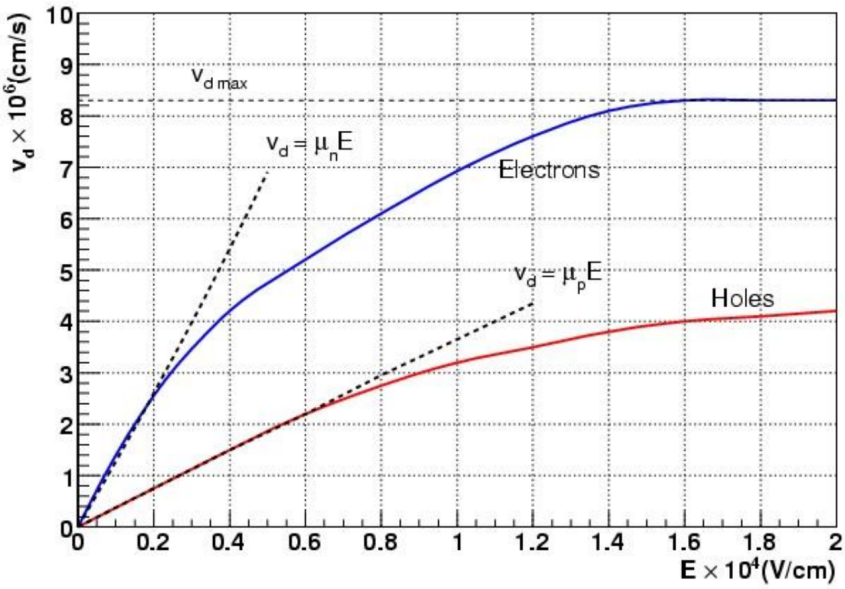

Figure 3.2: Drift velocities of electrons (blue) and holes (red). The full line is measured, the dotted is linear approximation [45].

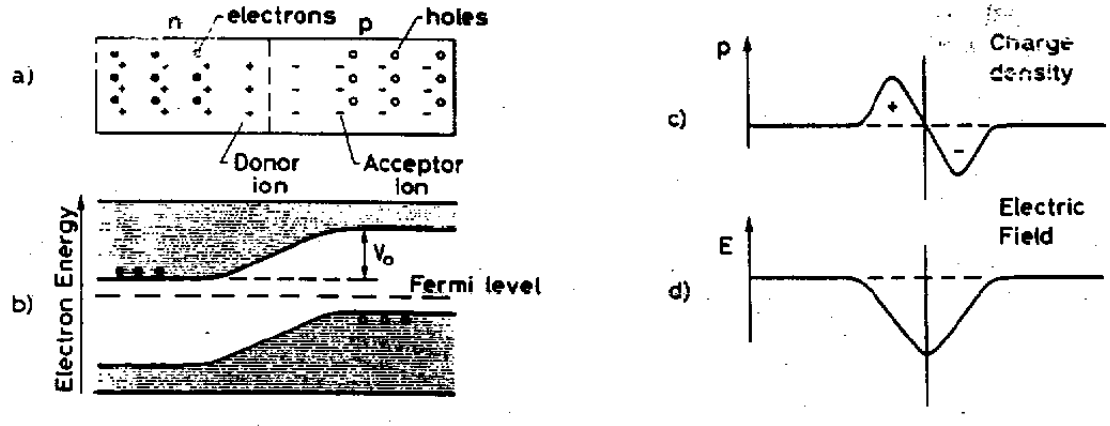

Figure 3.3: Left: Contact potential. Right: Charge build-up. From Ref. [44]

The width of the depletion zone is then given by [44]:

$$d \simeq \sqrt{\frac{2\varepsilon V_0}{eN_D}} \tag{3.5}$$

where ε is the dielectric constant, V_0 is the contact potential, e is the electron charge.

3.2 Semiconductor Detectors for Photon Detection

An ionizing particle passing through the depletion zone will give enough energy to the electron to jump to conduction band leaving a hole in the valence band. Thus an electron-hole pair is formed which will be swept away by the electric field. The moving of the charge produces an electrical current which is eventually registered as a signal. The principle of the operation reminds one of the ionization detectors, the first electronic detectors constructed for radiation detection. Their principle of operation is the collection of the electron-ion pairs as the radiation traverses the volume of the detector filled with gas. Similarity is exploited in the classification of the semiconductor detectors, which is given below.

Similarly as the ionization detectors, the semiconductor detectors intended for photon detection can be divided into devices operating:

1. with no internal amplification: PIN diode,
2. in proportional regime: APD,
3. in Geiger regime: G-APD.

The term PIN diode reflects the structure of the device, which has an intrinsic semiconductor between the heavily doped p- and n-type semiconductors. This layer reduces the capacitance of the detector which also reduces the noise. The electric field is high enough, even without an external field added, to separate the charges and create the signal. However, one photon produces one pair, that is 10^{-19} C of charge and at least 300 photons are needed to produce a detectable signal. Therefore, the PIN-diode is not usable for single photon detection, but it is used in the detectors where there are copious amounts of photons, such as scintillation detectors in calorimeters (BaBar [46] , Belle [7]).

If one applies an inverse voltage, called bias voltage V_b, to pn-junction, that is, brings a negative potential to p-type semiconductor and a positive potential to n-type semiconductor, the potential difference will be enlarged by V_b, now becoming $V_0 + V_b$. Along with the contact potential, the width of the depletion zone will rise (*cf.* Eq. 3.5). Consequently, the region usable for the radiation detection becomes larger. Typically, this bias voltage V_b is on the order of 100 V, while the contact potential is on the order of 1 V. However, if the bias voltage becomes too large, the field assisted electron-hole generation becomes dominant and the breakdown occurs.

By applying the strong external electric field, the photoelectron gains enough kinetic energy so it can generate a new electron-hole pair by impact ionization. Both the initial photoelectron and the new electron continue to accelerate in the electric field and gain enough energy to create new pairs; thus the avalanche is produced. The avalanche is stopped when the electrons reach the zone without electric field and the amplification stops. A device that uses this principle is Avalanche PhotoDiode

(APD). The APD has an internal amplification, called the gain of the device, on the order of 1000, which is high enough to register single photons. As an example, APDs are used as photon detectors in the electromagnetic calorimeter in Compact Muon Solenoid experiment at the LHC [47].

By removing the dynode system from the PMT and replacing the anode by an APD, a Hybrid Avalanche PhotoDiode (HAPD) is obtained. Such an HAPD is developed as a baseline photon detector for the ARICH subdetector in Belle II spectrometer, as explained in the Chapter 2, Section 2.4.2.

3.3 Silicon Photomultiplier

If the strength of the electric field in the APD is increased further, the holes will eventually also gain enough energy to produce new electron-hole pairs. The pairs are created in the complete volume of the depleted zone, *i.e.* in both directions: from the p- towards the n-type (electrons) and from the n- towards the p-type (hole). As in the case of the ionization detector operating with such a high voltage, the signal produced does not depend on the energy of the initial photon. Such operation regime is called Geiger regime, hence the device name Geiger-mode Avalanche Photodiode (G-APD).

As opposite from APD, the avalanche becomes diverging; every newly produced electron *and* hole gain enough kinetic energy to make new pairs in the depleted volume. The avalanche has to be stopped before crystal deteriorates. The avalanche is stopped, or quenched, with a passive resistor connected in series. The resistor bounds the electrical current, creating a voltage drop. The bias voltage drops and the avalanche stops.

Since one absorbed photon is sufficient to trigger the avalanche in the depleted volume, the number of produced pairs does not depend on the number of incident photons. To obtain the response which is proportional to the incident flux, the silicon is divided into small cells which are electrically isolated among themselves and all connected in parallel. The incident photons initiate avalanches in different cells and the collected charge is the multiple of a charge in one cell. The histogram of the collected charge from one SiPM initiated with a low intensity light, is shown in Fig. 3.4. In this single photon spectrum, each observed peak corresponds to a certain number of triggered cells, that is, initial photons. Because such a device can register single photons, just as the traditional vacuum photomultiplier tubes, they were named silicon photomultipliers.

The photograph of one SiPM with the cell structure visible is shown in Fig. 3.5. Two incoming photons that hit two neighbouring cells produce two avalanches and the signal registered has the double amplitude. However, if the photons hit the same cell, the signal of one avalanche is registered. The signal is linear to the incident energy only for the small number of incident photons.

3.3.1 SiPM Characteristics

In order to create electron-hole pairs and produce the detectable signal, photons needs to be absorbed in silicon at a certain depth, that is, in the depleted zone, where they can free the pairs. The attenuation of the photon flux at a distance d

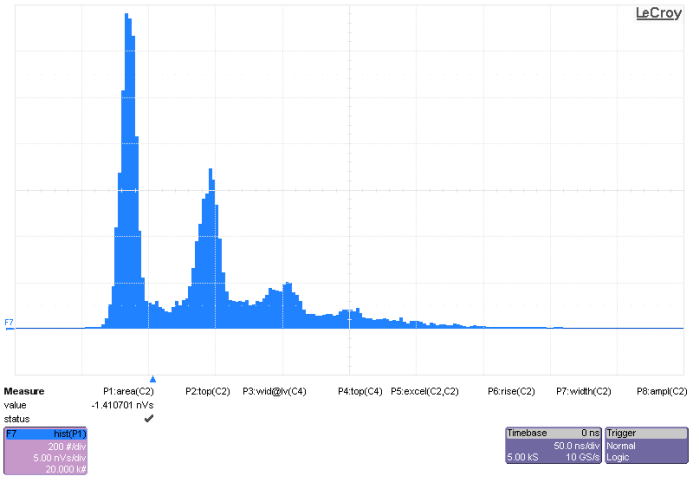

Figure 3.4: Histogram of the integrated charge, *i.e.* single photon spectrum, measured from one SiPM with 3600 cells (Hamamatsu array MPPC S11834).

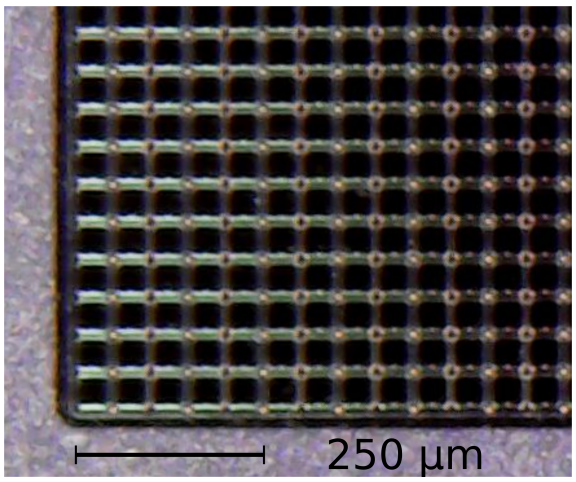

Figure 3.5: Photograph of Hamamatsu S11834 with 100× magnification. The individual cells are spaced at 50 μm inside one SiPM.

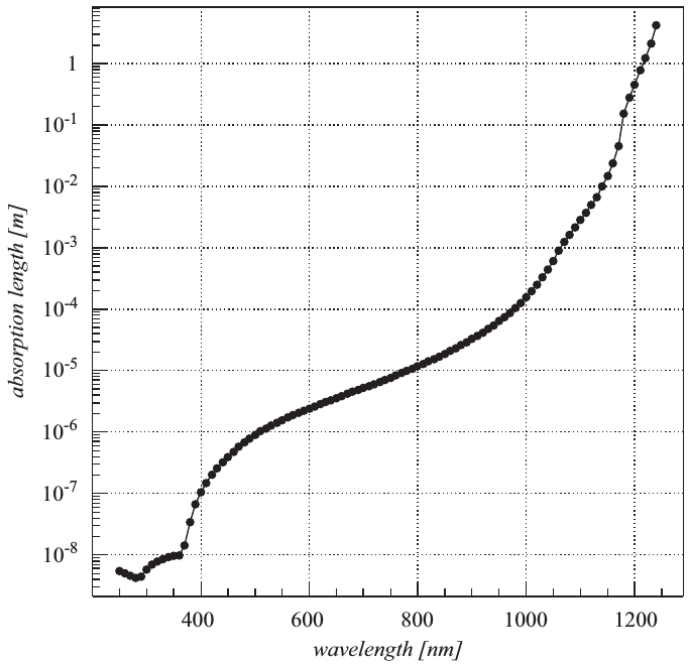

Figure 3.6: Absorption length in silicon as a function of the wavelength of the photon [48].

from the material surface $I(d)$ is given by:

$$I = I_0 \, e^{-d/\mu}, \tag{3.6}$$

where I_0 is the incident flux intensity and μ is the absorption length. The absorption length for silicon is given in Fig. 3.6. Therefore, the photons have to make it through the protective and insulation layer to get to the depletion zone.

A typical design of one SiPM cell is similar to the PIN diode design described above. The pn-junction is formed with high concentration of dopant crystals of both types, named p^+ and n^+ to stress the high concentration. The junction, about 4 μm in width, is grown on the n-type semiconductor basis (Fig. 3.7). Above the pn-junction, a very high concentration p^{++} layer is formed which acts as a conductor and spreads the potential uniformly. The depletion zone extends mostly to the n-side. If a photon with a shorter wavelength penetrates the silicon, it will most probably be absorbed already in the p-type semiconductor, due to its shorter range. The created photoelectron will be attracted to the positive potential at the n-side. On its path it traverses the avalanche zone and initiates the avalanche of both carrier types, that is, a multiplication process. If the incoming photon has longer wavelength, it will most probably pass to the n-side and produce an electron-hole pair there. The hole, which is attracted to the negative potential at the p^{++} layer, will probably traverse the avalanche zone also triggering the multiplication process. However, the holes have lower probability to start the avalanche than electrons, so this structure is more sensitive to the shorter wavelengths. A complementary devices, with n-on-p structure, are also produced; they have higher sensitivity for green and red light.

Design with individual cells makes it possible to keep small volumes of crystal in a state above the breakdown voltage for longer periods of time. Otherwise, if a large volume of silicon was biased above the breakdown voltage, the thermally

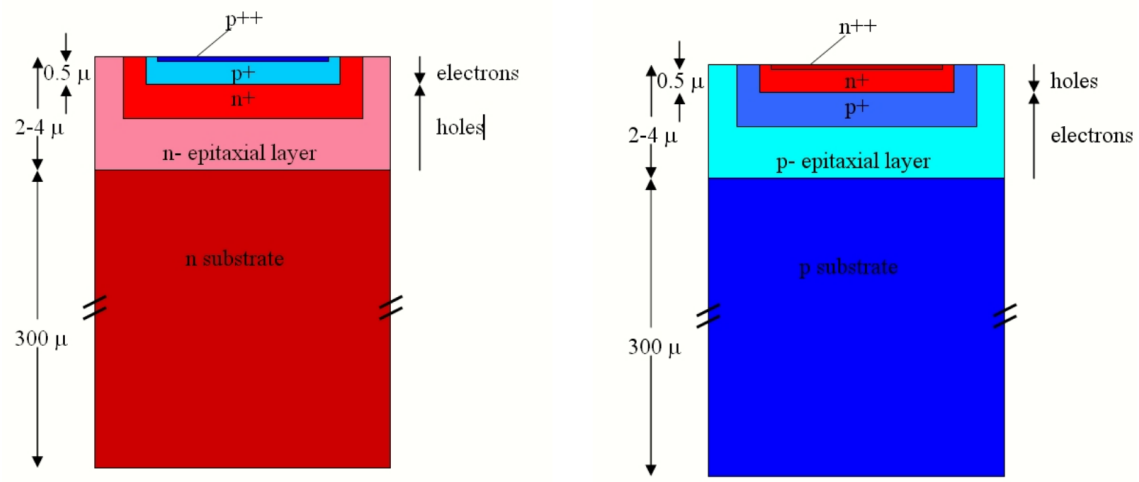

Figure 3.7: Schematic drawing of one SiPM cell in case of p-on-n design (blue light optimized, left) and n-on-p design (red light optimised, right) [45].

or electric field generated pairs would be initiating avalanches all the time and the device would be of no use.

During the avalanche, approximately 10^6 electron-hole pairs are produced in a cell. The number of pairs produced by an initial photon is called gain. A cell can be modelled as a capacitor charged to the V_{bias}. When the avalanche starts, the circuit is closed and the capacitor discharges. The charge flow creates a current, due to which the potential at the diode drops from the bias voltage V_{bias} to the breakdown voltage $V_{breakdown}$. The avalanche is stopped and the recharge process starts. In the case of parallel array of the cells the total signal amplitude A is:

$$A = \sum_{cells} A_{cell}. \tag{3.7}$$

where A_{cell} is the amplitude of a signal produced by one cell. The amplitude of a signal produced by one cell A_{cell} is the function of the cell capacitance C and the over-voltage $V_{overvoltage}$:

$$A_{cell} \simeq \frac{C}{e\, V_{overvoltage}}, \tag{3.8}$$

where e is the elementary charge and over-voltage is the potential difference between the bias voltage V_{bias} and the breakdown voltage $V_{breakdown}$:

$$V_{overvoltage} = V_{bias} - V_{breakdown}. \tag{3.9}$$

The breakdown voltage depends on the crystal purity and defects present. The amplitude and the number of cells fired N_{fired} is approximately proportional to the number of photons $N_{photons}$:

$$A \simeq N_{fired} = N_{total}\,(1 - e^{-N_{photons}\,PDE/N_{total}}) \tag{3.10}$$

where N_{total} is the total number of cells connected in parallel. If the number of photons approaches the number of cells, the saturation is observed. However, the energy resolution is of no importance for the detector operating in binary mode.

A detection capabilities of a photon detector are summarised in Photon Detection Efficiency (PDE). Photon detection efficiency of a SiPM is the product of the

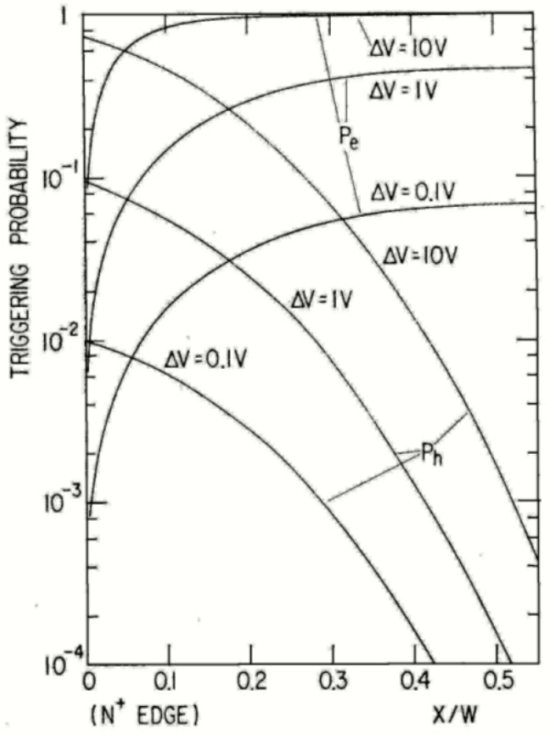

Figure 3.8: Triggering probability for electrons P_e and holes P_h as function of the position of the absorption X in the depleted zone of width W [49].

probability that the incoming photon will produce an electron-hole pair P_{QE}, the probability that the avalanche will be triggered P_{Geiger} and the fill factor, a ratio of active cell area to the total cell area ε_{fill} (containing the resistor and bonding wires):

$$PDE = P_{QE}\ P_{Geiger}\ \varepsilon_{fill}. \tag{3.11}$$

The probability P_{QE} that the photon gets absorbed and produces an electron-hole pair depends on the photon energy and was explained in the Sec. 3.1. The probability P_{Geiger} is the probability that the electron will not recombine with the hole before starting an avalanche. This probability depends on the position of the primary electron-hole pair and is different for electrons and holes. A theoretical model was proposed [49] and the probabilities calculated as function of the position of initial pair X inside the depleted region of width W (Fig. 3.8).

PDE of an SiPM with 50 μm cells (Hamamatsu MPPC S12572-050) is given as a function of the photon wavelength in Fig. 3.9, left. It depends also on the applied over-voltage $V_{overvoltage}$, as can be observed in Fig. 3.9, right, where the peak PDE values for three SiPMs with 25, 50 and 100 μm cell sizes are given as function of over-voltage. The peak values are considerably higher than QE of best HAPDs ($\simeq 34\%$).

PDE depends on the cell size through the gain. In a bigger cell more charge is produced during an avalanche, while smaller cells release less charge and thus have lower gain. The measured PDE as function of photon wavelength for three Hamamatsu SiPMs with different cell sizes is shown in Fig. 3.10. The device with the optimal cell size should be chosen in consideration of the needs for certain application. Although higher PDE is necessary for single photon detection, bigger cells have longer recovery time, that is the time needed to recharge the cell, resulting

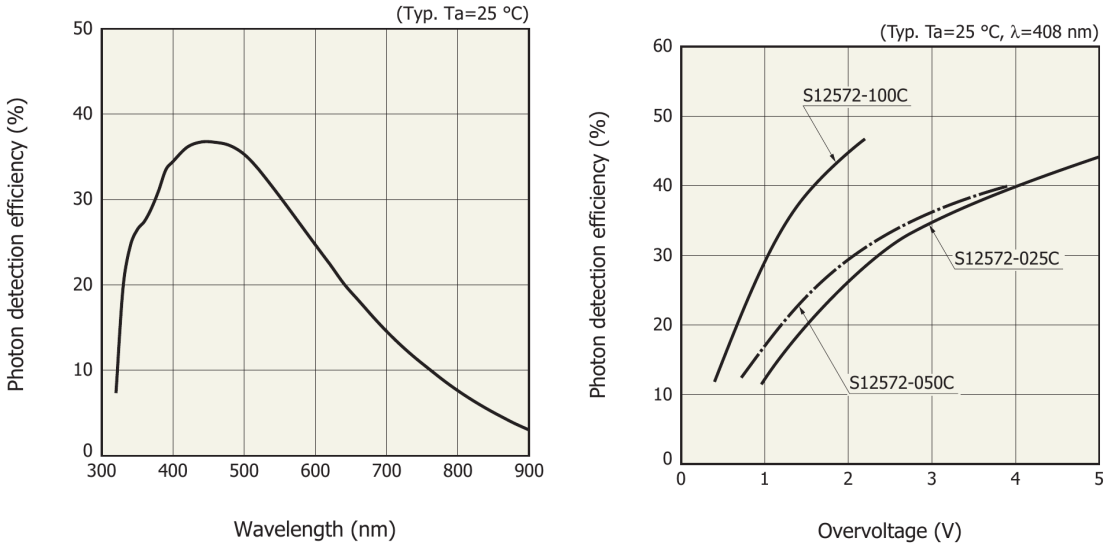

Figure 3.9: Left: Photon detection efficiency (PDE) of a SiPM (MPPC S12572-050C) as a function of the wavelength of the incident light. Right: Photon detection efficiency as a function of the over-voltage for SiPM with three different cell pitches (25, 50 and 100μm). Both are from Ref. [50].

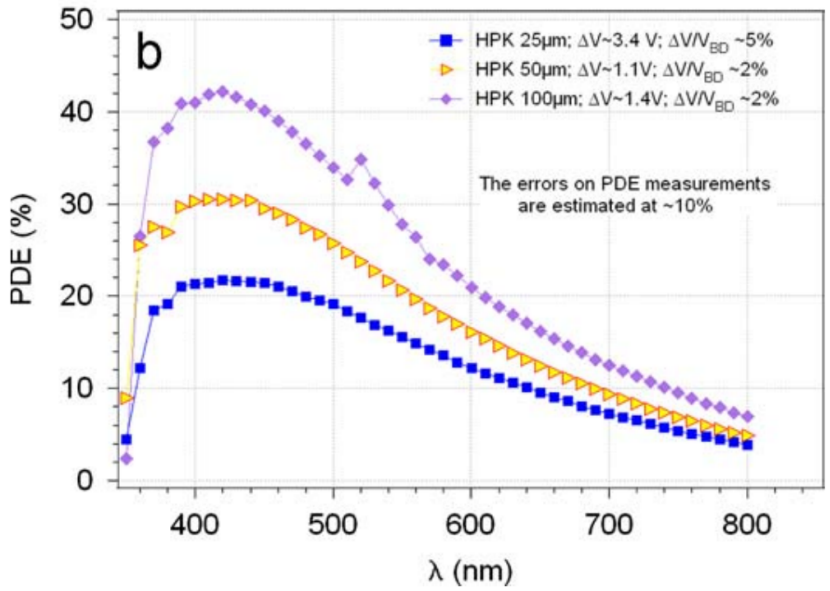

Figure 3.10: PDE as function of the wavelength of the incoming photon [51]

in higher dead time of the detector and reduced efficiency. Commercially available SiPMs have cell width ranging from 10 to 100 μm.

SiPMs have already been employed in high energy physics experiments:

— First large scale application was in the test hadron calorimeter of CALICE [52].

— Tokai-to-Kamioka neutrinos experiment uses SiPMs in the ND280 detector [53].

— Belle II end-cap K_L and muon EKLM sub-detector will use SiPMs [54]

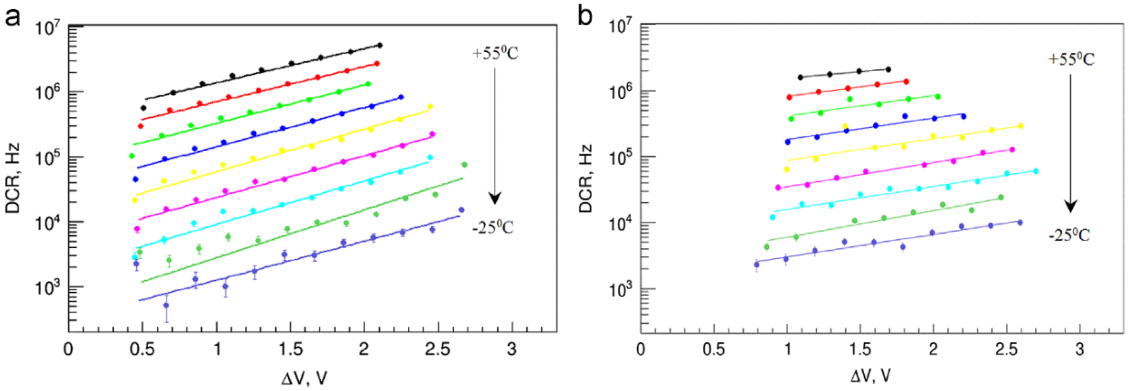

Figure 3.11: Dark counts of two Hamamatsu SiPMs as the function of the over-voltage and temperature (in steps of 10 °C) for S10362-11-050-U 1×1 mm^2 (*a*, left) and S10931-33-050P 3×3 mm^2 (*b*, right), both with 50 μm cell width [56].

— Electromagnetic calorimeter in muon $(g-2)$ experiment at Fermilab will use SiPMs [55].

3.3.2 Challenges with SiPMs

The most important source of noise are the thermally produced electron-hole pairs. Because the thermal excitations can give the electron enough energy to pass to the conduction band, the avalanche can be produced even when there is no incident light on the SiPM. In the analogy with the photomultipliers, the current produced by the charge flow when the detector is not illuminated is called the dark current. Thermally produced electron-hole pairs are approximately given by the Richardson formula:

$$I = AT^2 e^{-E_g/kT} \tag{3.12}$$

where A is some constant, E_g is the width of the energy gap, k is Boltzmann constant and T is temperature.

The signal detected at $^1/_2$ photo-electron amplitude is known as dark count. Typical dark count rates are in the range from 100 kHz/mm^2 (recently) to 1 MHz/mm^2 (previous devices) at room temperature. In Fig. 3.11 dark counts rate is shown as function of the over-voltage and temperature for two Hamamatsu SiPMs. As a practical guide, the dark current is halved by diminishing the temperature for every 8° C. However, cooling the detector is not always a convenient way of reducing the dark counts. In example of Belle II ARICH, as the space foreseen for the detector is small, adding the cooling system would pose serious difficulties.

In addition to dark counts, the counts without the presence of light can be produced in the field assisted electron transition to the conductive band. Eventual presence of the recombination centres in the crystal lattice, which introduce accessible energy levels in the forbidden gap, further enables this field assisted generation.

In an avalanche there is a certain probability that a photon will be produced by brehmsstrahlung. On average, one photon is produced on every 30,000 electron-hole pairs [57]. These photons can initiate new electron-hole pairs and contribute to the gain. However, they can also penetrate to the neighbouring cells and instantiate an avalanche there. Thus, double, triple and multiple signal amplitudes are produced,

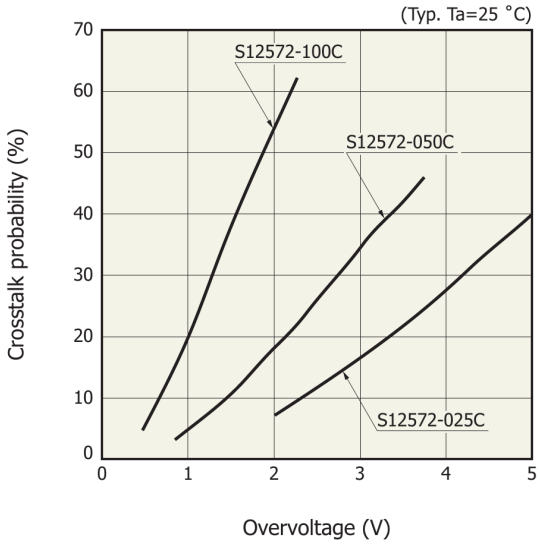

Figure 3.12: Cross talk probability as a function of over-voltage for the MPPC S12572 of three different cell pitches: 25, 50 and 100 μm .

as if two, three of more incident photons were registered, which is known as the cross-talk. The cross talk probability for Hamamatsu MPPC is given in Fig. 3.12. The cross-talk is the reason for the non-linear response of the device as it is impossible to know how many photons initial photons initiated the avalanches. To disable photons penetrating neighbouring cells, a trench is inserted in the silicon wafer which acts as an optical isolation between the cells. The latest generation Hamamatsu device uses this technique and has considerably lower probability of cross-talk.

Another specificity of SiPMs is the presence of the after-pulses, *i.e.* the counts present after the main signal was registered. The after-pulses are produced upon the release of a carrier trapped in the deep-lying levels. The signal height of the after-pulses depends on the recovery time of the cell. If it is triggered before the cell is completely recharged, the after-pulse amplitude is lower than one photo-electron pulse height.

One of the important issues with SiPMs as photon counters is their radiation hardness. Non-ionizing radiation causes silicon lattice defects which become trapping points for the carriers. Upon release, these carriers contribute to the overall dark counts rate. The studies of Hamamatsu MPPC 1×1 mm^2 irradiated with gammas and neutrons have been reported [58, 59, 60]. Gain and PDE do not change significantly after the irradiation with gammas, while the dark current rises slowly with the dose; at 90 Gy it rises drastically (Fig. 3.13). The damage is concentrated on the thick oxide layer.

In the neutron irradiation of the Hamamatsu MPPCs, gain and breakdown voltage show no significant changes up to integrated fluence of 10^{11} neutron/cm^2, but the dark counts rate begins to rise at 10^9 n/cm^2 (Fig. 3.14, left). The photography of MPPC (Fig. 3.14, right) after irradiation shows the hot spots (red dots) that are exclusively inside the sensitive area. At a fluence of 5×10^{10} neutron/cm^2, photon peaks in the single photon spectrum are not detectable and the photon counting becomes impossible (Fig. 3.15).

For comparison, the expected γ dose at ARICH in Belle II is ≈ 100 Gy in 10 years and the expected neutron fluence is $\approx 10^{12}$ neutrons per cm^2 in 10 years [61].

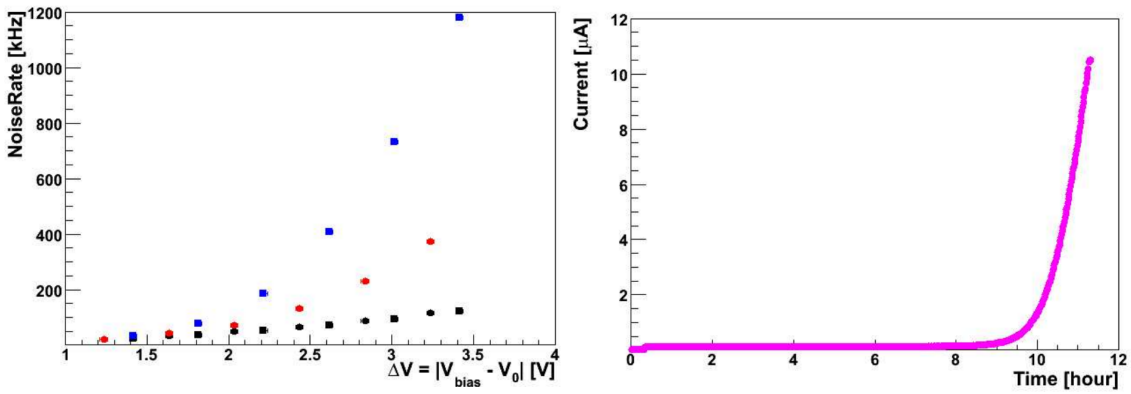

Figure 3.13: The Hamamatsu MPPC 1×1 mm^2 current during the irradiation with γ at 10 Gy per hour. Dark counts rate as the function of the over-voltage. Both from [59].

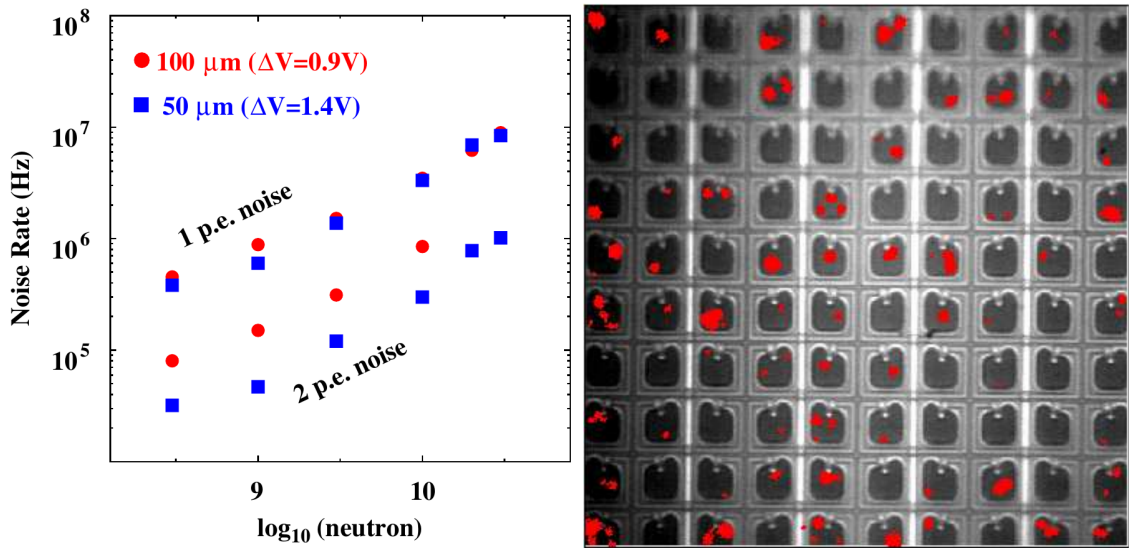

Figure 3.14: Left: Dark counts rate as a function of neutron fluence for two MPPCs with 50 and 100 μm cell sizes, both with active surface of 1×1 mm^2 [58]. Right: The infra-red photography of the 10^{11} neutron/cm^2 irradiated MPPC, the red points show the hot spots [59].

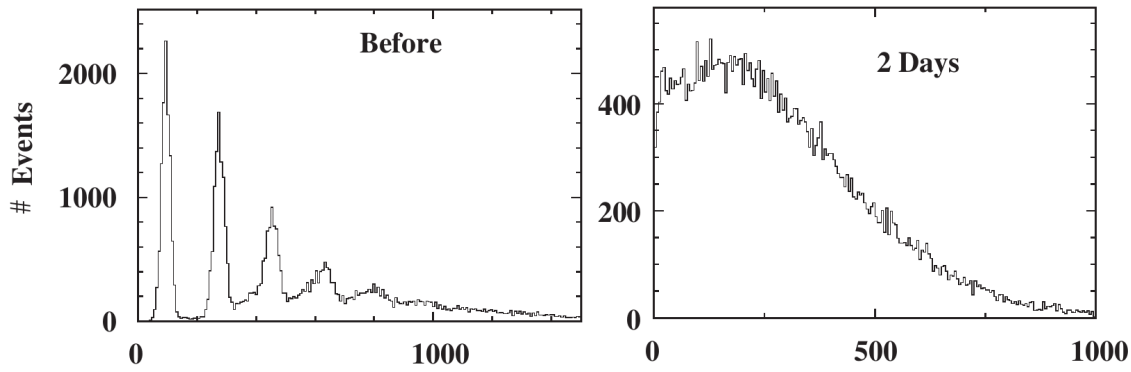

Figure 3.15: MPPC single photon spectrum before and two days after irradiation with 2×10^{10} neutron/cm^2 [58].

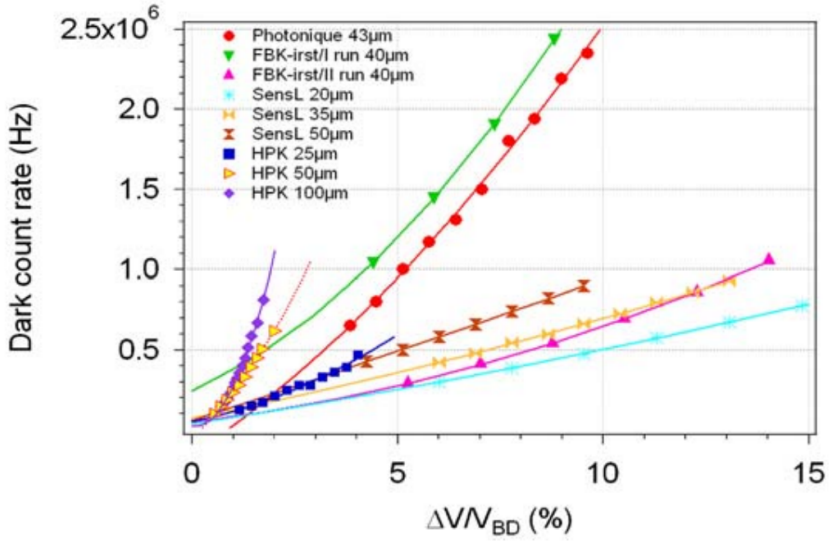

Figure 3.16: Dark counts as function of the relative over-voltage for SiPMs from different producers [51]. Hamamatsu Photonics MPPCs with three different cell sizes 10362-11-025, 050 and 100, with 1×1 mm^2 active area, are labelled with HPK 25μm, 50μm and 100μm, respectively.

3.4 Previous Studies of SiPM as Detector for RICH

A group of scientists at Jozef Stefan Institute has already shown that silicon photomultipliers can be used as a position sensitive detector of Cherenkov photons. SiPMs were used to detect Cherenkov photons emitted by cosmic rays in a 2.5 cm thick aerogel radiator, for the first time [62]. In this test Hamamatsu MPPC S10362-11-100U in metal packaging with 1 mm^2 area and 100 μm cell size was used as a photon detector. The larger cell size was preferred to the smaller available sizes (50 μm, 25 μm) because the positive effect of increased photon detection efficiency outweighs the negative effect of increased noise (*cf.* Fig. 3.10).[1] The dark counts rate given by the producer is 1 MHz [63]. Measured value is given in Fig. 3.16.

A SiPM photon detector consisting of 6 MPPCs, a power supply circuitry and signal read-out circuitry was constructed for this purpose. The raw distribution of all SiPM signals with respect to time relative to the scintillation counter trigger signal is shown in Fig. 3.17, left. The time distribution shows a clear evidence of a peak, but the relative background is quite high. By correcting for the time offset of individual SiPMs and plotting only the signals that correspond to a hit in the range of $\pm 2\sigma$ of the expected Cherenkov angle, the time distribution in Fig. 3.17, right is obtained. It can be seen that the Cherenkov peak is better pronounced and the background is considerably reduced, mainly owing to the reduction of dark noise. The distribution of the hits as a function of their Cherenkov angle is shown in Fig. 3.18.

In order to increase the sensitive area of the SiPM, a light concentrator was used. A hemispherical light concentrator obtained from the blue light emitting diode was used. The sketch of an individual SiPM with such a concentrator is shown in Fig.3.19 and the final photon detector in Fig. 3.20. The hits in Cherenkov space, without

[1] Although this is plausible for 1 mm^2 devices, it is not the case for the devices with larger active area, and, consequently, much higher number of cells.

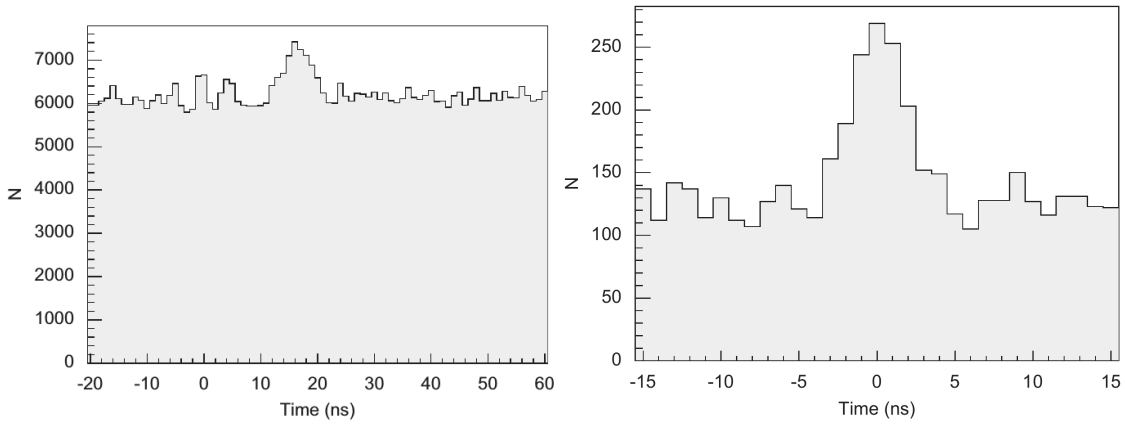

Figure 3.17: The Cherenkov photons radiated by cosmic particles in a 2.5 cm thick aerogel radiator were detected with SiPMs. Left: The raw measured time spectrum of all signals registered with silicon photomultipliers. Right: The time spectrum for only those SiPM signals that correspond to a Cherenkov angle within 2σ of the expected value [62].

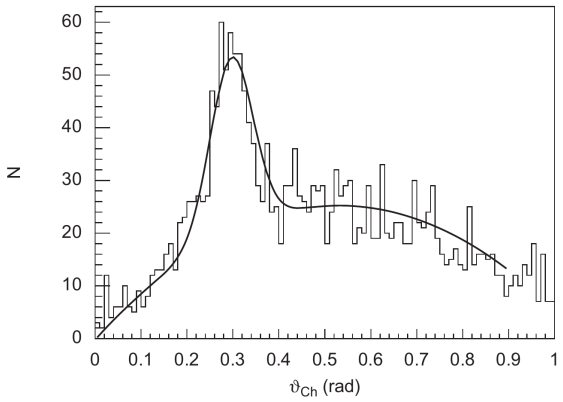

Figure 3.18: Distribution of the SiPM hits, falling in a narrow time window, as a function of Cherenkov angle.

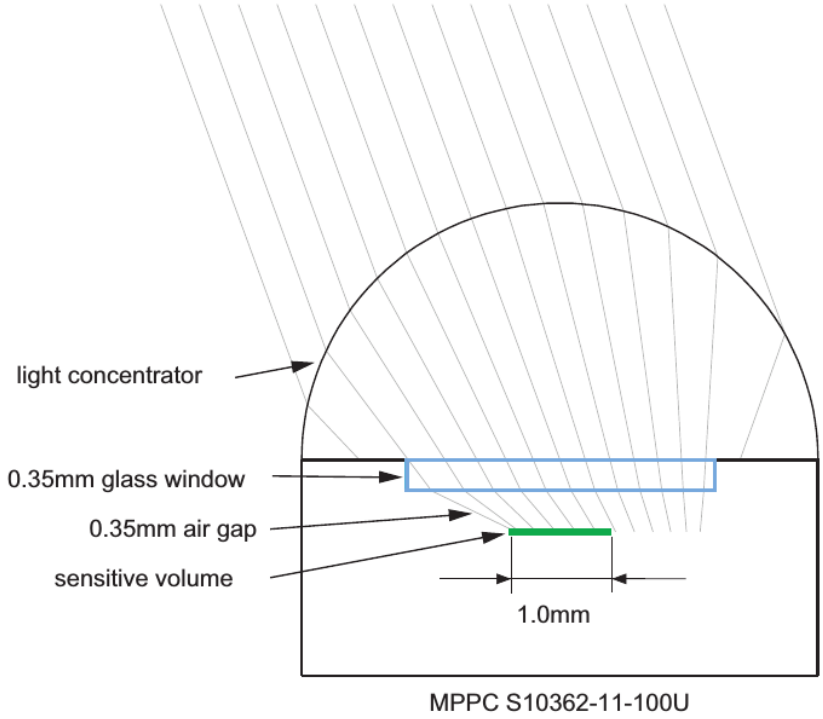

Figure 3.19: Hemispherical light concentrator with the main elements of the SiPM: the sensitive volume, the glass window, the air gap and the metal package [62].

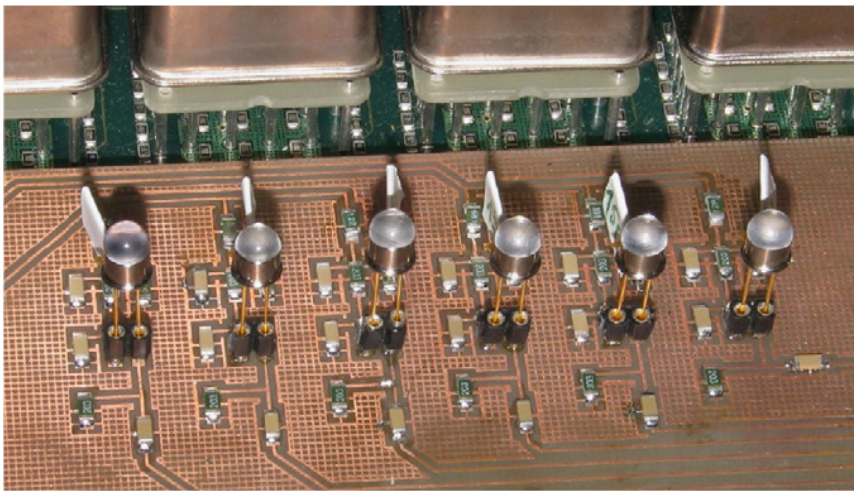

Figure 3.20: Array of 6 MPPC 10362-11-100U SiPMs with 1 mm^2 active area and 100 μm cells, equipped with light concentrator was used as a detector of Cherenkov photons in a cosmic ray test [62].

and with the light concentrators, are shown in Fig. 3.21.

A new type of the Hamamatsu SiPM, MPPC S10362-11-100P, with 1 mm^2 active area in Surface Mounted Device (SMD) packaging with a reduced protective layer thickness (300 μm) became available. The dark counts are the same as for metal package device, namely 1 MHz. The SiPM with 3×3 mm^2 active area, which would serve the Belle II ARICH needs better, has the dark counts rate of 12 MHz (10 MHz for the device with 50 μm cells) [63]. Eventually, 100 μm cell size device with 1×1 mm^2 area was chosen for the 64 individual channels detector, shown in Fig. 3.22,

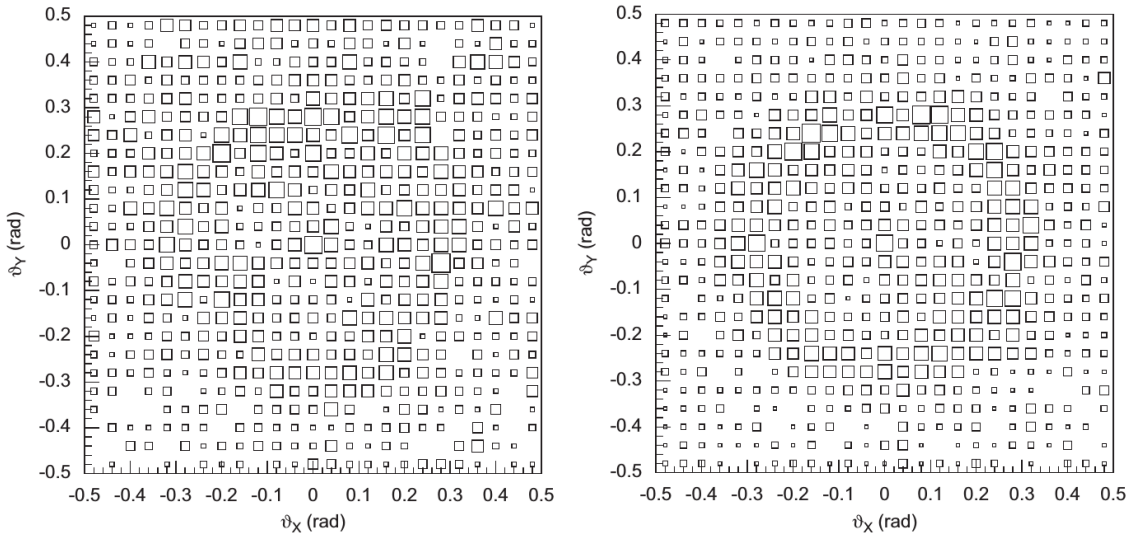

Figure 3.21: The SiPM hits accumulated for many tracks represented in Cherenkov angle space. The measurements were carried out without (left) and with (right) the hemispherical light concentrators. The ring can be clearly observed in the runs with the light concentrators.

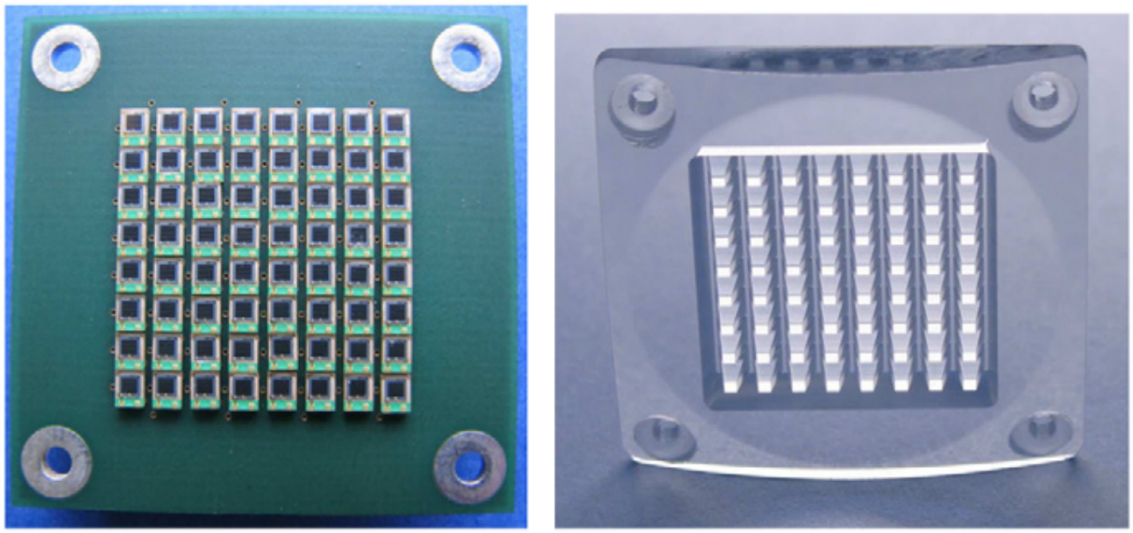

Figure 3.22: Photographs of: 8 × 8 array of Hamamatsu S10362-11-100P SiPMs (left); the system of light concentrators shaped as truncated pyramids (right).

left.

A RICH prototype consisting of a 10 mm thick aerogel radiator and the photon detector module with 64 MPPC S10362-11-100P was assembled and tested in an 120 GeV/c pion beam at CERN [38, 64, 65]. The pions radiated photons in the aerogel under an angle of 240 mrad relative to their track direction. The photons were detected with the module at a distance of 115 mm from the aerogel upstream surface. The array of 64 SiPMs was grouped into pads of 5.08 mm × 5.08 mm, consisting of 4 SiPMs each. Therefore, the geometrical efficiency of the bare module was:

$$\frac{4 \times 1 \text{ mm}^2}{5.08 \times 5.08 \text{ mm}^2} = 15.5\%.$$

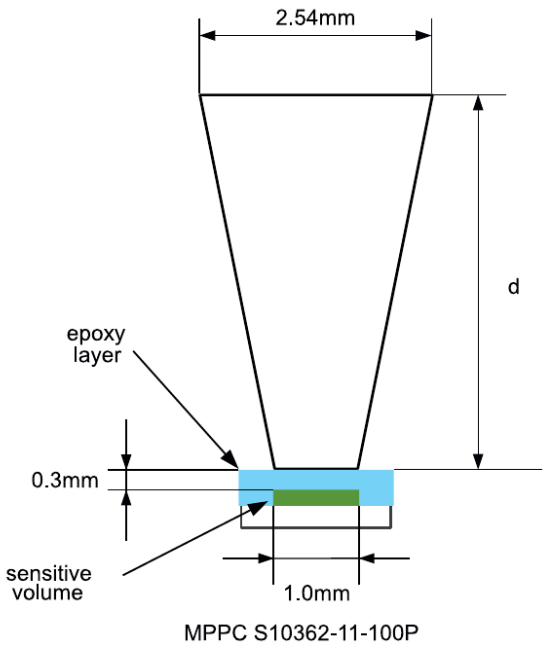

Figure 3.23: A pyramidal light concentrator seems to be better suited for the Hamamatsu S10362-11-100P Surface Mounted Device (SMD) type of SiPM that has a reduced protective layer thickness (0.3 mm) [66].

A further study of light concentrators, for the 64 channels detector, involved light concentrator shaped as truncated pyramid. The pyramid concentrators perform better than hemispherical for the new SMD packaged SiPMs with reduced protective epoxy layer Fig. 3.23, because considerably fewer rays miss the active area due to divergence at the exit window.

Eventually, the solid light concentrators were manufactured from an UV grade perspex lens used in HERA-B RICH optical system [67] (Fig. 3.22, right). The entry window of the produced light guide was 2.3 $\times$ 2.3 mm^2 and the expected acceptance was 54%, still 3.5$\times$ higher than the one of the bare SiPM module.

The time spectra of SiPM pulses measured in the test beam, both without and with the light concentrators, are shown in Fig. 3.24. There are 2.3$\times$ more Cherenkov hits registered with the light concentrators then without them. Selecting the SiPM pulses in a narrow detection time window would reduce the background hits further, as show in Fig.3.25 (left). This way the signal-to-noise ratio is improved in the way that a measurement of Cherenkov rings becomes possible. The hits accumulated from many particle tracks, transformed to Cherenkov space are shown in Fig. 3.25.

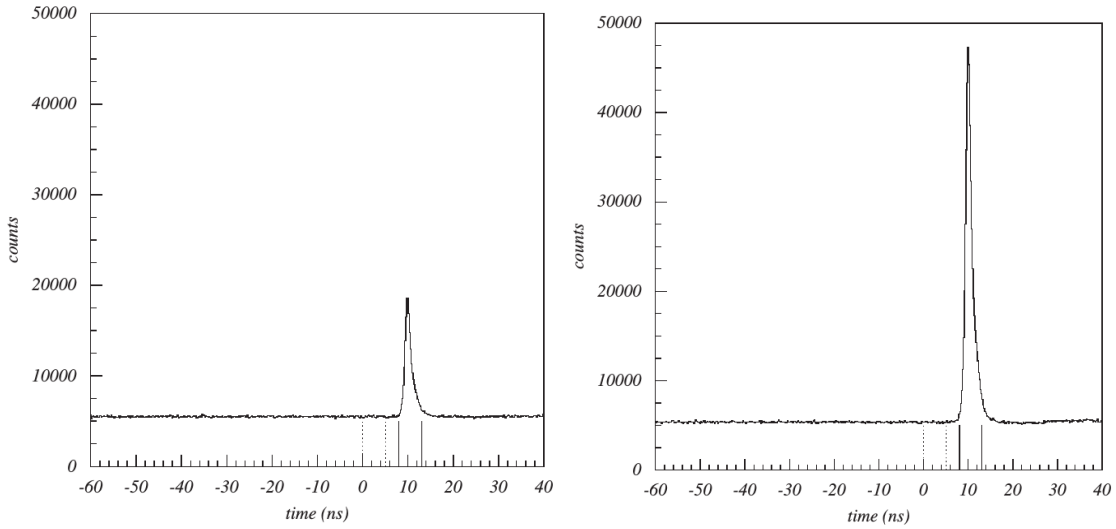

Figure 3.24: The time spectra for the SiPM pulses in the case without (left) and with (right) the light collection system. The indicated cuts correspond to on-time (full) and out-of-time (dashed) 5 ns windows [38].

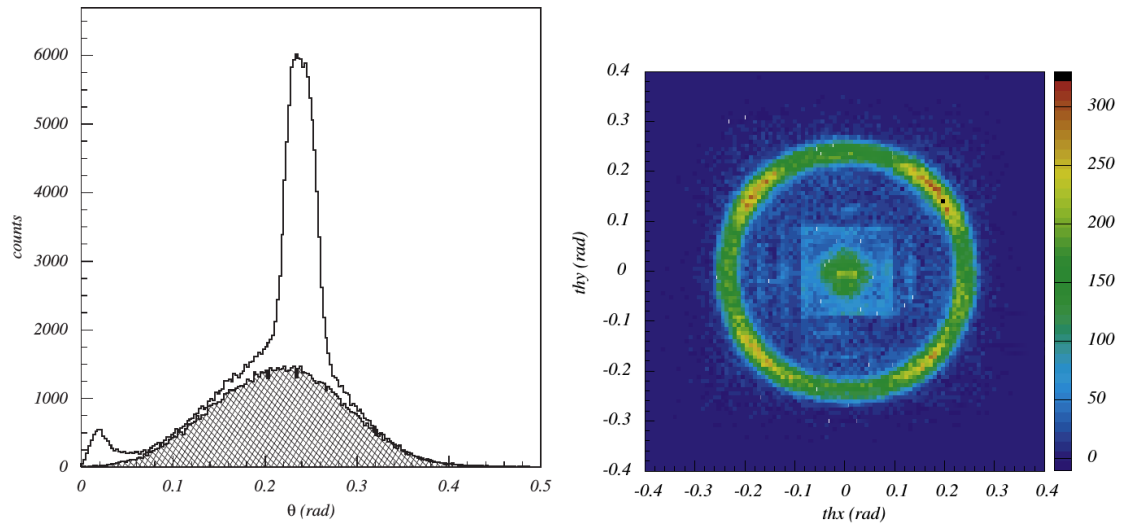

Figure 3.25: Left: The distribution of SiPM hits with respect to their corresponding Cherenkov angle for pulses inside the 5 ns time window (open histogram) and for pulses in a corresponding out-of-time window (shaded). The data are from measurements without light collections system. Right: The accumulated SiPM hits represented in Cherenkov angle space for measurements with the light collection system. Since the module area was smaller than Cherenkov ring area, the measurements were repeated for different module positions on a 3×3 grid. The azimuthal distribution of the Cherenkov ring is uneven due to limitations in acceptance [38].

Chapter 4

RICH Prototype

Design of prototype photon module is described. The specially machined light concentrators array increased the sensitivity of the SiPM array. The results of SiPM and photon module characterization tests are presented.

4.1 Photon Detector Module

4.1.1 MPPC S11834 - an Array of SiPMs

Recently, an array of 64 silicon photomultipliers became available from Hamamatsu. It is a prototype with a considerably reduced dark count noise compared to previous devices. This Multi-Pixel Photon Counter MPPC S11834-3388DF is an 8×8 silicon photo-multiplier array (Fig. 4.1) mounted on a surface-mount package with a flexible printed circuit (FPC) cable. Such mounting allows for compact design and the arrays can be combined together with almost no dead space between them. Each silicon photo-multiplier is one square channel with a side length $a = 3$ mm and an active area $A = 3 \times 3$ mm^2. The channels are spaced at $b = 5$ mm pitch that results in a dead space around each channel.

The device is of p-on-n type, therefore the peak sensitivity is in the blue region, at 440 nm. The technical specifications of the MPPC are given in Table 4.1. Each SiPM has an epoxy protective layer whose width has been reduced, compared to previous devices, to 300 μm.

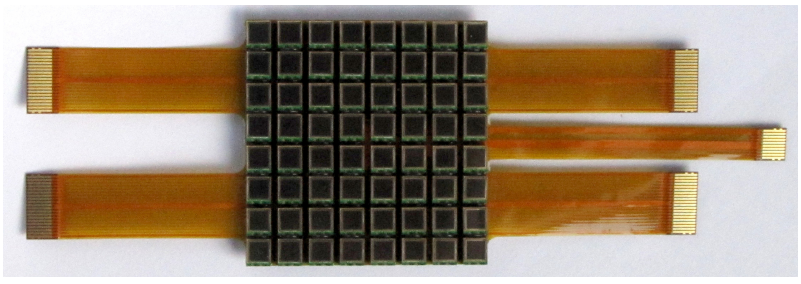

Figure 4.1: Photograph of 64 SiPM array Hamamatsu MPPC S11834-3388DF

Parameter	Value
Number of SiPMs	64
SiPM width, a	3 mm
SiPM pitch, b	5 mm
Effective photosensitive area per SiPM, A	3×3 mm^2
Cell pitch	50 μm
Number of cells per SiPM	3600
Fill factor, ε_{fill}	61.5%
Spectral response range	320 to 900 nm
Peak sensitivity wavelength, λ_{peak}	440 nm
Recommended operating voltage, V_{bias}	70±10 V
Photon detection efficiency, PDE	50%
Dark current per SiPM, I_d	Max. 3 μA
Terminal capacitance per SiPM, C_{tot}	320 pF
Temperature coefficient of bias, $(\mathrm{d}\,A/\mathrm{d}\,T)$	56 mV/°C
Gain, G	7.5×10^5

Table 4.1: Hamamatsu S11834 characteristics from data sheet [68].

4.1.2 Acceptance of MPPC array

The acceptance (or geometrical efficiency, a term used similarly) of the MPPC array $\varepsilon_{\text{array}}$ is:

$$\begin{aligned} \varepsilon_{\text{array}} &= \left(\frac{a}{b}\right)^2 \\ &= \left(\frac{3}{5}\right)^2 = 0.36, \end{aligned} \tag{4.1}$$

where a is width and b is pitch of SiPMs, both listed in the Table 4.1. The acceptance is considerably higher than the acceptance of the arrays available up to now (15.5%, *cf.* Chapter 3). Nevertheless, it is far from 1. To improve it, we decided to use a light concentrator that is able to concentrate the light from a larger (entry) surface to a smaller (exit) surface. Ideally, such a light concentrator would collect more photons and improve the efficiency by a collection ratio ζ. Ideal collection ratio is the one that results in the acceptance of 1.0:

$$\zeta_{ideal} = \left(\frac{b}{a}\right)^2 = 2.78, \tag{4.2}$$

and the improved acceptance would be:

$$\varepsilon_{acc} = \zeta_{ideal}\varepsilon_{\text{array}} = 1.0. \tag{4.3}$$

However, the attainable collection ratio ζ is always lower than ζ_{ideal}. This means that not all the photons that hit the larger, entry, window under different angle can be transferred to a smaller, exit, window.

To determine the dependence of the acceptance on the dimensions of the light concentrator (exit window side a and height d), a simple ray-tracing Monte Carlo simulation was written in C++ using ROOT framework [69] (Fig. 4.2). Rays are distributed at a certain angle or inside an angle interval (see later), uniformly over the area of the entry window. The Fresnel formulae are used to determine the coefficients of reflection and refraction at the entry window. The refracted ray is followed inside the light concentrator and reflection and refraction coefficients are calculated at the lateral sides. Finally, the ray exits at the exit window, where perfect optical coupling with SiPM is presumed and no reflection occurs. The distance between the exit window and the SiPM can be adjusted; ideally it would be 0 mm, but in the case of MPPC array, it was 0.300 mm, the same as the epoxy protective layer on top of every SiPM, through which the rays could escape.

In the previous studies of light concentrators for the 1×1 mm^2 SiPMs [64], two possible realisations of pyramidal concentrators: hollow and solid. A hollow light concentrator would be easy to produce as a funnel with reflecting sides, *e.g.* a four mirror walls (Fig. 4.3, left). A solid light concentrator is shaped as a truncated pyramid, made from glass or plastic (Fig. 4.4, left). Both types of concentrators collect light onto a smaller surface by reflection at the side walls, the solid concentrator relying on the total internal reflection. The simulation study of the acceptance as a function of the angle of incoming rays for both types shows that the hollow light concentrator loses efficiency for all incident angles because of the finite reflectivity of the mirrors (taken to be 90 % in the simulation), and because of the back reflection

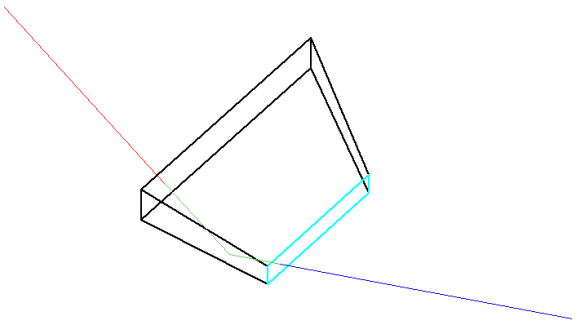

Figure 4.2: Left: Side view of ray-tracing simulation of a light concentrator with one ray displayed. The simulated ray is coloured red before hitting the concentrator, green inside the concentrator and blue after the refraction at lateral sides or exit window.

of the rays even at small incident angles (Fig. 4.3, right). Solid light concentrator performs better, since it benefits from the refraction at the entry surface. The loss due to reflection at the entry surface amounts to 4%, while the rays start to escape through the walls at the incident angle of $\approx 30^\circ$ (Fig. 4.4, right).

An optimal height of the light concentrator was inferred from the acceptance as a function of pyramid height d and exit window size a, while the size of the entrance window remained fixed and equal to the channel pitch b. For the study of the height of pyramids to be used for production, the light rays were distributed uniformly over the solid angle, with the polar angle $\theta \in [0^\circ,30^\circ]$ and azimuthal angle $\phi \in [0^\circ, 360^\circ]$ relative to the entry surface normal (Fig. 4.5, left). The acceptance as a function of pyramid height d and exit window size a is given in Fig. 4.5, right.

The chosen dimensions for production are $a = 3.0$ mm and $d = 3.0$ mm. With these dimensions, the acceptance of the array as a function of the polar angle θ, for the rays distributed uniformly inside this angle, is shown in Fig. 4.6, left. The resulting acceptance is $\varepsilon_{acc} \approx 0.90$ when the incoming rays are in the interval $\theta \in [0, 30]$. Fig. 4.6, right shows the case where the rays are simulated at a fixed polar angle θ. In the case of the perpendicular incidence, $\theta = 0^\circ$, the maximal acceptance is $\varepsilon_{acc} = 96\%$ since the reflectance at the entry window is included.

In a previous study [62], light concentrators with a hemispherical entrance window were also considered (Fig. 3.19). They show a four-fold improvement in response to perpendicular light. However, the pyramidal concentrators are better suited for the rectangular active area and are much easier to manufacture.

The concentrators were machined by Sinocera (Shanghai, China) from borosilicate glass (Chinese K9 specification, similar to Schott BK7); its refractive index is $n_{LC} = 1.53$ at $\lambda = 405$ nm and the transmittance is given in Fig.4.7. The transmittance losses are mainly due to the reflections at the entry and exit planes; the absorption is less than 1% and it was not taken into account in the simulations.

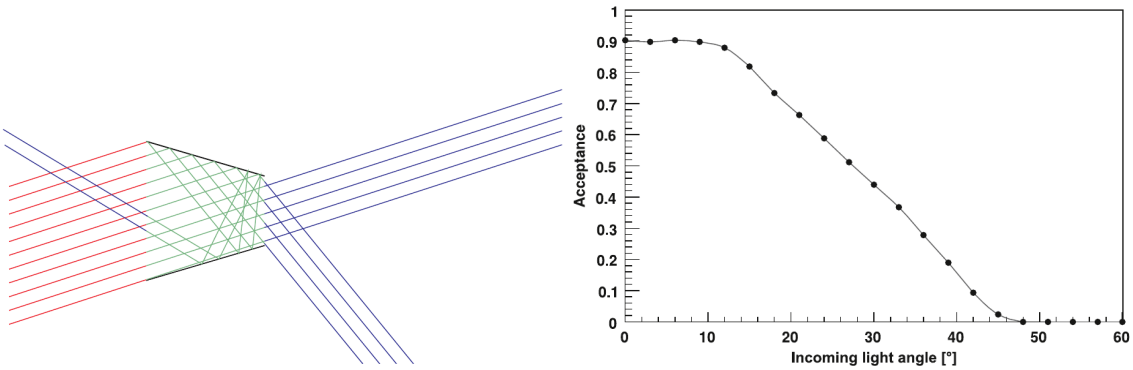

Figure 4.3: Left: Side view of ray-tracing simulation of a hollow light concentrator composed of mirrors. Right: Acceptance as a function of the angle of incoming light rays [64].

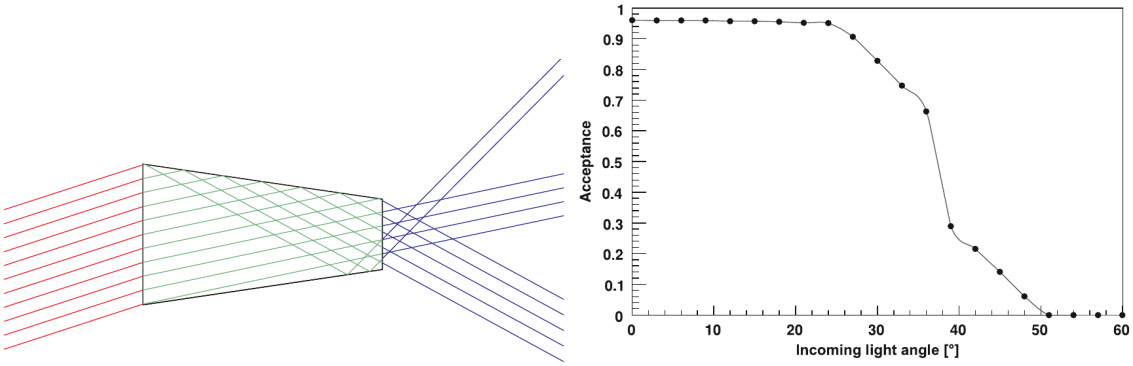

Figure 4.4: Left: Side view of ray-tracing simulation of solid light concentrator shaped as truncated pyramid. Right: Acceptance as a function of the angle of incoming light rays (right) [64].

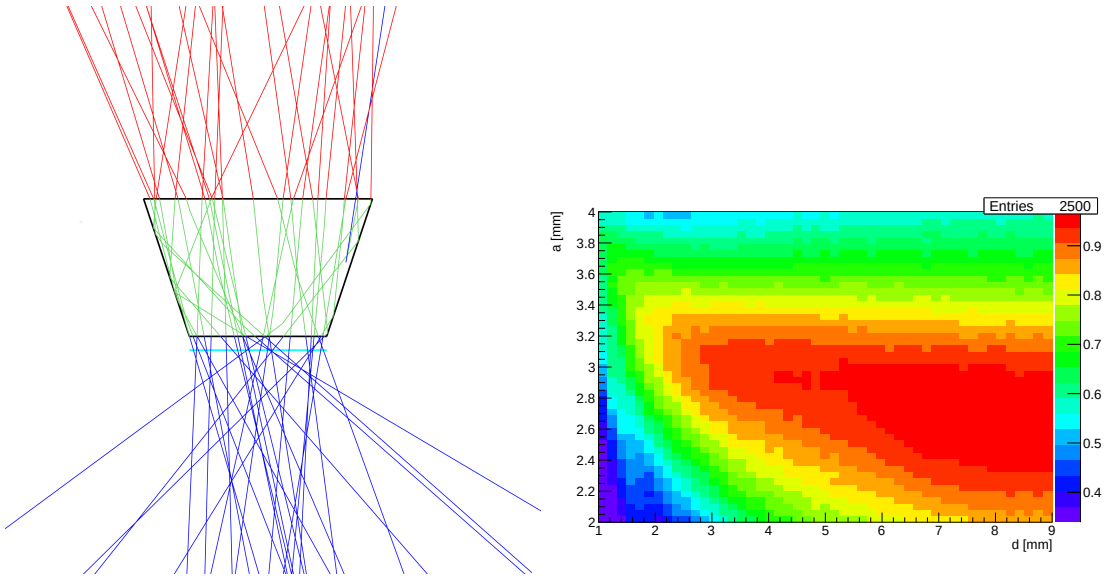

Figure 4.5: Left: The side view of the ray tracing simulation with rays distributed uniformly over $\cos\theta$ and with azimuthal angle inside the interval $\phi \in [0°, 360°]$. Right: Acceptance as a function of the length of the light concentrator d and the size of the exit window a.

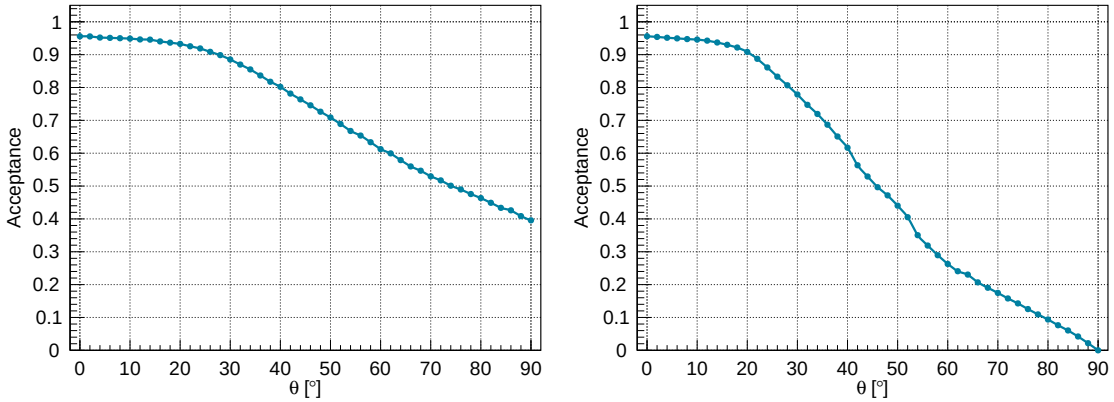

Figure 4.6: Left: Acceptance as a function of the maximal polar angle θ_{max} in the case when the rays are simulated in the interval $\theta \in [0, \theta_{max}$. Right: Acceptance as a function of the polar angle θ in the case when the rays are simulated at a fixed angle.

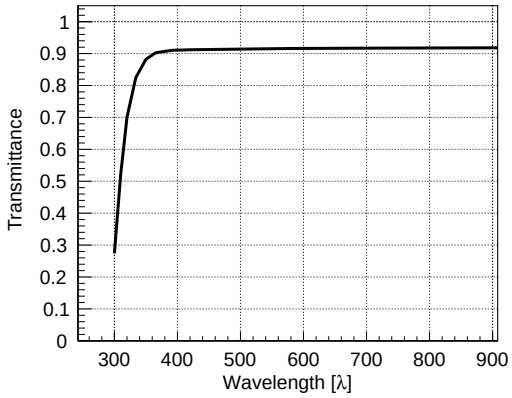

Figure 4.7: Schott BK7 5 mm glass transmittance as function of the wavelength [70].

Each pyramid was cut from glass and glued with optical cement ($n_{cement} = 1.48$) to the 1 mm thick common plate of the same glass (Fig. 4.8, left). The final light concentrator array is shown in Fig. 4.8, right.

The prototype photon module consists of the MPPC S11834 array in an aluminium support frame and the light concentrators in the front pressed against the MPPC with a cover (Fig. 4.9). To improve the optical coupling between the light concentrators and the epoxy layer ($n_{epoxy} \simeq 1.55$) on top of every SiPM, the optical grease with refractive index $n_{grease} = 1.46$ was used.[1]

4.2 Laboratory Set-up

The response of the photon detector module to low intensity light was tested in the laboratory set-up (Fig. 4.10). As a light source Advanced Laser Diode System EIG1000D with PiL040 head was used. The head emits blue light at $\lambda = 404 \pm 2$ nm. The duration of the pulse is $\tau_{laser} \approx 30$ ps FWHM at 35% tune, the setting that was used in all measurements.

[1] Rexon RX-688.

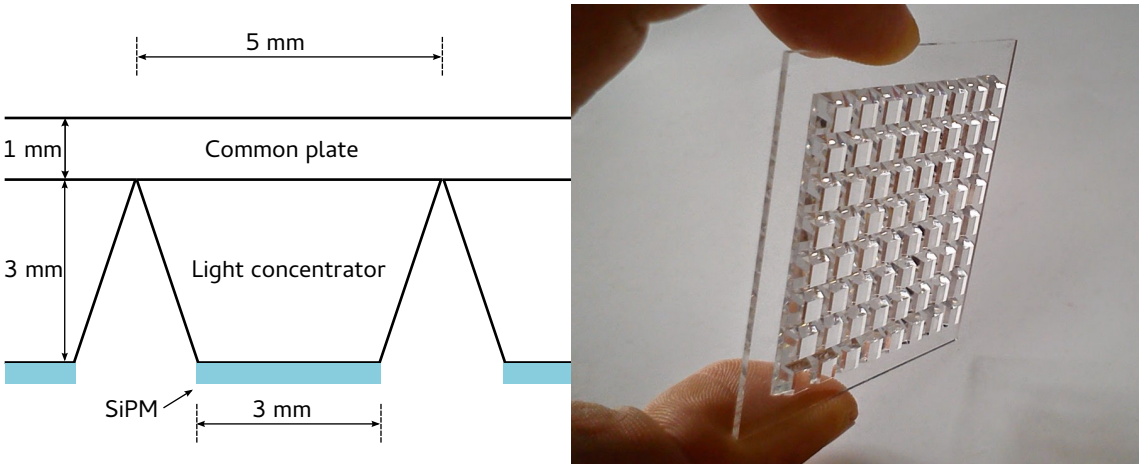

Figure 4.8: Left: Pyramids glued to a common plate with dimensions as chosen for the production. Right: Photograph of borosilicate concentrators array.

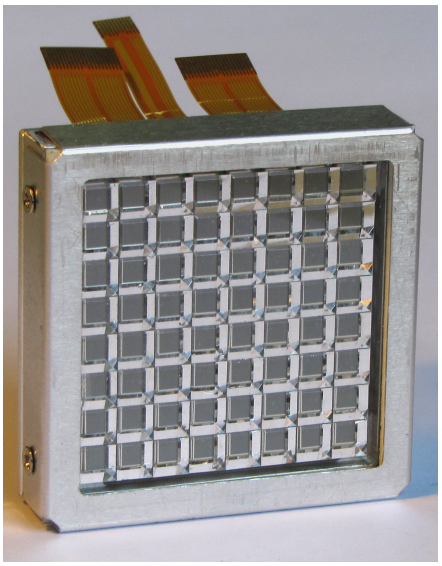

Figure 4.9: Prototype detector module: MPPC and light concentrators array assembled together in aluminium frame.

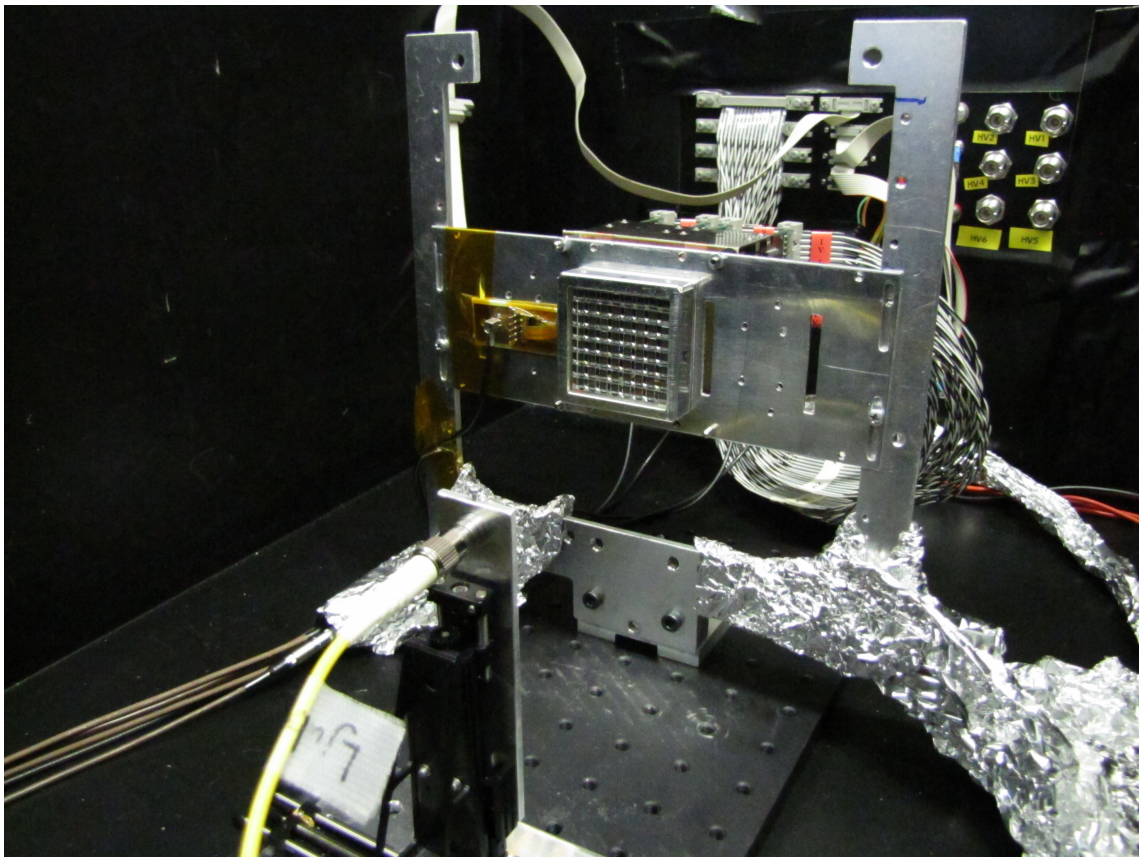

Figure 4.10: Laboratory set-up. The optical bench with the photon module mounted inside the light-tight box.

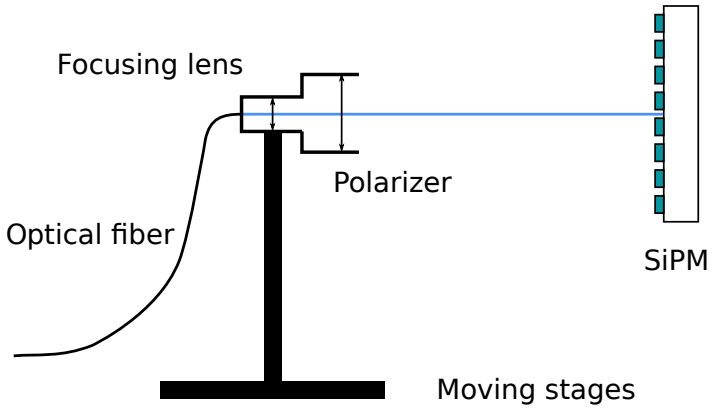

Figure 4.11: Optical path scheme.

The light from the laser head was attenuated to single photon level by a set of neutral density filters and fed with a collimator to a single mode optical fibre. A filter combination used was $0.03\% + 2 \times 25\% + 50\%$, resulting in the attenuation of approximately $10^5\times$. The fibre is fed into a light tight box with the photon module mounted inside (see optical path drawing in the Figure 4.11). At the end of the fibre a lens is attached, which focuses light to the detector surface. In addition, a polariser was used to study the influence of polarised light on the collection ratio of the concentrators. The lens (and the polariser) was attached to the moving stages with a positioning precision of 0.5 μm (National Aperture MM-3M-F).

The analogue signal was monitored with an oscilloscope LeCroy WavePro 7300A with a 3 GHz bandwidth.

4.2.1 Breakdown and Gain Measurements

To determine the operating voltage and the gain, a separate measurements were performed [71]. The set-up involved the MPPC array, an amplifier (ORTEC FTA820, 200× amplification) and a commercial charge to digital converter (CAEN V965, 16-channel dual range QDC).

The bias voltage of the four MPPC arrays is given in the Table 4.2.

The array no.4 was used for the beam test and for the light concentrator performance tests (Chapters 5 and 6). The breakdown voltage was measured for one SiPM in the array no.4 only; it was found to be $V_{breakdown} = 70.8$ V. The gain was measured to be $\approx 0.4 \times 10^5$ when array is biased at 72.1 V. The variation of the gain is small inside one array, as can be observed from the gain of all channels, normalized to unity, given in Fig. 4.12.

The approximate values of the over-voltage and gain in the set-up used in RICH prototype are obtained by adding a diode drop to the voltages in the previous measurement. Adding a diode drop, the breakdown voltage is $V_{breakdown} \simeq 71.5$ V. The gain was measured at $V_{bias} \simeq 72.8$ V. The operating voltage in the beam test

MPPC	$V_{bias}[V]$
1	72.8
2	72.8
3	72.8
4	72.1

Table 4.2: MPPC array number and bias voltage used in gain measurements.

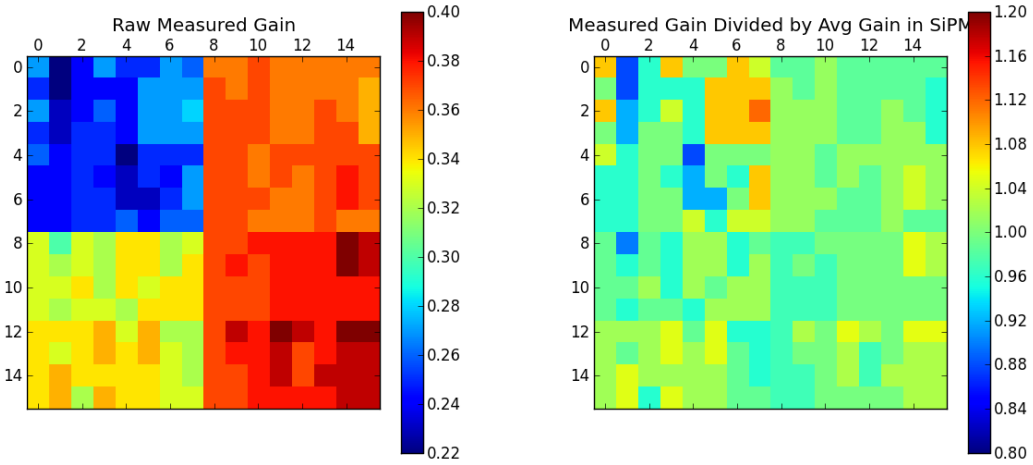

Figure 4.12: Left: Measured gain per SiPM ($\times 10^5$) for 4 MPPC arrays. The arrays no. 1, 2, 3 and 4 are in the top left (individual SiPMs are represented with bins in x direction: $0-7$, y-direction $0-7$), top right (bins in x-direction: $8-15$, y-direction: $0-7$), bottom left (bins in $x-$direction: $8-15$, y-direction: $0-7$) and bottom right (bins in $x-$-direction: $8-15$, y-direction: $8-15$) corners, respectively. Right: Relative variation of the gain measured for all 4 MPPC arrays. [71]

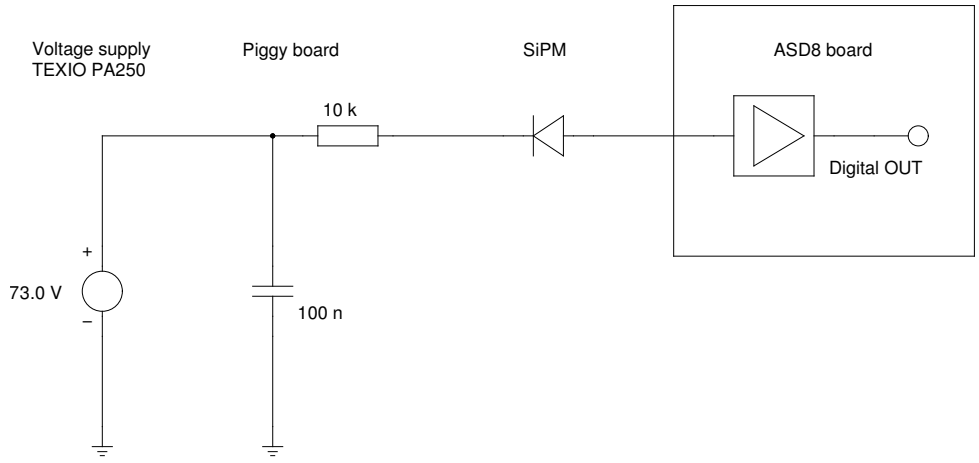

Figure 4.13: Electric scheme as used in the laboratory set-up. In the beam test, there was no filter on the piggy board, between the voltage supply and SiPM.

and most of the laboratory measurements was $V_{bias} = 73.0$ V, thus the gain was somewhat closer to the one given by the producer (7.5×10^5). The over-voltage was:

$$V_{over} = V_{bias} - V_{breakdown} = 1.5 \text{ V}. \tag{4.4}$$

4.2.2 Front-end Electronics and Data Acquisition

The signals from 64 SiPMs are fed to 4 front-end electronic boards for amplification and digitisation. The read-out circuit for one channel, together with the power supply for the SiPM bias voltage, is given in Fig. 4.13. The bias voltage for the SiPMs was delivered by voltage supply Texio PA250-0.42B. After the beam test, an additional low-pass filter was added to the voltage distribution board. The board lay-out is given in Appendix E. To prevent the damage from high signals or voltage spikes, the inputs of the amplifier chips are protected with diode limiters. Every input is biased via feedback from the shaper stage, so it is always at about 0.7 V.

The front-end boards use ASD8-B chips originally designed for read-out of the straw tracker tubes [72]. They were successfully used for the read-out in HERA-B RICH counter [73], as well as in other sub-detectors in HERA-B. Each ASD8-B chip has 8 digital channels; two chips per board are used, giving 16 digital channels per board. Every channel has implemented a charge pre-amplifier, shaper and discriminator. The charge pre-amplifier has a rather high amplification of 2.5 mV/fC. The charge sensitive amplifier is needed as read-out of the signal from semiconductor device, because the capacitance of the semiconductor changes during the avalanche. The charge amplifier acts basically as a charge integrator. The second stage of the ASD8-B chip is a pole-zero cancellation shaper with three consecutive integrators. Last stage is a timing discriminator which gives a digital output. The discriminator threshold voltage was provided by an digital-to-analogue converter, and it could be set to a value from 0 to 2 V.

Apart from 16 digital outputs, there is one analogue output per board, implemented to allow the signal monitoring. This output is implemented after the first integrator in the shaper stage and has its own additional final amplifier with 10× amplification. The peaking time of the analogue output is 7 ns and the output

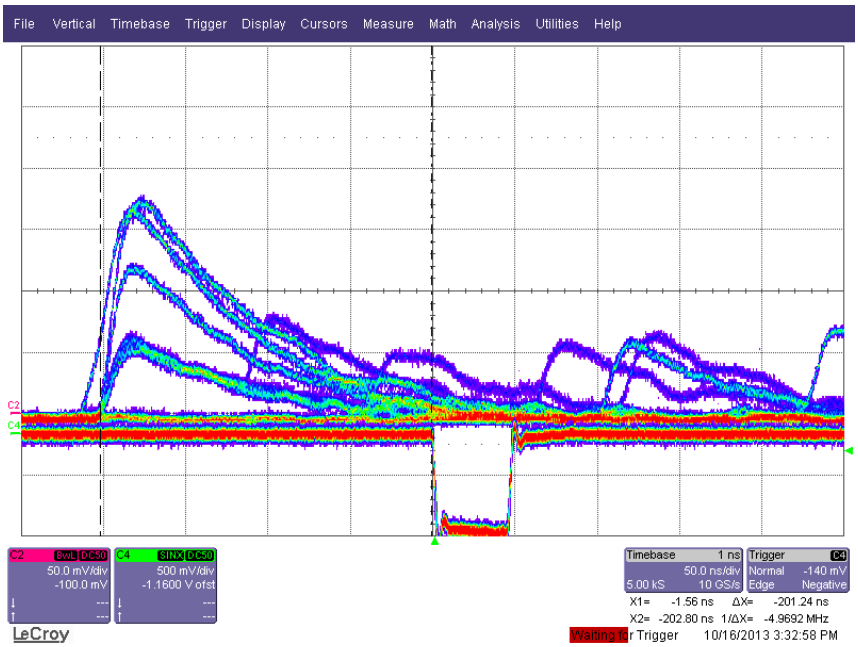

Figure 4.14: Superposition of SiPM signals on the oscilloscope, amplified with ASD8 analogue section (upper signal, $C2$). The oscilloscope is triggered by laser trigger (lower signal, $C4$). Horizontal scale 50 ns/division, vertical scale 50 mV/division.

pulse is proportional to the input signal up to $\approx$ 50 fC, after which the saturation is observed.

The ASD8 boards have good features that makes them good candidate for the readout of position detectors on high-rate experiments. These characteristics are [74]:

— low power consumption ($\approx$ 15 mW/channel),

— short measurement time of 5 ns,

— a good double pulse resolution of 20 ns and

— low operational threshold ($\approx$ 1 fC).

Fig. 4.14 shows the signal from SiPM produced by low intensity light, after the amplification with the ASD8-B analogue section. three different signal heights, caused by avalanches in one, two and three cells, can be clearly observed.

Although the ASD8 boards can work in wide range of input signals, they have a very high gain optimised for read-out of straw tracker tubes. Due to the high gain they are prone to saturate easily, which was already shown in the characterisation tests for HERA-B RICH [74]. Also, due to presence of the analogue feedback on the same board, a very good grounding and voltage supply circuitry is needed [75]. During the tests, I indeed had problems with pick-up noise and oscillations, which were removed only after shielding the electronic boards with tin foil.

The probability that two or more photons will hit the same channel in RICH is very small (*cf.* Chapter 6 for simulation results). It is therefore not necessary to register the height of the pulse, or in the other words, the photon sensor does not need to have energy resolution. To discriminate SiPM signal from the background

it is enough to register the signal from the digital output. For that purpose the signal from ASD8 discriminator was sent to commercially available time-to-digital converter (TDC) CAEN V673A. It is a 64-channel multi-hit TDC with 1.04 ns bin width. The signal block diagram of the whole SiPM read-out is given in Fig. 4.15.

The TDC signals were put through a VME controller to the personal computer, which stored the time stamp of the signal for every channel in an ASCII file for offline analysis. The automated data acquisition was written in C and using LabWindows IDE[2]. The STOP signal and the read-out sequence of the TDC buffers was vetoed by the PC.

The SiPM signals served as the START signals for the TDC, while the delayed laser trigger served as the common STOP signal. The relative time of the START signal with respect to the STOP signal were stored in the file, together with the moving stages x, y position. Using this information it was possible to correlate the position of the laser and the triggered channel, and to make two-dimensional scans across the SiPM in order to study its response to the low intensity light.

The temperature of the SiPMs was monitored by a Pt-100 Resistance Temperature Detector (RTD) mounted in the module frame, very close to the SiPM array. The signal from the sensor was distributed via FieldPoint system to a PC, where it was saved to MySQL database.

4.2.3 Time Distribution of Signal

In the measurements with ORTEC FTA820 amplifier [71], the observed signal rise time is ≈ 10 ns and the fall time 20 ns. The fall time corresponds to the recovery time of a single cell. The recovery time $t_{recovery}$ depends on the time constant of the cell $\tau = R_q\, C_{cell}$, where C_{cell} is the capacitance of the cell and R_q is the resistance of the quenching resistor. From the measured values of cell capacitance $C_{cell} = 53.6$ fF and quenching resistors $R_q = 400\ k\Omega$ for the MPPC S10931-050P [56] (3×3 in SMD packaging, produced in 2011) one can calculate the time constant:

$$t_{recovery} = R_q\, C_{cell} \simeq 20 \text{ ns}, \tag{4.5}$$

and the total dead time is $t_{dead} \simeq 30$ ns, which is in a good accordance with the laboratory measurements.

The efficiency of the detector is affected by the finite time needed to recharge the cell, because the detector can not detect photons that come during that time. The probability that photon is lost due to the dead time can be calculated from the average hit occupancy. For the future Belle II ARICH, this is $r = 300$ Hz/cm^2 [11]. The channel size in ARICH and our RICH prototype is approximately the same, 0.25 cm^2, so the amount of time the detector is insensitive is

$$\Delta = r \times t_{dead} = 2 \times 10^{-6}. \tag{4.6}$$

However, in the case of SiPM, the dead time produced by dark counts is much higher, $\nu_d = 3$ MHz, therefore the probability is:

$$\Delta = \nu_{dark} \times t_{dead} = 9\%. \tag{4.7}$$

[2]An Integrated Development Environment (IDE) by National Instruments.

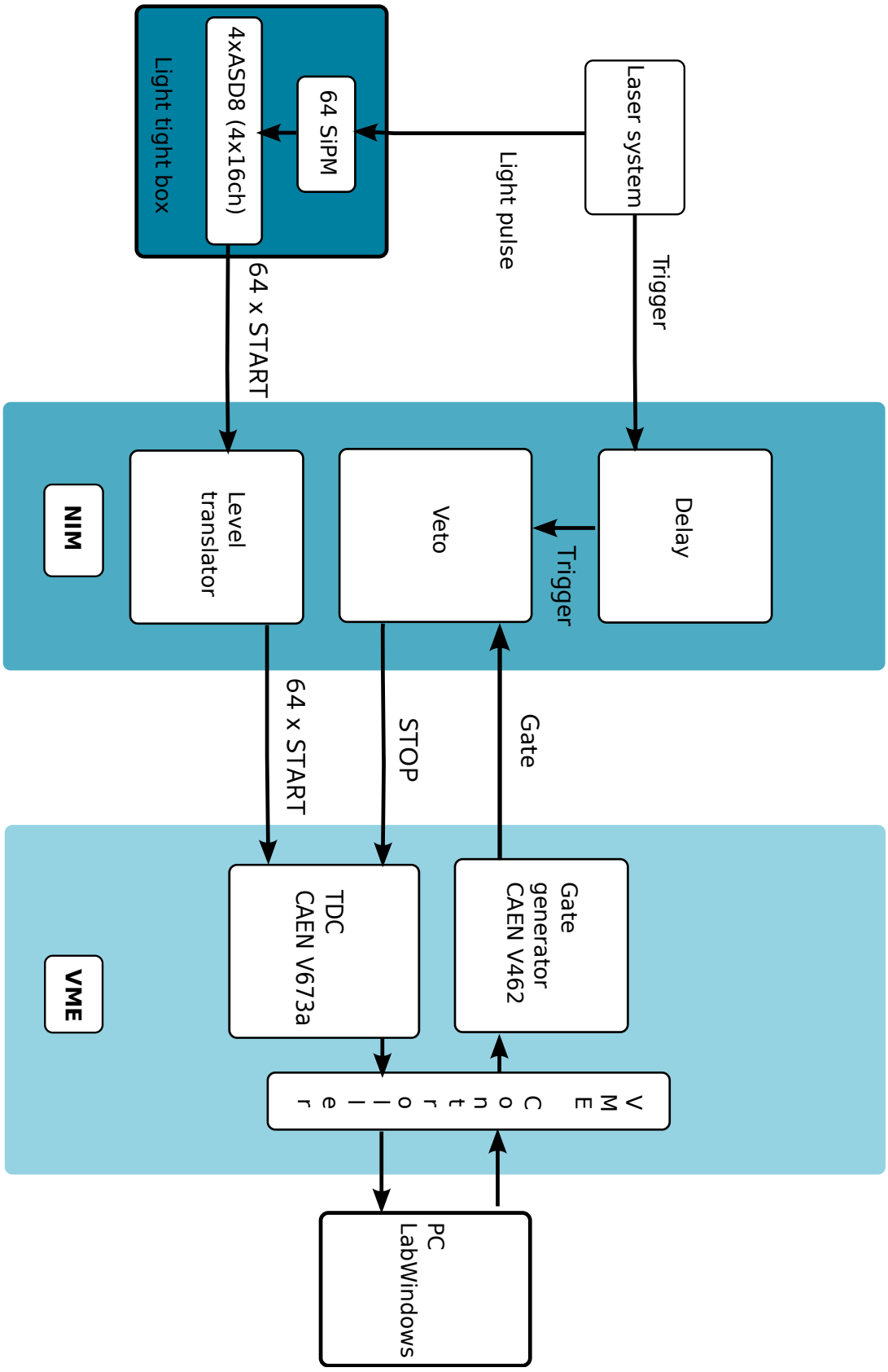

Figure 4.15: SiPM signal block diagram in laboratory set-up

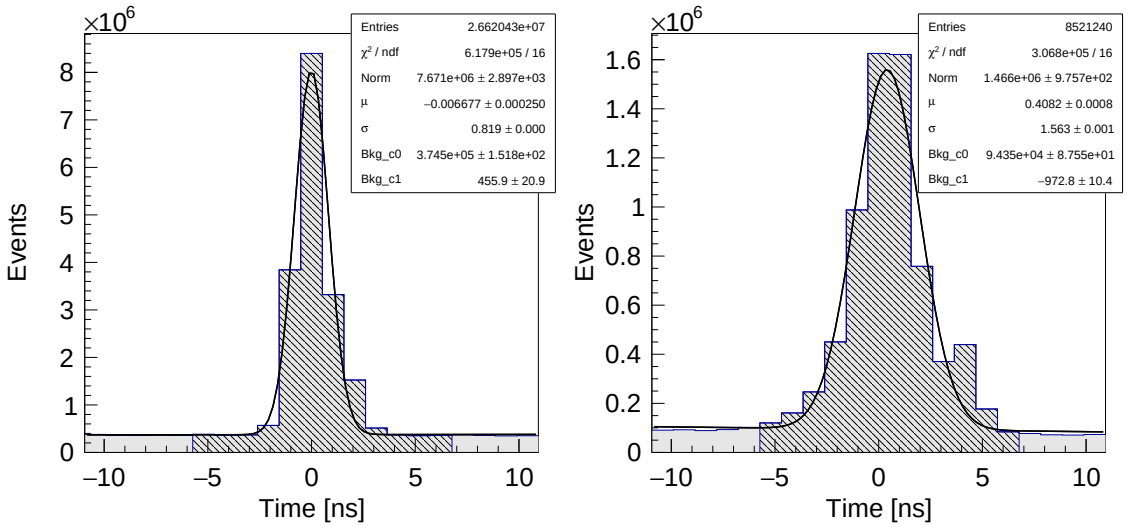

Figure 4.16: Left: Time of arrival distribution of SiPM hits triggered by a low intensity light focused to a single cell. The hatched histogram is the time window, $T_w = 10$ ns, in which lie the accepted hits. Right: Time of arrival distribution of SiPM hits in a sensitivity scan across the whole SiPM.

As have already been demonstrated in measurements with previous SiPMs (Chapter 3.4), with a narrow time window it was possible to register the Cherenkov photon hits using the similar electronics set-up with satisfying signal to noise ratio. For the laboratory tests we used the same method. The distribution of the signal arrival time is shown in the Figure 4.16, left. From the fit with the Gaussian function, the time resolution is inferred to be $\sigma_t \simeq 820$ ps when the hits are accumulated from SiPM response when the light is focused to a single cell. The main contributions to the time errors can be separated as follows:

1. the ASD8 chip contribute 500 ps,
2. the TDC resolution 300 ps,
3. laser pulse width is 30 ps,
4. single photon timing resolution for Hamamatsu S10262 with 3×3 mm^2 active area, the resolution is 250 ps [76].

Added in quadrature they result in total time resolution:

$$\sigma_t = \sqrt{\sum_i \sigma_i^2} \simeq 600 \text{ ps}. \tag{4.8}$$

When a channel is scanned over its whole active area, the resolution becomes much worse: $\sigma_t \simeq 1.6$ ns (Fig. 4.16, right).

It was shown in [76] that the single photon timing resolution of Hamamatsu MPPCs does not change significantly with changes in temperature $0 - 20°$C. Therefore, the long measurements were not influenced by the change in temperature of $\delta T = 1°$C.

4.3 Bench Tests

To check the operation of the assembled module, together with ASD8-B boards, we made measurements using the analogue outputs of ASD8-B boards. The accumulated amplitude signal for many triggers from SiPM 1 (with analogue output) is given in Fig. 4.17, top. The oscilloscope is triggered by the signal from the digital ASD8 out and the digital threshold is set to $V_{thr} = 0.3$ V. Setting the digital threshold to $V_{thr} = 1.5$ V, the electronic noise is removed and only the signals equal to, or larger, then one cell are detected (Fig. 4.17, bottom). The signal with the height of 3 or more photo-electrons is saturated, due to limitations of the ASD8-B boards.

The integrated charge produced by SiPM illuminated with low intensity light is shown in Fig. 4.18. The top histogram is produced with discriminator threshold set low (0.5 V), so that noise is also accepted. The discrete spectrum of collected charge, corresponding to number of detected photons, is clearly observed. The bottom histogram is produced with discriminator threshold set approximately at one half photon amplitude (1.5 V).

The module operated by detecting only timing information. No information about the photon flux was exploited. TDC hits that fall in time window of $T_w = 10$ ns were counted as signal hits. With such a time window, about 3σ events are accepted in the sensitivity scans over the whole area of SiPM. If the light intensity is low, the average number of detected photons N is proportional to the number of registered TDC hits:

$$N = \frac{\text{registered hits}}{\text{delivered triggers}}. \tag{4.9}$$

The dark current produce a signal that has the same height as if it was triggered by a photon. The signal produced by dark current as function of the bias voltage is given in Fig. 4.20, left. The dark counts rise with the bias voltage.

The laser beam was focused for each measurement by registering the SiPM signal when the laser moved above the edge of the sensitive zone. The registered distribution was fitted with the error function and the width of the underlying Gauss distribution was extracted. The measurement was repeated for different distances between the focusing lens and the MPPC. The minimal laser light waist obtained was $\sigma \simeq 5$ μm (Fig. 4.19).

With the low intensity laser light focused on the SiPM ($\sigma \simeq 50$ μm), the average number of detected photons as function of the bias voltage is given in Fig. 4.20, right. One can observe that the signal starts to rise not proportionally with the bias voltage. The curve has a linear part, where the number of registered hits rises proportionally with the bias voltage. The saturation zone follows, where the maximal gain is attained. It is typically at ≈ 2.5 V for this generation of the MPPCs. This dependence is probably due to the PDE saturation, the effect present in the n-on-p devices caused by the difference of the probability for the avalanche generation for electrons and holes, as explained in [77].

4.3.1 Average Number of Detected Photons

Collected charge spectrum should follow Poisson distribution. However, as has already been explained, the PDE of a SiPM depends on the bias voltage, and through it on the probability of cross-talk and after-pulses. The last two are responsible for

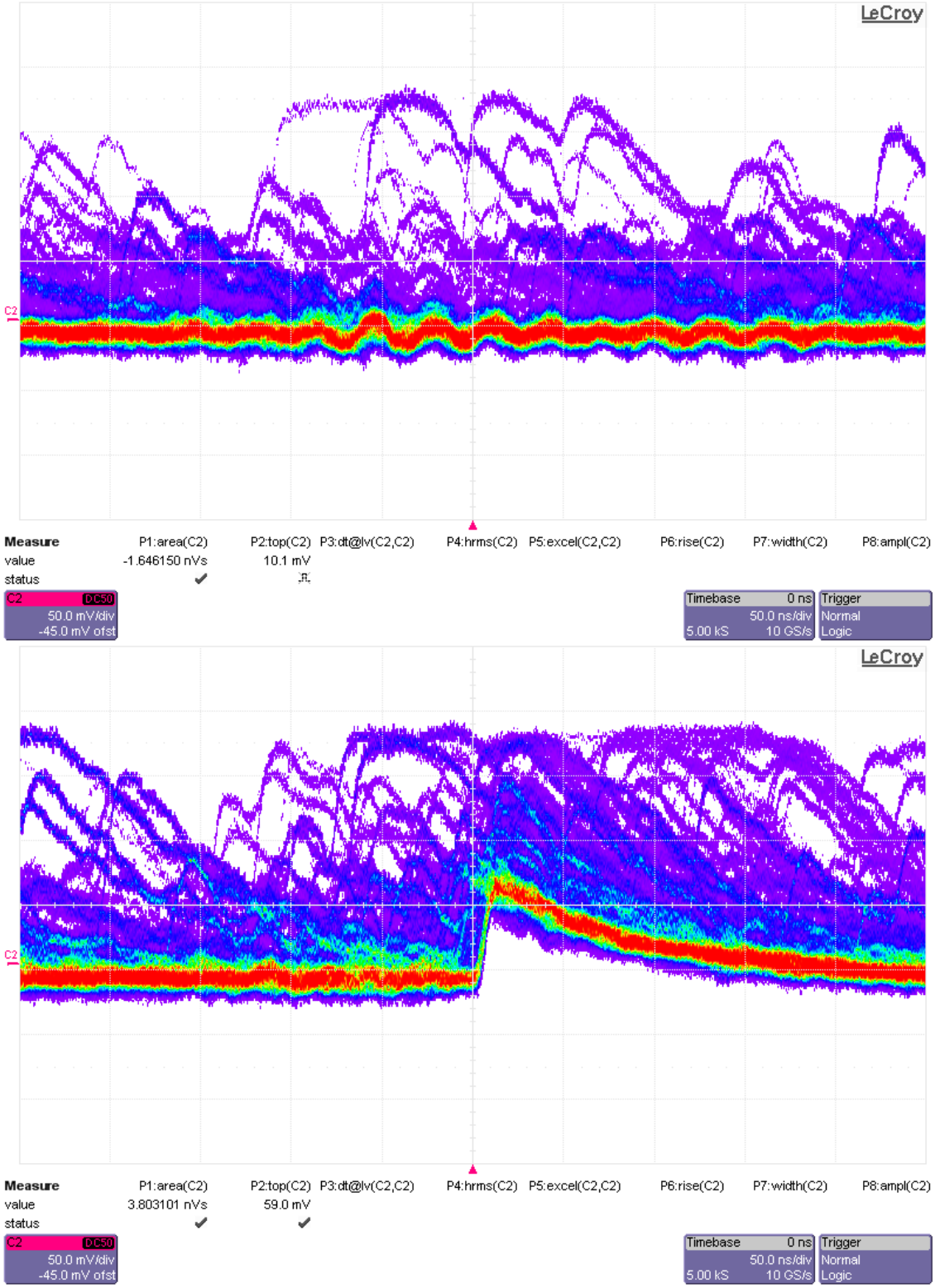

Figure 4.17: Superposition of SiPM signals on the oscilloscope without light (dark counts). Horizontal scale 50 ns/division, vertical scale 50 mV/division. The oscilloscope is triggered with the ASD8 digital output. The discriminator threshold is set to 0.3 V (top) and 1.5 V (bottom). The MPPC is biased at 73.0 V. Saturation of the signal is due to limitations of the ASD8-B boards.

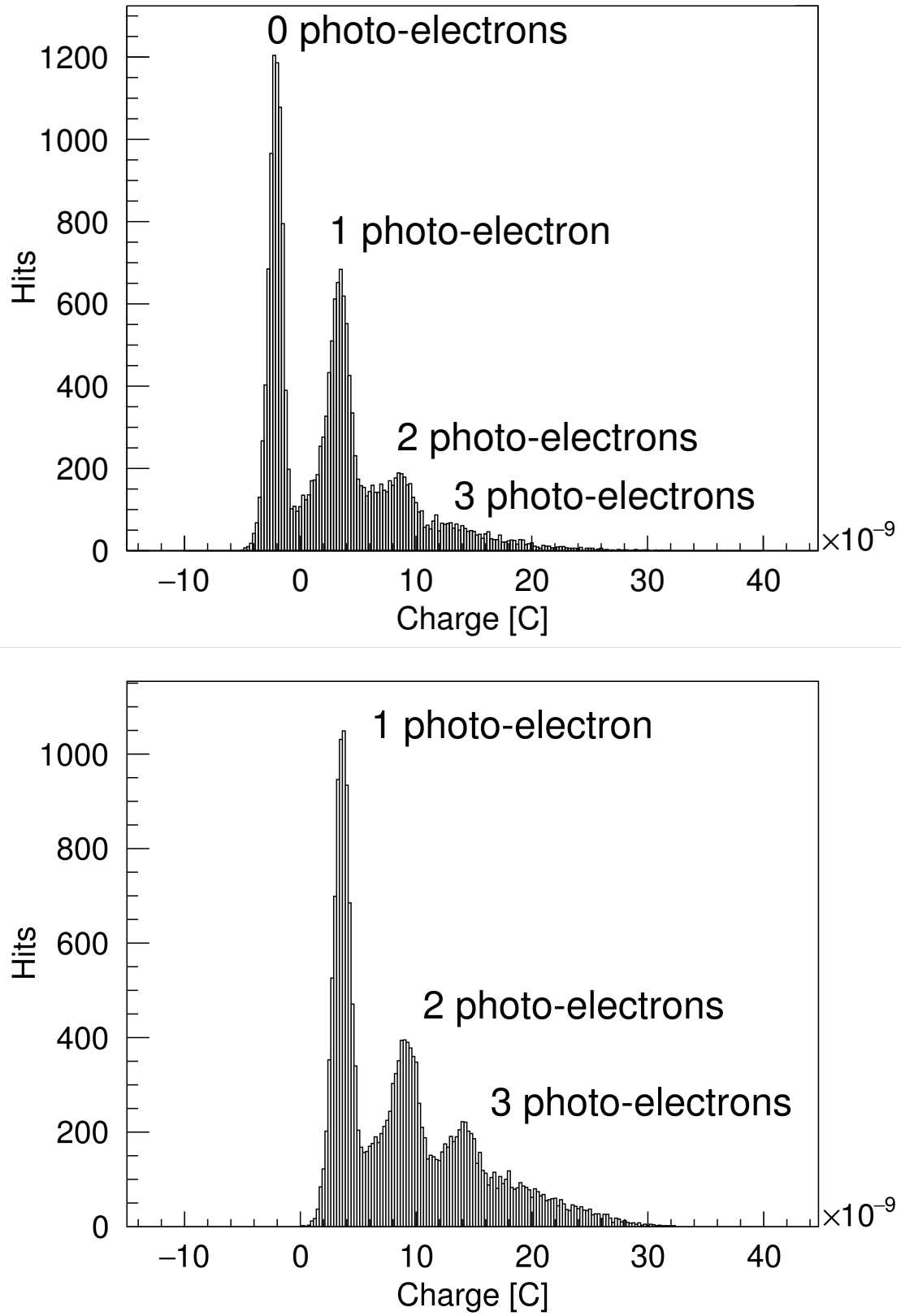

Figure 4.18: Integrated charge distribution from analogue output, SiPM no. 1. Oscilloscope is triggered with the digital output form the ASD8. The ASD8 discriminator threshold was set at $V_{thr} = 0.5$ V (top) and $V_{thr} = 1.5$ V (bottom). It can be observed that the 1.5 V sets the threshold to $\approx 1/2$ photo-electron amplitude.

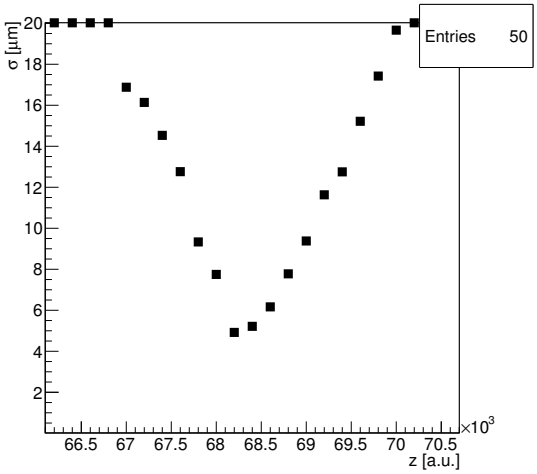

Figure 4.19: The laser waist width σ as a function of the distance between the focussing lens and the MPPC array. The distances along z axis are given in arbitrary units.

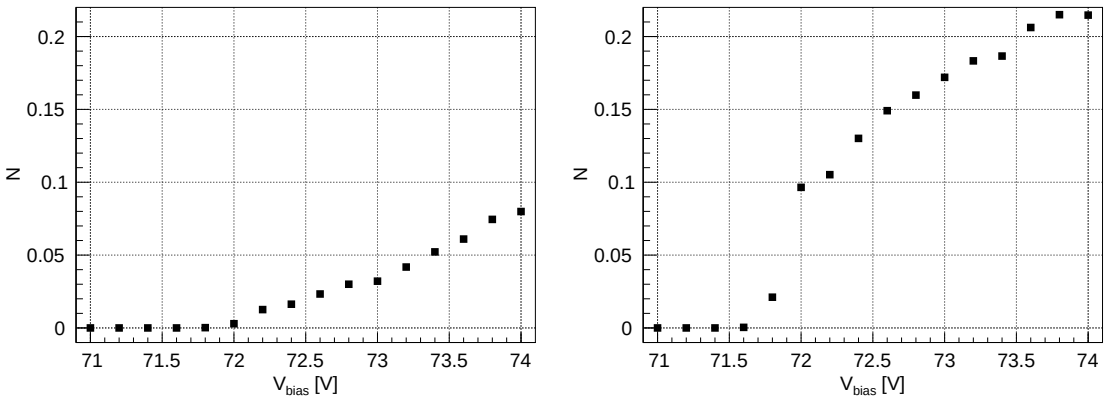

Figure 4.20: Left: Average number of detected photons N as function of bias voltage V_{bias} with random trigger and no light present. Right: Average number of detected photons N as function of bias voltage V_{bias} when the laser above the SiPM. The intensity of the laser light is kept constant.

the deviation of the single photon spectrum from the Poisson distribution. Due to the cross-talk, the number of the cells where avalanches are started is higher than the number of the incident photons. The cross-talk poses a problem in the detectors which measure the flux of photons; in the case of RICH prototype, which registers a hit only if the SiPM signal is above one-half signal amplitude, this is not the case.

The after-pulses influence was studied in [78], where it is shown that the primary dark pulses indeed follow the Poisson statistics for long time intervals, but the deviation is significant for short periods of measurement (i.e. short time window). However, the influence of the cross-talk in the case of our RICH prototype is accounted for in the noise rate.

To obtain the average number of the detected photons without the deviation cause by cross-talk and after-pulses, a simple method can be used [79]. The probability to observe zero events $P(0)$ of the Poisson statistics is

$$P(0) = e^{-n_{p.e.}}, \tag{4.10}$$

where $n_{p.e.}$ is the mean of the Poisson distribution. $P(0)$ is not affected by the cross-talk and after-pulses, therefore, the estimate of $n_{p.e.}$ is not affected by these effects. The zero-event probability is known since the zero events are the pedestal events in the single photon spectrum (Fig. 4.18, top), and the probability is the ratio of zero-events and total number of events N_{total}:

$$P(0) = \frac{N_{pedestal}}{N_{total}}. \tag{4.11}$$

Inverting the formula, the average number of detected photo-electrons $n_{p.e.}$ is

$$n_{p.e.} = -\ln P(0). \tag{4.12}$$

For every measurement in the laboratory set-up, the laser intensity was adjusted so that the signals with zero amplitude $N_{pedestal}$ are about 70-80% of the distribution. Then the 1 photo-electron signals constitute 20-30%.

4.3.2 Dark Counts Rate

Dark counts rate ν_{dark} is measured by registering the signals from SiPM without light present at a random trigger, at working voltage $V_{bias} = 73.0$:

$$\nu_{dark} = \frac{\text{Number of hits}}{\text{Time}} = \frac{\text{Number of hits}}{T_w \times \text{Rate}}\,[\text{Hz}], \tag{4.13}$$

where rate is the number of triggers sent. If the threshold of ASD8 discriminator is raised, the signals below the threshold are rejected, together with the noise, as can be observed in Fig 4.21.

From the same graph the approximate probability of registering the dark count as a hit can be estimated. The dark counts rate of the SiPM no. 18 at $V_{thr} = 1.5$ is $\nu_d = 3.3$ MHz per whole channel. Then the approximate probability of registering the background hit in the SiPM 18 can be calculated as

$$P_{background} = \nu_d\, T_w \tag{4.14}$$

$$= 3.3 \times 10^6 \text{ Hz} \times 10^{-8} \text{ s} \simeq 3.3\%. \tag{4.15}$$

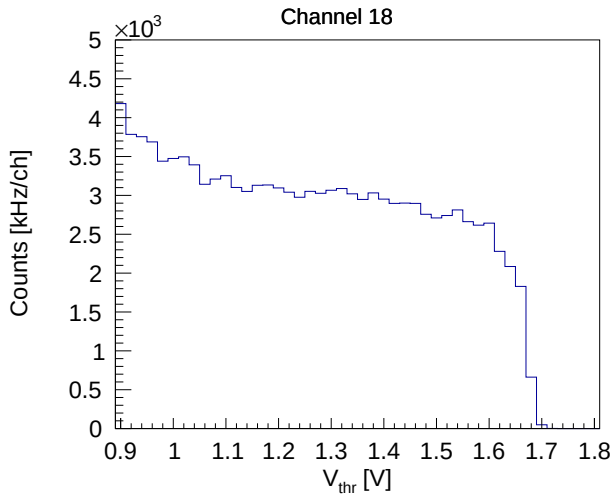

Figure 4.21: Dark counts registered in SiPM no. 18 as a function of the threshold voltage of digital discriminator.

4.3.3 Results

The average number of detected photons in the laser pulse, as given by the Eq. 4.9, was registered for different laser spot positions. The scan across SiPM no. 18 is shown in the Figure 4.22, top. The laser spot was focused to $\simeq 5$ μm and the step was 2 μm. The cell structure is visible and also it can be seen that the probability of detection inside one cell is not uniform, but is lower near the edges. The scan across the whole active area of the same SiPM (3600 micro-cells), with step size of 10 μm, is shown in the Fig. 4.22, bottom.

The response of all 64 SiPMs in MPPC array no. 4 is shown in Fig. 4.23.

When the light concentrator is added, the response of the module is enlarged to the area surrounding the SiPM (Fig. 4.24). However, the response is not uniform because of the reflections at the exit window. This will be discussed in detail in Chapter 6. A few elliptical areas of lower sensitivity arise from the air bubbles present in the optical cement with which pyramids are attached to the common plate.

The response of the photon detector module, consisting of SiPM, light concentrators and optical grease between them, shows good uniformity (Fig. 4.25). As before, a few elliptical areas are due to air bubbles in the optical cement. The non-alignment (vertical band of lower sensitivity at $x = 33.8$ μm) amounts to 100 μm and results in a loss of $\approx 0.5\%$.

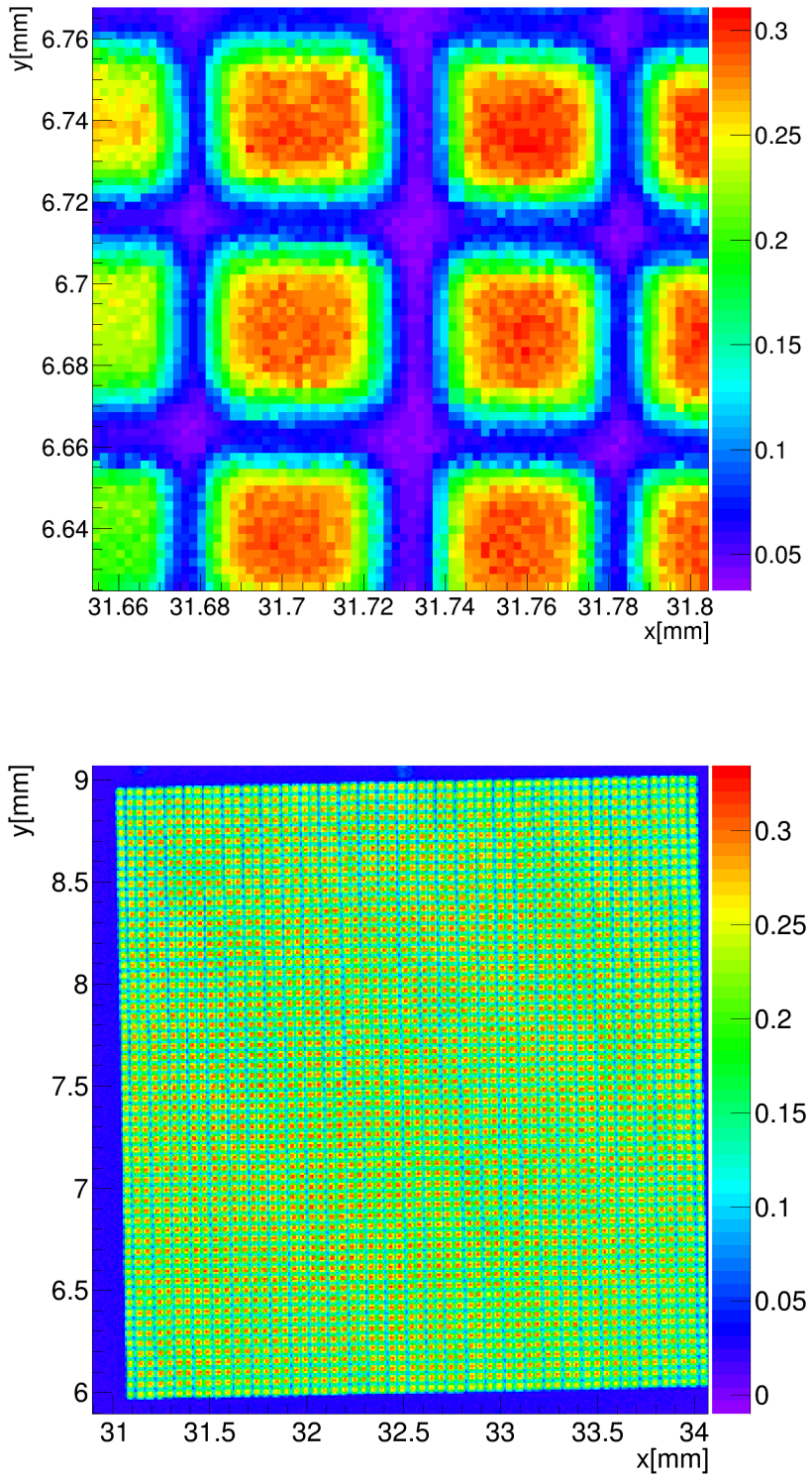

Figure 4.22: Top: Average number of detected photons in few cells. The laser spot was focused to $\sigma \simeq 5$ μm. Bottom: Average number of detected photons in a scan across the whole SiPM.The laser spot was focused to $\sigma \simeq 10$ μm. Cell structure (60×60) can easily be observed.

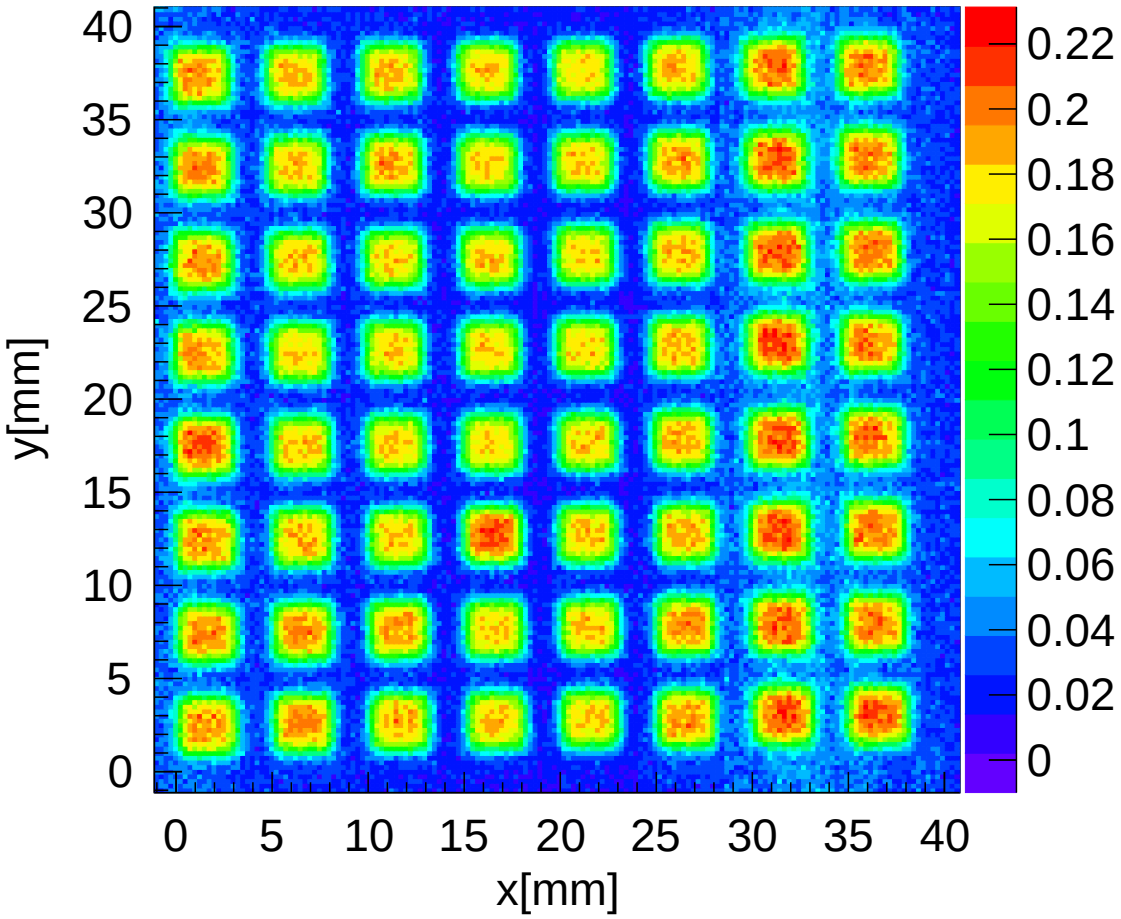

Figure 4.23: MPPC no. 4 (whole SiPM array) sensitivity scan without light concentrators. Laser spot was focused to $\sigma = 500$ μm.

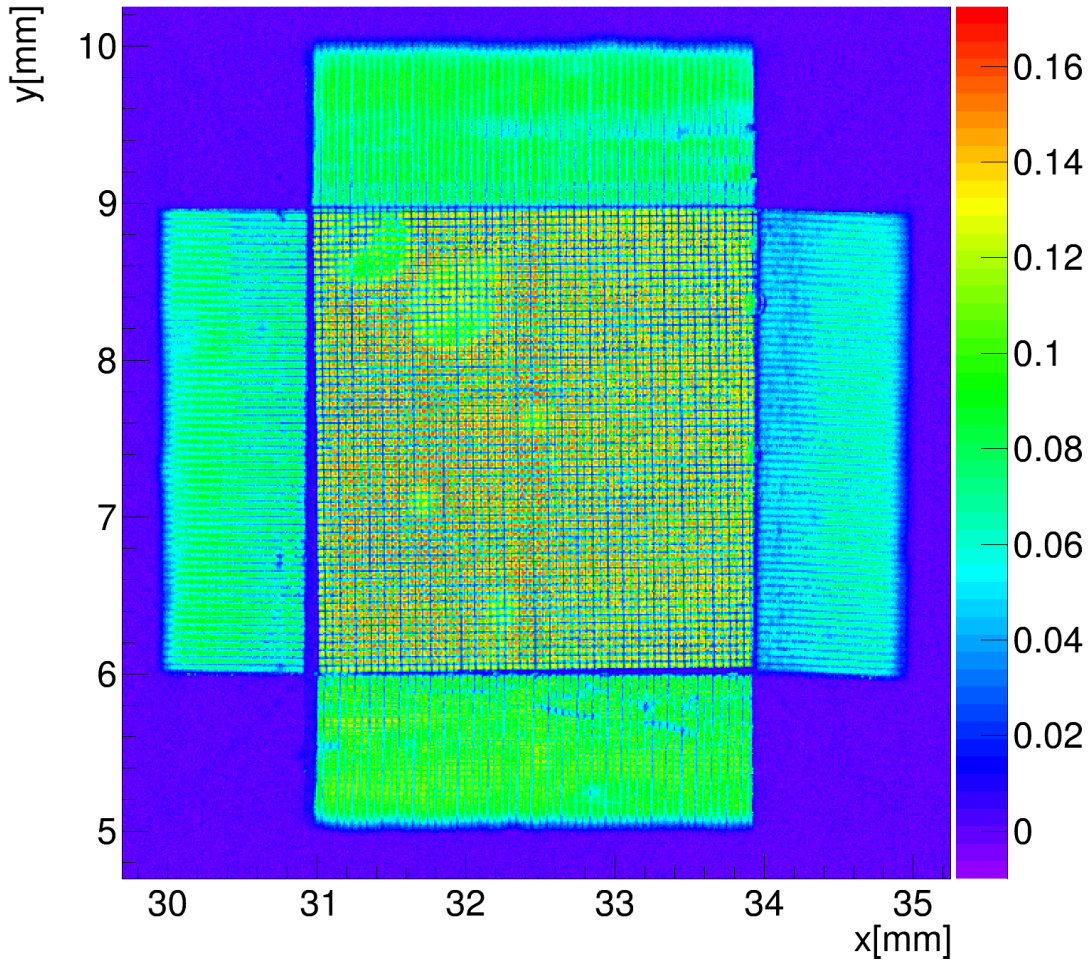

Figure 4.24: Average number of detected photons in SiPM no. 18 with the light concentrators, but without the optical grease. Laser spot focused to $\sigma \approx 10$ μm.

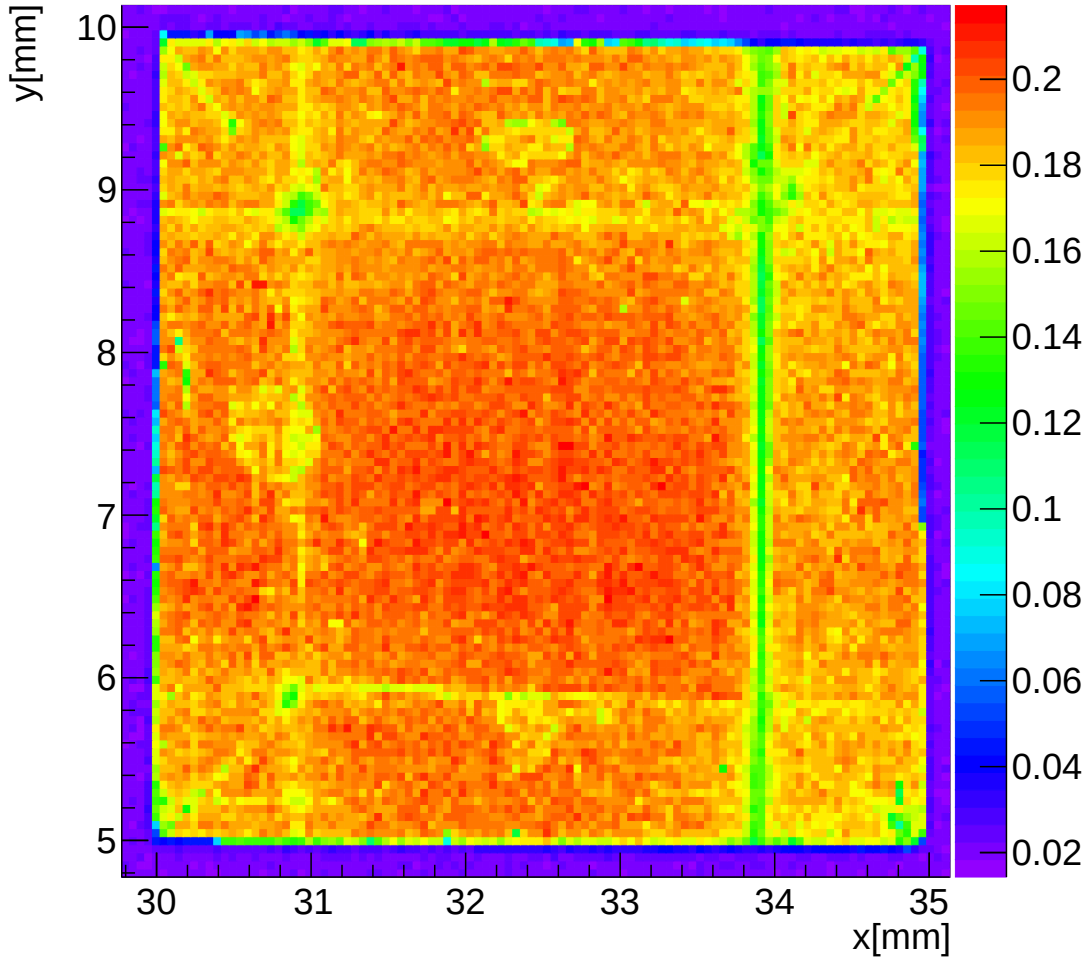

Figure 4.25: The average number of detected photons from SiPM no. 18, assembled with the light concentrators and optical grease between them. Laser spot focused to $\sigma \approx 50$ μm.

Chapter 5

RICH Prototype in Beam Test

The ability of the prototype photon detector with silicon photomultipliers to register Cherenkov photons emitted in aerogel was shown in a beam test. There were two main interests: the number of detected photons with the SiPM and the light concentrators performance.

5.1 Beam Test Set-up

The test of the photon detector module with the charged particles was performed at the DESY Institute (Hamburg, Germany) from 24$^{\text{th}}$ to 27$^{\text{th}}$ September 2013. The electrons obtained from the synchrotron pass through two dipole magnets and a collimator, which allows to choose the momentum of the electrons up to 7 GeV/c. For this test the electrons had $p = 5$ GeV/c. After the collimator, the electrons enter the T24 test area where the test set-up was.

The prototype RICH is assembled in an aluminium light-tight box (Fig. 5.1). The schematic drawing of the test set-up is shown in Fig. 5.2. RICH prototype includes two aerogels with refractive indices $n_1 = 1.0485$ (upstream) and $n_2 = 1.0619$ (downstream). The dimensions of aerogels are 100 mm $\times$ 100 mm in the plane perpendicular to the beam, and widths are $d_1 = 19.4$ mm and $d_2 = 20.2$ mm, respectively. The aerogel properties are summarised in Table 5.1. The photon detector impact surface is at a distance $L = 200$ mm from the entry plane of the upstream aerogel. Between the aerogels and the photon detector is the expansion volume for the Cherenkov ring. The read-out electronic boards are attached at the back, as described in the Chapter 4.

The electron track is reconstructed using the data provided by Multi-wire Proportional Chambers (MWPC). A MWPC is basically a position sensitive particle detector, often used for tracking purposes. The charged particle traversing the MWPC ionizes the gas inside. The electrons, accelerated by the electric field, pro-

Aerogel	Ref. index	Width [mm]	Λ [mm]	Expected θ_C [mrad]
1 (upstream)	1.0485	19.4	44.0	305.344
2 (downstream)	1.0619	20.2	54.8	343.124

Table 5.1: Aerogel summary table.

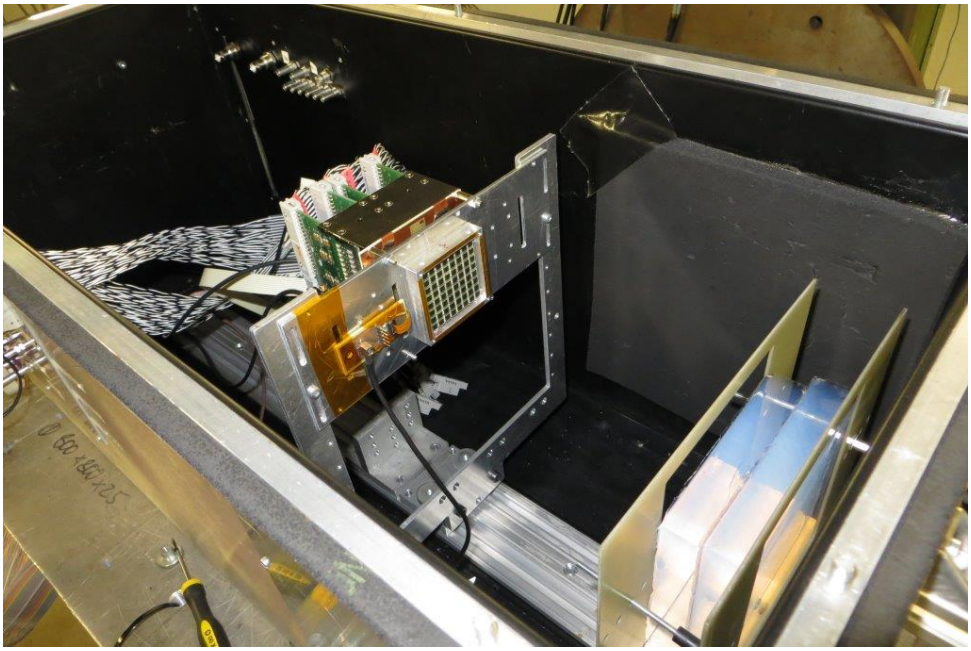

Figure 5.1: The prototype RICH with photon detector module in the beam test.

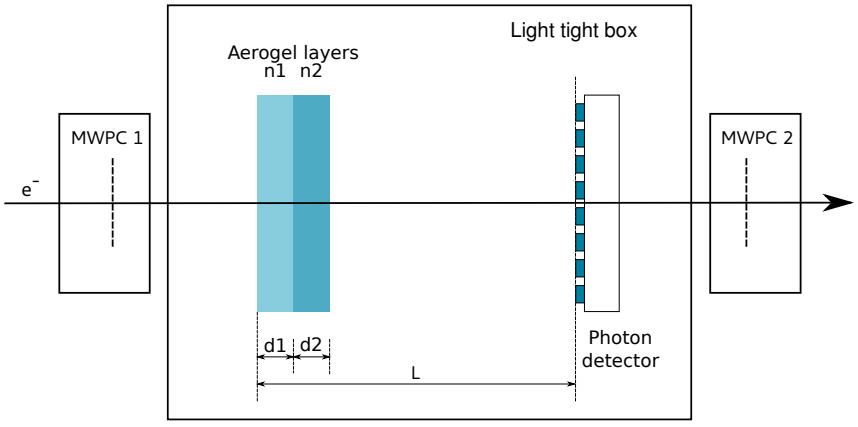

Figure 5.2: Schematic drawing of the set-up used in beam test.

duce an avalanche, resulting in an amplification of the signal. Detailed operational principles are given in standard textbooks [16, 44]. The MWPC employed has an active area of 50×50 mm^2 and is filled with Ar and CO_2 in the ratio of 70 : 30. The 24 anode wires, 15 μm in diameter, are tensioned on a frame and equidistantly spaced at 2 mm. Additional two anode wires at each ends have 20 μm in diameter to account for the uncompensated repulsion force. Two parallel cathode planes consist of strips 1.6 mm in width, which are spaced at 2 mm. The strips of the two cathode planes are perpendicular to each other. The distance between the cathode and anode plane is 1.5 mm. The detailed description of the operation, calibration and the electronic read-out can be found in [80, 81].

To reduce the number of electronic channels needed to read-out the MWPC a method with position to time conversion is used. The signal from the cathode strips is capacitively connected to a delay line. The induced signal from one strip separates into two signals, each travelling to the opposite ends of the delay line. The difference in the arrival time of the two signals determines the position of the charged particle. For this to be possible, a time-position calibration of the MWPC had to be performed [82].

The strips of one cathode plane are parallel with the anode wires, while the other cathode has the strips perpendicular to this plane. In this way one MWPC gives the position in two dimensions (the $x-y$ plane). The two MWPCs, attached at the opposite sides of the aluminium box, form a telescope, thus providing two additional points needed to reconstruct a line in space. The anodes of the MWPCs are connected to high voltages. The collected charge at anodes and cathodes is converted to the voltage signals with a charge-sensitive amplifiers (ORTEC FTA820). After the constant fraction discriminator (ORTEC CF8000), the signals are sent to 25 ps resolution TDC (CAEN V1290A).

The resolution of the tracking in the y-direction, perpendicular to the anode wires, is roughly given by the spacing of anode wires $s_a = 2$ mm:

$$\sigma_y = \frac{s_a}{\sqrt{12}} = 0.500 \text{ mm}. \tag{5.1}$$

The cathode signals were fitted with a Gaussian and a linear function. The width of Gaussian (parameter $P3$ in Fig. 5.3) gives slightly better result of $\sigma_1 = 0.233$ and $\sigma_2 = 0.294$ for the 1$^{\text{st}}$ and the 2$^{\text{nd}}$ MWPCs. The resolution along the x-direction, along anode wires, is much better.

The digitized signals from the photon detector read-out boards are passed to the CAEN V673A TDC, as in the laboratory set-up. The channel mapping is given in the Appendix A. The DAQ system is run by a PC. The time stamp of every hit for each photon detector channel, as well as MWPC time stamps are saved to a file for the later analysis.

In order to register the arrival time of the electron precisely, we added a scintillator counter to the set-up. The counter consists of the plastic scintillator, plastic wave guide and a photomultiplier. The signal from the scintillator is delayed so that it falls in the middle between the two signals from the MWPC anodes. The coincidence of these three signals forms the common STOP signal for the V673A TDC. The plastic scintillator was chosen because of its short time constant ($\tau \approx 1$ ns). Its uncertainty is the principal contribution to the timing error of the photon detector signal. The background hits are rejected using a narrow hit detection time window of 6 ns (Fig. 5.4).

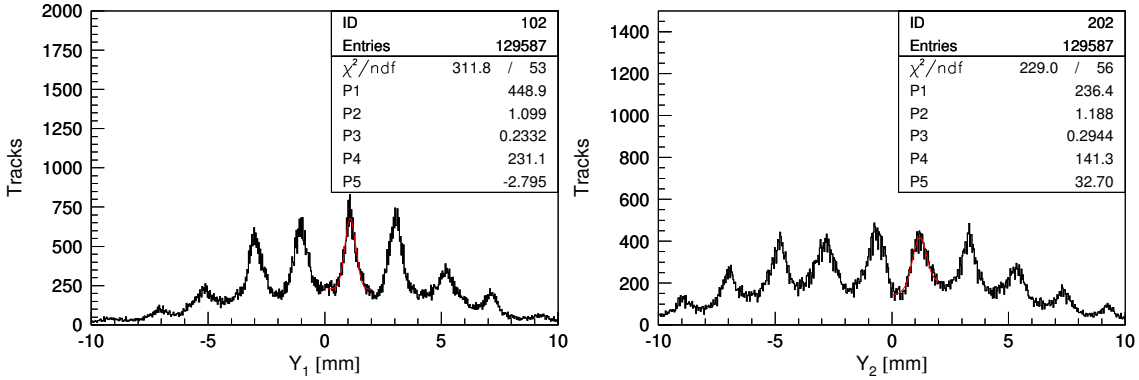

Figure 5.3: Tracking resolution in y-direction. Vertical cathode signals from MWPCs no. 1 (left) and no. 2 (right). One strip signal was fitted with a Gaussian and a linear function; the width of Gaussian, $P3$, gives a resolution estimate.

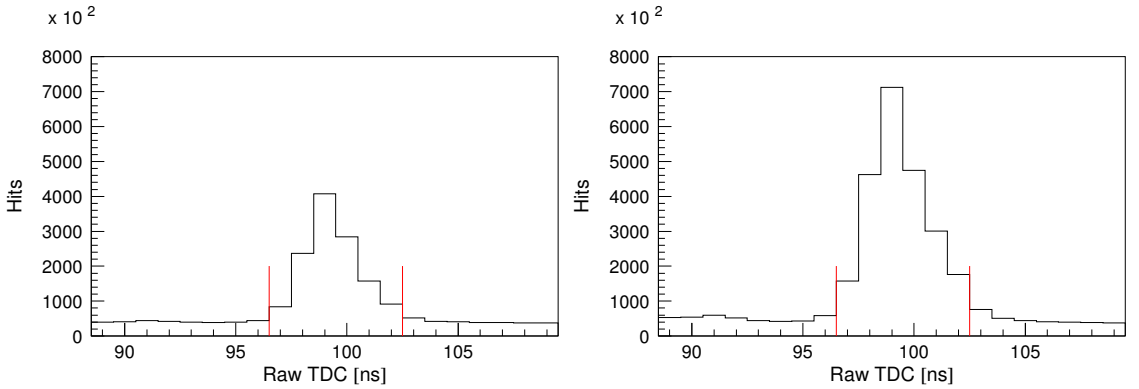

Figure 5.4: Time distribution of all registered hits in run 43 (left, bare module) and 48 (right, module with light concentrators), all channels added. The hit detection time window is indicated by the vertical lines.

The Cherenkov peak is observed only for time correlated hits, which is easily observed in the reconstructed hit time distributions. Each distribution in Fig. 5.5 is reconstructed from hits in $\triangle\, t = 1$ ns time window and windows are 1 ns apart.

5.2 Cherenkov Angle Reconstruction

The global coordinate system is the one associated with the tracking chambers and the set-up box: its origin is in the centre of the left side of the box in Fig.5.6. The electrons pass from left to right, in the $z-$direction. The track is defined with a direction vector $\mathbf{s}$ and a radius-vector of some point on the track, $\mathbf{r_0}$. The vectors $\mathbf{r_1}$ and $\mathbf{r_2}$ are the radius-vectors of the hit at the first and the second MWPC active plane, respectively. They are calculated from the difference in the arrival time of the signals from MWPC cathode strips. For one MWPC the x and y coordinates are obtained from the time signals:

$$x = k_x(\Delta_x - n_x), \tag{5.2}$$
$$y = k_y(\Delta_y - n_y), \tag{5.3}$$

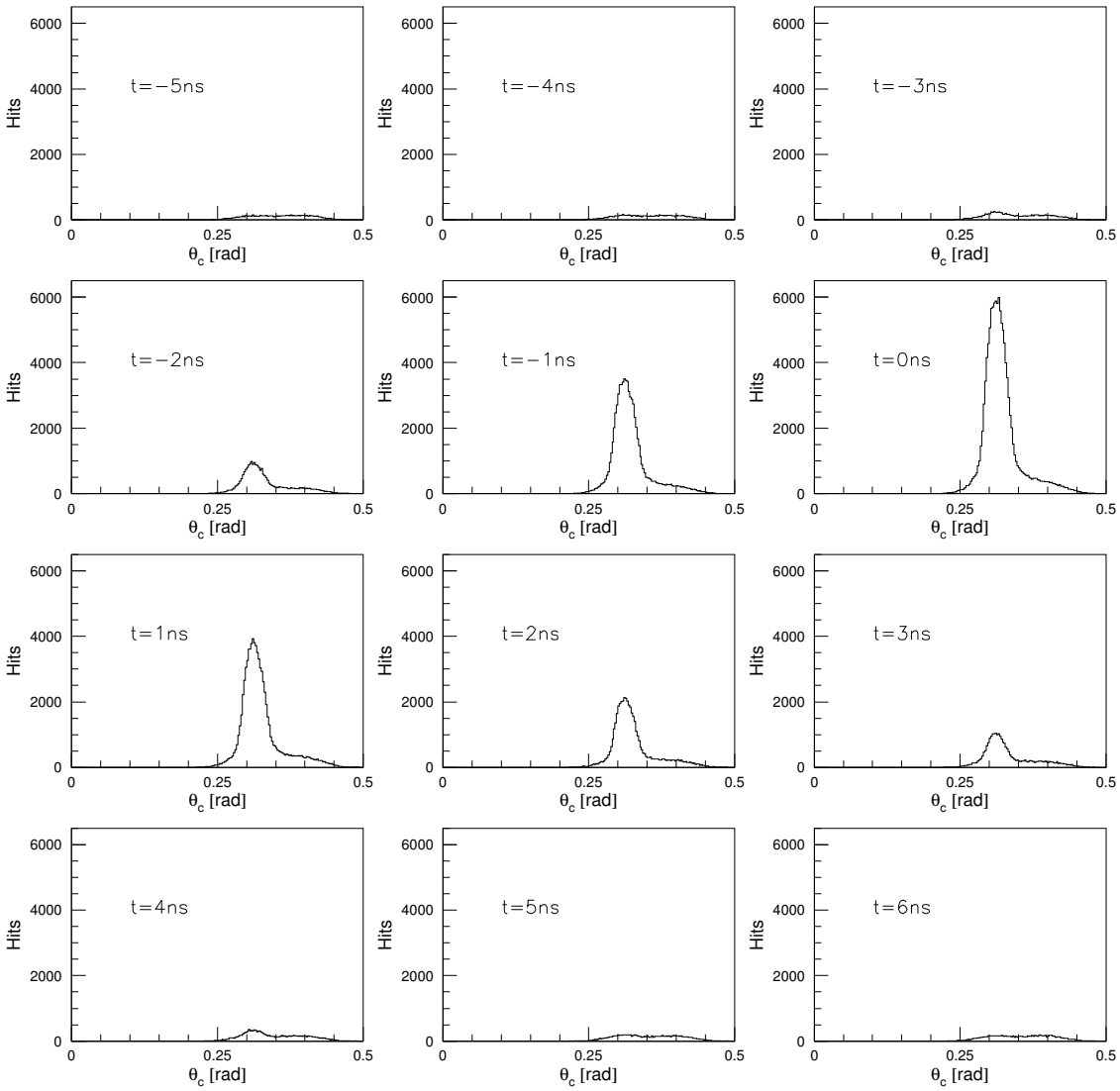

Figure 5.5: Distribution of Cherenkov angle for $\triangle\, t = 1$ ns time windows centred at different times, from -5 to $+6$ ns, run 43. One can observe that around the central window the Cherenkov angle is correctly reconstructed ($\theta_{\mathrm{C}} = 0.305$) and a Gaussian distribution emerges from a uniform background.

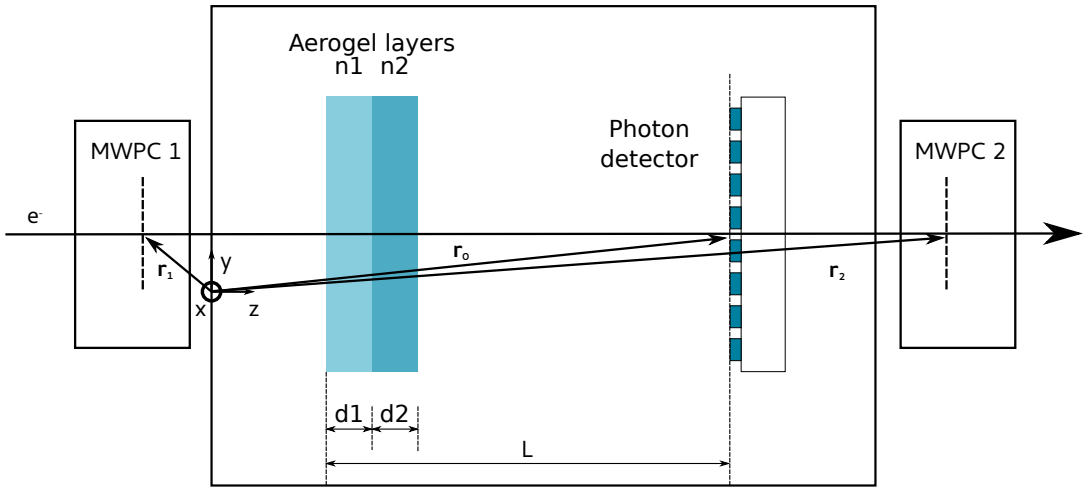

Figure 5.6: The schematic drawing of RICH counter in the test beam.

where $k_x(k_y)$ is the delay slope of the cathode strips in x (y) direction, $\Delta_x(\Delta_y)$ is the signal time difference and $n_x(n_y)$ is the time delay constant. The z component is the position of the MWPC in the global system. With the vectors $\mathbf{r_1}$ and $\mathbf{r_2}$ the direction vector of the track is:

$$\mathbf{s} = \frac{\mathbf{r_2} - \mathbf{r_1}}{|\mathbf{r_2} - \mathbf{r_1}|}. \tag{5.4}$$

For the point that uniquely defines the track $\mathbf{r_0}$ was chosen the point where the track intersects the photon detector plane. This point is at the same time the origin of the local co-ordinate system, *i.e.* the system associated with the RICH detector.

The Cherenkov angle is calculated using two known variables: hit position on the photon detector and the direction of charged particle $\mathbf{s}$. In the first approximation, the line between the mid-aerogel point and the channel centre is taken as the photon path and the Cherenkov angle calculated as the angle between this line and the direction $\mathbf{s}$. The Snell law of refraction is applied at the aerogel/air exit surface, at the air/light concentrators surface (if present) and at the SiPM epoxy window. As a result, the photon path line is corrected. An iterative process is started for every track—photon hit pair. The direction of the emitted photon is corrected subsequently and the new photon hit position calculated. The process continues until the correction to the photon direction in aerogel reaches certain threshold or until it exceeds the maximal number of iterations (100). If thus obtained Cherenkov angle θ_C lies within 10σ of the theoretically expected angle, it is accepted as the reconstructed hit. The light concentrators are included in the reconstruction simply as a window of width $d_{win} = 4.0$ mm and refractive index $n_{LC} = 1.53$.

The measurements were made in runs, *e.g* a certain number of events were recorded with the same parameters of the system, such as aerogel parameters, photon detector working voltage and position. Run numbers, same as in the run log, with parameter values are listed in the Appendix B. Runs, important for the analysis, will be listed here (see later). An example of reconstruction is shown in Fig. 5.7, left, showing the accumulated distribution of reconstructed hits for the 200,000 tracks in a set-up with one aerogel and without light concentrators. The average Cherenkov angle is calculated from a fit to the histogram with two functions, one for the signal

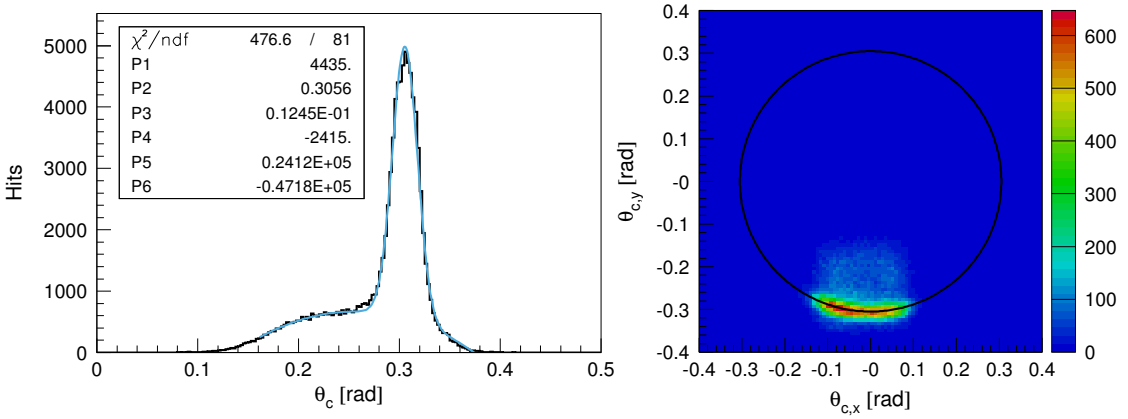

Figure 5.7: The accumulated distribution of reconstructed Cherenkov angle in run 38 with one aerogel layer. The solid line is a fit with a Gaussian for signal and a second order polynomial function for background (left). The accumulated hits in Cherenkov space (right). Only about $1/9^{\text{th}}$ of the whole ring circumference is covered by one MPPC. A superimposed circle, with the radius same as the expected Cherenkov angle, illustrates this.

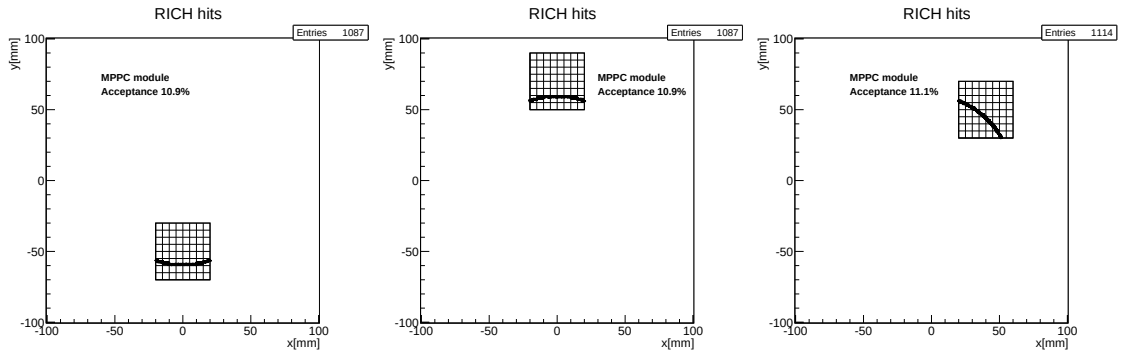

Figure 5.8: Photon detector positions 2, 3 and 6, and corresponding geometrical acceptances ε_f.

and one for the background hits. The histogram of accumulated photon hits in the Cherenkov space is given in the Fig 5.7, right.

The average number of detected photons was calculated as the integral of Gaussian function G:

$$N_{\text{det}} = \int_{-3P_3}^{+3P_3} \mathrm{G}(P_1, P_2, P_3)\,\mathrm{d}\theta, \tag{5.5}$$

where Gaussian function parameters, height P_1, mean P_2 and width P_3, are obtained from fit. The module covered only about $1/9^{\text{th}}$ of the Cherenkov ring circumference. In order to cover a larger part of the ring, the measurements were done for different positions of the detector, which are shown in Fig.5.8, together with corresponding geometrical efficiencies. They were calculated using a Monte Carlo simulation of RICH. Table 5.2 lists the position numbers used in the test, together with geometrical efficiencies ε_f.

The background was fitted with a second order polynomial and the average

Run	Module Positions	ε_f
23-41, 46, 52	2	0.109
43, 48	3	0.109
44	4	0.0
45	5	0.0
53	6	0.111

Table 5.2: Beam test run numbers, module positions (numbers as in the run log) and geometrical acceptance ε_f of the module at a given position.

number of background photons calculated from the integral of the function:

$$N_{\text{bkg}} = \int_{-3P_3}^{+3P_3} (P_4 + P_5\,\theta + P_6\,\theta^2)\,\mathrm{d}\theta. \tag{5.6}$$

The dominant sources of the background are Rayleigh scattered photons and dark counts. Both are supposed to be uniformly distributed over detector area. In Cherenkov space, the distribution becomes a linear function of Cherenkov angle θ. However, because of the limited geometrical efficiency of the module in ϕ direction, the distribution is distorted, as observed in Fig. 5.7.

The accumulated hits in Cherenkov space, combined from four photon detector positions are shown in Fig. 5.9. A circle, with radius equal to the expected Cherenkov ring radius, is superimposed and shows that the geometry calibration of the set-up is good. The hits in the centre of the ring are due to the radiation deposited by electrons in MPPC and Cherenkov photons emitted in light concentrators.

5.3 Calibration Runs

Before the measurement of the number of the detected photons with the SiPMs, and the light concentrators performance, several calibration runs were made to find the operating voltage for the SiPM and the threshold voltage for the ASD8 discriminator. Only one aerogel tile ($n = 1.045$) was used for this purpose. The time window was adjusted for every run because, as already observed in the laboratory measurements, changing either bias or threshold voltage produces a time walk. This effect can be observed in Figs. 5.10 and 5.11.

The average number of detected and background hits (Eqs. 5.5 and 5.6) as a function of bias and threshold voltage are shown in Fig. 5.12. As expected, by raising the threshold of the ASD8 discriminator at a constant bias voltage of MPPC, the background events are rejected and the S/N ratio raises. The discriminator works as a single channel analyser, so when the threshold comes to the upper bound, the discriminator turns off. Based on the measurements, we chose the working threshold voltage of $V_{thr} = 1.5$ V. Photon detection efficiency raises with bias voltage. Higher bias, however, raises the thermally produced electron-hole pairs which produce dark counts. Again, based on measurements, we chose bias voltage of $V_{bias} = 73.0$ V.

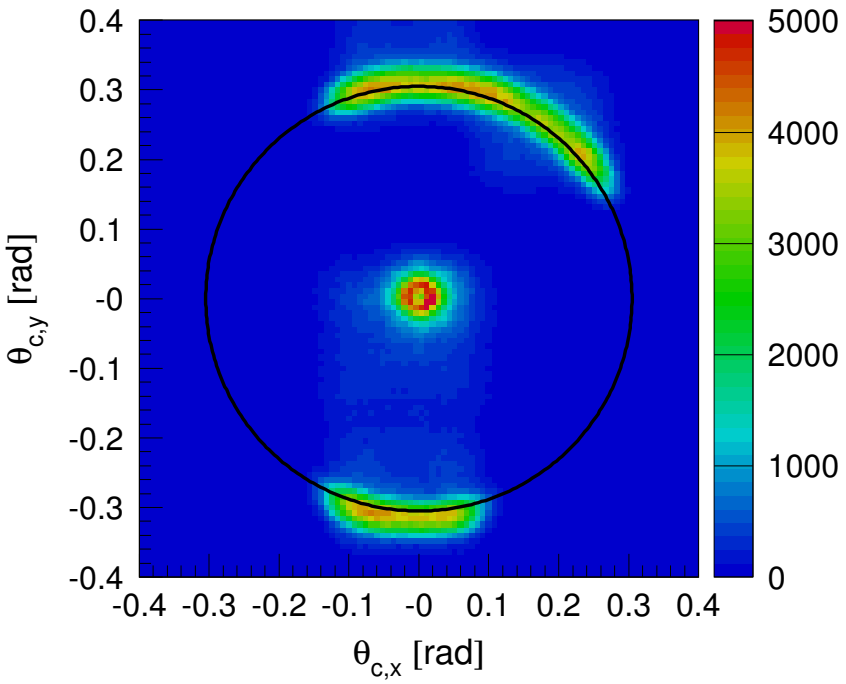

Figure 5.9: Accumulated hits at four detector positions 2, 3, 5 and 6, *i.e.* runs 48, 50, 52 and 53. A circle of radius equal to the expected Cherenkov angle is also shown. The hits in the centre are due to radiation deposited by e^- traversing the MPPC and by Cherenkov photons emitted in light concentrators.

In the case of one aerogel, one can expect that all the emitted photons are emitted under the theoretically predicted Cherenkov angle, that is $\theta_C^{\text{exp}} = 305.3$ mrad in the case of the upstream aerogel. The good agreement between this value and the measured values given in Tab. C.1, as well as the mean ring radius $R^{\text{exp}} = 63.2$, is a confirmation that the geometry is well calibrated.

The detailed analysis is given in the Appendix C, Tables C.1 and C.2.

5.4 Number of Detected Photons

Two aerogels were used in runs where we tested the light concentrators performance (runs 43 to 53). The aerogel properties are summarised in Table 5.1. For the reconstruction, two hypotheses were considered. The first hypothesis is that the photon was emitted in the upstream aerogel, and the second one is that it was emitted in the downstream aerogel. Both hypotheses give the same number of detected photons, but different Cherenkov angle and Cherenkov angle error.

The distribution of the reconstructed photons in the run without light concentrators is shown in Fig. 5.13. The histogram of accumulated hits in the run with light concentrators is shown in Fig. 5.14. There are about two times more photons with the light concentrators, than without them. We expected an improvement in acceptance of 2.5× and this will be discussed in Chapter 6.

The analysis results for all runs with two aerogels are presented in the Tab. 5.4. As expected, the number of detected photons is the same for both hypotheses. The reconstructed Cherenkov angle is systematically higher in the upstream aerogel hypothesis, while, for the downstream hypothesis, it is almost the exact as the expected

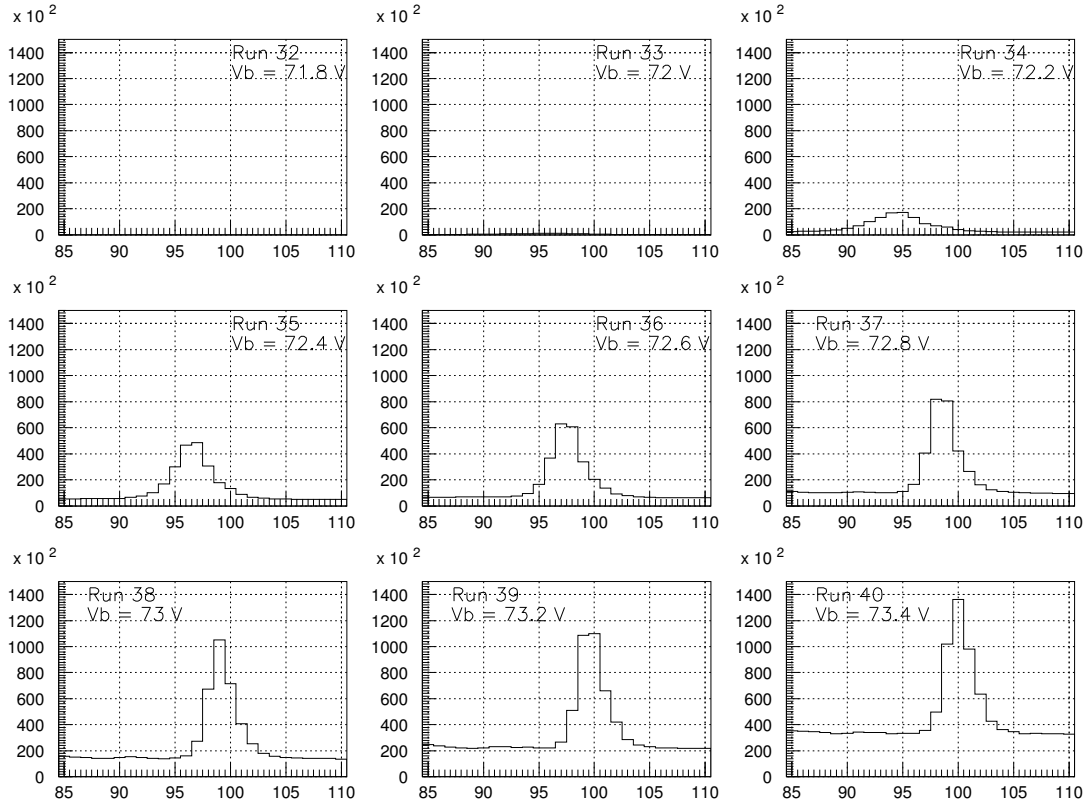

Figure 5.10: Time of arrival histograms (in ns) for the hits accumulated from all channels. Runs with different bias voltage V_b are shown. Discriminator threshold voltage was set to 1.5 V. Observe that the mean time of the distributions changes with bias voltage from 95 ns to 100 ns.

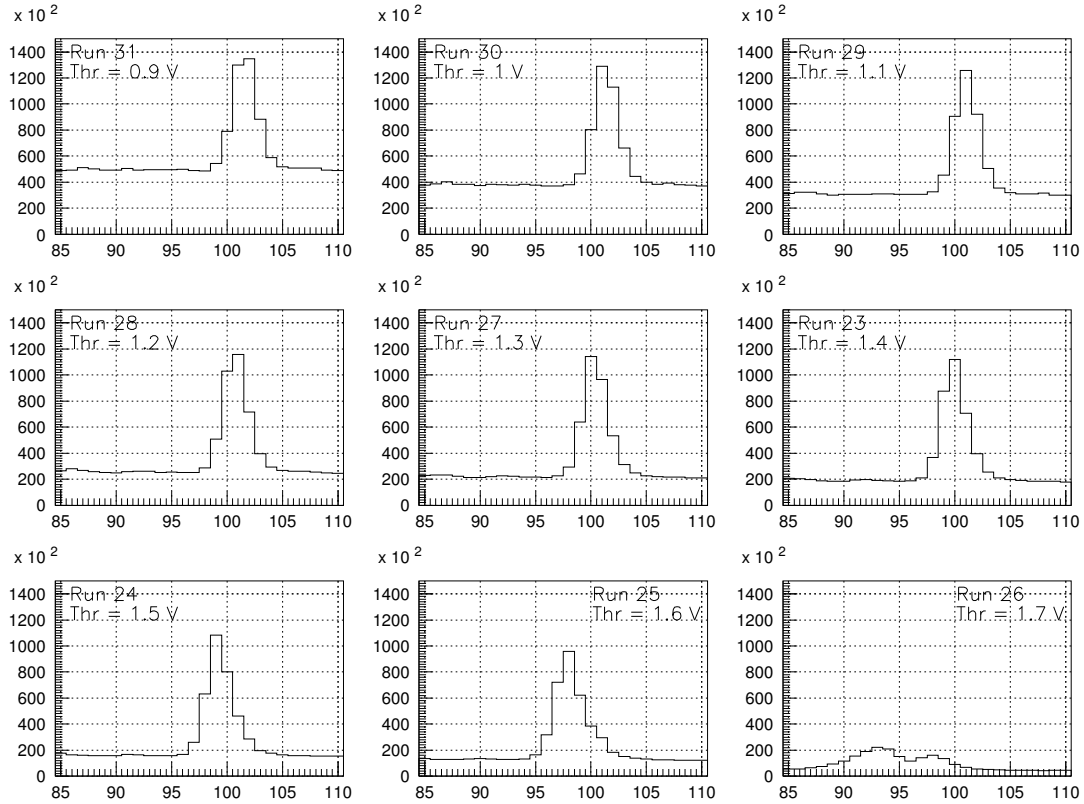

Figure 5.11: Time of arrival histograms (in ns) for the hits accumulated from all channels. Runs with different discriminator threshold voltage are shown. Bias voltage was 73.0 V. Observe that the mean time of the distributions changes with threshold voltage from 102 ns to 98 ns.

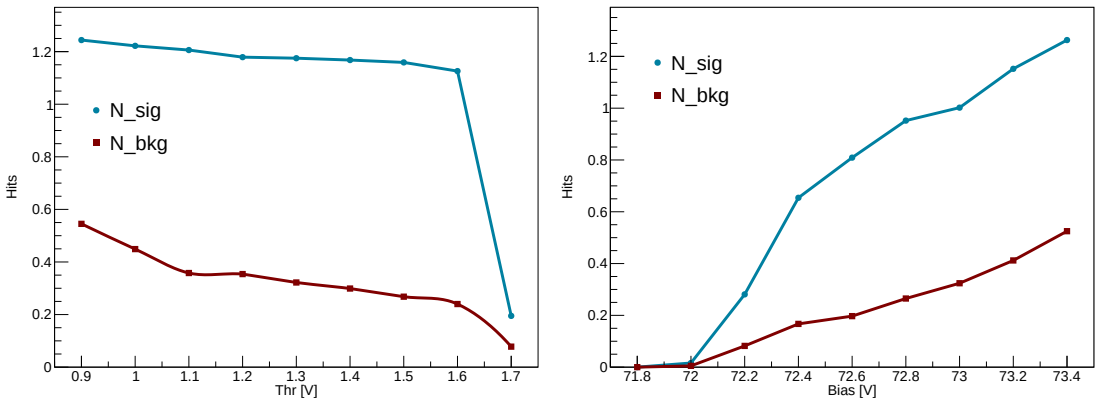

Figure 5.12: Left: Average number of detected hits as a function of ASD8 discriminator threshold at bias voltage of 73.0 V. Right: Average number of detected hits as a function of bias voltage at discriminator threshold voltage of 1.5 V.

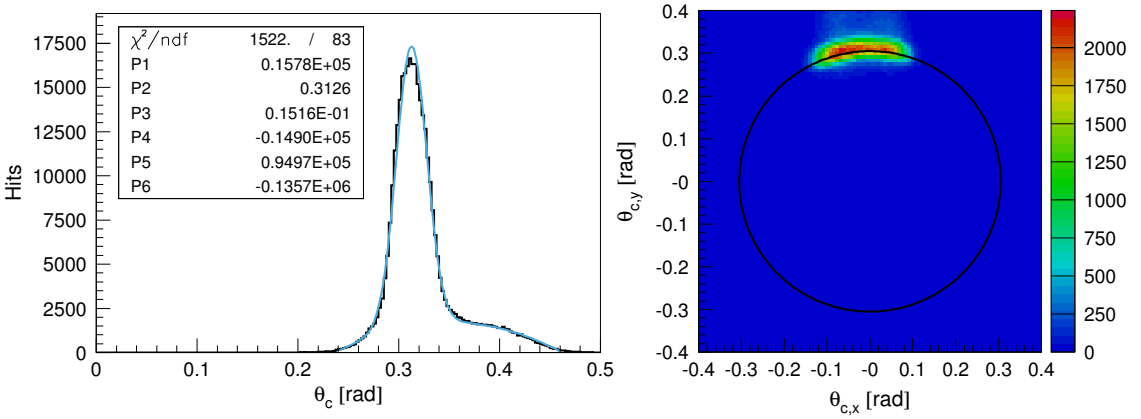

Figure 5.13: Reconstructed hits in the run without light concentrators (43). Left: Accumulated distribution of Cherenkov angle. The solid line is a fit with a Gaussian for signal and a second order polynomial function for background. Right: The accumulated hits in Cherenkov space. A circle with a radius of the expected Cherenkov angle ($\theta = 305.4$ mrad) is also shown.

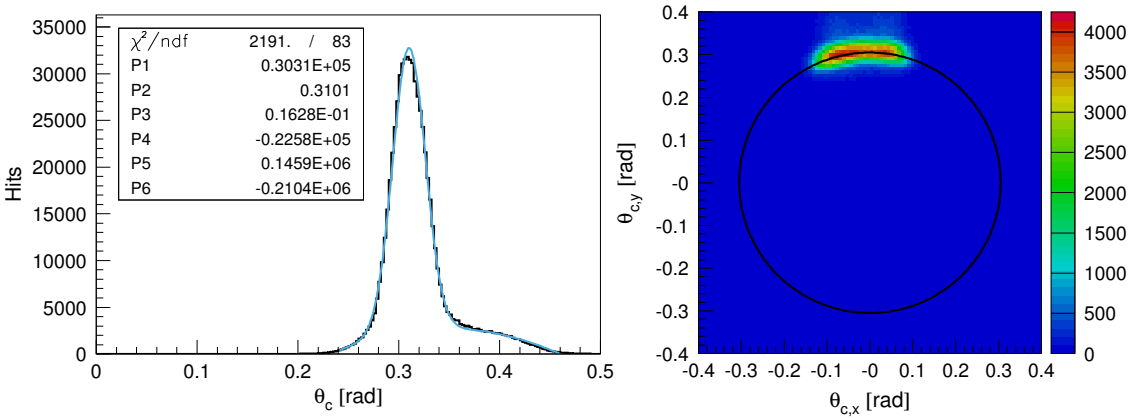

Figure 5.14: Reconstructed hits in the run with light concentrators (48). Left: Accumulated distribution of Cherenkov angle. The solid line is fitted function that is a sum of a Gaussian for the signal and a second order polynomial for the background. Right: The accumulated hits in Cherenkov space. A circle with radius of the expected Cherenkov angle for the upstream hypothesis is also shown.

value. This can be explained by the observation that there are more non-scattered photons produced in downstream aerogel, because of the higher transmission length (*cf.* Table 5.1 and Fig. 2.18).

Number of expected photons per electron N_{exp}^{track} (per ring) were calculated in Chapter 2 and are summarised in Table 5.3. To account for the geometrical efficiency of the prototype module at different positions, the number of photons is multiplied by the ε_f. Efficiency ε_f included, the number of expected photons in the beam test is:

$$N_{exp} = \varepsilon_f \times N_{exp}^{track}. \tag{5.7}$$

The number of expected photons N_{exp}, as registered with one detector module, is listed in the last column of Table 5.3.

Fig. 5.15 (left) shows the distribution of hits in a set-up without the light concentrators. The mean of the data histogram (full line) is $N_{data}^{wo} = 2.28$. Data distribution

Run	Detector	N_{exp}^{track}	ε_f	N_{exp}
43, 46	Without concentrators	25	0.109	2.7
48, 52	With concentrators	63	0.109	6.9
53	With concentrators	63	0.111	7.0

Table 5.3: Number of expected photons per electron track N_{exp}^{track} (from Eqs. 2.32, 2.34) for different detector set-up. Measurements are with two aerogel layers. Listed are the geometrical acceptance of one module ε_f and the resulting number of expected photons per module N_{exp}.

Hypothesis: upstream aerogel						
Run	Position	ε_f	θ [mrad]	σ_θ [mrad]	N_{det}	N_{bkg}
43	3	0.109	312.6	15.16	1.838	0.425
46	2	0.109	312.7	15.01	1.830	0.439
48	3	0.109	310.1	16.28	3.485	0.663
52	2	0.109	314.7	16.22	3.568	0.742
53	6	0.111	314.0	16.91	3.879	0.819
Hypothesis: downstream aerogel						
Run	Position	ε_f	θ [mrad]	σ_θ [mrad]	N_{det}	N_{bkg}
43	3	0.109	342.6	16.21	1.831	0.444
46	2	0.109	342.9	16.04	1.813	0.451
48	3	0.109	339.6	17.54	3.526	0.663
52	2	0.109	345.2	17.32	3.543	0.798
53	6	0.111	341.8	17.92	3.866	0.828

Table 5.4: Reconstruction of the Cherenkov angle from MPPC hits for runs 43-53, with two aerogel layers. Two emission hypotheses are considered: that the photon was emitted in the upstream aerogel and that it was emitted in the downstream aerogel.

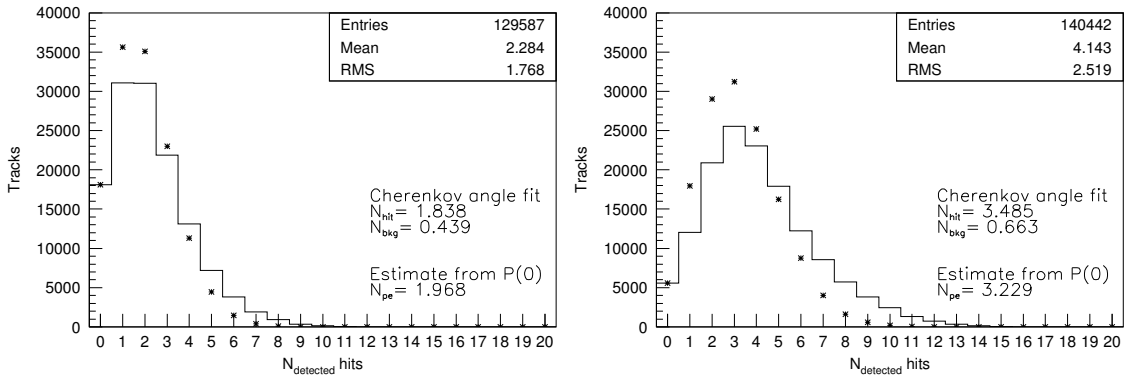

Figure 5.15: Left: Detected hits distribution (full line) in the set-up without the light concentrators, run 43. Poisson distribution with mean N_{hit} from Cherenkov angle fit (dots). Calculated Poisson mean from the zero bin value $P(0)$ is $N_{p.e.} \simeq 2.0$. Right: Detected hits distribution (full line) in the set-up with the light concentrators, run 48. As above, Poisson distribution from Cherenkov angle fit (dots) and mean from zero hits estimate is $N_{p.e.} \simeq 3.2$.

is distorted by noise. The measure of the deviation from Poisson distribution shows the $p-$value of the data histogram. It is $p = 0.13$, which means that the distortion is not statistically significant. The Poisson distribution with mean from fit $N_{hit} = 1.85$ (Eq. 5.5) is supposed to be uninfluenced by the noise and is the estimate of the true number of photons. The mean of Poisson statistics calculated from number of events in bin zero (stars graph) is $N_{p.e.} \simeq 2.0$.

Fig. 5.15 (right) shows the distribution of hits in a set-up with the light concentrators, run 48. The mean of the data histogram (full line) is $N^{wo}_{data} = 4.14$. The deviation from the Poisson hypothesis, as indicated by $p-$value, $p = 0.06$, is larger than in the case without light concentrators. However, this p-value means that the deviation is still not quite statistically significant. The Poisson distribution, obtained from the fit has the average $N_{hit} = 3.48$. The mean of Poisson statistics calculated from number of events in bin zero (stars graph) is $N_{p.e.} \simeq 3.3$, which underestimates the true number of detected hits.

The hits in channels and the distribution of the average number of detected hits are shown for position 2, runs 46 (without) and 52 (with light concentrators)For the run 53, position 6 (with light concentrators) in Appendix D.

5.4.1 Error on the Number of Detected Photons

The number of expected photons is higher than number of detected hits. The systematic over-estimate of the number of expected photons comes mainly from the following factors:

1. Lower PDE,
2. Light concentrators performance,
3. Photons distribution on one SiPM.

For calculation of N^{track}_{exp} the nominal PDE of 37%, as given by the producer, was taken. However, the true PDE was lower due to lower bias voltage and, consequently,

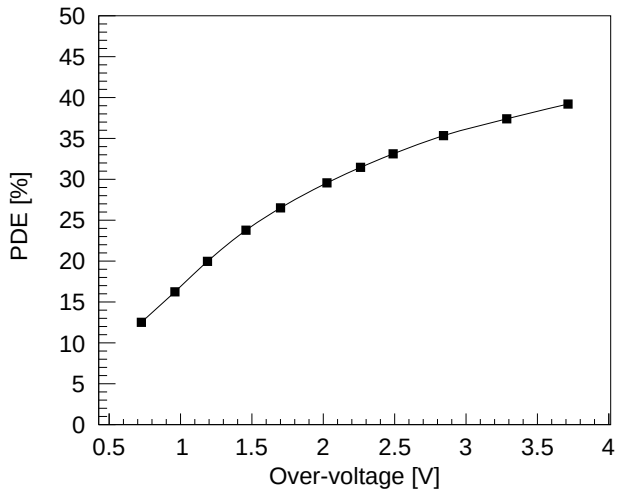

Figure 5.16: Peak of PDE as a function of over-voltage for Hamamatsu MPPC S12572. When biased at 1.5 V over-voltage, the peak PDE is ⅔ of nominal PDE. The curve is taken from producer's data-sheet [50].

lower gain of the device. In laboratory measurements, the breakdown voltage was found to be $V_{\text{breakdown}} = 70.8\text{V}$. The working bias voltage $V_{\text{bias}} = 73.0$ V when corrected for a diode drop of 0.7 V (because of the specific circuity applied, *cf.* 4.2) corresponds to the over-voltage $V_{over} = 1.5$ V. From graph in Fig. 5.16, it was calculated that the PDE at $V_{over} = 1.5$ was 0.65 of the nominal PDE ($V_{over} = 3.2$). Accordingly, the PDE was $\approx$ ⅔ of photons was registered. Recalculated values are 1.8 (runs 43, 46), 4.6 (runs 48, 52) and 4.7 (run 53).

In case of measurements with light concentrators, the acceptance $\varepsilon_{array} = 0.9$ was taken to be the exact one obtained from Monte Carlo simulations. The contributions from 2, performance of the light concentrators, and 3, losses due to non-zero probability of having multiple photons on one SiPM, will be discussed in Chapter 6.

5.4.2 Cherenkov Angle Error

The Cherenkov angle error was of a lesser importance for this beam test. The sources of Cherenkov angle error may be grouped into the following contributions:

1. Uncertainty of the emission point in the radiator. One cannot exactly know where the photon was emitted along the particle path through the radiator. The error is inherent to the proximity focusing scheme and cannot be removed. The expected radius was calculated with a simple model [23]. The model presumes that the radial distribution $\mathrm{d}N/\mathrm{d}R$ of the Cherenkov photons in each ring at the detector plane is uniform. Fig. 5.17 shows the photon distributions at detector plane, N_1 and N_2, produced by photons from aerogel 1 and 2, respectively. Parameters a_0 and a_1 are differences of the inner and outer radii of the upstream and downstream rings. The uniform distribution hypothesis is acceptable in the case of normal incidence and high transmission lengths of both radiators. The mean spread of the radial distribution σ_R of the Cherenkov photons, calculated in the model, is:

$$\sigma_R = \sqrt{\langle R^2 \rangle - \langle R \rangle^2}, \tag{5.8}$$

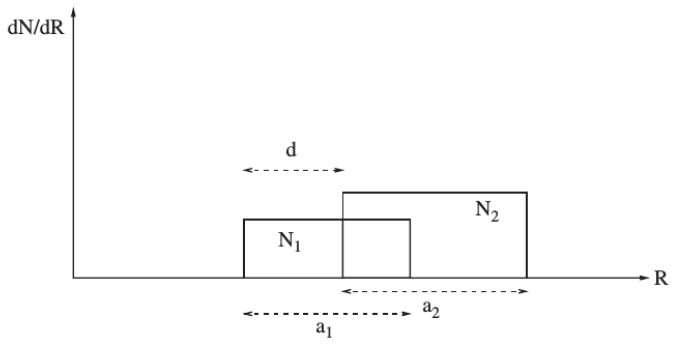

Figure 5.17: Contributions from the two radiator layers to the radial distribution of photon impact points on the detector plane [23].

and the angle error is:

$$\sigma_\theta^{\mathrm{EMP}} = \frac{\cos^2\theta}{l}\,\sigma_R = 10.9 \text{ mrad}, \tag{5.9}$$

where l is the distance between the mid-point of the upstream radiator and the detector plane and θ is the expected Cherenkov angle for this radiator. Such a large error is caused by the fact that the matching of the aerogels is not perfect ($\delta n = 0.009$, [23]), but is a bit larger ($\delta n = 0.013$) and the produced images do not overlap.

2. Finite pixel size of the photon detector $\Delta = 5$ mm. This produces an error of:

$$\sigma_\theta^{\mathrm{PIX}} = \frac{\cos^2\theta}{l\,\sqrt{12}}\,\Delta = 7.01 \text{ mrad}. \tag{5.10}$$

3. The reconstruction of the track position is bounded by the precision of the measurements with MWPC telescope. Only the coordinate error perpendicular to anode wires (along the vertical direction for both MWPCs) is considerable, due to anode wire distances, $s_a = 2\ mm$. This results in the uncertainty on y-coordinate measurement of $\sigma_y = {}^{s_a}/\sqrt{12}$ and the angle error of:

$$\sigma_\theta^y = \frac{1}{z_2 - z_1}\,\sqrt{1 + (\frac{z_0 - z_2}{z_0 - z_1})^2} = 1.63 \text{ mrad}, \tag{5.11}$$

where z_1 and z_2 are the z-coordinates of the two MWPC in the telescope and z_0 is the distance from the first MWPC to the photon detector plane.

4. Tracking error due to misalignment of the telescope in x, y-coordinates. The smallest notch of 1 mm of the used tool results in:

$$\sigma_\theta^{align} = 1.99 \text{ mrad}. \tag{5.12}$$

5. Tracking error due to multiple scattering of electrons in aluminium. The electron track is not a straight line, but is deviated between the two MWPCs in the telescope due to the scattering in aluminium box walls of width $x = 2$ mm.

The error on the angle with the electron momentum $p = 5$ GeV/c, $\beta = 0.999$ and the radiation length $x_0 = 89$ mm (from [16]) is:

$$\sigma_\theta^{multi} = \frac{2}{3} \frac{13.6 \text{ MeV}}{\beta\, c\, p \text{ MeV}} \sqrt{\frac{x}{x_0}} \left(1 + 0.038 \ln \frac{x}{x_0}\right) = 0.23 \text{ mrad.} \tag{5.13}$$

6. Since the wavelength of the emitted photon is not known *a priori*, the variation of the refractive index with wavelength attributes to chromatic error, which results in [83]:
$$\sigma_\theta^{chroma} \approx 2 \text{ mrad.} \tag{5.14}$$

7. Additional error is introduced by aerogel non-uniformity and is estimated to be [83]:
$$\sigma_\theta^{unkown} \approx 7 \text{ mrad.} \tag{5.15}$$

The listed errors are supposed to be non-correlated. Therefore, they can be summed quadratically to a total single photon error:

$$\sigma_\theta^{single} = 15.1 \text{ mrad.} \tag{5.16}$$

This is seen to be in a good accordance with the measured values for the runs without light concentrators (runs 43 and 46, *cf.* Table 5.4. However, the light concentrators introduce an error of $\approx 8 - 10$ mrad (runs 48-53), because their geometry is not included into the reconstruction of the Cherenkov angle. Finally, the errors in the case of the downstream hypothesis are larger, because of the shorter lever arm of the photon path.

Chapter 6

Light Concentrators Performance

The lower-than-expected acceptance of the light concentrators is discussed at the beginning. A possible improvement of the concentrators, regarding the optical cross-talk, is presented. The error on the number of detected photons introduced by a detector operating in binary mode is obtained from simulation. Eventually, a short summary of the light concentrators performance and their influence on particle separation is given.

The performance of the light concentrators in the beam test was lower than expected. The collection ratio of the light concentrators, ζ, we defined as the ratio of the number of detected photons with and without light concentrators. Two calculated collection ratios from the beam test are listed in Table 6.1. The ratios are different for two positions of photon detector because of the different geometrical efficiencies ε_f, calculated in Chapter 5. From simulations we would expect the collection ratio to be $\zeta \simeq 2.50$, while in the beam test it was significantly lower, ≈ 1.90.

In order to investigate further the performance of the concentrators, we measured their response to low intensity light in the laboratory set-up. The set-up was described in Chapter 4. At first, we measured the response of the module to laser light with perpendicular incidence. The average number of detected photons, N_{pe}^{wo}, as function of the laser spot position is shown in Fig. 6.1, left. The average number of detected photons of the module, assembled with the light concentrators, N_{pe}^{LC}, is shown in Fig. 6.1, right. The collection ratio was calculated as the ratio of these two numbers:

$$\zeta = \frac{N_{pe}^{LC}}{N_{pe}wo} = 2.13. \tag{6.1}$$

The observed collection ratio is significantly away from 2.78, the maximal ratio for the perpendicular incidence.

Runs	Pos.	ζ
48/43	3	1.90
52/46	2	1.95

Table 6.1: Collection efficiency of light concentrators ζ for two positions of the photon detector.

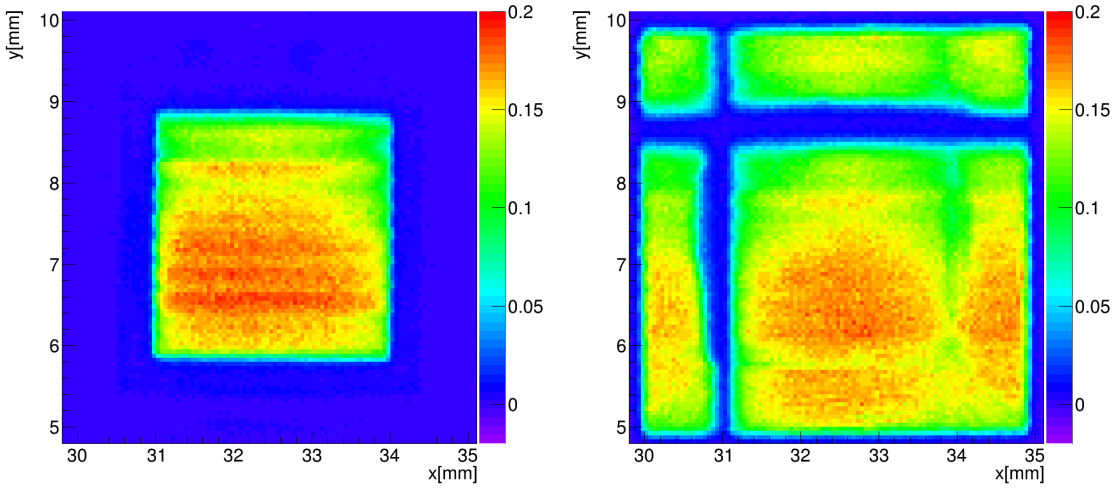

Figure 6.1: Response of the module to low intensity light. Left: Average number of detected photons $N_{p.e.}$ as a function of laser spot position. The module is assembled without light concentrators. Right: Module assembled with the light concentrators. The two bands of lower efficiency in the response with light concentrator, a vertical and a horizontal one, are due to optical coupling problems, will be discussed further in the text.

6.1 Optical Coupling Losses

In the beam test and laboratory measurements, we observed two effects, which we wanted to quantify. For that reason we employed the Monte Carlo simulation, described in Chapter 4.

The first effect is the imperfect coupling between the light concentrators and the SiPMs. In fact, the PCB, on which the SiPM array was assembled, was slightly deformed. Due to this deformation, there was an additional gap between the concentrators and the SiPMs, in the central part of the module. As a consequence, the surface of some of the channels was only partially coupled to concentrators, if the amount of applied grease was insufficient. This was the case in the beam test set-up (Fig. 6.2).

Fig. 6.3, showing two typical rays (black and red), explains this effect qualitatively. The black ray hits the part of the exit window which is optically coupled with the grease. That ray is registered by the module. The red ray hits the exit window, with the air on the other side, and internally reflects. The simulated response of the module is shown in the Fig. 6.4, left. The rays are distributed uniformly under normal incidence at the light concentrator entry window. The coupled area is circular. The simulation of bad coupling with insufficient grease resulted in the collection ratio of $\zeta = 2.30$. Fig. 6.5 (left) shows the distribution of the rays according to the physical phenomena they undergo in the simulation. The entries in the graph contain number of rays that:

1. Miss the light concentrator,
2. Are back-reflected at the entry window,
3. Are refracted at the plate side,

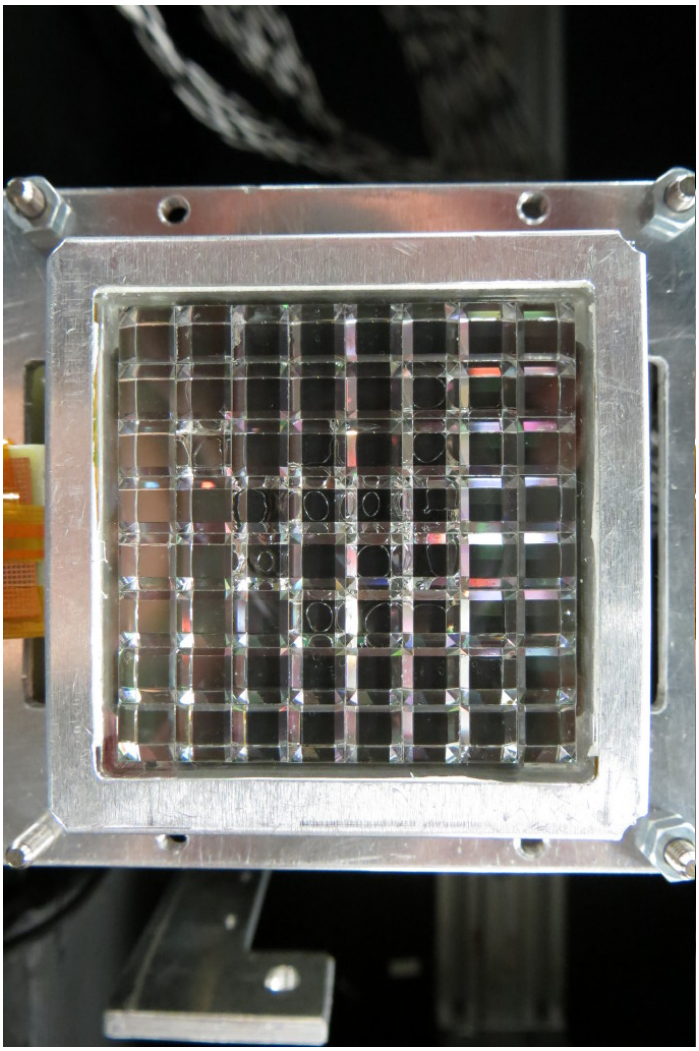

Figure 6.2: Photograph of photon detector module in the beam test set-up. Observe that certain SiPMs in the central part are only partially coupled to concentrators.

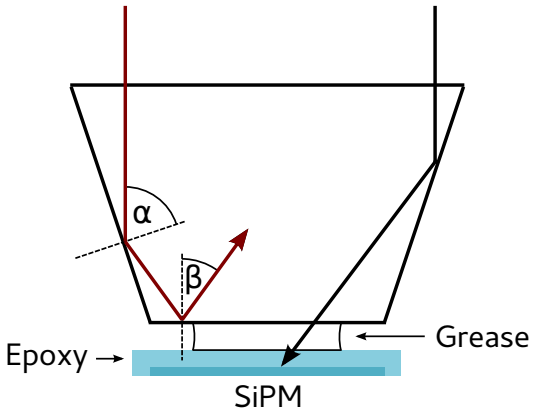

Figure 6.3: Two typical rays when the light concentrator and SiPM are partially coupled with optical grease (grease thickness is exaggerated). The reflection angles are $\alpha = 71.6°$, $\beta = 36.8°$ ($\beta = 51°$ if ray is reflected twice, at adjacent sides).

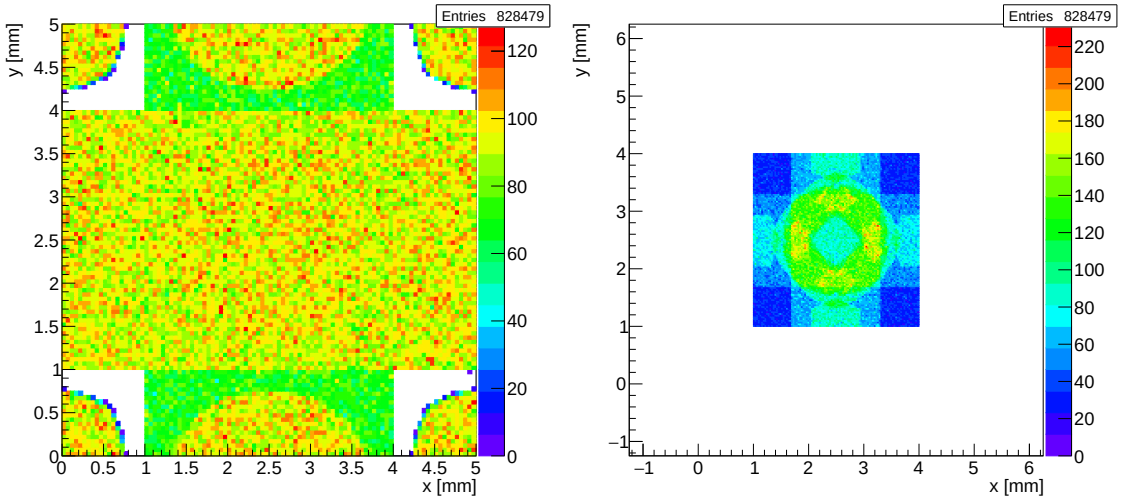

Figure 6.4: Simulation of module response in the case of bad optical coupling between the concentrator and the photon detector. Rays are distributed uniformly, under normal incidence at the light concentrator entry window. Left: Histogram of detected rays impact points at the light concentrator entry window. Right: Histogram of ray impact points in the x, y active detector plane.

4. Are refracted at concentrator side,
5. Are internally reflected at the exit window,
6. Enter the concentrator,
7. Exit the concentrator through the exit window,
8. Are simulated.

It can be observed that most of the rays are lost due to the internal reflection at the exit window (Fig. 6.5, right).

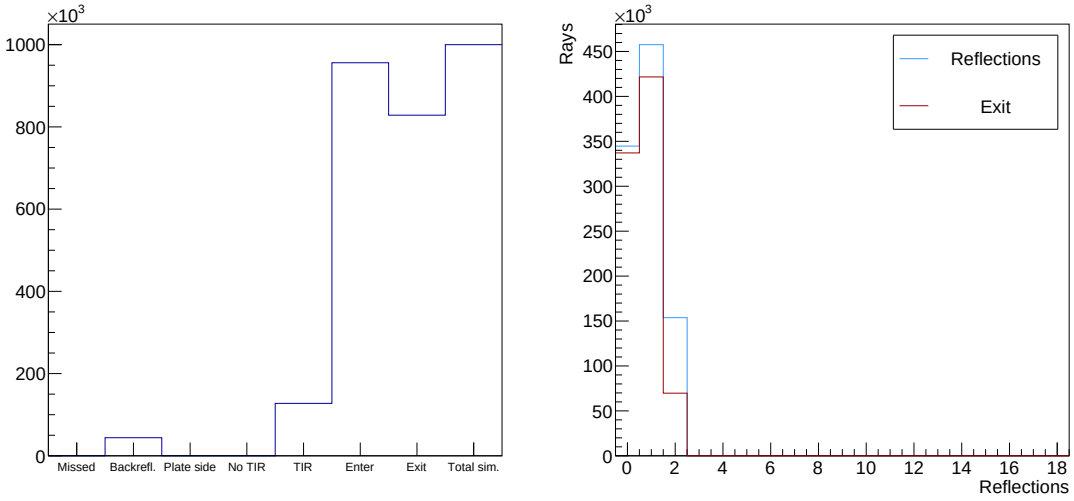

Figure 6.5: Left: Ray histogram according to the physical phenomena it undergoes. For the explanation, see text. Right: Histogram of number of reflection of all simulated rays (blue) and rays that hit the SiPM active area (red).

	Incidence 0°			Incidence 18.5°		
Sources of loss	Net	Cumulative	Ratio	Net	Cumulative	Ratio
Ideal coupling	0%	0%	2.78	3%	3%	2.70
Grease coupling	4%	4%	2.67	(5±2)%	(8±2)%	2.56
Misalignment	7%	11%	2.47	(4±2)%	(12±3)%	2.45
Measured		26%	2.13		34%	1.90

Table 6.2: Net, cumulative losses and collection ratio in the case of rays simulated at 0° and 18.5° to the surface normal.

The second effect was observed in the case the grease was applied in excess, as in the case of the laboratory set-up Fig.6.1. The light escape at the lateral sides of the pyramid, producing the effect of low efficiency bands. By simulating the low efficiency zone of the same width as observed in the measurement, the estimate of the loss fraction due to an excess of grease is 4%. The second effect that contributed to the low efficiency bands was the misalignment of the SiPMs and the concentrators. This effect alone can be observed in the measurement without the optical grease (Fig. 4.24) and it resulted in a further 7% loss.

The summary of the loss factors with light perpendicular to the entry surface is given in the Table 6.2 (three leftmost columns). Taken all previously discussed estimates into account, the expected ratio dropped to 2.47 in the laboratory set-up.

A similar analysis can be carried out for the beam test geometry. A first step was to distribute rays at angles which are in accordance with the geometrical efficiency of one module. The rays are simulated at a fixed polar angle $\theta = 18.5°$ and at azimuthal angle in range $\varphi \in [-19.4°, 19.4°]$ relative to the entry surface normal, thus imitating the Cherenkov light in our prototype RICH. With the ideal optical

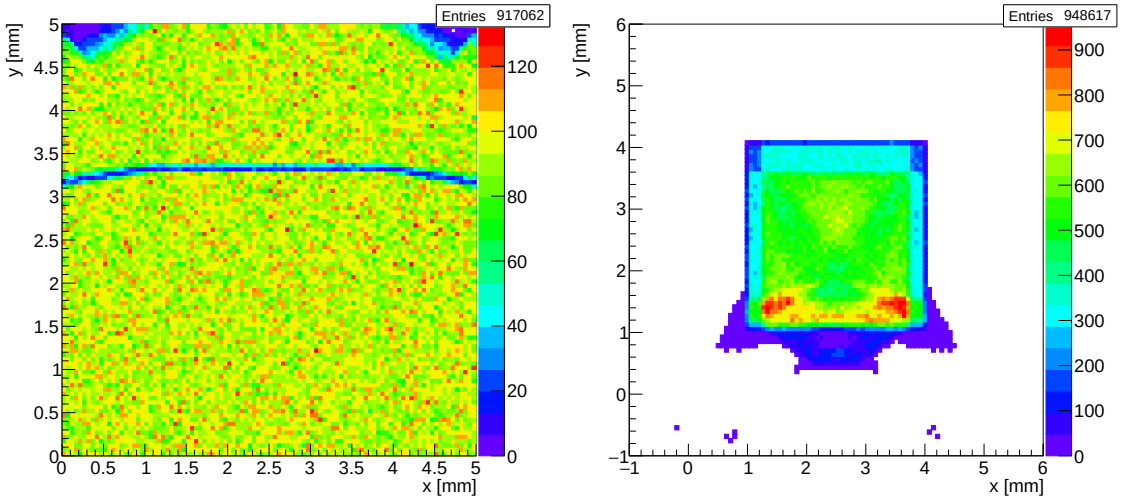

Figure 6.6: Simulation of ideal optical coupling between the concentrator and the photon detector for oblique incidence, as in the beam test $\theta = 18.5°, \phi \in [-19.4°, 19.4°]$. Left: Rays impact points at the light concentrator entry window. Right: Rays impact points in the x, y active detector plane.

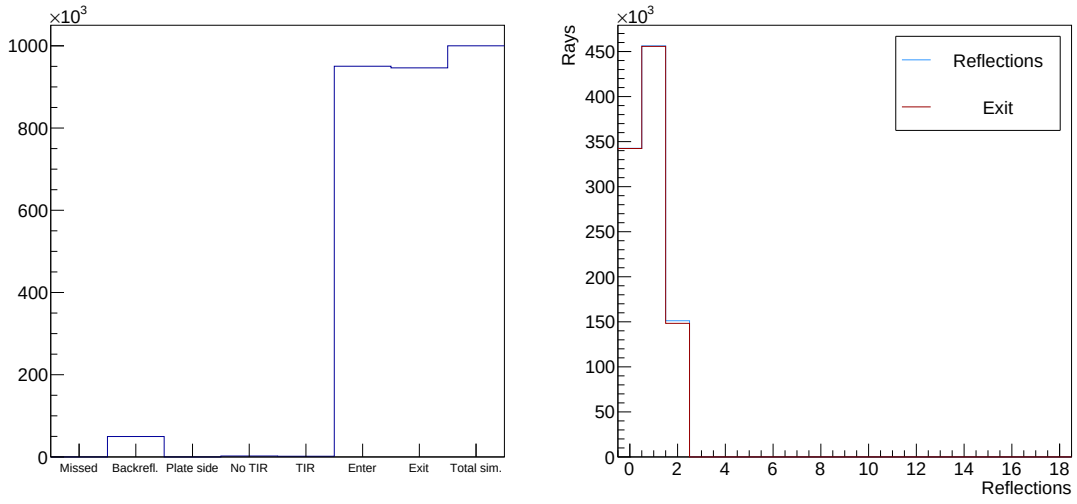

Figure 6.7: Simulation of ideal optical coupling between the concentrator and the photon detector for oblique incidence. Left: Ray histogram according to the physical process it undergoes. Right: Histogram of number of reflection of all simulated rays (blue) and rays that hit the SiPM active area (red).

coupling between the concentrator and the SiPM the collection ratio is $\zeta = 2.55$. Fig. 6.6 shows the ray impact points at the entry window. The low efficiency band is caused by the rays lost due to the finite thickness of the protective layer. This is also confirmed by the distribution of the rays with respect to the physical process they undergo in the concentrators (Fig. 6.7), which shows that the refraction and reflection losses are small.

To understand the losses due to imperfect optical coupling in case of the beam test data, we studied the response of the module, assembled without the optical

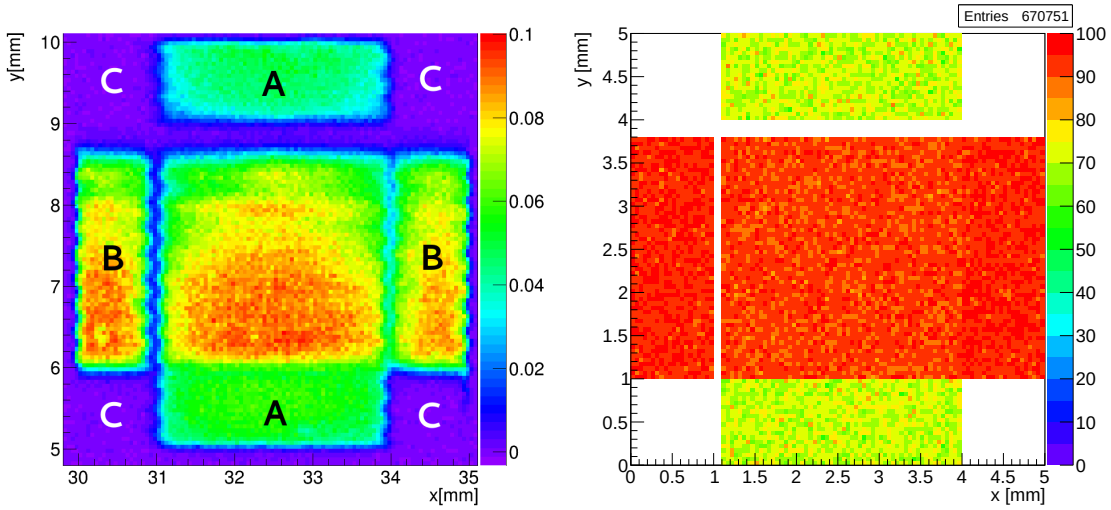

Figure 6.8: Average number of detected photons in response to linearly polarized light without the optical grease (left). Monte Carlo study with the same parameters (right).

grease, to polarized light. In that case, there is an air gap between the light concentrator and the SiPM, and the light collection efficiency shows a pronounced dependence on the polarization state of light. In the response of the module (Fig. 6.8, left) one can observe several distinctive zones. The central 3×3 mm^2 zone corresponds to the light rays that pass through the concentrator without reflections. The two zones of lower efficiency (A) and the two zones with the approximately equal efficiency as the central zone (B) include rays that reflect once at the lateral sides before hitting the exit window. The zones C comprise rays that reflect from two adjacent lateral sides and show no detected photons at all.

The difference in efficiency can be understood using the Fresnel formulae. A ray incident above the zone A will totally reflect from the lateral side ($\alpha = 71.6°$, Fig. 6.3) and will hit the exit window at an incidence angle of $\beta = 36.8°$. Suppose the ray is s-polarized at the exit window. At this β, which is smaller than the critical angle $\beta_c = 41°$, about 26% rays will internally reflect (Fig. 6.9). The same ray is p-polarized if incident above zone B, in which case the internal reflection is negligible. The ray incident above zone C will reflect twice and the incident angle will be $\beta = 51°$. Since this is larger than β_c, all such rays will be totally reflected, independent of their polarization state.

For the simulation of the rays distributed as in the beam test, but with the bad optical coupling, the coupled area was approximated by a circle with diameter d. As a measure of the coupling we introduced the coupling ratio η, which is the ratio of the circle area to the SiPM area, a:

$$\eta = \frac{d^2\pi/4}{a^2}. \tag{6.2}$$

For illustration, the impact ray points are shown in Fig. 6.10 for the coupling ratio $\eta = 1.0$ (*i.e.* inscribed circle). From the ray statistics (Fig. 6.11 it can be observed that the most of the rays are lost due to internal reflection at the exit window–air surface.

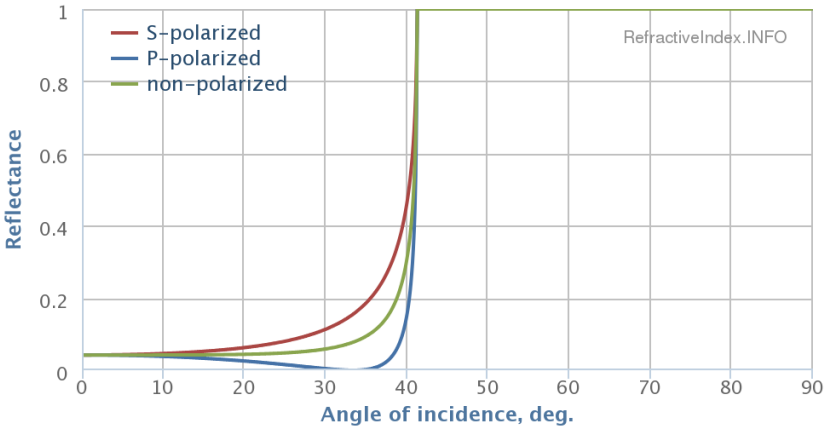

Figure 6.9: Reflectance of p-wave, s-wave and non-polarised wave at the boundary glass - air calculated with the Fresnel formulae. Observe the critical angle $\beta_c = 41°$ above which every ray is totally internally reflected. Graph generated with [84] for Schott BK7 glass.

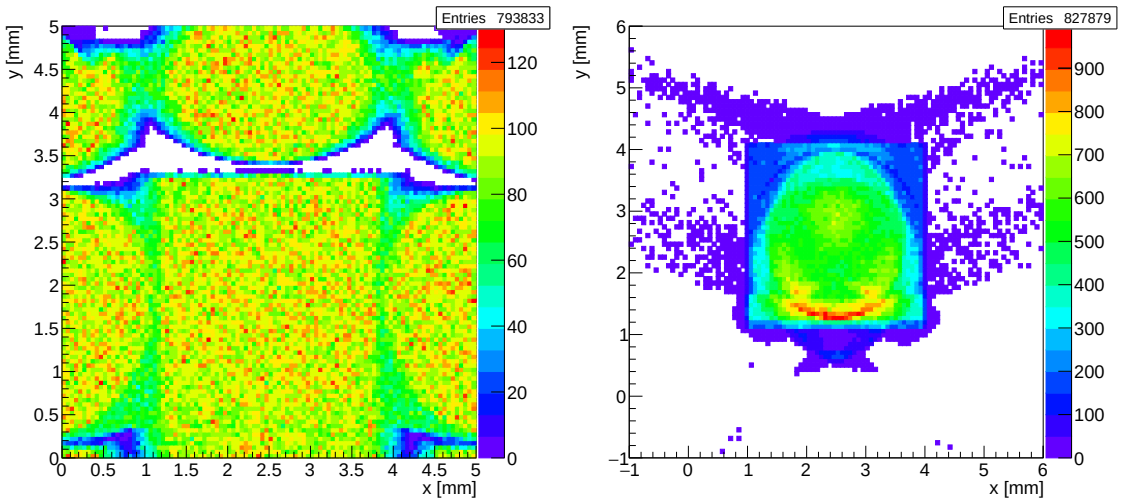

Figure 6.10: Simulation of bad optical coupling between the concentrator and the photon detector for oblique incidence. Left: Ray impact points at the light concentrator entry window. Left: Rays impact points in the x, y active detector plane.

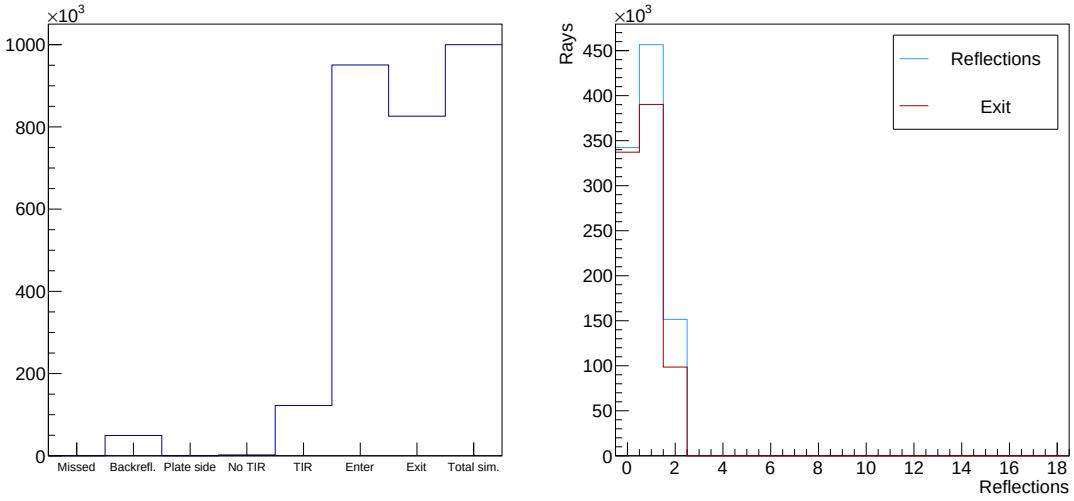

Figure 6.11: Simulation of bad optical coupling between the concentrator and the photon detector for oblique incidence. Left: Ray histogram according to the physical process it undergoes. Right: Histogram of number of reflection of all simulated rays (blue) and rays that hit the SiPM active area (red).

To obtain the estimate for the beam test data, the ratio of the coupled area of the concentrator to the non-coupled area was calculated from the photograph of the module in Fig. 6.12, for every SiPM in the array. The acceptance ϵ_i for each SiPM was than simulated and weighted with a factor w_i, proportional to the number of photons detected with the SiPM i. The calculated values of the ratio η_i, the acceptance ε, weighting factor w and reduced SiPM acceptance $w \times \varepsilon$ are given in the Table 6.3. The sum of reduced acceptances per channel is the average reduced acceptance of the array:

$$\varepsilon_{array} = \sum w_i \times \varepsilon_i = 86.91\%, \tag{6.3}$$

and the corresponding collection ratio is:

$$\zeta = \varepsilon/\varepsilon_{array} = 0.869/0.36 = 2.42. \tag{6.4}$$

This is 5% away from the ideal coupling $\zeta = 2.78$. Than the overall inefficiency introduced by the coupling was calculated to be 5% with the systematic uncertainty of 2%. The losses in the beam test are summarised in Table 6.2, three rightmost columns.

The systematic errors in optical coupling study were estimated by varying the coupling ratio η and by varying the weighting factor w, resulting in $5\% \pm 2\%$ loss. Taken into account the misalignment loss $4\% \pm 2\%$, the resulting cumulative loss was $12\% \pm 3\%$ (systematic uncertainties added in quadrature) and expected collection ratio dropped to 2.45.

The statistical error of the light concentrator simulations was estimated using the binomial distribution. The simulated geometrical efficiency ε is taken as the probability of success. Then, the variation is (for large N):

$$\sigma = \sqrt{\frac{\varepsilon\,(1-\varepsilon)}{N}} = 0.05\%, \tag{6.5}$$

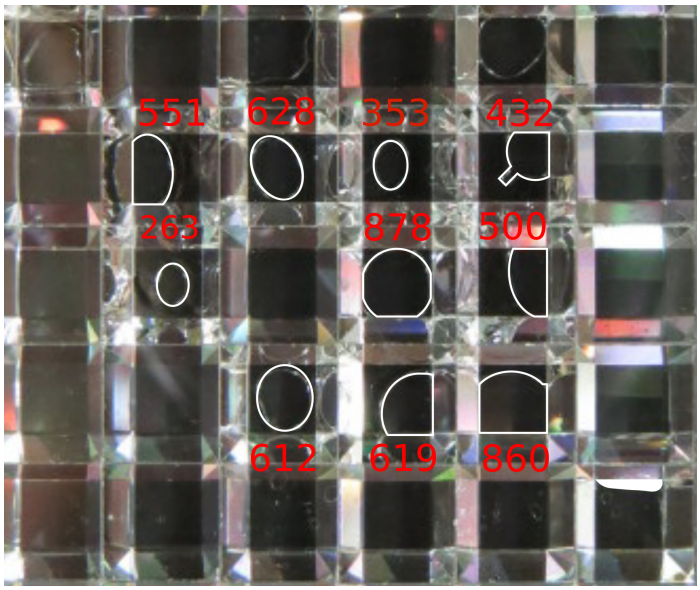

Figure 6.12: Photograph of MPPC array in the beam test with optically coupled areas drawn. The numbers represent the area (in pixels) used for the calculation of the coupling ratio η.

SiPM	η	ε[%]	w	$w \times \varepsilon$ [%]
34	0.8999	85.44	0.04271	3.65
20	0.5621	71.79	0.04271	3.07
52	0.5689	72.04	0.04271	3.08
36	0.7905	82.14	0.03751	3.08
6	0.2415	57.46	0.02403	1.38
38	0.4598	67.36	0.03270	2.20
25	0.5063	69.39	0.00814	0.56
9	0.5771	72.32	0.00601	0.43
41	0.3246	61.24	0.00601	0.37
57	0.3975	64.53	0.00601	0.39
other	-	91.42	0.75147	68.70
Sum			1.00	86.91

Table 6.3: Calculation of the average acceptance due to bad optical coupling. Listed are coupling ratio η, simulated acceptance ε and weighting factor (relative number of detected photons) w for all SiPMs in the array. The average acceptance is $\varepsilon_{module} = w \times \varepsilon = 86.9\%$ which results in $\zeta = 2.42$. SiPM positions correspond to beam test mapping, given in Appendix A, Fig. A.2.

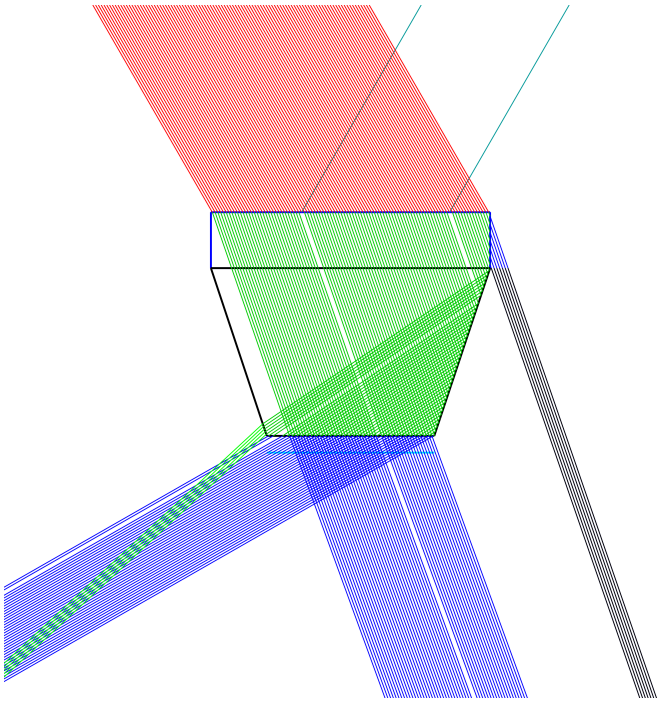

Figure 6.13: Side view of concentrator simulation with uniform distribution of rays at a fixed polar angle, $\theta = 30°$. The green refracted rays exit at the left side of the pyramid due to lack of total internal reflection.

where $N = 10^6$ is the number of simulated rays per concentrator.

6.2 Teflon Filling

At oblique incidence some rays are lost due to refraction at the pyramid sides. We tested if we could get some of these registered by reflection from the teflon filling in the concentrator array. The rays simulated uniformly at $\theta = 30°, \phi = 0°$ are shown in Fig. 6.13. From the graph of the registered and side refracted rays as function of the simulated incident angle in Fig. 6.14 one can observe that the refraction losses start at 22°.

Our first attempt was to use the teflon tape to fill the space between the pyramids. The choice of white teflon was motivated by its high reflectance which might result in detecting the photons that are refracted at pyramid sides. However, the tape soaked up the optical grease which then improved the optical contact between the teflon tape and the pyramid sides. The benefit from the total internal reflection, even for the perpendicular rays, was lost. In consequence the average number of registered photons over the total area of one pyramid dropped significantly (Fig.6.15).

A second attempt was to machine a grid of teflon which would fill the array. The height of the teflon filling after grinding of the sides was 1.8 mm, which was sufficient to reach above the half pyramid height (Fig. 6.16, left). The pyramid angle is $\alpha = 18.4°$ and the grid was cut with a knife at an angle $\beta = 10°$; therefore, the grid and the pyramid have only one contact point. The photograph of the grid, positioned on the MPPC array before the light concentrators, is shown in Fig. 6.16, right.

To study the effect of the teflon filling, the laser light now came under an angle of

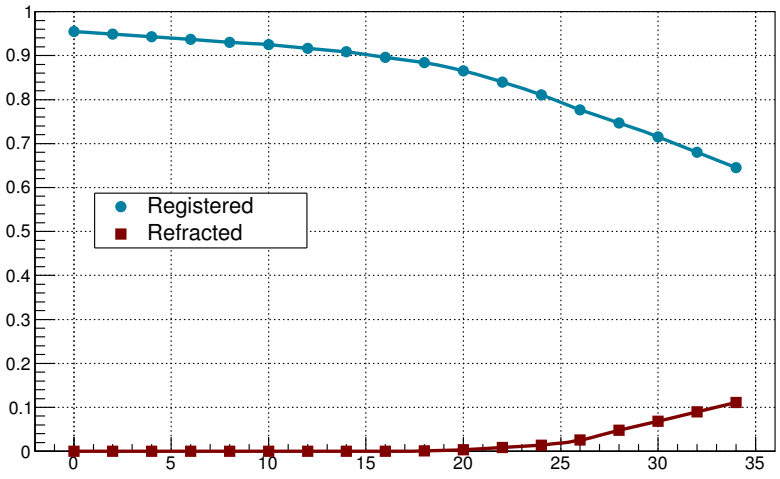

Figure 6.14: Simulation of accepted and refracted rays as function of the incident angle θ. Uniform distribution at every θ and $\phi = 0°$, fixed. Expected 8% loss for rays incident at $\theta = 30°$.

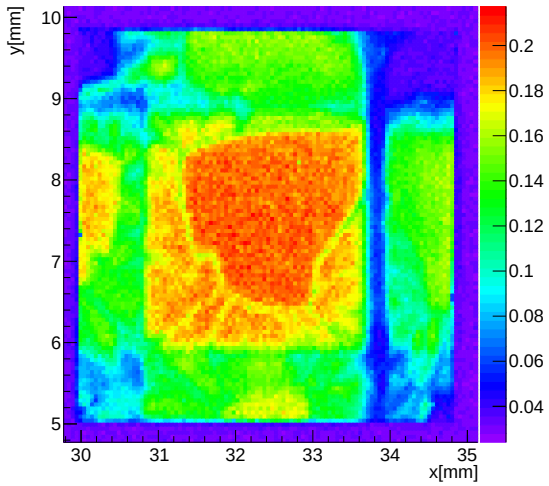

Figure 6.15: Teflon tape filling. The tape soaks up the optical grease and there is no improvement in the number of registered photons.

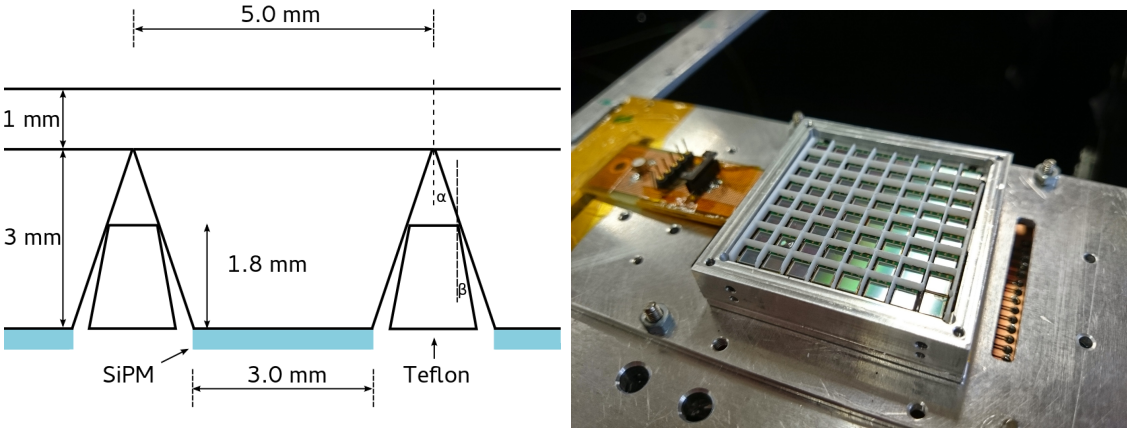

Figure 6.16: Left: Sketch of the teflon filling between the light concentrators. The angles α, β values are explained in text. Right: Photograph of the teflon filling on the MPPC array.

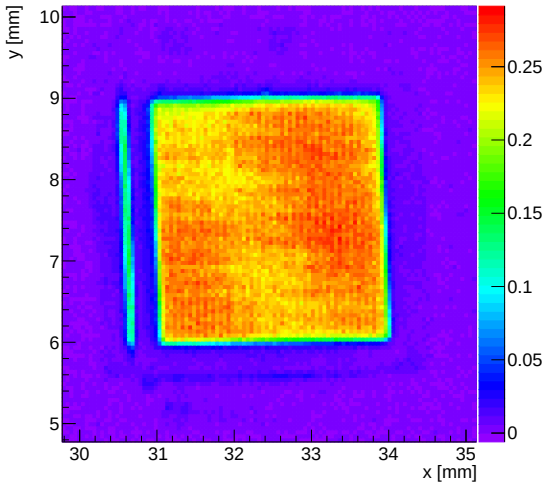

Figure 6.17: Average number of detected photons in channel 18 as function of laser position. Laser light is incident at $\theta = 30°$ to the normal and focussed to a spot of $\sigma \approx 60$ μm. Step size was 50 μm.

$\approx 30°$. The position z of the focusing lens was corrected to obtain the approximately same size of the spot, which is now elliptic. The response of the bare module to laser spot focused to $\sigma_x \approx 60$ μm is given in Fig. 6.17 and shows no significant difference than at 0° incidence. Then the response of the module with light concentrators was studied. The figure 6.18 shows the response of the module without and with the teflon grid between the pyramids. Light is incident at $\theta = 30°$ to the normal and focused to $\sigma \approx 50$ μm. There is no significantly more registered hits with the grid. The overall number of registered photons with the grid is slightly higher (7%) then without it, but it is not far away from systematic errors which are estimated to $\approx 5\%$. The influence of the temperature variation during the scan ($\Delta t = 0.8°$ C) is too small to be significant.

Fig. 6.19 shows the simulated detector response in the case of a uniform distribution of rays under $\theta = 30°, \phi = 0°$. One can observe the zone A where the rays

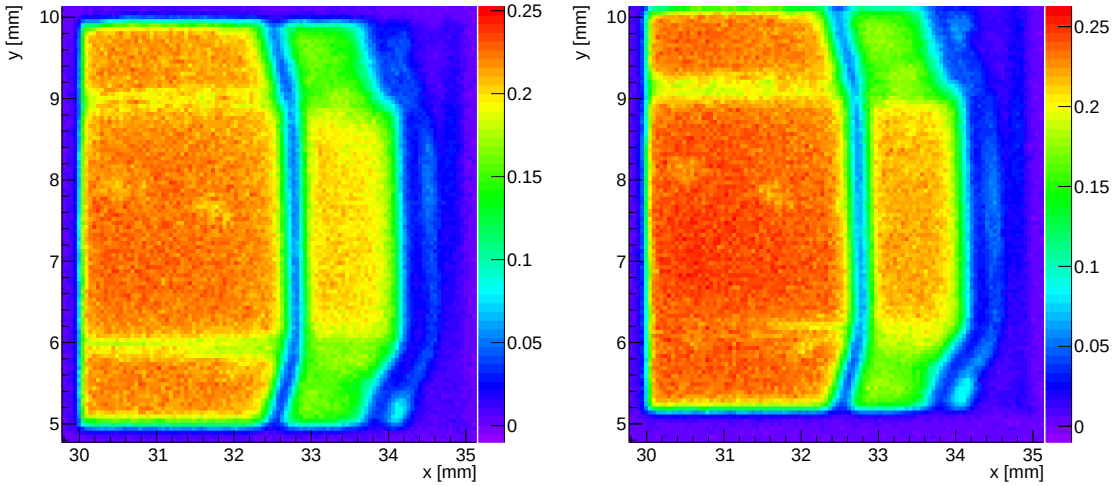

Figure 6.18: Average number of detected photons in channel 18 as function of laser position. Laser light is incident at $\theta = 30°$to the normal and focused to $\sigma \approx 50\mu$m. Response of the module without (left) and with the teflon filling (right) between the pyramids. There is no significantly more registered hits with teflon. Slightly more hits registered with the teflon (7%) might come from systematic errors; the influence of the temperature variation (0.8° C) is excluded.

are lost due to refraction at the side (*cf.* also Fig. 6.13, showing the side view of ray tracing simulation). The zone B corresponds to rays that are lost due to the gap introduced by epoxy layer. The histogram of the impact points of rays that are refracted at the pyramid side, due to lack of total internal reflection, is shown in Fig. 6.19, right. In the response of the neighbour channel 3 (*cf.* list of channels Appendix A, Fig. A.1) without the teflon grid (Fig. 6.20), one can observe that when the laser is above the zone A in channel 18, the refracted rays are registered in the channel 3. With the teflon grid this optical cross-talk is significantly reduced.

In Fig. 6.21 the simulated detector response in the case of a uniform distribution of rays under polar angle $\theta = 30°$ and various azimuthal angles $\phi = (10, 20, 30, 45)°$ can be observed. Nevertheless, the loss due to refraction at side is highest at $\phi = 0$, 8% and there was no need to check the response of the module for other ϕ values.

6.3 Double Hits

The detector module operated in a binary mode, that is, a hit was registered if the signal from photon sensor exceeded certain threshold. The amplitude information from the photon sensor signal was not exploited, which means that if multiple photons hit the same SiPM, they would still be registered as one hit. This binary operation mode is motivated by the following assumptions:

1. The number of emitted photons per particle track is small,

2. The granularity of the detector is high and, therefore, the probability of two or more photons hitting one SiPM is small.

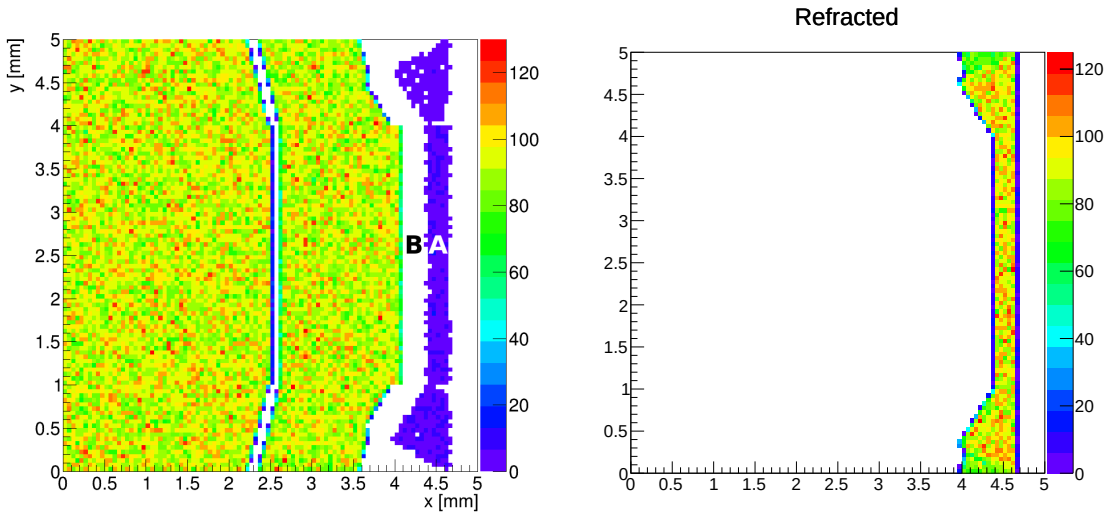

Figure 6.19: Left: Simulated detector response in the case of a uniform distribution of rays under $\theta = 30°$. The histogram shows the impact points of registered rays at the entry window. The zones A and B are explained in the text. Right: The histogram of the impact points of rays that are refracted at the pyramid sides because of lack of total internal reflection.

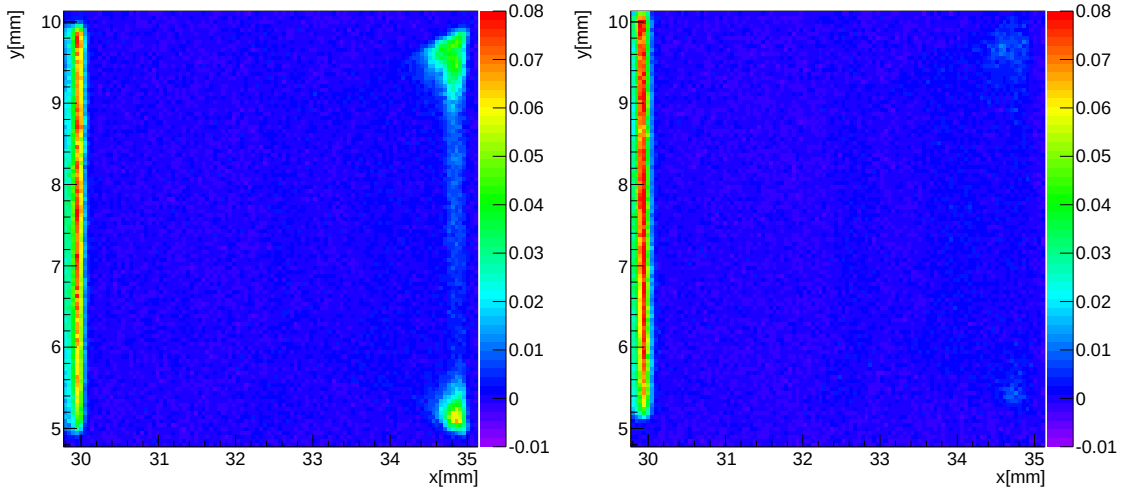

Figure 6.20: Registered hits in the neighbour channel 3 while the laser spot is above the channel 18. Left: Some of the rays refracted at pyramid side (*cf.* Fig. 6.19) are registered in this channel. Right: If the teflon grid is put between the channels, the cross-talk is significantly reduced.

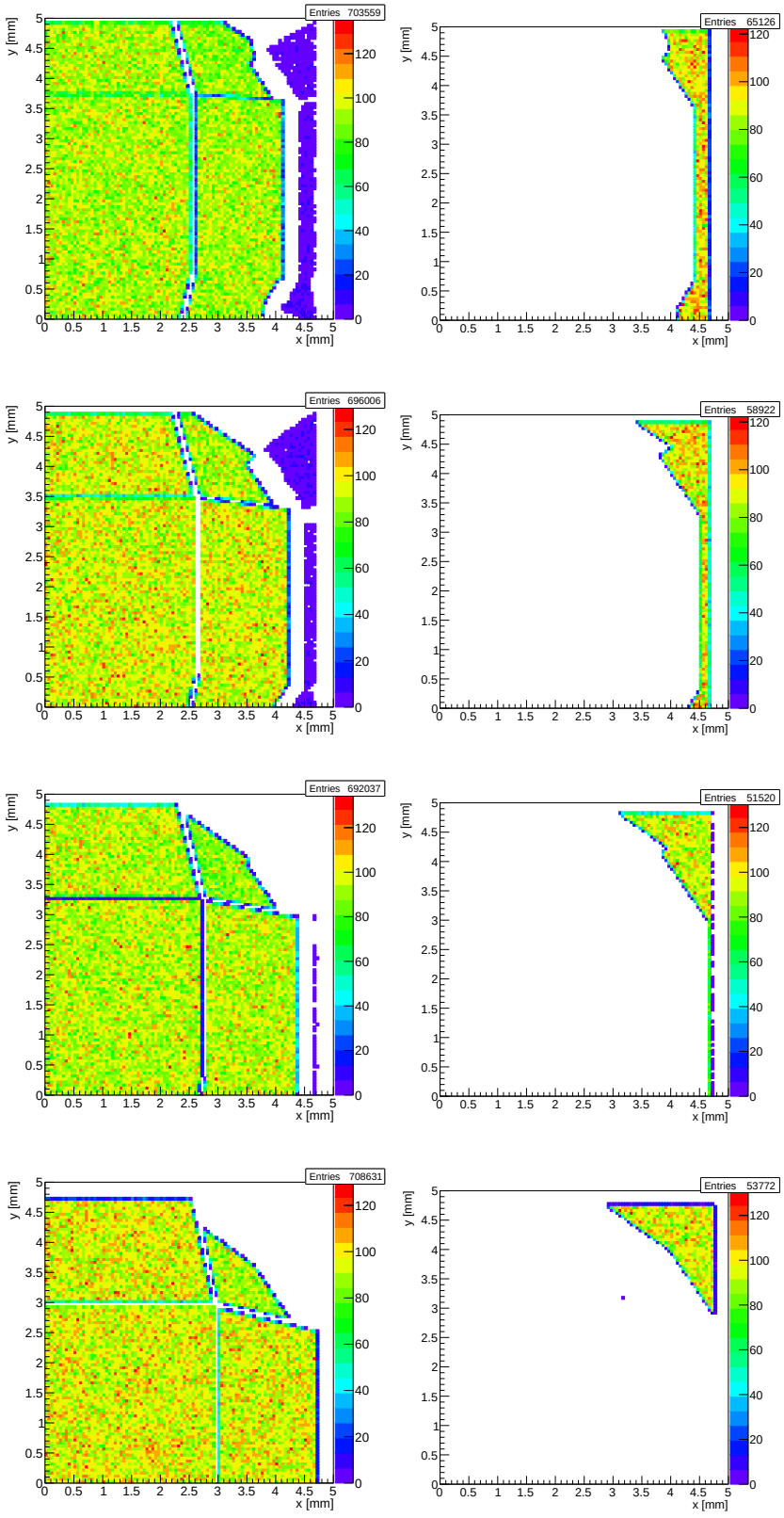

Figure 6.21: Simulated detector response in the case of a uniform distribution of 10^6 rays under azimuthal angle $\theta = 30°$ and polar angles $\phi = (10, 20, 30, 45)°$. The impact points of registered rays at the entry window are given on the left. The impact points of the refracted rays at the pyramid sides are given on the right. There are 7%, 6%, 5% and 5% of refracted (unregistered) rays, respectively.

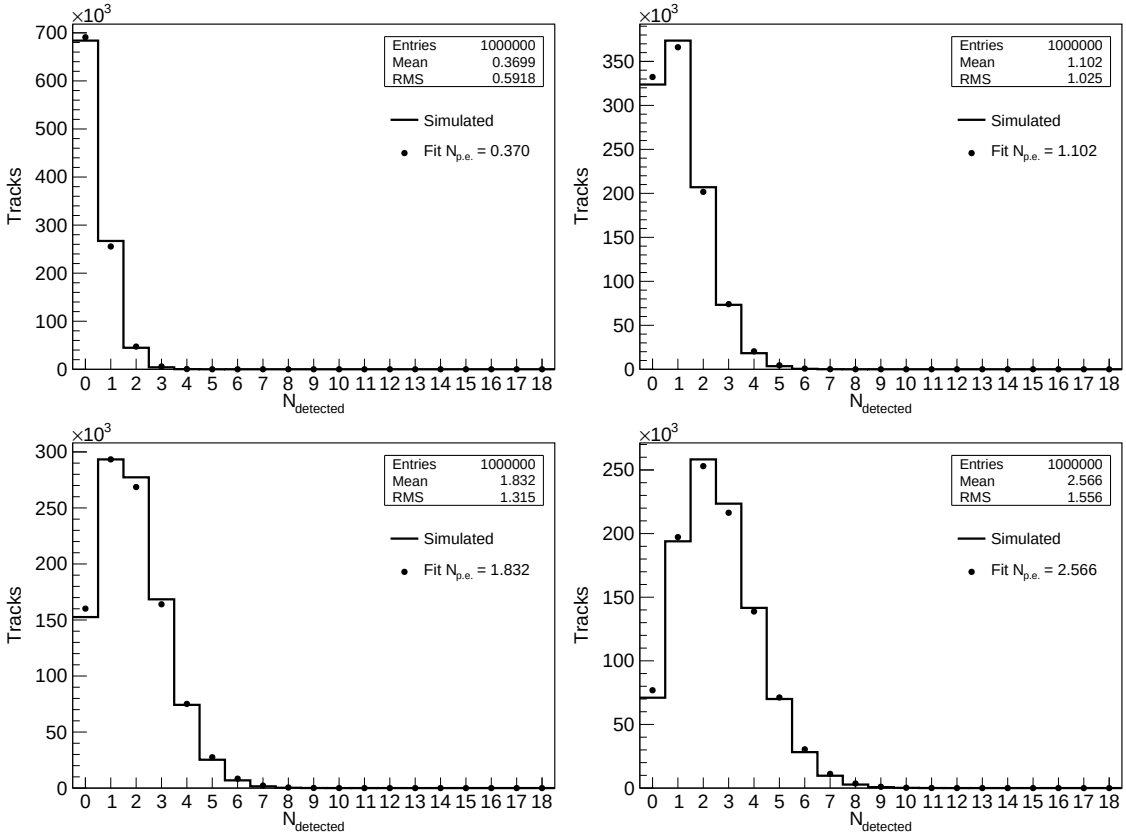

Figure 6.22: Histogram of the registered number of photons per track with the 8×8 photon module without the light concentrators. 10 (up, left), 30 (up, right), 50 (bottom, left) and 70 (bottom, right) simulated photons per track.

As a result of the binary operation mode, the complexity of front-end electronics was significantly reduced. However, the binary operation introduces an error in photon counting, because the registered number of hits is smaller than would be the number of registered photons.

A prototype RICH was simulated in C++ in order to obtain an estimate of the losses introduced by the multiple hits in one channel. Only the geometrical efficiency was simulated, without taking into account physical processes in aerogel. The photons were emitted in the centre of the upstream aerogel with parameters from the beam test, namely Cherenkov angle, $\theta = 0.304$, and the single photon error, $\sigma_\theta = 15.2$ mrad.

At first, the 8×8 SiPM array was simulated without the light concentrators, that is with the geometrical efficiency of each channel $\epsilon_{array} = 0.36$. The module is simulated in the position 3, as in the run 43 ($y = 72$ mm in the global coordinate system). Then the module was simulated with the light concentrators of ideal collection ratio $\zeta = 2.78$.

The average number of detected photons $N_{p.e}^{wo}$, with the module assembled without the light concentrators, for 10, 30, 50 and 70 detected photons is given in the Fig. 6.22. The average number of detected photons $N_{p.e.}$ with the module assembled with the light concentrators with ideal collection ratio $\zeta = 2.78$ is given in the Fig. 6.23.

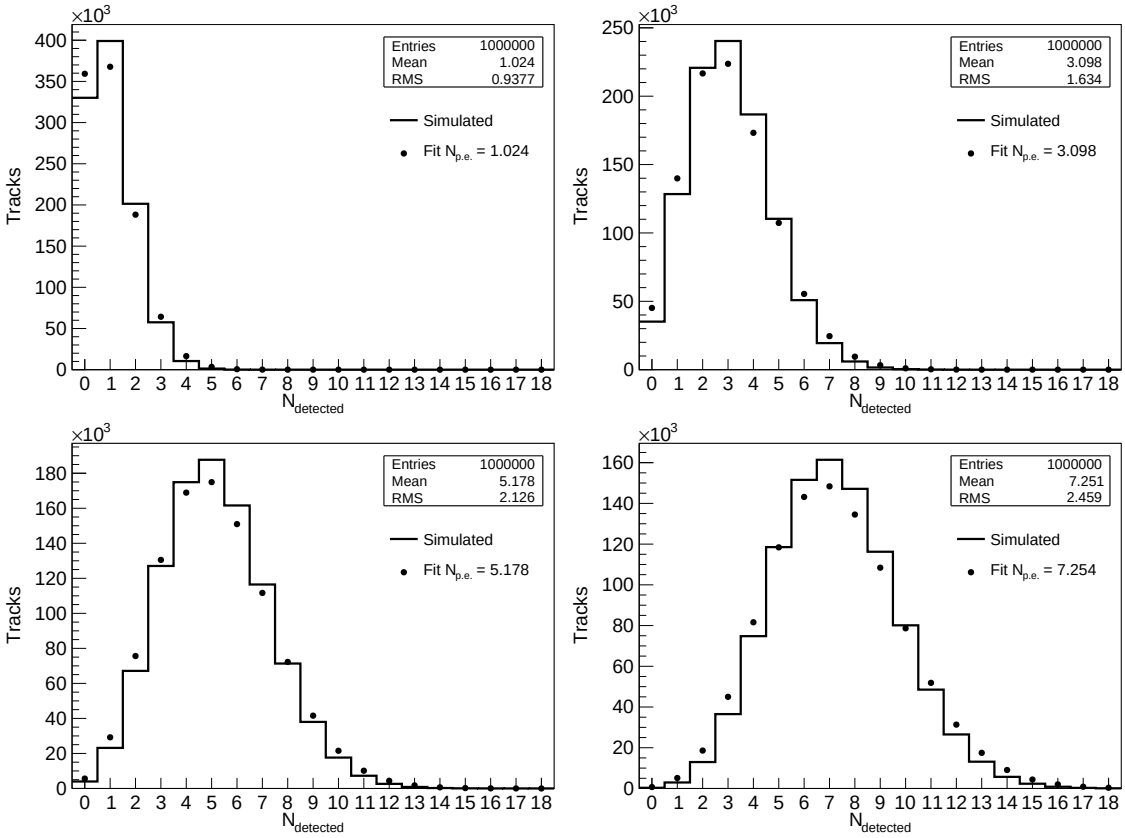

Figure 6.23: Histogram of the registered number of photons per track with the 8×8 photon module with the light concentrators. 10 (up, left), 30 (up, right), 50 (bottom, left) and 70 (bottom, right) simulated photons per track.

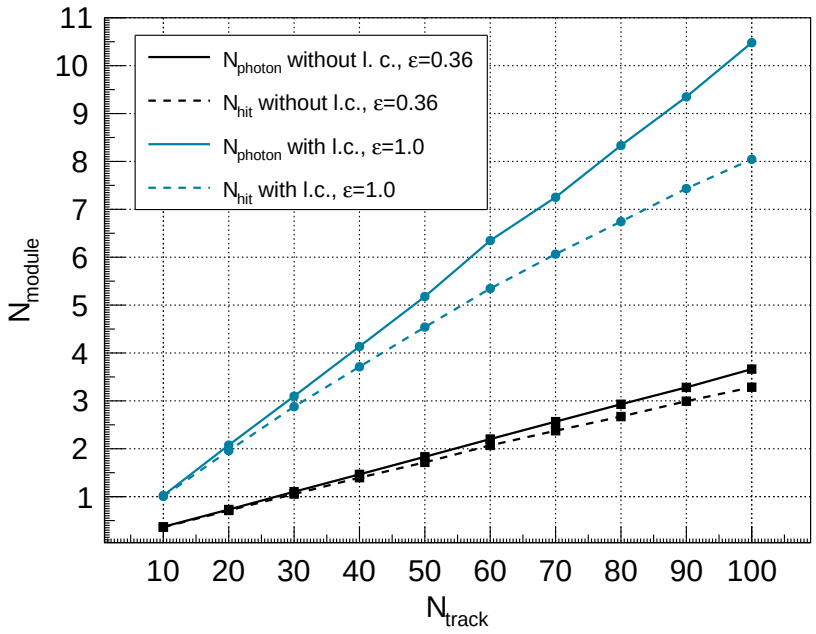

Figure 6.24: Detected photons and hits per module as a function of the number of simulated photons per track N_{track}. Module is simulated with the acceptance of the bare MPPC array, 0.36 (black), and with improved acceptance, 1.0 (cyan), with ideal light concentrators.

The results of simulation of geometrical acceptance are summarised in Fig. 6.24. It shows the number of detected photons, N_{photon}, and the number of detected hits, N_{hit}, as registered with the prototype module, as a function of the simulated photons per track, N_{track}, that is, whole Cherenkov ring. Both are shown for two cases, firstly for the module acceptance without the light concentrators, $\varepsilon = 0.36$, and secondly for the improved acceptance with the light concentrators, $\varepsilon = 1.0$. Because registered hits do not include double and multiple photon hits on one SiPM, the number of detected hits, N_{hit}, is lower than the number of detected photons. In the case of detector without the light concentrators, the average number of detected hits, $N_{det} = 1.85$ (as in the run 43), would result if $N \approx 50$ photons were detected per track. The histogram of number of detected photons with simulated 50 photons is given in Fig. 6.25, left.

The distribution of the detected photons in the channel 2 is given in Fig. 6.25, right. This channel is approximately at the centre of the photon radial distribution (see Appendix A, Fig. A.2 for channel positions). The probability to register two or more photons is calculated as $P(\geq 2) = 1 - P(0) - P(1)$, as well as the ratio of this probability and the probability to register one photon. The ratio, $P(2)/P(1) = 6\%$, is an estimate of the loss caused by double hits in a binary detector. In the case of the module without the light concentrators, the binary mode losses are smaller than optical coupling losses.

The histogram of number of detected photons per track, when the module is assembled with the light concentrators, is shown in Fig. 6.25, left. The histogram of detected photons in channel 2 is shown in Fig. 6.26, right. The ratio of the probabilities to register multiple and one photon, $P(\geq 2)/P(1) = 18\%$, is higher than in the case without the light concentrators. The probability calculated here

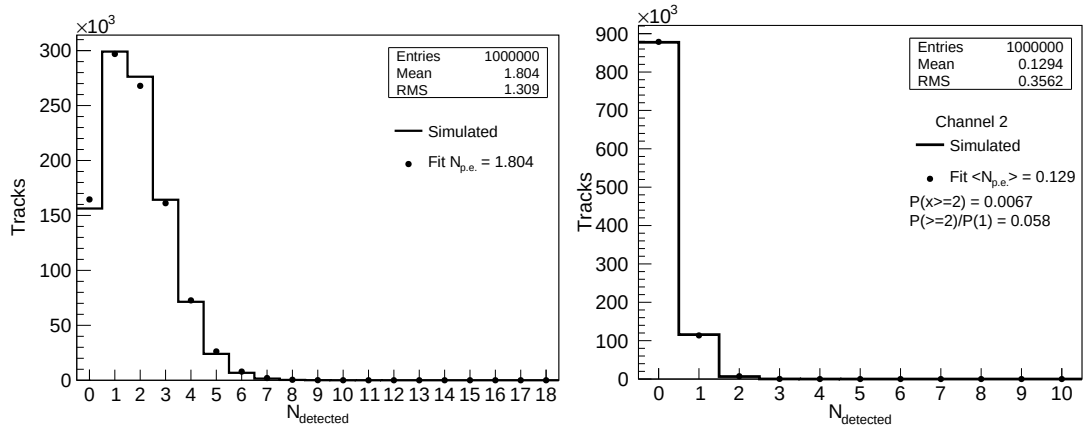

Figure 6.25: Left: Histogram of detected photons per track in the simulation of the geometrical acceptance of the prototype module *without* light concentrators. There are 50 simulated photons per track. Right: Histogram of detected photons with only SiPM 2.

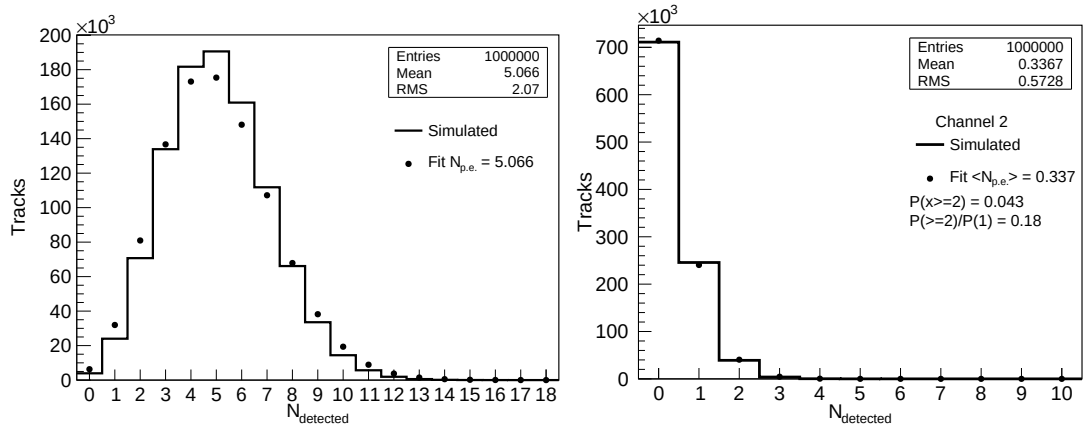

Figure 6.26: Left: Histogram of detected photons per track in the simulation of the geometrical acceptance of the MPPC array *with* the light concentrators. There were 50 simulated photons per track. Right: Histogram of detected photons with only SiPM 2.

is maximal; other SiPMs, which are hit by fewer Cherenkov photons, have smaller probability to detect multiple photons.

6.4 Summary

The Hamamatsu MPPC S11834 array proved to be an excellent sensor of Cherenkov photons. With the light concentrators, the geometrical acceptance of the array improved, and, as a consequence, the number of detected photons increased almost by a factor of two (1.90). However, this is lower than the ideal value of 2.78, as discussed in the text. This departure is explained to be caused by mechanical imperfections of the MPPC array, due to which the ratio dropped to 2.45.

The still remaining difference between the measured (1.90) and the expected (2.45) ratio is attributed to multiple hits on one SiPM and, to a lesser extent, to the production imperfections (glueing, air bubbles).

Run	$N_{\mathrm{det,track}}$	σ_{track}	$^{K}/_{\pi}$ separation
43	18.4	3.77	6.1
46	18.3	3.74	6.1
48	34.9	2.93	7.8
52	35.6	2.90	7.9
53	39.1	3.01	7.6

Table 6.4: Light concentrators overall performance and influence on separation of kaons and pions at $p = 4$ GeV/c.

Multiple hits due to binary operating regime of the detector introduce an error in photon counting. The error is small for the module assembled with the MPPC array only (6%), but it becomes the dominant source (18%) when the number of detected photons per SiPM increases, due to improved acceptance with the light concentrators.

Nevertheless, the light concentrators improve the separation of the kaons and pions at $p = 4$ GeV/c to $\approx 8\sigma$, while without concentrators it is $\sigma = 6.1$. The result is remarkable, having in mind that the Belle II goal is 4σ. The separation in different runs are summarised in the Table 6.4.

Chapter 7

Conclusion

We tested the SiPM as a photon sensor for RICH detector. The SiPM was compared to its two main rivals in photo-detection, a hybrid avalanche photo-diode and a micro-channel plate PMTs. The main advantages of SiPM are immunity to high magnetic fields and a high photon detection efficiency at a low operating voltage. Its small and robust packaging allows for compact design. Because the position information plays a crucial role in RICH, we used an array of 64 individual SiPMs. In order to improve a rather low acceptance of the array, 36%, we designed an array of light concentrators, which were cut and polished from glass.

The prototype photon detection module consisted of the SiPMs, light concentrators and the front-end electronics boards. The complexity of the electronics was significantly reduced by registering only the timing information from the module. The amplitude information was not exploited, thus, the detector worked in a binary mode. By employing a narrow time detection window of 6 ns, it was possible to reject most of the thermally generated noise.

The assembled module was tested in an electron test beam. The light concentrators almost doubled the number of registered photons. The number of registered photons per Cherenkov ring was 18 and 35, without and with the light concentrators, respectively. The errors in the observed number of detected photons were attributed to two main sources. The first source is the imperfect optical coupling of the light concentrators to the SiPMs. The second source are the multiple hits, introduced by the binary mode of operation.

The pion *vs.* kaon separation with SiPM array was 2σ above the minimal separation, 4σ, and almost 4σ above it with the light concentrators employed. However, the major drawback of SiPMs for the use in $B-$factories is their radiation hardness. Neutron irradiation increases the dark count noise and SiPM loses the possibility of single photon counting. In Belle II, this would come after just one month of operation. A possible solution would be to lower the temperature by cooling, which would decrease the dark counts rate. Nevertheless, at present level of maturity, SiPM do not seem well suited for storage ring experiments. The detectors with low background radiation and/or experiments at cryogenic temperatures would clearly benefit by employing SiPMs.

Bibliography

[1] K. A. Olive *et al.* (Particle Data Group), "Review of Particle Physics", Chin. Phys. **C38**, 090001 (2014).

[2] T. D. Lee and C. N. Yang, "Question of Parity Conservation in Weak Interactions", Phys. Rev. **104**, 254 (1956).

[3] C. S. Wu *et al.*, "Experimental Test of Parity Conservation in Beta Decay", Phys. Rev. **105**, 1413 (1957).

[4] J. W. Cronin, J. H. Christenson, V. L. Fitch and R. Turlay, "Evidence for the 2π Decay of the K_2^0 Meson", Phys. Rev. Lett. **138**, 13 (1964).

[5] A. D. Sakharov, "Violation of CP Invariance, C Asymmetry, and Baryon Asymmetry of the Universe", Pisma Zh. Eksp. Teor. Fiz. **5**, 24 (1967).

[6] M. Kobayashi and T. Maskawa, "CP-violation in the Renormalizable Theory of Weak Interaction", Prog. Theor. Phys. **42**, 652 (1973).

[7] A. Abashian *et al.*, "The Belle detector", Nucl. Instr. and Meth. A **479**, 117 (2002).

[8] K. Abe *et al.*, "Measurement of ϕ_3 with Dalitz plot analysis of $B^{\pm} \to D^{(*)}K^{\pm}$ decay at Belle", Belle Report **0476** (2004).

[9] K. Abe *et al.*, "Observation of mixing-induced CP violation in the neutral B meson system", Physical Review D **66**, 032007 (2002).

[10] M. Starič *et al.*, "Evidence for $D^0 - \bar{D}^0$ Mixing", Phys. Rev. Lett. **98**, 211803 (2007).

[11] K. Abe *et al.*, *Letter of Intent for KEK Super B Factory* (KEK Report, 2004).

[12] T. Abe *et al.*, *Belle II Technical Design Report*, Tech. Rep. (KEK, 2010).

[13] A. J. Bevan, B. Golob, T. Mannel, S. Prell and B. D. Yabsley, eds., *The Physics of the B factories*, SLAC-PUB-15968, KEK preprint 2014-3 ed., Vol. C74 (Eur. Phys. J., 2014) p. 3026.

[14] J. N. Marx and D. R. Nygren, "The Time Projection Chamber", Physics Today **31**, 46 (1978).

[15] P. Čerenkov, "Visible Radiation Produced by Electrons Moving in a Medium with Velocities Exceeding that of Light", Phys. Rev. **52**, 378 (1937).

[16] C. Grupen, *Particle Detectors* (Cambridge University Press, 1996).

[17] J. V. Jelley, *Čerenkov Radiation and its applications* (Pergamon Press, 1958).

[18] T. Ypsilantis and J. Seguinot, "Theory of ring imaging Cherenkov counters", Nucl. Instr. and Meth. A **343**, 30 (1994).

[19] T. Matsumoto *et al.*, "Studies of proximity focusing RICH with an aerogel radiator using flat-panel multi-anode PMTs (Hamamatsu H8500)", Nucl. **521**, 367 (2004).

[20] T. Iijima *et al.*, "A novel type of proximity focusing RICH counter with multiple refractive index aerogel radiator", Nucl. Instr. and Meth. A **548**, 383 (2005).

[21] P. Križan, "Aerogel RICH", in *talk given at Super B Factory Workshop in Hawaii* (Honolulu, Hawaii, 2004).

[22] M. Tabata *et al.*, "Development of transparent silica aerogel over a wide range of densities", Nucl. Instr. and Meth. A **623**, 339 (2010).

[23] P. Križan, S. Korpar and T. Iijima, "Study of nonhomogeneous aerogel radiator in a proximity focusing RICH detector", Nucl. Instr. and Meth. A **565**, 457 (2006).

[24] M. Tabata, I. Adachi, Y. Hatakeyama, H. Kawai, T. Morita and K. Nishikawa, "Optical and Radiographical Characterisation of Silica Aerogel for Cherenkov Radiator", IEEE Trans. Nucl. Sc. **59**, 2506 (2012).

[25] D. E. Fields *et al.*, "Use of aerogel for imaging Cherenkov counters", Nucl. Instr. and Meth. A **349**, 431 (1994).

[26] I. Adachi *et al.*, "Study of a threshold Cherenkov counter based on silica aerogels with low refractive indices", Nucl. Instr. and Meth. A **355**, 390 (1995).

[27] T. Ypsilantis and J. Seguinot, "Particle identification for LHC-B: a dedicated collider B experiment at the LHC", Nucl. Instr. and Meth. A **368**, 229 (1995).

[28] Y. Sakemi, "Dual radiator RICH of HERMES for π, K, p identification", Nucl. Instr. and Meth. A **453**, 284 (2000).

[29] E. Aschenauer *et al.*, "Optical characterization of n=1.03 silica aerogel used as radiator in the RICH of HERMES", Nucl. Instr. and Meth. A **440**, 338 (2000).

[30] S. Agostinelli *et al.*, "Geant4 — a Simulation Toolkit", Nucl. Instr. and Meth. A **506**, 250 (2003).

[31] I. Adachi *et al.*, "Study of a 144 channel multi-anode hybrid avalanche photo-detector for the Belle II RICH counter", Nucl. Instr. and Meth. A **639**, 103 (2011).

[32] S. Korpar *et al.*, "A 144-channel HAPD for the Aerogel RICH at Belle II", Nucl. Instr. and Meth. A **766**, 145 (2014).

[33] S. Nishida *et al.*, "Development of a 144-channel Hybrid Avalanche Photo-Detector for Belle II ring-imaging Cherenkov counter with an aerogel radiator", Nucl. Instr. and Meth. A **787**, 59 (2015).

[34] S. Korpar *et al.*, "Status and perspectives of solid state photon detectors", Nucl. Instr. and Meth. A **639**, 88 (2011).

[35] P. Križan *et al.*, "Tests of Burle 85011 64-anode MCP PMT as a detector of Cherenkov photons", Nucl. Instr. and Meth. A **567**, 124 (2006).

[36] S. Korpar, P. Križan and R. Pestotnik, "Timing and cross-talk properties of BURLE multi-channel MCP PMTs", Proceedings of Science **PD07**, 021 (2007).

[37] R. Pestotnik *et al.*, "Silicon photomultiplier as a position sensitive detector of Cherenkov photons", Nucl. Instr. and Meth. A **581**, 457 (2007).

[38] S. Korpar *et al.*, "A module of silicon photo-multipliers for detection of Cherenkov radiation", Nucl. Instr. and Meth. A **613**, 195 (2010).

[39] Korpar, S. *et al.*, "Test of the Hamamatsu MPPC module S11834 as a RICH photon detector", Nucl. Instr. and Meth. A **766**, 107 (2014).

[40] E. Tahirović, S. Korpar, P. Križan and R. Pestotnik, "Characterization of the Hamamatsu MPPC S11834 as photon sensor for RICH", Nucl. Instr. and Meth. A **787**, 203 (2015).

[41] R. Pestotnik, Private communication.

[42] K. Kuroda, "Position sensitive photomultiplier", Nuclear Instruments and Methods in Physics Research **196**, 187 (1982).

[43] M. Salomon and S. Williams, "A multi-anode photomultiplier with position sensitivity", Nucl. Instr. and Meth. A **241**, 210 (1985).

[44] W. R. Leo, *Techniques for Nuclear and Particle Physics Experiments* (Springer-Verlag, 1994).

[45] D. Renker and E. Lorenz, "Advances in solid state photon detectors", JINST **4**, P04004 (2009).

[46] B. Aubert *et al.*, "The BABAR detector", Nucl. Instr. and Meth. A **479**, 1 (2002).

[47] K. Deiters *et al.*, "Properties of the most recent avalanche photodiodes for the CMS electromagnetic calorimeter", Nucl. Instr. and Meth. A **442**, 193 (2000).

[48] M. A. Green and M. J. Keevers, "Optical properties of intrinsic silicon at 300 K", Progress in Photovoltaics: Research and Applications **3**, 189 (1995).

[49] W. G. Oldham *et al.*, "Triggering phenomena in avalanche diodes", IEEE Transactions on Electron Devices **19**, 1056 (1972).

[50] S. S. D. Hamamatsu Photonics K.K., "MPPC S12572-025, -050, -100C/P" (2013), technical data.

[51] N. Dinu *et al.*, "Electro-optical characterization of SiPM: A comparative study", Nucl. Instr. and Meth. A **610**, 423 (2009).

[52] M. Danilov, "Scintillator tile hadron calorimeter with novel SiPM readout", Nucl. Instr. and Meth. A **581**, 451 (2007).

[53] Y. Kudenko, "The near neutrino detector for the T2K experiment", Nucl. Instr. and Meth. A **598**, 289 (2009).

[54] T. Aushev *et al.*, "A scintillator based endcap K_L and muon detector for the Belle II experiment", Nucl. Instr. and Meth. A **789**, 134 (2015).

[55] A. T. Fienberg *et al.*, "Studies of an array PbF_2 Cherenkov crystals with large-area SiPM readout", Nucl. Instr. and Meth. A **783**, 12 (2015).

[56] N. Dinu *et al.*, "Studies of MPPC sensors down to cryogenic temperatures", Nucl. Instr. and Meth. A **787**, 275 (2015).

[57] A. Lacaita *et al.*, "On the brehmsstrahlung origin of hot-carrier-induced photons in silicon devices", IEEE Trans. on Electron Devices **40**, 577 (1993).

[58] I. Nakamura, "Radiation damage of pixelated photon detector by neutron irradiation", Nucl. Instr. and Meth. A **610**, 110 (2009).

[59] Y. Sudo, "Study of the Multi Pixel Photon Counter for the ILC Scintillator-Strip Calorimeter", Proceedings of Science **PD09**, 005 (2009).

[60] M. Angelone *et al.*, "Silicon photo-multiplier radiation hardness tests with a beam controlled neutron source", Nucl. Instr. and Meth. A **623**, 921 (2010).

[61] S. Shiizuka *et al.*, "Study of 144-channel hybrid avalanche photo-detector for Belle II RICH counter", Nucl. Instr. and Meth. A **628**, 315 (2011).

[62] S. Korpar *et al.*, "Measurement of Cherenkov photons with silicon photomultipliers", Nucl. Instr. and Meth. A **594**, 13 (2008).

[63] S. S. D. Hamamatsu Photonics K.K., "MPPC Product Catalogue" (2010).

[64] R. Dolenec *et al.*, "Test of silicon photomultiplier module for detection of Cherenkov photons", Nucl. Instr. and Meth. A **628**, 398 (2011).

[65] R. Pestotnik *et al.*, "Module of silicon photomultipliers as a detector of individual Cherenkov photons", Nucl. Instr. and Meth. A **639**, 99 (2011).

[66] S. Korpar *et al.*, "Measurement of Cherenkov photons by SiPMs with light guides", Nucl. Instr. and Meth. A **610**, 427 (2010).

[67] D. Broemmelsiek, "HERA-B RICH light collection system", Nucl. Instr. and Meth. A **433**, 136 (1999).

[68] S. S. D. Hamamatsu Photonics K.K., "Discrete MPPC array S11834-3388DF" (2012), product information.

[69] R. Brun and F. Rademakers, "ROOT - An Object Oriented Data Analysis Framework", in *Proceedings AIHENP'96 Workshop, Lausanne*, Vol. 389 (Nucl. Instr. and Meth. A, 1996) pp. 81–86.

[70] I. Optics, "BK7 Schott Glass", Specifications (2012).

[71] M. Zgubič, "Silicon PhotoMultiplier Tests" (2013), IJS internal, Unpublished.

[72] Newcomer, F. M. *et al.*, "A Fast, Low Power, Amplifier-Shaper-Discriminator for High Rate Straw Tracking Systems", IEEE Trans. Nucl. Sc. **40**, 630 (1993).

[73] J. Arino *et al.*, "The HERA-B ring imaging Cherenkov counter", Nucl. Instr. and Meth. A **516**, 445 (2004).

[74] J. Arino *et al.*, "Using ASD8 as readout of multianode photomultipliers for single photoelectron discrimination in the HERA-B RICH detector", Nucl. Instr. and Meth. A **457**, 627 (2001).

[75] K. Berkhan, H. Kolanoski, M. Pohl, U. Uwer and S. Vassiliev, "Large-system Experience with the ASD-8 Chip in the HERA-B Experiment", in *Fifth Workshop on Electronics for LHC Experiments, Snowmass, USA* (1999).

[76] V. Puill *et al.*, "Single photoelectron timing resolution of SiPM as a function of the bias voltage, the wavelength and the temperature", Nucl. Instr. and Meth. A **695**, 354 (2012).

[77] T. Murase *et al.*, "Development of PPD: characterization and simulation", Proceedings of Science **PD09**, 003 (2009).

[78] Y. Musienko, "Advances in multipixel Geiger-mode Avalanche photodiodes (silicon photomultipliers)", Nucl. Instr. and Meth. A **598**, 213 (2009).

[79] Y. Musienko *et al.*, "The gain, photon detection efficiency and excess noise factor of multi-pixel Geiger-mode avalanche photodiodes", Nucl. Instr. and Meth. A **567**, 57 (2006).

[80] M. Starič, *Razvoj nabojnega signala pri večžičnih proporcionalnih komorah*, Master's thesis, Univerza Edvarda Kardelja v Ljubljani (1988).

[81] M. Starič, *Razvoj, izdelava in preizkus prototipa aparature za pozitronsko tomografijo*, Ph.D. thesis, Univerza v Ljubljani (1992).

[82] S. Korpar, *Razvoj, izdelava in preizkus detektorja Čerenkovih obročev*, Ph.D. thesis, Univerza v Ljubljani, Fakulteta za matematiko in fiziko (1997).

[83] P. Križan *et al.*, "Proximity focusing RICH with flat panel PMT as photon detector and aerogel as radiator", Nucl. Instr. and Meth. A **553**, 58 (2005).

[84] M. Polyanskiy, "Refractive index database" (2014).

Appendix A

Photon Detector Channel Positions

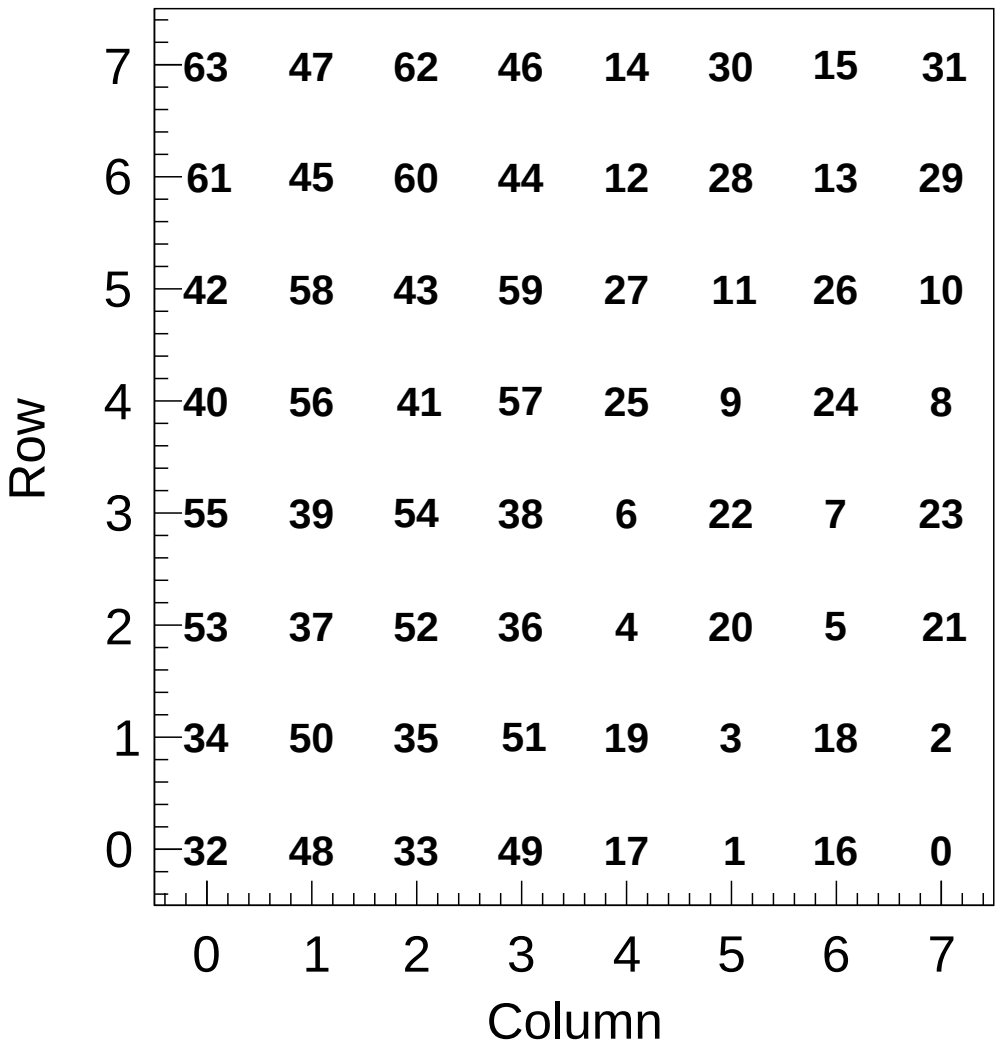

Figure A.1: SiPM positions in laboratory set-up given as a row and a column in the 8×8 array. The numbers correspond to TDC channels.

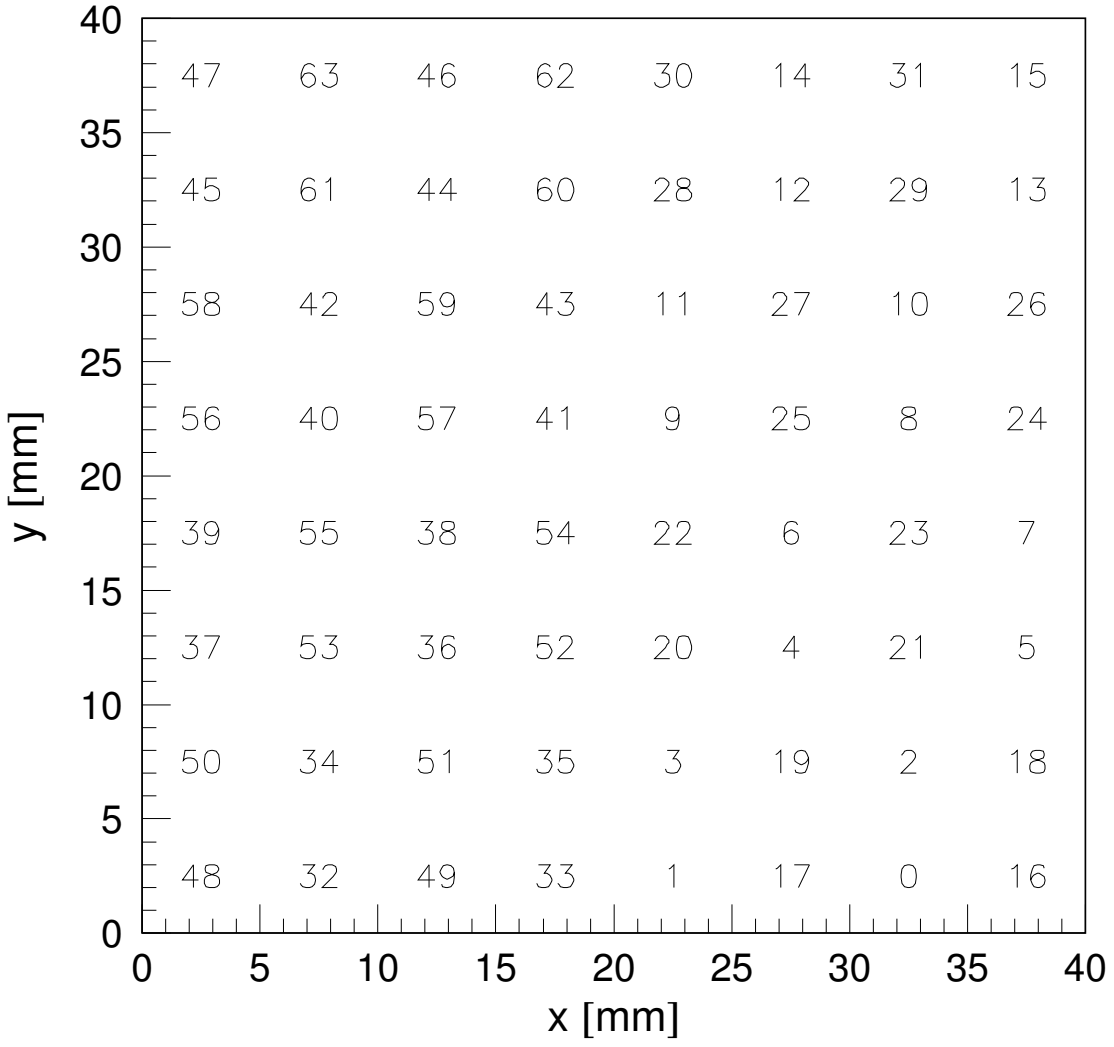

Figure A.2: SiPM positions in beam test set-up. The positions are given in local coordinate system of photon module. The numbers correspond to TDC channels.

Appendix B

Run Log in Beam Test

Run	No. of events	Module position	Aerogel set-up	Run type
1-8				Junk
9	50k	1	a1	$V_{bias} = 73.2$ V
10	100k	1	a1	$p = 4$ GeV, $V_{bias} = 73.2$ V
11	100k	1	a1	73.4V
12	100k	1	a1	72.8V
13	100k	1	a1	72.6V
14	100k	1	a1	72.4V
15	100k	1	a1	72.2V
16	100k	1	a1	72.0V
17	100k	1	a1	71.8V
18	100k	1	a1	73.0V
19	100k	1	a1	ASD V_{thr}=1.4 V
20	100k	1	a1	lead collimator 9x9 mm
21	200k	1	a1	$p = 5$ GeV
22	200k	2	a1	no bias
23	200k	2	a1	$V_{bias} = 73.0$ V, $V_{thr} = 1.4$ V
24	200k	2	a1	$V_thr = 1.5$ V
25	200k	2	a1	1.6V
26	200k	2	a1	1.7V
27	200k	2	a1	1.3V

28	200k	2	a1	1.2V
29	200k	2	a1	1.1V
30	200k	2	a1	1.0V
31	200k	2	a1	0.9V
32	200k	2	a1	V_thr = 1.5V, V_{bias} = 71.8V
33	200k	2	a1	V_{bias} = 72.0 V
34	200k	2	a1	72.2V
35	200k	2	a1	72.4V
36	200k	2	a1	72.6V
37	200k	2	a1	72.8V
38	200k	2	a1	73.0V
39	200k	2	a1	73.2V
40	200k	2	a1	73.4V
41	200k	3	a1	V_{bias} = 73.0 V, V_{thr}=1.5 V
42	500k	3b	a1+a2	wo LG
43	500k	3a	a1+a2	wo LG
44	500k	4a	a1+a2	wo LG
45	500k	5a	a1+a2	wo LG
46	500k	2a	a1+a2	wo LG
47	500k	3a	a1+a2	LG
48	500k	3b	a1+a2	LG
49	500k	4b	a1+a2	LG
50	500k	5b	a1+a2	LG
51	50k	2b	a1+a2	LG
52	1M	2b	a1+a2	LG
53	500k	6	a1+a2	LG

Table B.1: Run log. Prototype RICH in T24 electron test beam at DESY (Germany), from 24th to 27th September 2013. Aerogel characteristics are given in the Table 5.1.

Appendix C

Bias and Threshold Scans

Run	V_{bias} [V]	θ [mrad]	σ [mrad]	N_{signal}	N_{bkg}
32	71.8	0	0	0	0
33	72.0	305.0	12.04	0.016	0.005
34	72.2	306.1	12.17	0.281	0.082
35	72.4	305.7	12.47	0.654	0.167
36	72.6	305.5	12.59	0.809	0.197
37	72.8	305.5	12.57	0.952	0.265
38	73.0	305.6	12.45	1.002	0.324
39	73.2	305.6	12.54	1.152	0.412
40	73.4	305.9	12.70	1.263	0.525

Table C.1: Bias scan in electron test beam. The bias in the first run is too low to register any photons. In the following runs, the Cherenkov angle is correctly reconstructed and the number of detected photons rises, as expected.

Run	V_{thr} [V]	θ [mrad]	σ [mrad]	N_{signal}	N_{bkg}
31	0.9	306.3	13.84	1.244	0.545
30	1.0	306.2	13.54	1.222	0.449
29	1.1	305.9	13.17	1.206	0.358
28	1.2	306.2	13.24	1.179	0.354
27	1.3	306.0	13.14	1.175	0.322
23	1.4	306.0	13.06	1.168	0.299
24	1.5	305.5	13.10	1.159	0.268
25	1.6	305.4	13.23	1.126	0.240
26	1.7	307.8	11.83	0.195	0.078

Table C.2: ASD8 discriminator threshold scans in electron test beam. Raising the threshold, the signals with a lower amplitude stay under it and are not registered; (mainly electronics) noise stays under the threshold.

Appendix D

Number of Detected Photons

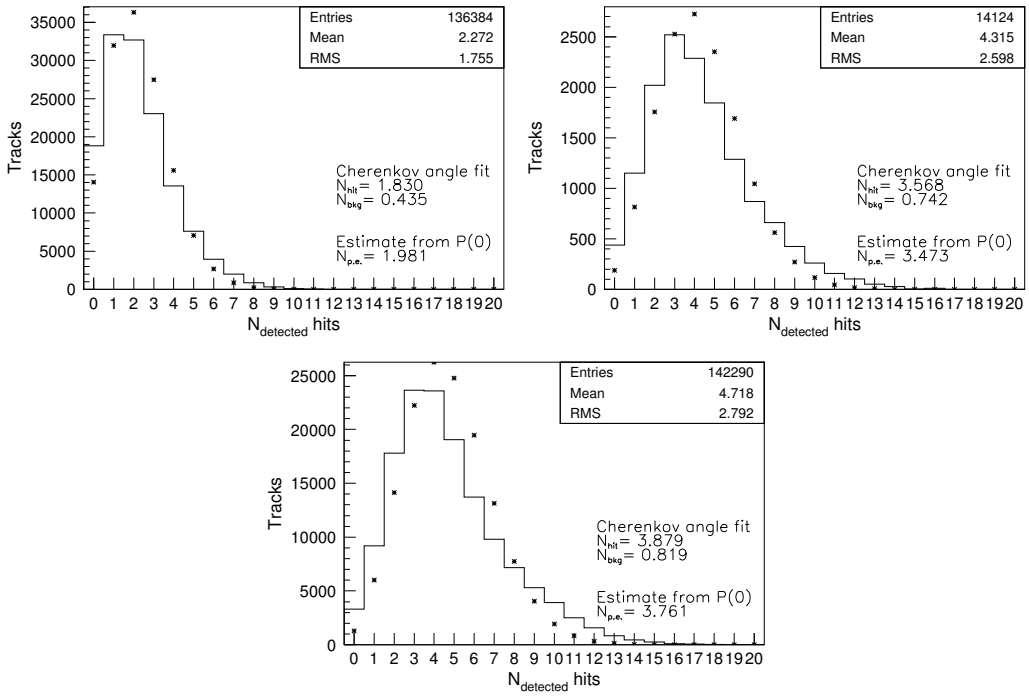

Figure D.1: Histogram of detected photons per track in run 46 (without light concentrators, top left), 52 (with light concentrators, top right) and 53 (with light concentrators, bottom).

Appendix E

Technical Drawings

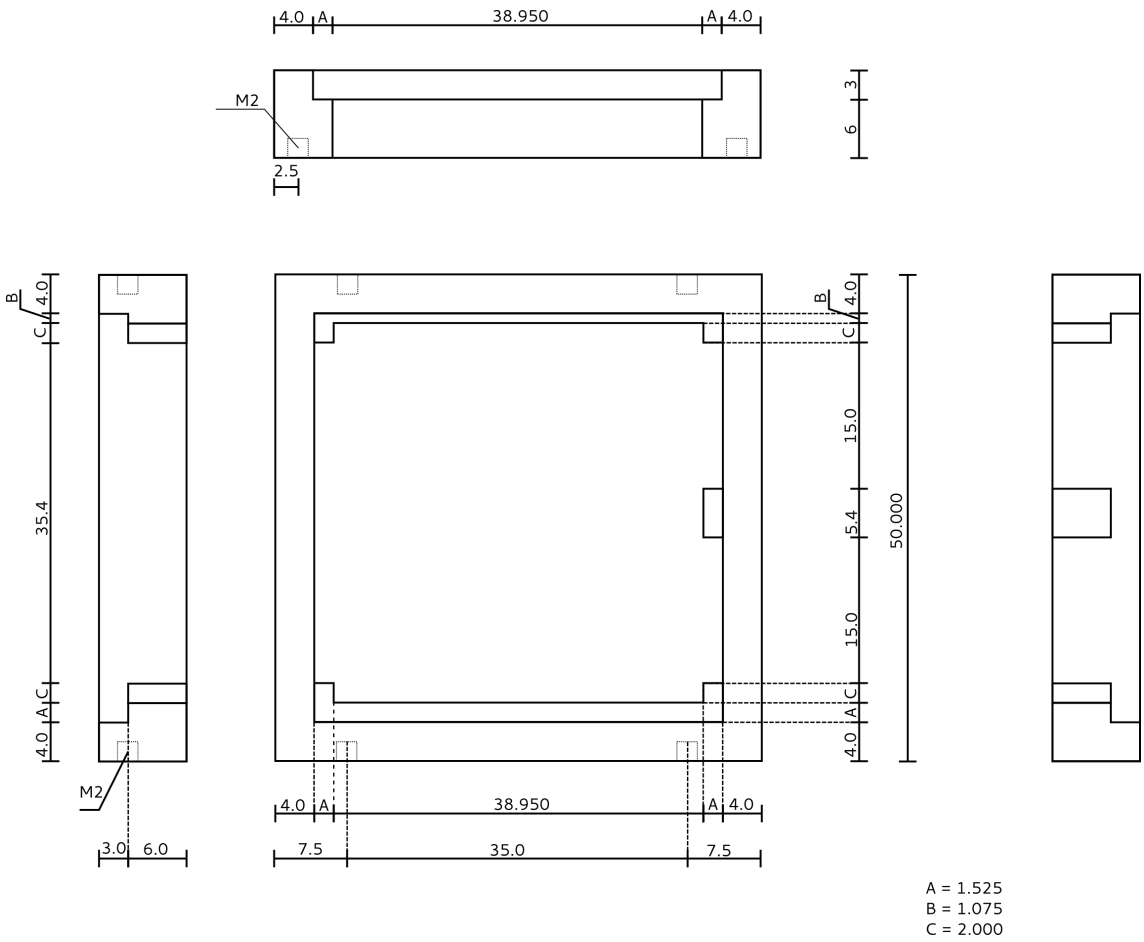

Figure E.1: Photon module support frame

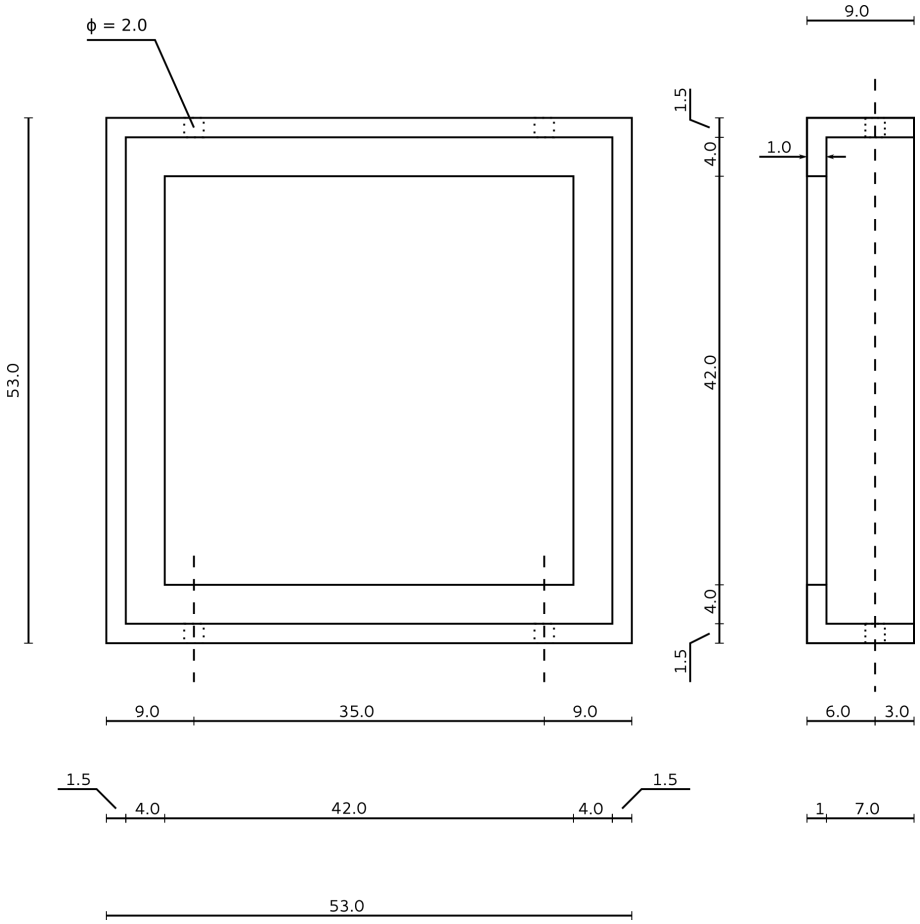

Figure E.2: Module frame cover (light concentrators).

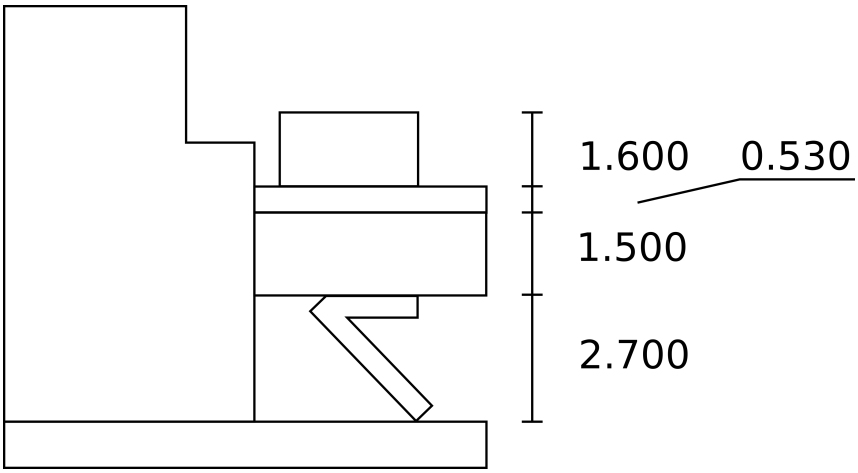

Figure E.3: Module frame section with MPPC only in the frame.

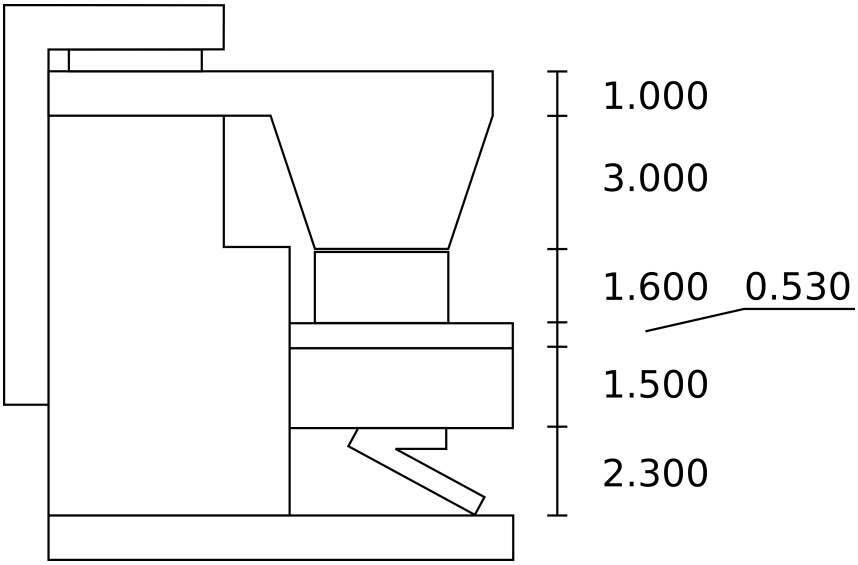

Figure E.4: Module frame section with MPPC and light concentrators in the frame.

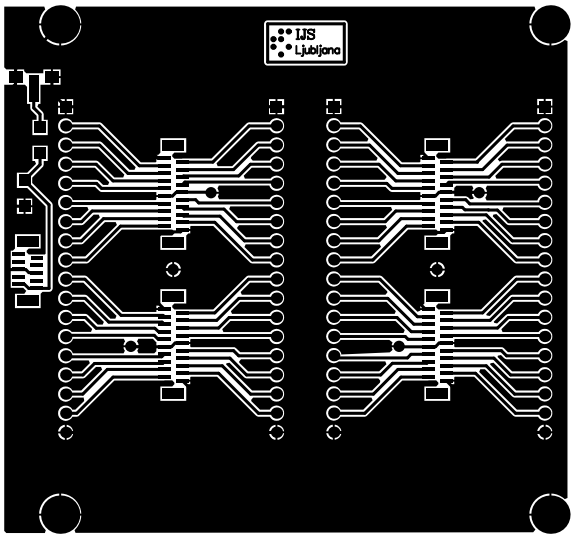

Figure E.5: Voltage supply interface board for one MPPC array (64 SiPMs, 4 ASD8 boards).

Razširjeni povzetek v slovenskem jeziku

Identifikacija osnovnih delcev igra ključno vlogo v številnih eksperimentih v fiziki visokih energij. Posebej v eksperimentih, ki so narejeni za preučevanje kršitve CP simetrije v razpadih B-mezonov, je identifikacija delcev zelo pomembna. V takšnih eksperimentih (tovarnah B-mezonov), imajo procesi, ki nas zanimajo, v končnih stanjih pogosto pione in kaone.

Predhodno delo foto-detektorske skupine na Institutu Jožef Stefan me je motiviralo za preizkus novega fotonskega detektorja v detektorju obročev Čerenkova (RICH). Vrednosti parametrov prototipa RICH-a so prevzete iz pod-detektorja ARICH, ki bo del bodočega spektrometra Belle II (Institut KEK, Japonska).

Za ločevanje med nabiti delci, je potrebno poznati maso m in naboj Z delca. Naboj se lahko določi iz predznaka ukrivljenosti tira delca v magnetnem polju. Masa je dana z formulo, ki povezuje gibalno količino in hitrost delca v:

$$p = \gamma m v,$$

kjer je γ Lorentzov faktor. Gibalna količina se lahko izračuna iz ukrivljenosti tira v magnetnem polju. Torej, edina neznana veličina je hitrost delca v. Za določanje hitrosti se lahko koristijo razne metode, kot je meritev energijske izgube delca v nekem materialu ali meritev časa preleta delca. Nobena od teh dveh metod ni primerna za meritev hitrosti delcev, katerih energija leži v razponu $1 - 4$ GeV, kar je ena od zahtev v spektrometru Belle II.

7.1 Identifikacija delcev z poddetekotorjem RICH

Ena od metod je tudi efekt sevanja Čerenkova, ki se uporablja v detektorjih obročev Čerenkova (RICH). Ko nabit delec prečka skozi medij (sevalec) z lomnim količnikom n, s hitrostjo večjo kot je fazna hitrost svetlobe c/n, sevalec izseva šibko svetlobo pod kotom Čerenkova θ, danim z:

$$\cos\theta = \frac{c}{v\, n}.$$

Ker je lomni količnik sevalca znan, se lahko kot Čerenkova uporabi za določanje hitrosti delca. Število fotonov izsevanih na interval valovne dolžine je dano z:

$$\frac{\mathrm{d}N}{\mathrm{d}\lambda} = 2\pi\alpha\, d\, \sin^2\theta\, \frac{1}{\lambda^2} \tag{7.1}$$

Število izsevanih fotonov je majhno (reda velikosti 10), zaradi česar mora biti fotonski senzor občutljiv na posamezne fotone. Fotoni so izsevani v stožcu ki postane

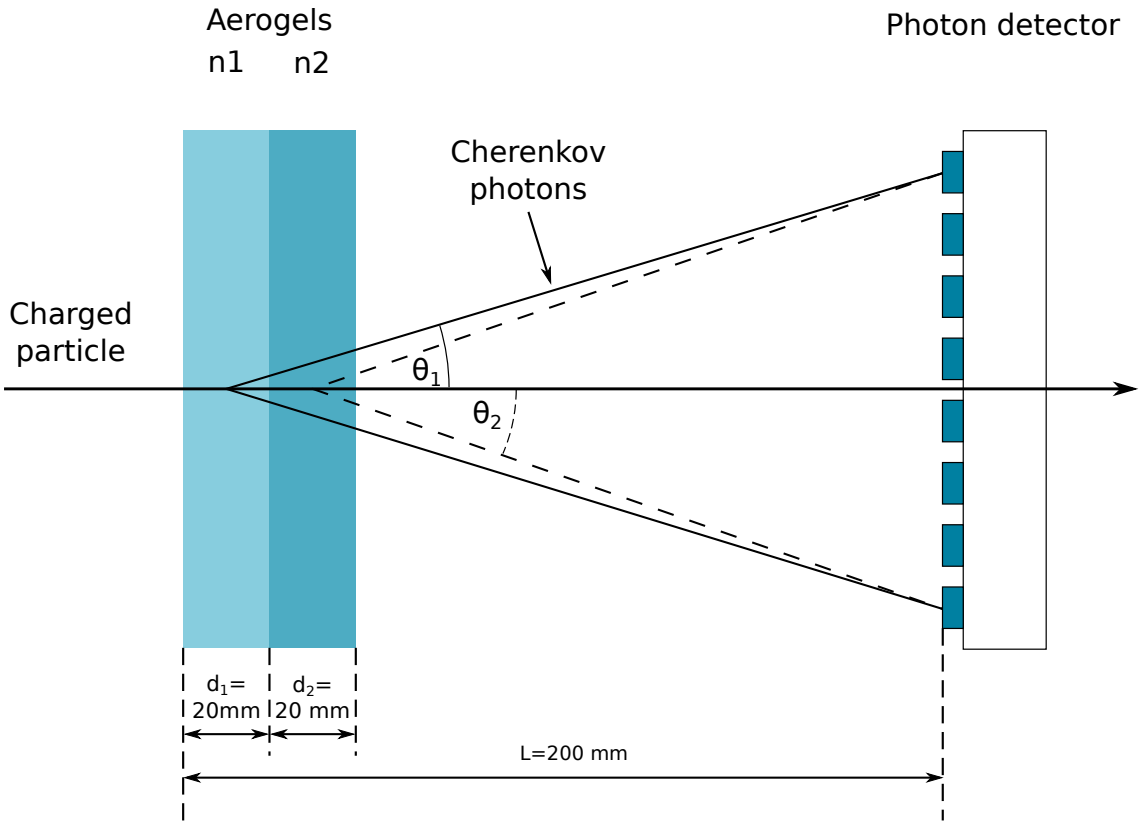

Slika 7.6: RICH z bližinskim fokusiranjem z nehomogenim radijatorjem iz aerogela.

obroč, ko je projiciran na površino fotonskega senzorja. To postavi drugi pogoj: prostorno ločljivost. Tretji pomembni pogoj je neobčutljivost na močno magnetno polje.

Skica detektorja RICH v Belle II je prikazana na Sl. 7.6. Z namenom detekcije čimvečjega števila fotonov, se uporablja nehomogen sevalec, iz dveh plasti aerogela, z bližinskim fokusiranjem (brez optičnega sistema za fokusiranje fotonov).

Princip ločevanja se vidi na Sl. 7.7, kjer je dan kot Čerenkova kot funkcija gibalne količine delca, za pione in kaone. V Belle II eksperimentu je zahtevano ločevanje, večje od 4σ, za pione in kaone z gibalno količino v razponu $p \in [1, 4]$ GeV/c. Ker je razlika kota med pioni in kaoni $\delta\theta = 23.5$ mrad, mora biti napaka na meritvi kota:

$$\sigma_\theta < \frac{23.5}{4} \text{ mrad} = 5.9 \text{ mrad}. \tag{7.2}$$

Napaka meritve se zmanjša z večjim številom detektiranih fotonov, N_{det}. Če je število zadetkov ozadja majhno, je napaka σ_{sled} dana kot napaka na srednji vrednosti posameznih fotonov σ_θ:

$$\sigma_{sled} = \frac{\sigma_\theta}{\sqrt{N_{det}}}. \tag{7.3}$$

Za osnovni detektor svetlobe v detektorju RICH je bila izbrana hibridna plazovna fotopomnoževalka (HAPD). Poleg dobrih lastnosti HAPD-jev, imajo te tudi nekatere pomanjkljivosti, kot je zmanjšanje izkoristka pri delovanju v magnetnem polju, visoka delovna napetost ($\approx$ 8 kV), ter visoka cena. To je bil razlog za testiranje novega tipa fotonskega senzorja, silicijeve fotopomnoževalke, kot senzorja za RICH. Kot alternativni senzor v RICH-u je bila preučevana tudi mikro-kanalna

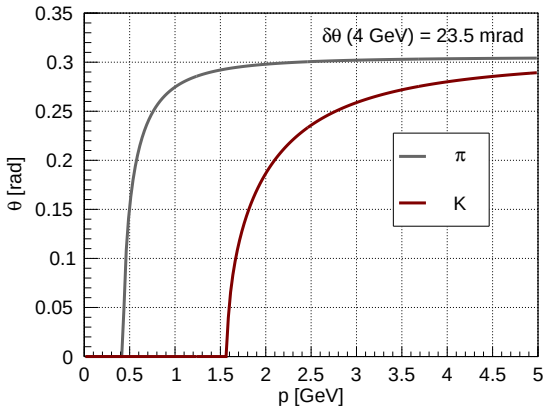

Slika 7.7: Kot Čerenkova v aerogelu z lomnim količnikom $n = 1.0485$ kot funkcija tipa delca ter gibalne količine. Razlika kotov pri 4 GeV (zgornja kinematska meja za Belle II) je $\delta\theta = 23.5$ mrad.

plošča (MCP PMT), vendar je bila zavrnjena zaradi hitrega zmanjšanja izkoristka detekcije fotonov.

7.2 Silicijeva fotopomnoževalka kot senzor posameznih fotonov

Silicijeva fotopomnoževalka (SiPM) je polprevodniški fotonski detektor, občutljiv na posamezne fotone. V osnovi je to silicijeva foto-dioda, ki deluje v Geigerjevem režimu. Silicijev substrat je razdeljen na posamezne celice, ki so med seboj električno izolirane (Sl. 7.8), priklopljene na inverzno napetost in vzdrževane v kritičnem stanju nad plazovno napetostjo. Foton, ki pride znotraj silikona se konvertira v par elektron-vrzel (Einsteinov efekt) ki potem sproži plaz v celici. Veliko število celic je vezano paralelno, in tvorijo en kanal. Število parov v plazu, sproženih z enim začetnim fotonom, se imenuje pomnoževalni faktor. Pomnoževalni faktor je funkcija delovne napetosti in velikosti celice, tipično je reda velikosti 10^6.

Zmogljivost SiPM-ja je karakterizirana z izkoristkom detekcije fotonov (PDE), ki vsebuje kvantni izkoristek QE, verjetnost za plaz ter geometrijski izkoristek celične strukture. Odvisnost PDE-ja od valovne dolžine fotona za Hamamatsujev SiPM je dana na Sl. 7.9, skupaj s številom izsevanih fotonov v aerogelu ($n = 1.0485$, $d = 19.4$ mm, $\Lambda = 44.0$ mm) na interval valovne dolžine (enačba 7.1), ter verjetnostjo za prehod skozi aerogel brez sipanja. Za primerjavo z drugimi fotonskimi detektorji, so podani tudi QE HAPD-ja ter MCP PMT-ja.

V primerjavi z HAPD, SiPM izkaže naslednje prednosti:

1. Je popolno neobčutljiv na magnetno polje (testirano do 7 T),
2. Ima večji PDE pri nižji delovni napetosti,
3. Je bolj občutljiv na modro svetlobo,
4. Je kompakten in robusten,
5. Ima nižjo ceno za velike količine.

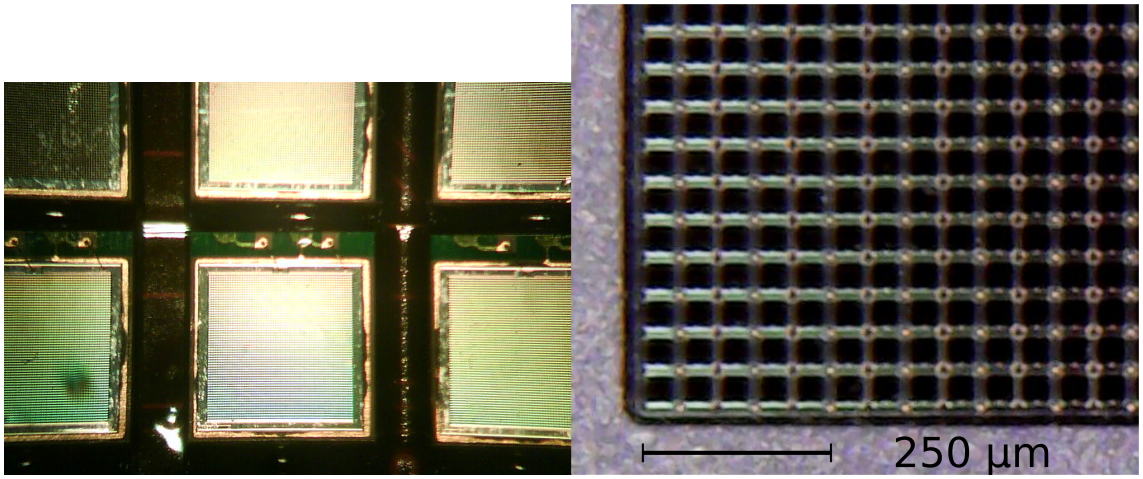

Slika 7.8: Levo: Fotografija enega SiPM-ja (povečanje 2×) v matriki iz 64 SiPM-ov Hamamatsu MPPC S11834. En SiPM ima $60 \times 60 = 3600$ celic paralelno električno povezanih. Desno: Fotografija posameznih celic znotraj SiPM-ja (povečanje 100×), ki so oddaljene med seboj za 50 μm.

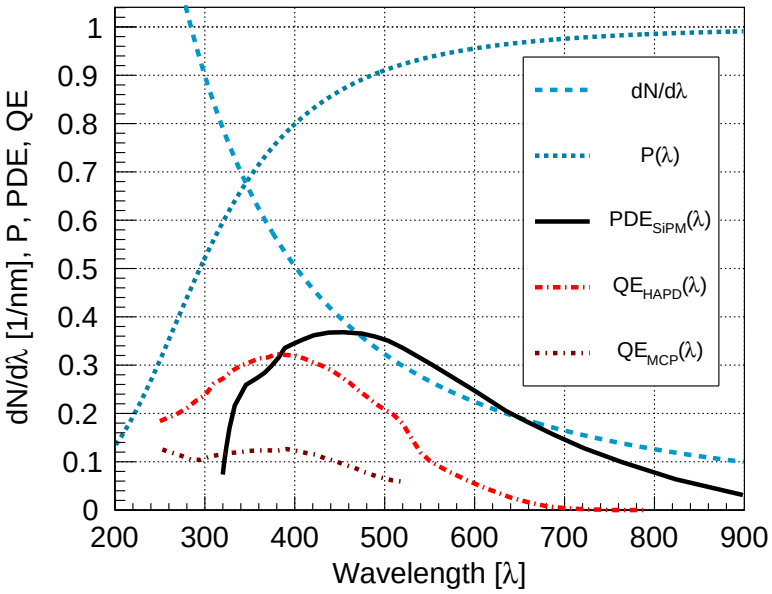

Slika 7.9: Število izsevanih fotonov na interval valovne dolžine, srednja verjetnost, da foton pride izven aerogela brez sipanja P, PDE SiPM na nominalni delovni napetosti. Za primerjavo so prikazani še QE HAPD-ja in MCP PMT-ja.

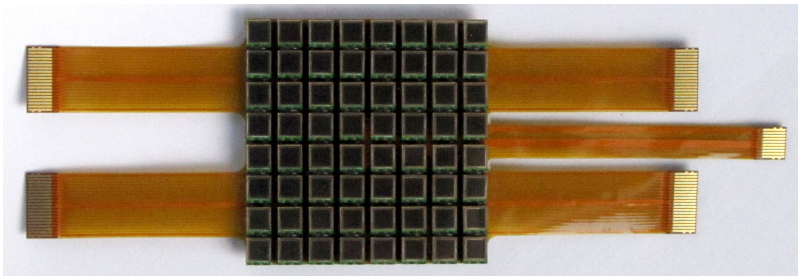

Slika 7.10: Fotografija matrike 64 SiPM-ov Hamamatsu MPPC S11834-3388DF.

Komercialni SiPM-ji imajo širino $1-4$ mm, kar pomeni da se pozicijska ločljivost ujema z HAPD-ji.

Izziv, ki ga postavi SiPM kot detektor posameznih fotonov, je visok nivo šuma. Termično vzbujeni pari elektron-vrzel, povzročijo signal podoben signalu enega fotona, tudi če ni prisotnih fotonov. Takšen signal se, podobno kot za klasične fotopomnoževalke, imenuje temni sunek. Temnih sunkov v SiPM-jih je tipično $100-1000$ kHz/mm^2. Zvišajo se z delovno napetostjo in z temperaturo. Metoda, ki je bila uporabljena za znižanje šuma v primeru RICH, bo razložena v nadaljevanju.

7.3 Fotonski modul

Prototip fotonskega modula je bil narejen s Hamamatsujevo matriko iz 64 SiPM-jev (Sl.7.10). Vsak SiPM ima aktivno površino 3×3 mm^2. Pomembne lastnosti matrike so dane v Tabeli 7.1.

Geometrijski izkoristek matrike $\varepsilon_{\text{array}}$ je relativno majhen:

$$\begin{aligned} \varepsilon_{\text{array}} &= \left(\frac{a}{b}\right)^2 \\ &= \left(\frac{3}{5}\right)^2 = 0.36, \end{aligned} \tag{7.4}$$

a je širina enega SiPM-ja in b razdalja med SiPM-ji (*cf.* Tabelo7.1). Z namenom zvišanja izkoristka, je bila uporabljena matrika zbiralcev svetlobe.

Zbiralniki svetlobe so narejeni kot piramide iz borosilikatnega stekla. Za dimenzije piramid je bila uporabljena simulacija sledenja žarkom. Piramida s simularinim žarkom je prikazana na Sl.7.11, levo. Za določanje širine izstopnega okna a in višine piramide d, so bili žarki razporejeni znotraj kota $\theta \in [0°, 30°]$, enakomerno po kosinusu kota θ. Izkoristek kot funkcija širine in višine je prikazan na Sl. 7.11, desno. Izbrane dimenzije za proizvodnjo so bile $a = 3$mm in $d = 3$mm. Pri teh dimenzijah naj bi bil izkoristek za žarke, ki so razporejeni enakomerno znotraj kota $\theta \in [0°, 30°]$, $\varepsilon_{acc} \approx 90\%$. Izkoristek kot funkcija mejnega kota θ je dan na Sl. 7.12.

Fotonski modul, prikazan na Sl. 7.13, je sestavljen iz aluminijskega okvirja, v katerem je MPPC matrika, spredaj so pritrjeni zbiralniki, zadaj pa čitalna elektronika. Za izboljšanje optičnega stika med zaščitnim slojem iz epoksi smole na SiPM-jih (lomni količnik $n_{epoxy} = 1.55$) in zbiralniki svetlobe, je bila uporabljena optična mast ($n_{grease} = 1.46$).

Signali iz 64 SiPM so bili ojačani z elektroniko ASD8-B, zasnovano na ASD-8 čipih. ASD8 čipi zadoščajo večino kriterijev za RICH: veliko ojačanje (2.5 mV/fC),

Parametar	Vrednost
Število kanalov	64
Širina kanala, a	3 mm
Razdalja med kanali, b	5 mm
Efektivna fotosenzitivna površina na kanal, A	3×3 mm^2
Razdalja med celicami	50 μm
Število celic na kanal	3600
Geometrijski izkoristek, ε_{fill}	61.5%
Razpon spektralnega odziva	320 to 900 nm
Valovna dolžina vrha občutljivosti, λ_{peak}	440 nm
Priporočena delovna napetost, V_{bias}	70±10 V
Učinkovitost zaznavanja fotonov, PDE	50%
Temni tok na kanal, I_d	Max. 3 μA
Kapacitivnost na kanal, C_{tot}	320 pF
Temperaturni koeficient delovne napetosti, $(\mathrm{d}\,A/\mathrm{d}\,T)$	56 mV/°C
Pomnoževalni faktor, G	7.5×10^5

Tabela 7.1: Lastnosti matrike MPPC S11834.

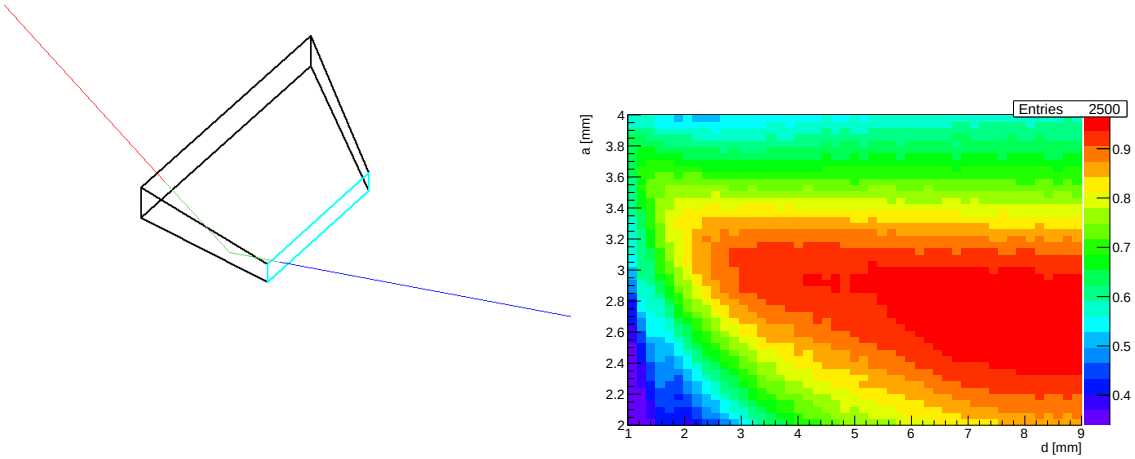

Slika 7.11: Levo: Simulacija sledenja žarkom skozi zbiralnik svetlobe z enim prikazanim žarkom. Simulirani žarek preden zadene zbiralnik je rdeče, v zbiralniku zelene, ter po prelomu na bočnih straneh ali izstopnem oknu modre barve. Desno: Izkoristek kot funkcija širine izstopnega okna a in višine piramide d.

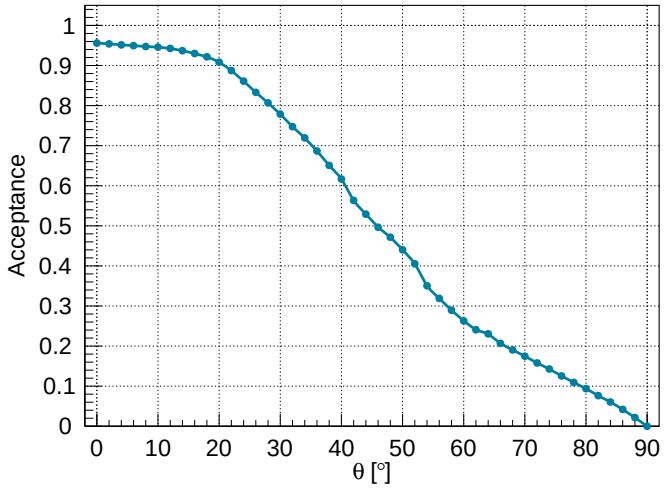

Slika 7.12: Izkoristek kot funkcija polarnega kota θ.

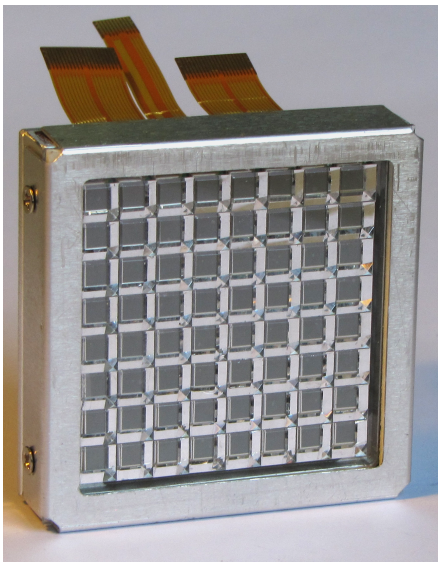

Slika 7.13: Prototip detektorskega modula: MPPC matrika in zbiralniki svetlobe sestavljeni skupaj v aluminijskem okvirju.

kratek meritveni čas (5 ns) in dobro resolucijo med dvema pulzoma (20 ns). Digitalni signali iz ASD-8 so bili priklopljeni na časovno-digitalni konverter (TDC). V laboratorijskih testih je bil signal laserja uporabljen kot skupni STOP signal, v testnem žarku pa je bil to signal iz scintilatorja. Časovna razlika med posamezni signali in STOP signalom je bila shranjena v datoteko na računalniku za kasnejšo analizo.

V laboratorijskih testih je bil raziskan odziv senzorja na šibke pulze svetlobe. Na Sl. 7.14 je prikazana porazdelitev integriranega naboja. Prag za diskriminacijo signala je bil nameščen nizko (0.5V) na zgornji sliki, zaradi česar so vidni tudi signali šuma (0 foto-elektronov). Jasno se vidijo vrhovi, ki nastanejo ko je sprožena ena, dve in več celic v SiPM-u. Na spodnji sliki je prag za diskriminacijo postavljen višje, 1.5V, tako kot v testnem žarku. Vidi se, da takšen prag odgovarja približno polovici razdalje med signalom proženim pri enem in nič fotonov.

S pomočjo računalniško vodenih pomičnih mizic se je žarek laserske svetlobe lahko premikal po površini senzorja. Z laserskim snopom fokusiranim na 5 μm postane vidna celična struktura posameznega SiPM-ja, kot je razvidno iz Sl. 7.15.

Odziv enega SiPM-ja, sestavljenega z zbiralnikom svetlobe je dana na Sl. 7.16. Laserski snop je bil fokusiran na $\sigma = 50$ μm. Lahko se vidi, da je odziv enakomeren po celi površini zbiralnika svetlobe $5 \times 5\text{mm}^2$.

Prototip fotonskega modula je bil preizkušen v testnem žarku z elektroni Instituta DESY (Sl. 7.17). Visoko energetski elektroni ($p = 5$ GeV/c) so prečkali skozi sevalec, ki je izseval fotone Čerenkova. Ti so bili zaznani z fotonskim modulom. Za sledenje tira elektronov je bil uporabljen teleskop iz dveh večžičnih proporcionalnih komor (MWPC).

Signali iz SiPM-ov so prožili časovno-digitalni pretvornik, pri tem je zakasnjen signal iz scintilatorja služil kot skupni STOP signal. Časovna porazdelitev signalov v primeru meritev brez in z zbiralniki svetlobe, je prikazana na Sl.7.18. S pomočjo ozkega časovnega okna (6 ns, prikazan z navpičnimi črticami na histogramu), je večina ozadja lahko odstranjena.

Za določanje delovne napetosti SiPM-ov ter napetosti digitalnega diskriminatorja so bile najprej opravljene kalibracijske meritve. Število detektiranih fotonov, skupaj s številom fotonov ozadja, kot funkcija delovne napetosti pri konstantnemu pragu diskriminatorja (1.5 V), so prikazani na Sl. 7.19, levo. Lahko se vidi, da se z višanjem delovne napetosti, zviša število detektiranih fotonov. Število zadetkov ozadja se tudi zviša. Graf na Sl. 7.19, desno, prikazuje število detektiranih fotonov kot funkcijo praga diskriminatorja, pri konstantni delovni napetosti (73.0 V). Z zvišanjem praga diskriminacije, je zaznano vedno manj elektronskega šuma. Ko je prag diskriminacije blizu zgornje meje, se diskriminator izklopi, in ni več zaznanih signalov. Na osnovi meritev sta bila izbrana delovna napetost (73.0 V) in prag diskriminacije (1.5 V).

Povprečno število detektiranih fotonov je bilo izračunano na naslednji način. Iz podatka o tiru elektrona in koordinate zadetega kanala fotonskega senzorja, je bil izračunan izsevani kot Čerenkova. Pri tem je bil upoštevan lom svetlobe na izhodu iz aerogela, na vhodu v SiPM, ter na vhodu v zbiralnik svetlobe, če je ta bil uporabljen. Histogram rekonstruiranega kota Čerenkova za več akumuliranih dogodkov, je prikazan na Sl.7.20, levo. Iz rezultatov prilagajanja z Gausovo funkcijo je izračunano povprečno število detektiranih fotonov na elektron. Za prilagajanje ozadja je bil uporabljen polinom druge stopnje. Ozadje ni enakomerno zaradi omejenega geometrijskega izkoristka enega modula v smeri ϕ, kar je razvidno iz grafa zadetkov v prostoru Čerenkova (desna stran). En modul je pokril približno 0.11

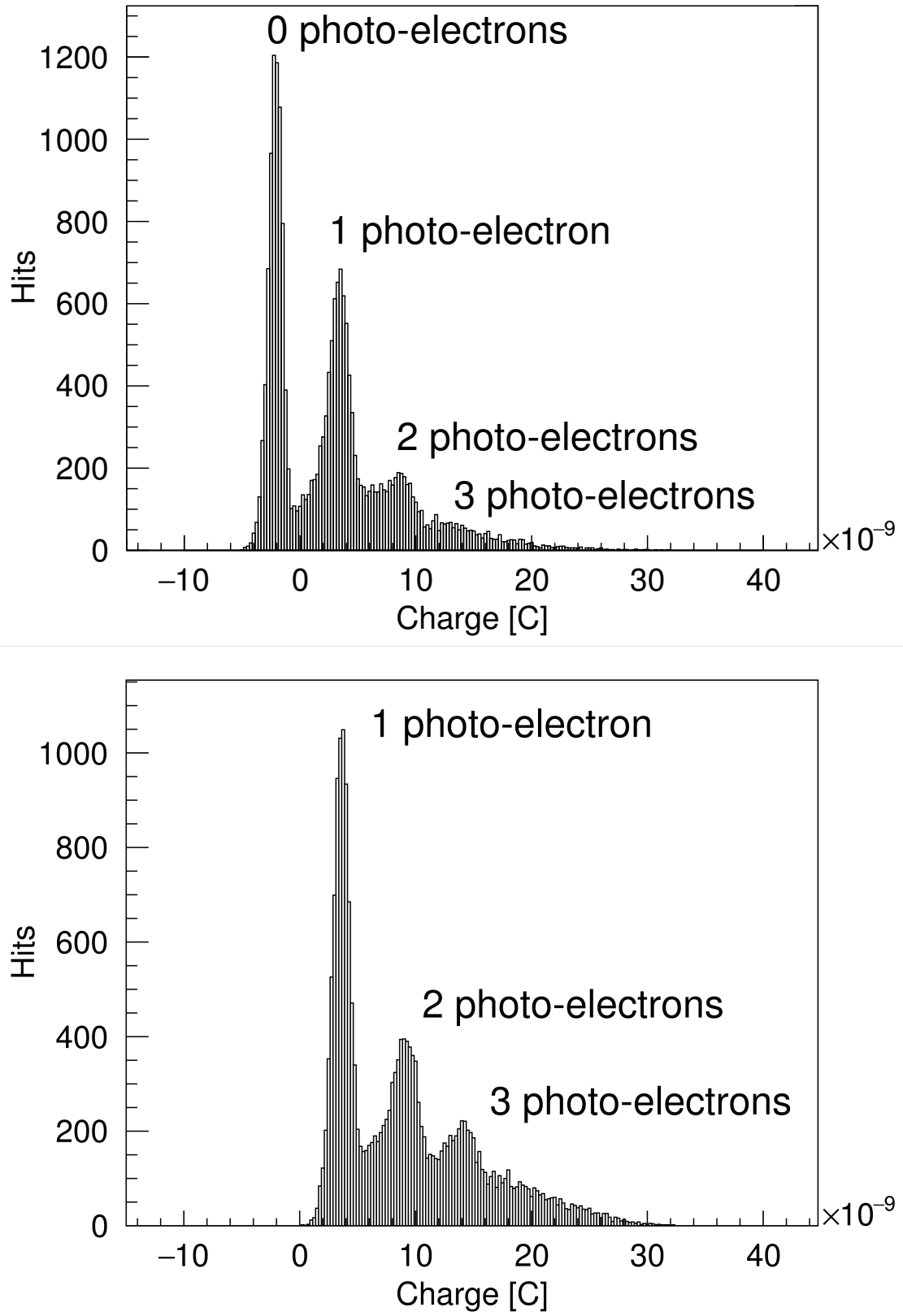

Slika 7.14: Porazdelitev integriranega naboja iz analognega izhoda, SiPM št. 1. Za proženje osciloskopa je uporabljen signal iz digitalnega izhoda ASD8. Prag diskriminatorja je nastavljen na 0.5 V (zgoraj) in 1.5 V (spodaj). Vidi se, da nastavitev 1.5 V na diskriminatorju pomeni proženje približno na polovici med 0 in 1 fotonskim vrhom, kar ustreza amplitudi ≈ 0.5 fotoelektrona.

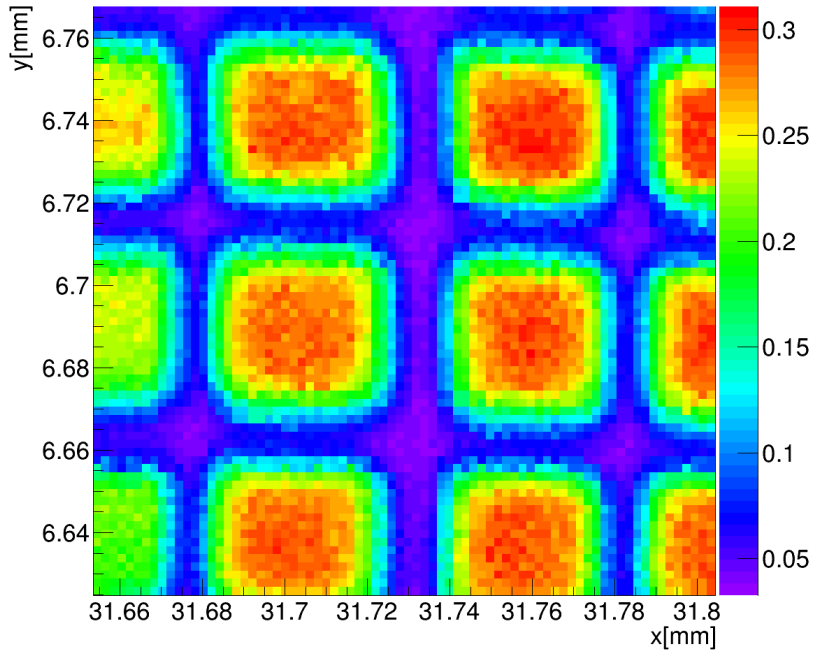

Slika 7.15: Povprečno število detektiranih fotonov v nekaj celicah znotraj SiPM-a 18.

Aerogel	Lomni kol.	Debelina [mm]	Aten. dolžina Λ [mm]	Prič. θ_C [mrad]
1 (upstream)	1.0485	19.4	44.0	305.344
2 (downstream)	1.0619	20.2	54.8	343.124

Tabela 7.2: Tabela z karakteristikami aerogelov, uporabljenih v testnem žarku.

obsega obroča. Na grafu je narisan tudi krog z radijem, enakim pričakovanemu kotu Čerenkova za en aerogel.

V meritvah izkoristka zbiralnikov svetlobe sta bila uporabljena dva aerogela, velikosti 100×100 mm v $x-y$ smeri. Debelina v z-smeri, skupaj z lomnim količnikom ter atenuacijsko dolžino, so dani v Tabeli 7.2.

Število pričakovanih fotonov (na interval valovne dolžine) v prvem in drugem aerogelu se lahko izračuna iz enačbe 7.1, z upoštevanjem Rayleighevega sipanja v aerogelih $P_{1,2}$, izkoristka zbiralnega sistema $\varepsilon_{geo} = 0.90$, ter občutljivosti detektorja S, enakega PDE-ju v primeru SiPM-a:

$$\frac{\mathrm{d}N_{exp,1}}{\mathrm{d}\lambda} = N_0 \sin^2\theta_1 \, \Lambda_1(\lambda) \, \cos\theta_1 \left[1 - e^{-d_1/\Lambda_1(\lambda)\cos(\theta_1)}\right] e^{-d_2/\Lambda_2(\lambda)\cos(\theta_1)} \varepsilon_{\mathrm{geo}} \, S(\lambda) \, \frac{1}{\lambda^2}, \tag{7.5a}$$

$$\frac{\mathrm{d}N_{exp,2}}{\mathrm{d}\lambda} = N_0 \sin^2\theta_2 \, \Lambda_2(\lambda) \, \cos\theta_2 \left[1 - e^{-d_2/\Lambda_2(\lambda)\cos(\theta_2)}\right] \varepsilon_{\mathrm{geo}} \, S(\lambda) \, \frac{1}{\lambda^2}, \tag{7.5b}$$

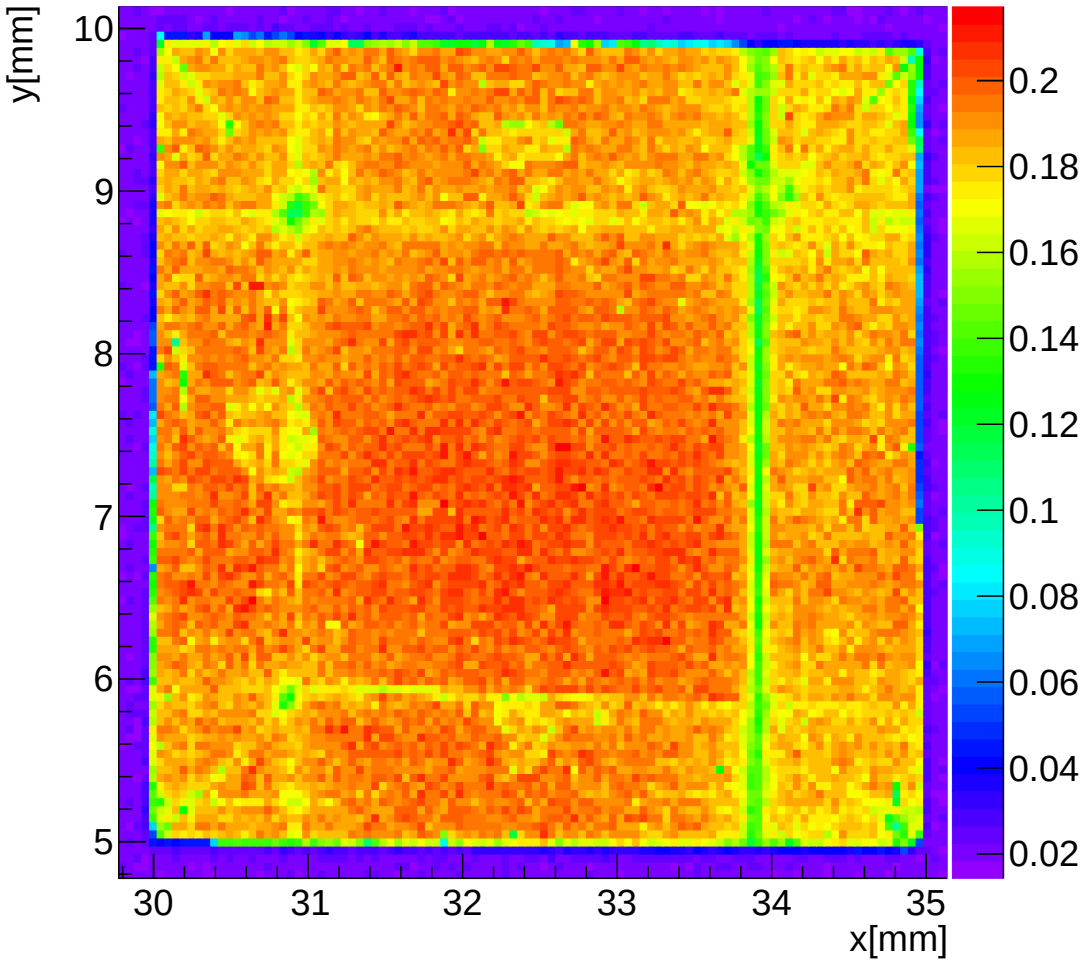

Slika 7.16: Povprečno število detektiranih fotonov v SiPM št. 18, sestavljenem skupaj z zbiralnikom svetlobe ter optično mastjo med njima.

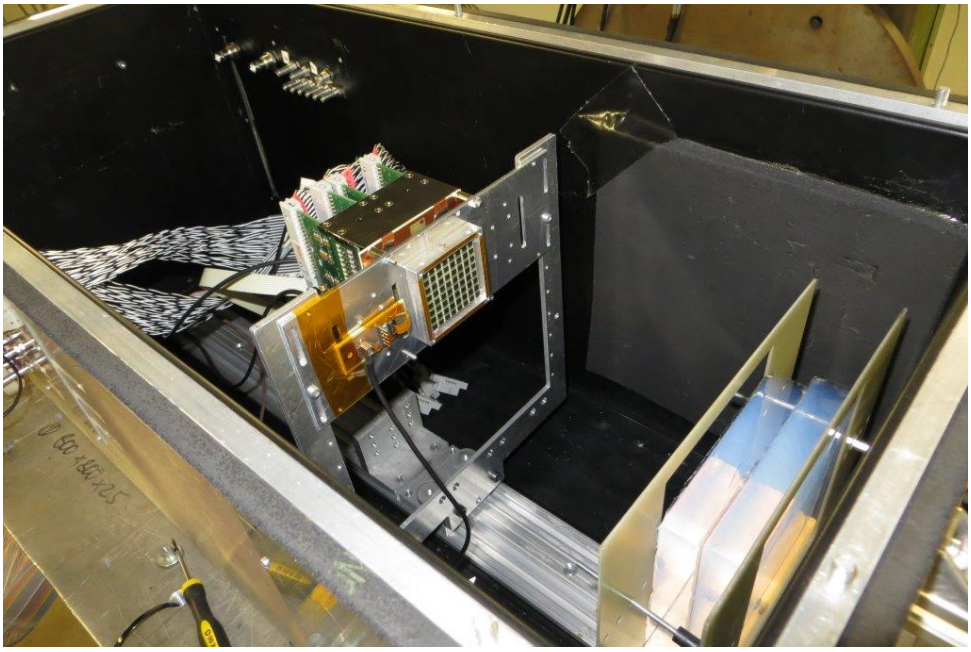

Slika 7.17: Fotografija RICH prototipa z detektorskim modulom fotonov v testnem žarku.

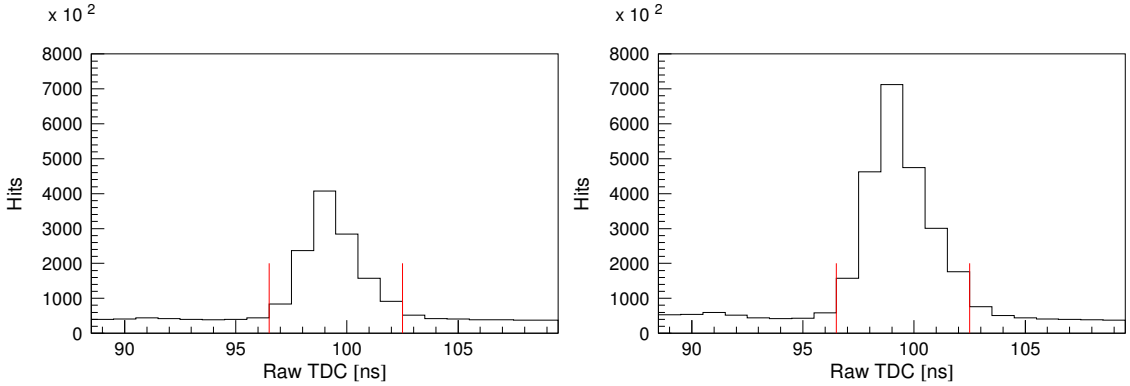

Slika 7.18: Časovna porazdelitev vseh registriranih dogodkov v meritvah brez zbiralnikov svetlobe (levo) in z zbiralniki svetlobe (desno). Časovno okno za detekcijo dogodkov je označeno z rdečimi navpičnimi črticami.

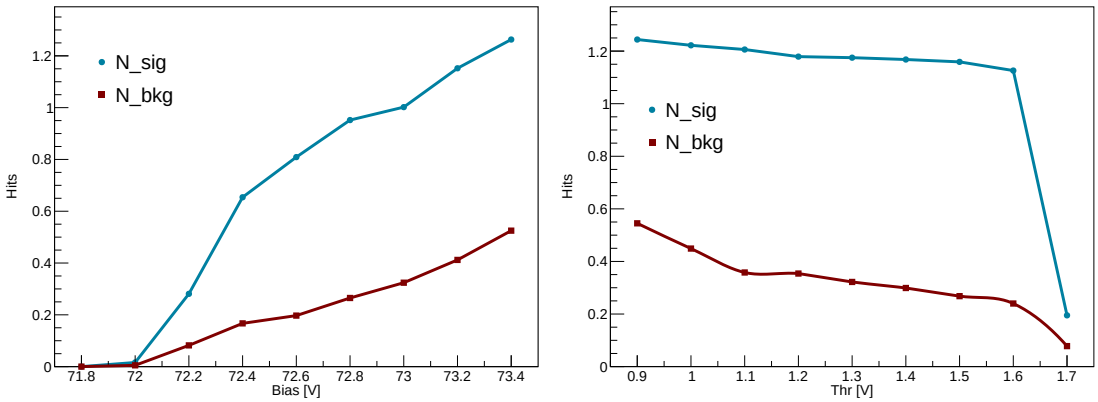

Slika 7.19: Število signalnih dogodkov N_{sig} in dogodkov ozadja N_{bkg} kot funkcija praga ASD8 diskriminatorja (levo) in delovne napetosti MPPC-ja (desno).

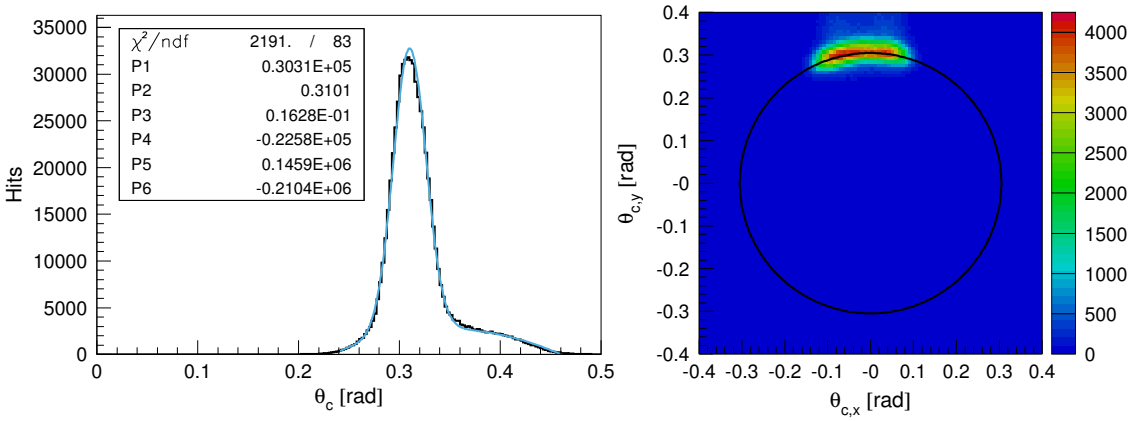

Slika 7.20: Rekonstruirani zadetki v meritvi z dvema aerogeloma in z zbiralniki svetlobe. Na levem grafu je histogram zadetkov po kotu Čerenkova. Funkcija za prilagajanje je vsota Gausove in polinoma druge stopnje. Na desnem grafu so akumulirani zadetki v Čerenkovem prostoru. Prikazan je tudi krog z radijem, enakim pričakovanem kotu Čerenkova.

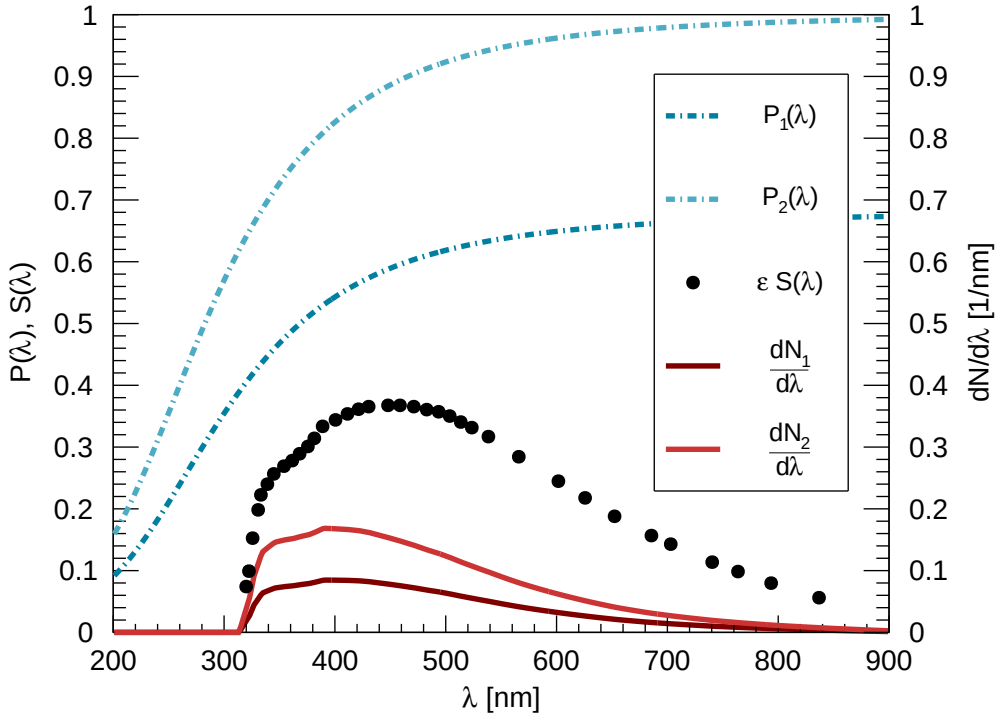

Slika 7.21: Verjetnost prehoda skozi dve plasti aerogela $P_1(\lambda)$ in $P_2(\lambda)$, občutljivost SiPM-a $S(\lambda)$, ter število detektiranih fotonov na interval valovne dolžine $^{\mathrm{d}N}/_{\mathrm{d}\lambda}$ (Eq. 7.5).

kjer je konstanta $N_0 = 2\pi\alpha$. Obe enačbi sta narisani na Sl. 7.21. Kot rezultat numerične integracije, se za število pričakovanih fotonov na cel obroč dobi:

$$N_{exp,1} + N_{exp,2} = 19 + 38 = 57. \tag{7.6}$$

Brez zbiralnikov svetlobe sta geometrijski izkoristek $\varepsilon = 0.36$ in število pričakovanih fotonov na obroč $N_{exp}^{wo} = 28$. Ko je upoštevan geometrijski izkoristek enega modula, $\varepsilon_f = 0.11$, se dobi $N_{exp} = 6.2$ in $N_{exp}^{wo} = 3.0$ fotonov, respektivno.

Izmerjene vrednosti povprečnega števila detektiranih fotonov sta $N_{LC} \approx 3.5$ z zbiralniki in $N_{wo} \approx 1.8$ brez. Iz razmera števila detektiranih fotonov brez in z zbiralci svetlobe je določen faktor zvišanja geometrijskega izkoristka ζ:

$$\zeta = \frac{N_{LC}}{N_{wo}} = 1.90 \tag{7.7}$$

7.4 Izkoristek zbiralnikov svetlobe

Pri oceni števila zaznanih fotonov, niso upoštevani:

1. Znižanje PDE-ja zaradi nižje delovne napetosti od nominalne,
2. Problemi optičnega stika zbiralnikov svetlobe s SiPM-ji,
3. Večfotonski zadetki na enem SiPM-ju.

Za izračun pričakovanega števila fotonov je bil uporabljen PDE iz Hamamatsujevega kataloga, z vrhom 37% pri 440 nm. Ta je dan pri nominalnem faktorju ojačanja in nominalni napetosti. Delovna napetost je bila nižja od nominalne, zaradi česar je bil PDE približno 2/3 nominalnega. Če to upoštevamo, je pričakovano število fotonov v meritvah brez zbiralnikov svetlobe $N_{exp}^{wo} = 2.0$, z zbiralniki pa $N_{exp}^{LC} = 4.0$.

Nadaljne izgube prinaša nepopoln optični stik zbiralnikov svetlobe s SiPM-ji. Zaradi končne debeline zaščitne plasti epoksi smole na SiPM-ju (300 μm), lahko vpadni žarki, ki se lomijo na izstopnem oknu pod kotom, zgrešijo aktivno površino SiPM-ja. To prinaša okoli 3% izgub. Poleg tega je v testnem žarku MPPC matrika bila zvita, zaradi česar SiPM-ji v sredini matrike niso imeli popolnega optičnega stika z zbiralniki svetlobe. S pomočjo simulacije sledenja žarkom je bila izračunana napaka na izkoristku zbiralnikov svetlobe pri takšnem optičnem stiku, in je znašala $5 \pm 2\%$. Drugi izvor manjšega števila detektiranih fotonov je neporavnanost zbiralnikov svetlobe in SiPM-ja, ki je znašala ± 100 μm, kar prinese dodatnih $4 \pm 2\%$ izgub.

7.5 Zaključek

Fotonski detektor je deloval v binarnem režimu, kar pomeni da je bil zadetek registriran, če je bil signal višji od določenega praga diskriminatorja. Informacija o številu fotonov na ta način ni bila izkoriščena, kar pomeni, da če več fotonov zadene en SiPM, bodo registrirani kot en foton. Binarni režim je motiviran z dvema predpostavkama:

1. Število izsevanih fotonov na delec je majhno,
2. Granularnost detektroja je velika, tako da je verjetnost, da dva ali več fotonov zadenejo en SiPM, majhna.

Kot rezultat binarnega režima, je kompleksnost čitalne elektronike močno zmanjšana.

Vendar, zaradi tega število zadetkov ne odgovarja številu prisotnih fotonov. Za oceno napake na število fotonov ki jo prinaša registrirano število zadetkov, je bila uporabljena simulacija geometrijskega izkoristka MPPC matrike (brez in z zbiralniki svetlobe). Histogram števila fotonov, ki zadenejo SiPM na poziciji 2 (*cf.* Dodatek A za pozicije SiPM-jev znotraj matrike) je prikazan na Sl. 7.22, levo. Simuliranih je 50 fotonov na tir, detektor pa je bil brez zbiralnikov svetlobe. Dana je tudi verjetnost za večfotonske zadetke, izračunana kot $P(\geq 2) = 1 - P(0) - P(1)$, ter razmerje $P(\geq 2)/P(1) = 6\%$. Le ta je ocena maksimalne izgube števila zaznanih fotonov v primeru detektorja brez zbiralnikov svetlobe.

Histogram števila fotonov ki zadenejo SiPM 2, z zbiralniki svetlobe (z izkoristkom 100%), je prikazan na Sl. 7.22, desno. Razmerje med večfotonski in enofotonski zadetki je $P(\geq 2)/P(1) = 18\%$, kar je precej večje, glede na detektor brez zbiralnikov svetlobe.

Prototip modula z Hamamatsujevo matriko SiPM-ov, MPPC S11834, se je izkazal kot odličen senzor posameznih fotonov za RICH. To potrjuje izjemno veliko število fotonov na sled, registriranih s testnim žarkom. Ločevanje med kaoni in pioni (z gibalno količino 4 GeV/c) znaša $\approx 8\sigma$, če je modul sestavljen z zbiralniki svetlobe. Tudi brez zbiralnikov je separacija večja od minimalnega zahteva v Belle II (4σ), in znaša $\approx 6\sigma$.

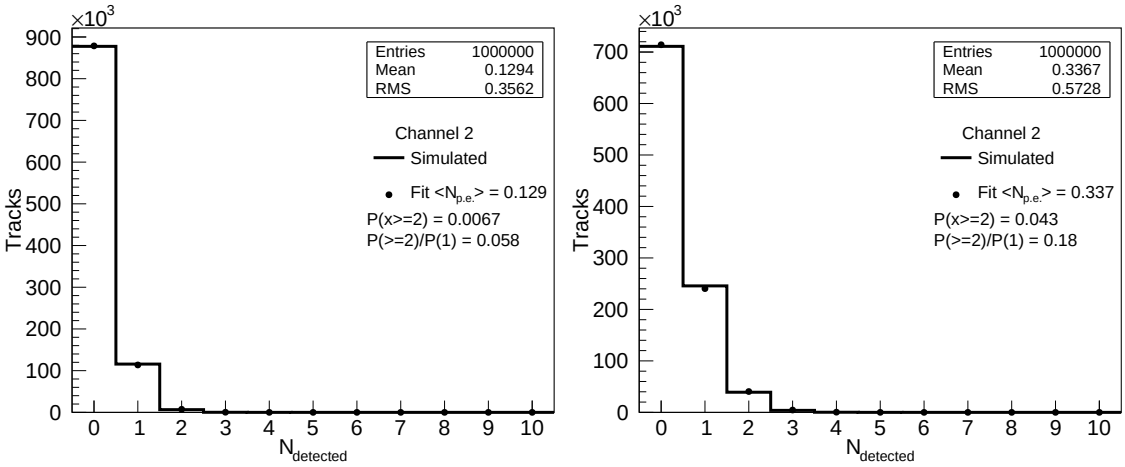

Slika 7.22: Levo: Histogram registriranih fotonov z SiPM na poziciji 2, simulacija detektorja brez zbiralnikov svetlobe. Desno: Histogram registriranih fotonov z SiPM na poziciji 2, simulacija z zbiralniki svetlobe. Prikazani so še rezultati prilagajanja Poissonove porazdelitve (točke), izračunana verjetnost za večfotonske zadetke in razmerje verjetnosti za večfotonske in enofotonske zadetke.

Index